THE FORMATION OF γ' PHASE IN DIRECTIONALLY SOLIDIFIED IN 738 ALLOY

A thesis submitted for the degree of
DOCTOR OF PHILOSOPHY
of the
University of London

by

RUBEN ROSENTHAL, BSc, DIC

Department of Metallurgy and
Materials Science
Royal School of Mines
Imperial College of Science and
Technology
London

February 1983

The present work has been carried out under sponsorship of the following Institutions :

From Brazil : Secretaria de Tecnologia Industrial
(STI/MIC)
Conselho Nacional de Desenvolvimento
Cientifico e Tecnologico (CNP_q)

From England: National Physical Laboratory

ACKNOWLEDGEMENTS

I am very grateful to my supervisor, Dr D.R.F. West, for his guidance, helpful suggestions and understanding throughout these years.

I wish to thank Dr M. McLean from the National Physical Laboratory for supplying the alloy for this research and a series of other facilities either at NPL or through offered grants; more important, however, were his supporting words during this period. Also from NPL, my special thanks to Dr P. Quested, Miss P. Henderson and Mr K. Menzies.

From the Department at Imperial College, I am indebted to the technicians who have always collaborated in the best possible way; in particular I wish to mention the excellency of the work carried out by the staff from the workshop, photographic section, 5th and 6th floor, electron microscopes and X-rays. I would like to make Mr G. Briers, from the TEM section, and Miss P. Martin from the photographic section, the direct recipients of this acknowledgement.

- To Dr P. Nash who transmitted his knowledge on nicke-based alloys.

- To my friends and family for the always present support.

- To my Brazilian sponsors, STI/MIC and CNPq; I am particularly grateful to Sr W.P. Longo and Sr J.C. Miguez Suarez for the concession of the sponsorship.

ABSTRACT

The research programme consisted primarily of a detailed investigation of the effect of variations in the solidification rate R and temperature gradient G, on the structure of directionally solidified IN 738 alloy, low carbon type; the effect of post-solidification heat treatments and creep structures have also been examined.

The solidification rates studied ranged from 9.6 mm hr^{-1} to 1200 mm hr^{-1} (the temperature gradients were 13° and 20°C mm^{-1}) and the resulting structures varied from a near plane-front condition to a very fine dendritic solidification; the experimental values for the arm spacings were found to fit well in a $(GR)^{a}$ relationship.

EDX analysis was carried out of the microsegregation and composition of the main phases present, viz. γ', γ, MC and $M_{23}C_6$; all the collected data is included and the possibilities for errors are discussed.

The γ' phase was found to be formed as continuously precipitated particles, heterogeneously nucleated particles at the grain boundaries, γ-γ' eutectic colonies and for some of the casting conditions ($12 \leq R \leq 120$ mm hr^{-1}) as fan-shaped cells of discontinuously precipitated γ' rods. The early stages for the discontinuous reaction have been investigated, mostly by the use of an 'interrupted solidification' technique and a possible initiation mechanism is proposed; the discontinuous rods were found to present dendritic-type surface perturbations, apparently as a result of the large inter-rod spacing

and the local matrix supersaturation resulting from the continuous cooling conditions. The formation of 'ogdoadically diced' cubes during continuous γ' precipitation for some of the cooling rates has also been investigated and given a similar theoretical approach to that considered for the dendritic perturbations at the discontinuous rods.

The kinetics studies related to the coarsening rates of the continuously precipitated γ' during isothermal treatment, at temperatures ranging from 850°C to 1050°C, and to the grain boundary migration rate during discontinuous reaction. For the latter, the effect of two distinct driving forces could be investigated : a chemical driving force associated with the primary discontinuous reaction during the solidification cooling, and an interfacial free energy reduction associated with a discontinuous coarsening reaction during isothermal treatment; the velocity of the migrating boundary in this case was found to be approximately 10^{-4} times slower as compared with the chemically driven reaction.

TABLE OF CONTENTS

LIST OF TABLES

LIST OF FIGURES

CHAPTER 1

LITERATURE REVIEW

1.1 Strengthening Mechanisms in Conventional Nickel-based Alloys[1,2,3]

1.1.1 Introduction

The strengthening of nickel-based alloys results mainly from the solid solution hardening of the face centred cubic γ matrix and from precipitation hardening. The γ phase is mainly strengthened by the presence of one or more of the following elements : cobalt, iron, chromium, molybdenum, tungsten, vanadium, titanium and aluminium; their role is achieved by affecting the lattice parameter and elastic modulus. Alloying elements also lower the stacking fault energy, thus inhibiting cross slip.[147]

The precipitation of discrete carbide particles at the grain boundaries, has an important role in stabilising the structure against high temperature deformation by preventing grain boundary motion. The carbides most commonly found in superalloys are MC, $M_{23}C_6$, M_6C, M_7C_3 and M_3C_2. They can nevertheless be quite deleterious to mechanical properties when forming a continuous layer at the grain boundaries, and in the cellular or acicular morphologies.

The main strengthening however results from the precipitation of the ordered γ' (Ni_3Al) phase. When in stoichiometric composition it has a lattice parameter of 3,589 Å. Several elements like chromium, titanium, iron, niobium, tantalum, vanadium and cobalt can form part of the γ' composition, by partially substituting for one or both of its components (Fig.1.1) and causing a change in γ' solvus temperature (Fig.1.2),

lattice parameter and other physical properties.

γ' particles when having a cubic morphology present the cube faces parallel to both {100}γ and {100}γ'; slip occurs mainly by the {111}<110> system but {110} planes can also be favoured.

1.1.2 Strengthening Mechanisms by γ'

Order Strengthening

When ordered, coherent particles of γ' are sheared by mobile dislocations, an anti-phase boundary (APB) is created, thus strengthening the alloy. Dislocations will nevertheless tend to move in pairs, as the movement of a second dislocation is facilitated by the elimination of the APB already created, but the strength increment will then be smaller.

For a single dislocation shearing, the strength increment is given (from Brown and Ham)[4] by

$$\Delta\tau = \frac{\gamma_o^{3/2}}{b} \left[\frac{4 f r}{\pi T}\right]^{1/2} \qquad (1)$$

and for the dislocation pair

$$\Delta\tau = \frac{\gamma_o}{2b} \left\{\left[\frac{4 \gamma_o f r}{\pi T}\right]^{1/2} - f\right\} \qquad (2)$$

where γ_o is the specific APB energy, r the average dimension of the particle intersected by a slip band, b the Burgers vector of the matrix, f the volume fraction of precipitates and T the line tension of a dislocation; since faults other than APBs may occur, the formula is more correct when considering Γ, the fault energy for shearing, instead of γ_o.

A structure with two different sizes of precipitates could

prevent dislocations from moving in pairs and avoid the drop in strength[4] compared to the single dislocation mechanism referred to above.

Dislocation by-passing of γ'

As the γ' particles increase in size, they will be by-passed either by looping or by dislocation climb; the critical size for the change of mechanism from cutting into by-passing depends on the alloy, and can vary from about 300 Å to 2500 Å, the higher sizes for alloys with high γ' volume fraction.

The increment in the critical resolved shear stress (CRSS) due to dislocation looping is given (from Orowan)[107] by

$$\Delta\tau_{CRSS} = 0.2\ Gb\ \phi\ \frac{2}{\lambda}\ \ell n\ \frac{h}{2b} \qquad (3)$$

where h is the mean particle diameter,
ϕ is the angle between the Burgers vector and the tangent to the dislocation line, λ the mean interparticle spacing, G the shear modulus of the matrix lattice; the looping mechanism requires a higher stress than climbing, the mechanism change occurring at $\sigma = \frac{Gb}{\lambda}$. Equation 3 applies only for particle sizes bigger than those corresponding to the peak strength. It can be seen in Figure 1.3 how the hardness changes in a Ni-Cr-Ti alloy with the mean particle diameter.

1.1.3 Factors affeting the γ' Strengthening Mechanisms

a) Coherency Strains

Small differences between the lattice parameter of the matrix and precipitates give rise to coherency strains, contributing to the alloy strengthening; these can be effective both during cutting and by-pass mechanisms.

The increment in the CRSS can be given (from Gerold and Haberkorn[5]) by :

$$\Delta\tau_{CRSS} = 3\ GE^{3/2}\ (\frac{hf}{2b})^{1/2} \qquad (4)$$

where G is the γ shear modulus, E the constrained lattice strain, h the mean particle diameter, f the γ' volume fraction.

b) Modulus Mismatch

γ-γ' modulus mismatch also contributes to hardening during dislocation cutting.[145]

c) Volume Percent of γ'

Beardmore et al[6] showed for a series of Ni-Cr-Al alloys that the γ' volume percent effect on the alloy mechanical properties depended on the testing temperature; for temperatures above 900°C the flow stress was directly proportional to the amount of γ', while for temperatures below 500°C there was a peak in strength at about 25% of γ'; for these low temperature tests the presence of hyperfine γ' (= 75 Å) resulting from cooling from the ageing temperature, was responsible for a great part of the strength performance.

d) γ/γ' Interfacial Area

The role of the interface between γ' and γ is mainly felt at very low strain rates, as found in creep tests. A fine and uniform γ' dispersion maximises creep properties, as shown by Jackson et al[7]; dislocation-particle interaction increases with a fine precipitate, as interparticle spacing decreases, resulting then in a decrease in the minimum creep rate $\dot{\varepsilon}$.

1.1.4 Phase Stability

Superalloys may undergo deterioration of their properties due to some phase transformations or coarsening occurring with long exposure at certain levels of temperature; the coarsening mechanisms are to be reviewed in Section 2; some phases that may be formed are sigma, Laves, μ, η and $M_{23}C_6$; the last mentioned often originates from the reaction $MC + \gamma \rightarrow M_{23}C_6 + \gamma'$.

1.2 Precipitation and Growth Mechanisms

1.2.1 Continuous Precipitation

The formation of the initial nuclei is followed by a growth mechanism which involves long range solute diffusion in the matrix (volume or lattice diffusion), the solute atoms coming from the supersaturated matrix; as full precipitation occurs, a particle coarsening mechanism becomes effective where small particles dissolve supplying solute atoms for the bigger particle 'growth'. This mechanism is usually referred to as Ostwald ripening.

Greenwood[8] deduced the critical radius for particle growth rather than dissolving from applying the Gibbs-Thomson equation for the equilibrium concentration of solute, with a particle radius r, and the Fick's law applied at the precipitate-matrix interface

$$r_{crit} = \frac{2\,\gamma V C_e}{kT\Delta} \qquad (5)$$

where γ - particle-matrix surface energy

V - atomic volume of solute

C_e - solute composition in equilibrium with a particle of infinite size

Δ - supersaturation level

An equation for the particle coarsening has been derived by Lifshitz and Slyozov[9], and independently by Wagner[10] (LSW theory)

$$\bar{r}^3 - \bar{r}o^3 = k\,t \qquad (6)$$

where $k = \frac{8\,\gamma\,D\,C_e\,V_m^2}{9\,RT}$ is the coarsening rate, and

D = diffusion coefficient of solute in the matrix

V_m = molar volume of the precipitates

$\bar{r}$ = mean particle radius

$\bar{r}o$ = mean particle radius at the onset of coarsening.

This has been rewritten by Ardell as

$$k = \frac{2\,\gamma\,D\,C_e\,V_m^2}{RT\,(\rho_m)^2}$$

where ρ_m is the ratio between the largest and the mean particle radius and has been introduced to consider the effect of high volume fraction of particles on the coarsening rate due to the occurrence of particle coalescence. By the LSW theory the cut-off in the distribution of particle sizes, or maximum particle size is at $\rho = 1.5$ times the average partice size and no correction was introduced in the case of large volume fractions of precipitate.

In another approach Ardell[11] considered modifications in the diffusion gradient at the particle-matrix interface as the volume fraction increases and proposed the equation

$$\bar{r}^3 - \bar{r}_o^3 = \left(\frac{6\,\gamma\,D\,V_m^2\,C_e\,\bar{\rho}^3}{RT\,\nu}\right) t \qquad (7)$$

known as the Modified LSW (MLSW) theory where $\nu = f\,(\rho_{max}, \phi)$, ϕ is the volume fraction and $\bar{\rho} = \int_o^{\rho m} \rho\, g(\rho)\, d\rho$, $g(\rho)$ being the distribution

function; the theoretical distribution of particle sizes is predicted to broaden quickly with increasing volume fractions (ϕ). When ϕ approaches zero the MLSW theory agrees with LSW, but as ϕ increases and reaches values of > 0.08, one of the LSW assumptions, namely steady state diffusion to a randomly distributed spherical particle, fails.

The applicability of both theories to Ni-base alloys is to be considered next but the effect of volume fraction on coarsening as predicted by the MLSW theory seems to have applied only to Livingston's[12] data on the coarsening of Co precipitates on Cu-Co alloys. One interesting point in the LSW theory is that the critical radius for particle coarsening rather than dissolution was proved to be equal to the mean particle size at a certain time.

Continuous Precipitation of γ' in Ni-base Alloys

a) Ben Israel and Fine[13] suggested that the modulated γ' structure in a Ni-Ti alloy was the result of spinodal decomposition and growth; Ardell and Nicholson[14], in another paper with an appendix about elastic interactions between particles by Eshelby, demonstrated that an aligned structure can be obtained without passing through the spinodal decomposition temperature. Gentry and Fine[15] studying different compositions of Ni-Al alloys suggested that prior to γ' precipitation in a Ni - 11.1 at % Al alloy a ferromagnetic phase has precipitated, and with a Ni - 13.8 at % Al composition γ' resulted from spinodal decomposition. The absence of ordered γ' in the early stages of precipitation as reported above may also suggest that γ' was initially formed with a "disordered" arrangement of the Ni and Al atoms and lattice order would be established gradually.

Ardell and Nicholson[16] studied γ' coarsening behaviour in a Ni-Al matrix and successfully applied the LSW theory to their results,

even though several assumptions made by the theory were not followed and should have brought a change in the geometry of the diffusion flux, viz :

- particles were cubic instead of spherical
- particles became aligned in the <100> direction as coarsening proceeded
- the distance between particles became smaller than their own diameter with coarsening due to large volume fraction of precipitates.

However, it seems that the high symmetry of the cubic particles with crystallographically equivalent planes, the absence of large coherency strains (γ-γ' misfit was about 0.5%) and the fact that some of the requirements of the theory do not appear to be very critical, account for the good agreement between experiments and theory. The activation energy for the coarsening process was calculated to be 270.5 kJ/mole, in agreement with that for Al diffusion in Ni; the γ-γ' interfacial free energy (γ_{100}) was derived to be approximately 30 mJ/m^2 (this value was later recalculated by Ardell[17] as 14 mJ/m^2).

Ardell and Nicholson/Eshelby[14] showed that the alignment of the cubic particles along a preferred direction (resulting in plate formation) is a result of elastic interactions between particles leading to coalescence through a mechanism of selective coarsening; the preferential alignment in <100> directions is possibly to favour the plates aligning perpendicular to a direction of minimum Young's modulus. The preferred cubic particle shape is probably associated with the minimising of the strain energy when the particle-matrix misfit is greater than $\sim$ 0.1%. Hagel and Beattie[18] have suggested that

up to 0.2% misfit particles remain as spheres, from 0.5 - 1% as cubes and more than 1.3% as plates. Their view on the importance of the strain energy in determining whether a tendency towards alignment exists, was reinforced by the presence of coarsened and aligned γ' at the strain (tension) field of edge dislocations while the compression side behaved as an unfavourable position for the γ' coarsening.

In some cases particles grow until they become separated by a distance much less than their diameter but no coalescence took place as has been observed by Westbrook[19] when examining sets of eight γ' particles distributed as if they were forming a larger cubic particle (such a structure was named 'ogdoadically diced cubes'); he proposed that it originated from a single nucleus. Ardell and Nicholson[14] considered that this singular structure would rather result from the elastic interactions between particles and their resistance to coalescence. Nash[20] proposed that the γ' resistance to coalescence in Ni-Al-Co resulted from the ordered structure of γ' particles : when two neighbouring γ' particles are coarsening they reduce their interparticle spacing and could eventually coalesce; nevertheless there is some probability of the two particles being out of phase and a positive energy barrier equal to the antiphase boundary energy would halt coalescence. Particles continue to grow in the other directions giving origin to odd shaped particles and when they eventually become incoherent the particle surface energy increases to values of the order of the APB energy; then a reduction of the surface energy can result from the elimination of two γ/γ' interfaces by particle coalescence. Nash has also verified that Co additions have not affected γ' morphology and that coalescence of particles occurred mostly at lower aging temperatures, when the volume fraction was higher; diffusion mechanisms were slower and did not allow the coalesced particles to grow further and recover an

equilibrium cubic shape.

The orientated coalescence resulting from elastic interactions and leading to plate formation is to be distinguished from random coalescence where the joined particles can eventually recover the previous cubic shape with further coarsening. Aligned γ' morphology could also be obtained by applying orientated stresses during high temperature annealing[21], resulting in blocks aligned in the same direction as the stress axis in the case of compressive stress and in a perpendicular alignment, for tensile stresses.

Van der Molen et al[22] found that for high γ' volume fractions in Udimet 700 a $t^{1/3}$ relation was still obeyed, but the cut-off of the particle size distribution was twice the mean average size. Chellman and Ardell[23] verified that the Ni-Al and Ni-Al-Cr systems followed the LSW theory; the Ni-Al system containing from 0.09 - 0.60 volume fraction of γ' particles exhibited a cubic shape for a small γ-γ' misfit while for Ni-Al-Cr (almost misfit free) the shape remained spherical. However, for one particular Ni-Al-Cr composition resulting in high γ' volume fraction (0.6) particles were cubic at most sizes possibly due to differences in the flux of solute atoms when the interparticle distance decreased. Their investigation also concluded that the γ' volume fraction had no effect on the coarsening rate of the γ' precipitates (in full agreement with the LSW theory).

The large volume fraction of precipitates was not solely responsible for the broadening of the predicted LSW theoretical particle size distribution in Ni-Si alloys, but also the lattice misfit, as suggested by Rastogi and Ardell[24]; they have also found that coarsening of Ni_3Si particles in a Ni - 6.5 wt % Si alloy followed the LSW theory but subsequent loss of γ' coherency caused a pronounced departure from the $t^{1/3}$ equation; they proposed that this could be

expected from the theory, as the lack of coherence would result in an increased surface energy and consequently higher growth rate.

Biss and Sponseller[25], also working with Ni-Cr-Al alloys, found results more consistent with the MLSW. The coarsening of γ' precipitates in IN 738 (conventionally cast) was found to obey the LSW theory (section 1.4.1).

This section on γ' precipitation and growth (coarsening) can be summarised as follows :

- for high saturation conditions the matrix may form γ' by spinodal decomposition while at low saturation normal nucleation and growth mechanisms are expected.
- particles nucleate as spheres as this minimises the surface energy/unit volume; as they increase size the low surface energy in the <100> planes and reduction in the strain energy will force a change into cubic particles; formation of plate shaped particles results from elastic interactions between particles favoured by a reduction in the surface energy.
- γ-γ' systems are likely to follow the LSW theory but some broadening of the particle size distribution would result from increased volume fractions and possibly from misfit considerations.

1.2.2 Coarsening of Grain Boundary Precipitates

Particles situated at grain boundaries are fed by interfacial diffusion; Kirchner[26] verified that the mean particle radius for

coarsening was proportional to $t^{1/4}$ and that the particle size distribution was initially unstable but approached a steady state condition after a certain time. Ardell[27] studied precipitation at high angle boundaries and concluded that as the volume fraction of precipitates increased, the coarsening rate constant increased and also the theoretical distribution broadened, with a $t^{1/4}$ relation being always followed; for low angle boundaries the distribution of particle sizes was found to be independent of volume fraction, the precipitate coarsening being controlled by the dislocation network in the boundary, changing from a $t^{1/5}$ relation when the particle radius is smaller than the dislocation spacing, to a $t^{1/4}$ dependence as particle radius becomes much higher than the dislocation spacing.

1.2.3 Discontinuous Precipitation

Discontinuous or cellular precipitation consists of a two phase lamellar structure originating from grain boundary migration, by a mechanism which involves short range solute redistribution behind the moving interface; such a structure is generally considered to have a deleterious effect on the mechanical properties of many alloys. Several theories have been developed concerning the related mechanisms for discontinuous formation and growth, and have been recently reviewed[20,28,29].

a) Initiation mechanisms

Tu and Turnbull[30], examining the nucleation of cellular precipitates in Pb-Sn bicrystals, proposed an initiation mechanism based on the precipitation of a small plate in a favourably orientated part of the grain boundary (Fig.1.4), resulting in the formation of a low energy coherent interface (habit plane) with one grain and a high energy incoherent interface with the other. The requirement for the

precipitate to lie in a habit plane, gave origin to a torque which caused a small deflection of the grain boundary followed by further migration in order to reduce the high energy associated with the incoherent precipitate interface. Compositional changes across the grain boundary supplied driving force (chemical) for development of the reaction. This mechanism has been also observed to apply to Ag-Cu and Cu-Ti alloys.

Fournelle and Clark[31] proposed a different mechanism based on observations of a Cu-In alloy (Fig.1.5); in this case, a slight curvature in the grain boundary originated the initial driving force for boundary migration, and as precipitation occurred at the boundary (with or without a habit plane) it exerted a pinning effect with occurrence of subsequent boundary bowing between the precipitates. The depletion of solute behind the bowed grain boundary supplied the driving force for further migration; similar mechanisms have been observed in Cu-Sb[32], Ni-Sn[33], Ni-Au[29], Ni-Cu-Au[29].

More recently Nes and Billdal[34] proposed a mechanism to explain the formation of fan-shape cells in an Al-Zr alloy (Fig.1.6); the Al_3Zr precipitate initially formed perpendicular to the grain boundary in order to minimise its high energy contact surface with the grain boundary (the interface with the matrix is low energy); due to the fast grain boundary diffusion, a tendency developed for morphological changes at the precipitate, as observed in Fig.1.6b. As this would increase the energy associated with the precipitate-boundary interface the Al_3Zr precipitate exerted a pulling force on the grain boundary thus activating a migrating mechanism; lamellae branching and further growth finally resulted in a fan-shape cell (Figs.1.6c,d).

b) Growth mechanisms

C.S. Smith[35] observed that the growth mechanism for the discontinuous reaction involved solute diffusion in a high angle boundary, the matrix having the same crystallographic orientation as the grain from which growth occurs, and the lamellae presenting an orientation relationship relative to the matrix that minimised the surface energy.

The basic driving force for the discontinuous reaction is suggested to result from a chemical driving force reflecting compositional changes across the grain boundary[35,36], but other factors like the matrix coherency strain, a surface energy term (for discontinuous-coarsening reactions) and a deformation term (mainly when recrystallization occurs), may also add to the driving force.

Several theories have been developed in order to explain the growth kinetics of the discontinuous reaction and the main equations are listed in Table 1.1.

An early model proposed by Zener[37] was based on the morphological similarity between pearlite and the discontinuous phase, however the slow diffusion rates for volume diffusion controlled (pearlite decomposition) mechanisms were later found not to apply to experimentally determined fast growth rates associated with the discontinuous reaction.

Turnbull[38] applying some of the Zener considerations, but using the grain boundary for the solute transport mechanism, proposed a mechanism whereby the interlamellar spacing should maximise the growth rate. Cahn[39] proposed that the free energy should also be minimised (several other assumptions are made in his theory). Aaronson[40] has re-derived the equation from Turnbull and considered the effect of curved lamellae tips.

Hillert[28] reviewed some of the theories for discontinuous

precipitation discussing the validity of the assumptions previously made; he proposed that the occurrence of continuous precipitation in the region ahead of the moving boundary acts as a barrier since it decreases the chemical driving force. Sulonen[41] considered that coherency strains arising from compositional differences ahead of the grain boundary would exert a driving force for the boundary movement; Bohm[42] has proposed that difference in sizes between solute atoms in the parent phase (a minimum of 11% size difference) could be used for predicting the occurrence of the reaction in Cu-based alloys. These ideas were later incorporated by Hillert[28] into his theory of volume diffusion ahead of the interface. Aaronson and Clark[43] also considered the effect of continuous precipitation on the interface movement and introduced a modification to the Turnbull equation. Hornbogen[44] has dealt with the same problem by expressing the growth rate change with time by characterising both solute concentration ahead of the interface and particle radius as time functions. In some cases there is a competition between continuous and discontinuous mechanisms, leading to a decrease and even a halt in the interface movement, or on the contrary if the chemical driving force is high enough, to a consumption of all the continuously transformed material; it is expected that initial transformation is via continuous precipitation but coarsening of the coherent precipitates would not decrease the free energy as quickly as the formation of discontinuous precipitation in regions where there is an adequate compositional gradient for the occurrence of the discontinuous reaction.

In a recent paper Meyrick[45] proposed a mechanism to explain the driving force for the grain boundary bowing for cellular precipitation in Cu-Sb alloys. After grain boundary precipitation

the solute content at the boundary decreases and the boundary energy is raised; the boundary would then move in order to restore its solute concentration and decrease its energy, provided this reduction exceeds the energy increase due to the increased grain boundary area; this mechanism, associated with interface diffusion and preceded by a nucleation mechanism possibly like one of those described by Tu and Turnbull or Fournelle and Clark, would result in discontinuous precipitation. Cahn[109] also in a recent analysis pointed out that if $V > \frac{D_L}{\lambda}$, no lattice diffusion ahead of the interface occurs (thus the concentration gradient across the boundary is maintained) and the interface movement will not decrease.

V is the velocity of each element of the boundary

D_L is the lattice diffusivity

λ is the interatomic distance

He also proposed that the initiation of the cellular precipitation is not related to any specific defect or asymmetry in the grain boundary.

The effect of lattice strain due to prior deformation is usually to increase the formation of discontinuous precipitate[31], mainly if recrystallization follows (see reference on Ni-based alloys, section 1.2.3d), but continuous precipitation may be favoured by the lattice strain, thus competing with the cellular reaction.

Gust[46] discussed the validity of the theories based on the assumption of constant interlamellar spacing, λ, at constant temperature, average values for compositional differences and grain boundary diffusivity, and suggested that individual cells should instead be characterised.

c) The effect of grain boundary structure on growth kinetics

Hornbogen[44] suggested that the velocity of the reaction front depends on two terms : a high driving force or a high mobility, the degree of mobility being dependent on the structure of the front, and determined by the jump frequency ζ^{-1} and the thickness λ of the grain boundary. Gleiter[47] showed that high coincidence boundaries where step density was low, presented low mobility; however, if the grain boundary acts as a sink or a source for vacancies, mobility would increase[48].

Wirth and Gleiter[49] investigated the effect of undercooling on the initiation of cellular reaction at low and high energy grain boundaries, and explained an enhancement of 10^3 in the diffusion coefficient between a static and a migrating boundary in terms of different atomic structures between both types of boundaries; this difference could result from grain boundary precipitation[50], dislocation incorporation[51], vacancy drag or production[52,53]. Vacancies can be produced by annihilation of dislocations or by the grain boundary itself; however vacancy interaction with the boundary can also decrease the driving force[53].

Balluffi and Cahn[54] proposed a mechanism where differences in the diffusion coefficient of the atoms along the grain boundary cause a self-sustaining climb of dislocations and motion of their associated grain boundary steps. There is however, very little evidence from other reported experiments of unequal solute diffusion rates in grain boundaries. Recent results by Mittemeijer and Beers[55], and verified by Grovenor[56] on Cu-Ni bi-layer specimens, revealed that the diffusion coefficients on moving interfaces were of the same order as those for stationary boundaries.

d) Discontinuous precipitation of γ' in Ni-based alloys

Discontinuous precipitation has been found in many systems such as Ni-Al[57], Ni-Si[57], Ni-Be[57], Co-Ni-Ti[59], Ni-Cr-Al[57], Ni-Co-Al[60], Ni-Cr-Nb[58], Co-Ni-Ti-Al[59], Ni-Cr-Co-Nb[58], Ni-Cr-Nb-Ti[58] and also in some commercial alloys[61], but for the Ti and Nb containing alloys, a more stable phase such as Ni_3Ti (η) or Ni_3Nb (δ) forms preferentially. Hagel and Beattie[18] have suggested that discontinuously precipitated γ' forms when the γ-γ' mismatch is higher than 1%, but Hornbogen and Roth[57] observed discontinuous γ' in a Ni-Cr-Al alloy with 0% γ-γ' mismatch.

In deformed Ni-Al alloys[62] discontinuous precipitation also formed within the grains; it could also be seen associated with a recrystallisation front.[63] In deformed Ni-Cr-Nb, Ni-Cr-Co-Nb, Ni-Cr-Nb-Ti[58] alloys discontinuous precipitation was observed at twin boundaries.

Tsinenko et al[59] confirmed that γ' lamellae were incoherent with the matrix in Co-Ni-Ti and Co-Ni-Ti-Al alloys, the discontinuously transformed regions presenting much higher microhardness values; the activation energy for the process was 139 kJ/mole which suggested an interface controlled mechanism as the energy required for volume diffusion would be considerably higher than this value. Increase in aluminium content and plastic deformation prior to aging were found to aid cellular transformation; the amount of transformed material followed an Avrami[146] type time dependent equation with n = 0.7, i.e. less than the minimum expected, n = 1, for grain boundary nucleation. Nash[20] found values for the coefficients k and n from plotting the fraction of discontinuously transformed material f as $\log(\ln 1/_{1-f})$ vs log (aging time) for Ni-Co-Al alloys, also finding values of n < 1. Reversion temperature experiments by Nash showed that dissolution of

the cellular region above the solvus was by a return of the moving boundary to its prior position and in this case the n coefficient was calculated to be 1 showing that continuous precipitation ahead of the interface, causing a time dependent growth rate, was responsible for previous low values of n. Cobalt was found to increase the propensity for discontinuous transformation, and in high Co content alloys, depending on temperature, the transformation occurred completely by the discontinuous mode in reasonable agreement with some previous observations that Co decreases the coarsening of continuously precipitated γ'.

Tsinenko et al[59] also verified that impingement of γ' lamellae was followed by a second reaction where the lamellae were coarser and spacing between them larger, the driving force for the second reaction being the reduction in surface area per unit volume; Fournelle[64] suggested that the second coarsening reaction for η Ni_3Ti lamellae in an Fe-30 wt % Ni-6 wt % Ti alloy was the result of impingement during lateral growth as seen in Fig.1.7, this mechanism also explaining the apparent discontinuous nucleation on both sides of the grain boundary. Fournelle tried to apply a coarsening theory by Livingston and Cahn[65] to calculate the second reaction growth rate, but there was no agreement with his results. This theory predicts that reduction in the surface energy with decomposition of the first cells is the driving force for the reaction

$$-\Delta F = 2\,\gamma\,\nu\,\left(\frac{1}{\lambda_1} - \frac{1}{\lambda_2}\right) \qquad (8)$$

where ΔF - free energy ($J\ mol^{-1}$)

γ - interlamellar surface energy

ν - molar volume

λ_1, λ_2 - lamellar spacings

but it does not take into account the remaining chemical free energy from the incomplete growth of the first lamellae. Petermann and Hornbogen[66] have considered this effect and Fournelle from their results has concluded that Ni diffusion at the grain boundary controlled both first and second reactions (from 400° to 800°C) but the theory did not hold satisfactorily at 900°C. It seems that not all the chemical free energy available from the incomplete first reaction would be used in driving the second[64].

Nash[20] has made an extensive study of the γ' lamellae morphology and growth mechanisms in Ni-Co-Al alloys; the shape could vary from long straight parallel lamellae at early stages to large irregular blocks as the moving boundary advances; the lamellae grew initially coherently with the matrix and perpendicular to the growth front but continuous precipitation ahead of the interfaces decreased the driving force for discontinuous growth, and the lamellae became incoherent in order to reduce the free energy and complete the reaction resulting in coarser lamellae morphology. The discontinuous regions were found to have higher hardness.

Barlow and Ralph[67] have studied the effect of carbon and chromium on the propensity for discontinuous reaction in Nimonic 80A; they verified that an increase in chromium content favoured discontinuous precipitation as the γ'/γ and $M_{23}C_6/\gamma$ mismatches increased and hence the interfacial energies (the interfacial energy has been postulated by Hagel and Beattie[18] to be a critical parameter for discontinuous phase nucleation). Decrease in the carbon content will reduce $M_{23}C_6$ precipitation thus increasing chromium content at grain boundaries and result in a higher propensity for cellular precipitation; in the low carbon Nimonic 80A variant earlier stages of discontinuous nucleation resulted in the formation of $M_{23}C_6$ lamellae; later γ'

lamellae were formed and grew aligned with the carbide.

Discontinuously formed γ' has been observed in directionally solidified IN 738 (section 1.4.2) for some casting conditions.

1.3 Directional Solidification (DS) of Nickel Based Alloys

The effect of unidirectional heat flow during the solidification of nickel-based superalloys is to provide a columnar structure aligned with the flow, provided there is no nucleation ahead of the advancing solid-liquid interface[68,69]; the resulting decrease in grain boundaries transverse to the major stress axis greatly improves some mechanical properties, like creep and ductility, as cracks usually propagate along grain boundaries, and resistance to high temperature stress rupture, by inhibiting grain boundary sliding. Directionally solidified materials are required to present adequate creep strength and ductility, thermal fatigue resistance, and oxidation/corrosion resistance.

For most systems the preferred columnar grain orientation is [001], which in consequence increases the intrinsic yield stress with temperature, as octahedral slip (rather than cube) prevails for the dispersed γ'(Ni_3Al) phase at this orientation[69]. Piearcey and Tekelson[70] have compared the rupture lives for Mar-M200 with the stress axis aligned to the [001], [111], [011] directions and found that in fact the [001] orientation has resulted in longer lives, followed by [111].

Directional solidification can also be used to produce single crystals and, depending on the composition, aligned eutectic composites. Tiller et al[71] verified (for Hastelloy-X)that by increasing the solidification rate, R, or decreasing the temperature gradient at the solid-liquid interface, G, the interface shape changed

from planar to cellular, then cellular dendritic and finally dendritic. Depending on the alloy and on the specific requirements for its performance one or other kind of structure may better apply; for Hastelloy-X the dendritic structure proved to be stronger and more ductile than the cellular structure, since for the former the impurities were isolated in the interdendritic region while for the cellular solidification the low melting phases were located at the grain boundaries, and were therefore more detrimental to mechanical properties.

Tien and Gamble[72] suppressed the dendritic structure in Mar M200 by altering G and R based on the constitutional supercooling proposition for binary alloys (Tiller and Rutter[110], viz. $\frac{G}{R} \geq \frac{\Delta T}{D}$ where ΔT is the melting range of the alloy and D the effective diffusion coefficient of atoms in the liquid, supposed to be approximately 5.10^{-5} cm^2 sec^{-1}. The resulting structure and properties depended on whether the alloy was carbide free due to low carbon levels (planar front interface) or with carbide formation (cellular interface); the ductility associated with the cellular structure was four times that from the dendritic solidification mode; a great improvement was also expected from planar front single crystals as carbides that are a main site for crack initiation become unnecessary as grain boundary strengtheners, and could be suppressed by low carbon contents. With the dendritic structure γ' particle sizes were more heterogeneous consisting of smaller particles in the core (lower Al and Ti contents) and bigger ones in the interdendritic regions; other reported[73] disadvantages were : carbides aligned both parallel and perpendicular to the growth direction; higher number of freckles were also present as they are associated with low $\frac{G}{R}$ values; higher porosity as gas bubbles were more easily trapped; low melting point γ' eutectic was

formed due to segregation. For the cellular structure γ' sizes were more uniform thus retarding coarsening and improving high temperature creep strength; carbides were aligned parallel to the growth direction and γ' eutectic was avoided. The planar front structure resulted in a highly uniform distribution of γ' particles.

It has been noted by McLean and Schubert[74] that alloys with a narrow melting range like Mar M200 and Mar M246 present a good improvement in rupture life when directionally solidified, while others like IN 738 with a large melting range show no significant improvements under the same $\frac{G}{R}$ ratio conditions and probably should require solidification at higher $\frac{G}{R}$ ratio. Several alloy compositions are listed in the appendix.

The solidification rate R will affect the primary dendritic arm spacing due to the effect on time for solute diffusion; Kotler et al[75] verified that for Pb-Sn alloys primary (λ_p) and secondary (λ_s) arm spacings are differently affected by variations in G and R : as R increased both λ_s and λ_p decreased but λ_s decreased more, and as G increased λ_p decreased and λ_s was not affected. Smaller dendritic arm spacing resulted in better tensile properties for steels.

McLean and Schubert[74] verified for IN 738 and other nickel based alloys that the dendritic spacing and γ' particle size are directly related to the cooling rate (GR). Several proposed relations between the dendritic spacing and its controlling parameters are listed in Table 1.2.

Merz et al[77] have studied the effect of the cooling rate GR on the segregation ratio of a Ni-Al-Ta dendritic monocrystal and found that by increasing the local cooling rate, the segregation ratio (maximum concentration/minimum concentration ratio) of both Al and Ta increased, but the effect of increasing both the cooling rate and undercooling was to improve the homogenization of a Ni - 30 wt % Cu

alloy. As homogenization of nickel-alloys is difficult to achieve by heat treatments, removal of segregation effects can be better performed by suppressing the dendritic structure with proper control of the $\frac{G}{R}$ ratio (high values) or if the dendritic structure is to be kept, reducing the dendritic spacing (high GR values) possibly followed by post-solidification heat-treatments. Piearcey et al[69] observed in Mar M200 that W strongly segregated to the dendrite core; the core was also rich in Co and poor in Cr, Ti, Ni; the structure far from the chill was coarser as the solidification rate was lower, resulting in larger grains and tertiary dendritic arm spacing, coarser γ-γ' eutectic and MC carbides, and increased porosity.

Bhambri et al[78] verified that Al segregation in IN 713C was preferentially in the dendritic core against normal observations in other Ni-alloys; Nb and Mo showed relative high segregation ratios. The volume fraction of γ-γ' eutectic did not change with cooling rate in contrast to the behaviour of IN 100 where the amount of eutectic was drastically reduced by very slow cooling[79]; the size of the eutectic regions increased with decreasing cooling rate (far from the chill). The eutectic region was rich in Ni, Al, Ti and poor in Co, W, Cr and its formation considered to be detrimental to the alloy properties as desirable elements for strengthening were found concentrated in the eutectic; however, the removal of the eutectic by solution heat treatment was not recommended as incipient melting could occur. Bhambri et al[78] also observed only a small degree of macrosegregation along the ingot; γ' particle size and volume fraction were unchanged with cooling rate as was also the case in Mar M200.

Viatour et al[80] found that the eutectic was coarser with slow cooling rates in Mar M002, and it was a preferential site for crack initiation; the temperature for eutectic formation was at

1220°C as identified by differential thermal analysis (DTA), and some MC carbides formed at 1400°C while the liquidus temperature was 1330°C.

Bhambri et al also detected unmelted carbides which, during the slow movement of the planar solid-liquid interface, could have been pushed ahead of the interface and the resulting structure was almost carbide free; the carbide shape was found to vary with solidification structure : octahedral shaped for the planar front condition with faces parallel to {111} planes (minimum interfacial energy), plate-like and orientated along the growth direction for the cellular growth, and, for dendritic growth, the shape depended on the cooling rate, being octahedral for low GR and dendritic shaped for high GR. Also for IN 713C, Fegan et al[81] concluded that the volume fraction of MC carbide remained constant along the ingot but the carbide-matrix interfacial area decreased with increasing solidification time; coarsening of the carbide particles depended on normal diffusion process and "collisional" coalescence.

Fernandez et al[82] have used a process of interrupting the directional solidification by fast cooling (quench) in order to follow the transformations in IN 100 dendritic monocrystals; MC carbides formed at 1265°C and grew from the melt while γ-γ' eutectic formed at 1224°C and γ' at 1168°C. The carbide geometry was studied for different conditions of G and R; low $\frac{G}{R}$ values resulting in faceted MC carbide morphology and high values resulting in a Chinese script morphology with the particle sizes decreasing with increasing GR. Script carbides could increase crack propagation while faceted carbides were not deleterious.

Hf was found to be important for directional solidification as it inhibited intergranular cracking[102], but it also induced γ-γ' eutectic formation with Hf segregation to the associated carbides;[103] increase in Hf content up to 0.9 wt % was reported to increase the stress rupture life and elongation[104].

1.4 IN 738 Alloy

1.4.1 IN 738 conventionally cast

In the conventionally cast condition IN 738 has many current application, viz. as blade material for electrical power generation turbines, facing temperatures up to 880°C, for industrial and marine gas turbines[83,84] and it presents good creep rupture strength up to 1000°C. The nominal composition (wt%) of the alloy is[85]

C	Co	Cr	Mo	W	Ta	Cb	Al	Ti
.17	8.50	16.00	1.75	2.60	1.75	.90	3.40	3.40

B	Zr	Ni
.01	0.10	Bal

Prior to service the component is submitted to a standard heat treatment : 2 hours at 1120°C, air cooled, plus 24 hours (or 16 hours) aging at 843°C, air cooled; Bieber and Mihalisin[85] concluded that this treatment gave better stress rupture properties when compared with various other treatments. In the cast condition the phases present consisted of MC carbides, eutectic γ-γ', irregular shaped γ' particles; after the standard heat treatment, $M_{23}C_6$ precipitated at grain boundaries, the matrix decreased its tendency to σ formation, fine γ' particles precipitated after cooling from 1120°C, and the coarse γ' particles became more cubic shaped, while γ-γ' eutectic and MC carbides remained unchanged. The γ-γ' eutectic dissolution temperature was found to be about 1205°C but the stress rupture properties were not improved after complete removal of the eutectic by heat treatment; the temperature for complete solutioning of γ' was estimated to be in the range 1150-1177°C and the γ' composition was $(Ni_{.922}, Co_{.058}, Cr_{.017}, Mo_{.002}, W_{.002})_3 (Al_{.518}, Ti_{.352}, Ta_{.046}, Nb_{.041}, W_{.019}, Cr_{.027})$ while the carbide composition was $(Ti_{.50}, Ta_{.20}, Nb_{.20}, W_{.04}, Mo_{.03},$

$Cr_{.02}$, $Zr_{.01}$)C. The deformation process involved dislocation "looping" rather than "cutting" during rupture tests at 815°C as γ' presented high strength due to the Ti and some Ta, Nb in its composition.

Hoffelner[86] et al could identify after long exposure heat treatments the phases γ, γ', MC, $M_{23}C_6$, M_6C, M_3B_2, M_2CS and sigma (σ). M_2CS was formed only in the low carbon alloy associated with the γ-γ' eutectic islands while sigma was formed after 20,000 hours at 788°C also with a low carbon (0.11%) variant alloy. The γ' volume fraction slightly increased with heat treatment up to 48%; both fine and coarse particle coarsening followed a log $t^{1/3}$ relation and with longer times the morphology changed from blocky into spherical. After the standard aging treatment the γ' size distribution consisted of fine particles of 0.14 μm and coarser ones of 0.58 μm (diameter).

McColvin[87] extensively studied the effect of the standard heat treatment and of a coating treatment on phase morphology and creep rupture properties. With solution treatment at 1120°C only the fine γ' from the core region went into solution due to the smaller Al and Ti concentration levels in the core thus decreasing the γ' solvus. Very fine particles, resulting from the air cooling, formed in the core and also between the large particles in the interdendritic region and coarsened with aging at 843°C resulting in a "bimodal" size distribution of particles comprising ∿ 50% volume fraction; a coarse ring of γ' particles outlined the core (due to high Al and Ti concentrations). It was also verified that for a heat treatment corresponding to a coating process the creep rupture life substantially dropped, mainly for thin castings, as the resulting γ' distribution was different from that of thick castings.

Stevens and Flewitt[88] have accurately determined the γ' solvus temperature for complete γ' solutioning as 1170 ± 3°C; they verified

that aging at 827°C gave a maximum γ' volume fraction (0.45) with a large fraction of γ' spheroids and peak hardness. The initial as-cast distribution of γ' consisted of particles of approximate cubic morphology (0.4 μm diagonal) which after the standard heat treatment resulted in regular shaped cuboidal particles (0.4 μm diagonal) and a fine distribution of spheroidal particles (0.05 - 0.1 μm diameter).

The mean spacing between cuboids decreases during coarsening while that between spheroids increases (Fig.1.8); thus during creep deformation, one or the other precipitate morphology controls the creep rate (Fig.1.9), the total strengthening depending on the volume fraction of both particle sizes and temperature. Studying the effect of time on particle growth[83], both precipitate sizes obeyed the LSW coarsening equation even with the spheroids feeding the coarser cuboids until total consumption, the total volume fraction remaining unchanged; by the LSW theory, the spheroidal particle coarsening should not have followed the $t^{1/3}$ equation due to the variation in volume fraction.

The activation energy for coarsening was estimated[83] as 2.69×10^5 J/mol in good agreement with energies for Al and Ti diffusion in Ni. The distribution of particle sizes revealed a cut-off of 1.75 $\bar{r}$, with $\bar{r}$ = 30.5 nm. Creep deformation at 750°C (stress = 460 MN m^{-2}) and 850°C (stress = 260 MN m^{-2}) did not affect the coarsening rate of the γ' spheroids; the creep curves did not show pronounced primary creep or normal steady state secondary creep but a continuously increasing curve (Fig.1.10 and Table 1.3).

Stevens and Flewitt[106] also verified that by applying a regenerative (standard) heat treatment to a creep tested material the γ' morphology could be restored to a near pre-tested condition; cavities were observed

to appear at the tertiary creep stage, but they could also be eliminated if heat-treatment cycles under hydrostatic pressure were applied.

McColvin's results[87] on creep deformation showed that dislocation climb was rate controlling at high temperatures - low stresses, as the stress was insufficient to cut particles or bow dislocations around the coarser particles; for larger interparticle spacings the stress necessary for dislocation bowing is lower and should be rate controlling, but the presence of small spheroidal particles then inhibited this mechanism.

The Ansell and Weertmann[89] equation predicts for low stress conditions ($\sigma < \frac{\mu b}{\lambda}$)

$$\dot{\varepsilon} \alpha \frac{1}{h^2} \tag{9}$$

where $\dot{\varepsilon}$ - creep rate

h - particle size

λ - interparticle spacing

b - Burger's vector

μ - shear modulus

At lower temperature-high stress conditions particle cutting and/or dislocation bowing controlled the creep rate, as small particles could not inhibit dislocation movement at high stress levels. Then for high stress levels[89] ($\sigma > \frac{\mu b}{\lambda}$)

$$\dot{\varepsilon} \alpha \frac{\lambda^2}{h} \tag{10}$$

or $\dot{\varepsilon} \alpha h$ as the interparticle spacing is related to the particle size.

McLean and Schubert pointed out that γ' distribution was the

main factor to be considered at high stress creep, while grain boundary morphology and orientation should control creep rupture at low stress or high temperature levels. Lindblom[90] also mentioned the effect of solid solution hardening, carbide precipitation and increased grain size in improving creep life.

The effect of volume fraction of precipitates on creep rate has been calculated by Hornbogen and Gleiter[91] as $\dot{\varepsilon} \alpha f^{1/3}$ and by Brown and Ham[4] as $\dot{\varepsilon} \alpha (Af^{-\frac{1}{2}} - f)$, A = a constant. Lupino[92] verified that after standard heat treatment the creep rate of IN 738 was proportional to $f^{1/3}$ and after aging $\dot{\varepsilon} \alpha (f^{-\frac{1}{2}} - 1)$.

McColvin[93] tried to improve the high cycle fatigue resistance of IN 738 by reducing grain size through increasing the cooling rate and by hot isostatic pressing (HIP), as this method would suppress porosity and give a very homogeneous structure. HIP has resulted in better fatigue properties but both methods failed in improving tensile and creep properties; the fracture after fatigue rupture was transgranular with porosity associated with crack nucleation. Bacon and Smart[94] found that interdendritic microporosity did not markedly affect fatigue crack propagation as compared with its effect on strength levels, although it can be the initiating site of fatigue cracks.

Bachelet and Lesoult[95] verified that microporosity increased in IN 738 with increasing superheat and decreasing mould temperature. Increasing carbon content also resulted in increased porosity, probably due to carbide hampering capillarity feeding.

Thermal fatigue properties of IN 738 are good, but deterioration can happen after long exposures at high temperatures. Speidel[108] verified that by reapplying the standard heat treatment the previous performance could be restored. Strain cycling in conjunction with

temperature was found to be less deleterious to IN 738 properties than it proved to be with other superalloys. With high cycle/high temperature long time experiments, creep strength rather than fatigue was the limiting factor; also at high temperature, fatigue crack propagation was intergranular while at low temperatures it was both inter and intragranular. A fine grain structure was reported to improve thermal fatigue while carbide films, low melting phases and porosity were deleterious.

1.4.2 IN 738 Directionally Solidified

Quested et al[96] prepared IN 738 by directional solidification using a method based on the Bridgman-Stockbarger crystal technique where the casting is removed at a controlled withdrawal rate. The solidification rate and the withdrawal rate were the same due to the applied coolant system; the furnace and the processing are described in Chapter 2. Different casting parameters were considered, viz. solidification rates of 9.6, 30, 60, 300, 600 and 1200 mm hr^{-1} while the temperature gradient was about 13°C mm^{-1} for most withdrawal rates except for a very fast rate (1200 mm hr^{-1}) where a higher temperature gradient of 20°C mm^{-1} was needed.

Under these conditions the transition from planar to cellular front was at 9.6 mm hr^{-1}, from cellular to cellular-dendritic at 30 - 60 mm hr^{-1}, from cellular-dendritic to dendritic at 300 mm hr^{-1}.

Primary and secondary arm spacing were differently affected by the cooling rate

$$\lambda_p \alpha (GR)^{-0.3} \quad (11)$$

$$\lambda_s \alpha (GR)^{-0.4} \quad (12)$$

The phases present were identified with the help of an interference film technique.

MC carbides were concentrated in the intercellular or interdendritic regions and their shape and size varied according to the solidification rate. $M_{23}C_6$ precipitated at the grain boundaries after the materials were submitted to the standard ageing treatment (the same applied for the conventionally cast material). γ' distribution was more homogeneous near conditions of planar front and particle size decreased at higher solidification rates but no detailed study was undertaken; discontinuous γ' precipitation was present at solidification rates varying from 30 to 60 mm/hr^{-1}.

Microprobe analysis showed that Cr, Co, W segregated to the core region and Ni, Al, Ta, Nb, Ti were higher in the interdendritic regions; dendritic segregation together with slow cooling rates would lead to discontinuous precipitation.[96]

Quested et al[96] also compared the creep properties of the different structures, and concluded that the optimum creep behaviour at 850°C and under a stress of 250 MN m^{-2} was obtained for a solidification rate of 300 mm hr^{-1} after the standard heat-treatment was applied; this gave greater creep strength, longer rupture life and higher ductility.

Henderson[105] concluded that the magnitude of the threshold (friction) stress σ_o for creep was the sum of the respective stresses for dislocation climb around the γ' cuboids and spheroids, and that the spheroids contributed to over 50% of this value.

DTA analysis for IN 738 LC suggested[97] :

Liquidus temperature	1332°C
carbide formation	1329 - 1300°C

eutectic γ-γ' formation	1205 - 1198°C
solidus temperature	1198°C
γ' solvus (interdendritic region)	1198 - 1170°C

Other experiments however refer to the liquidus temperature as 1315°C and raise some doubts about the accuracy of the results above.

Scarlin[98] verified that discontinuous precipitation of γ' also formed at higher solidification rates (150 mm hr^{-1}), with composition similar to the continuous γ'; the advancing boundary appeared to be parallel to {111} planes. The microhardness of the region was 25% less when compared to the continuous precipitated region and it was suggested that this could lead to stress concentration, resulting in cavitation and failure. The driving force for the discontinuous reaction was proposed to be the energy decrease due to the reduction of chemical potential. A 2 hrs heat treatment at 1120°C caused some breaking up of the lamellae due to partial solution, followed by reprecipitation of small γ' particles occurring during cooling; after 200 hours at 1100°C complete breaking up of the lamellae had occurred. Discontinuous precipitation of γ' occurred during recrystallization[99] at 1120°C, and the kinetics of recrystallization were found to be independent of the size of primary γ' particles.

Woodford and Frawley[100] studied the effect of grain boundary orientation to the stress axis on creep rupture properties and verified that the longitudinal orientation presented the best rupture life at high temperature - low stresses but when conditions changed to low temperature - high stresses the rupture life was the worst of all the orientations. Ductility was higher for the longitudinal orientation but creep strength was higher for the diagonal and

transverse orientation; failure for the longitudinal orientation was transgranular and for the transverse, was intergranular with secondary intergranular cracks.

Crack initiation in thermal fatigue occurred at the same stress for directionally solidified and conventionally cast IN 738 at 850°C[101] but crack growth was less with the aligned structure.

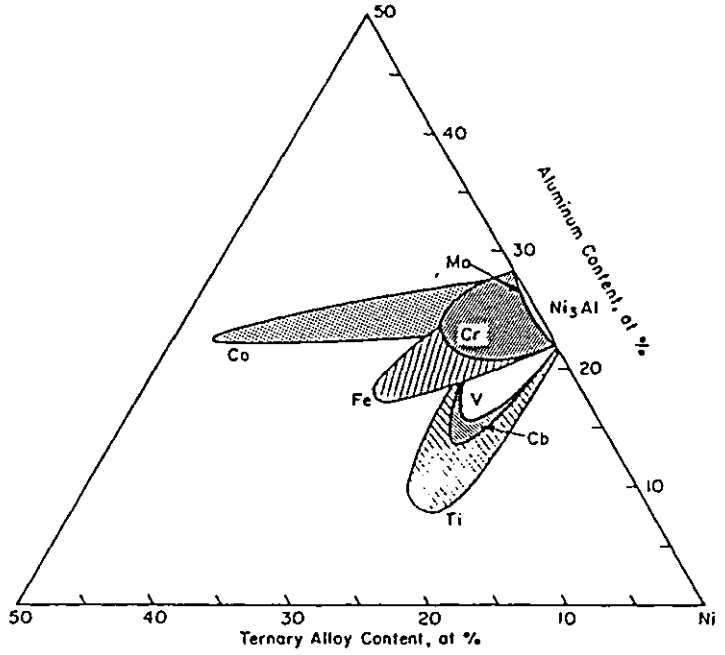

Fig. 1.1 Semischematic presentation of Ni_3Al solid-solution field approximately 2100°F (1100°C) for various alloys [2].

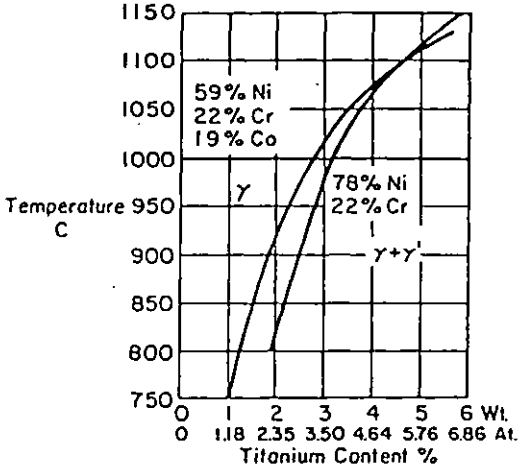

Fig. 1.2 Effect of substituting cobalt in a nickel-base system on the γ' solvus. Ti - Al ratio = 1 : 1 Heslop[140]

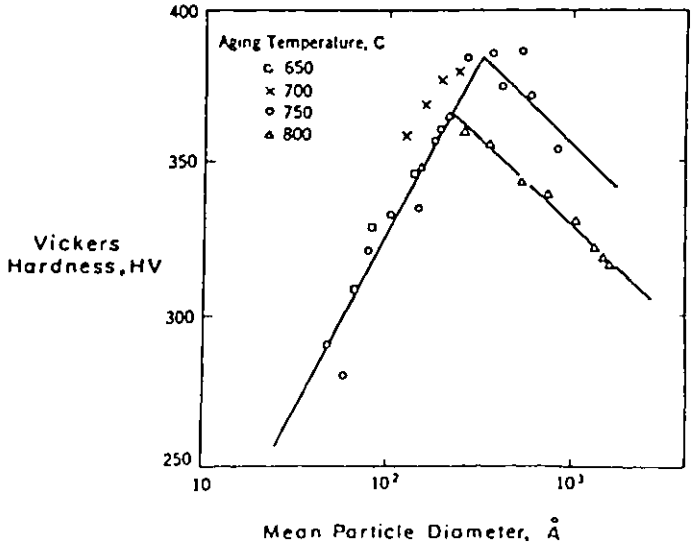

Fig. 1.3 Effect of particle size on hardness of Ni-Cr-Al-Ti alloys[141]

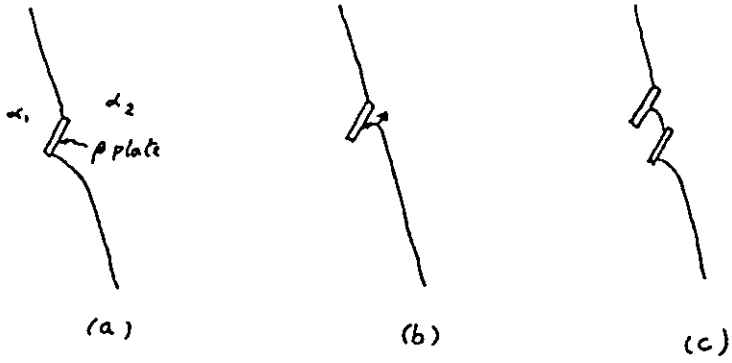

Fig.1.4 Tu and Turnbull cellular precipitation mechanism[30]

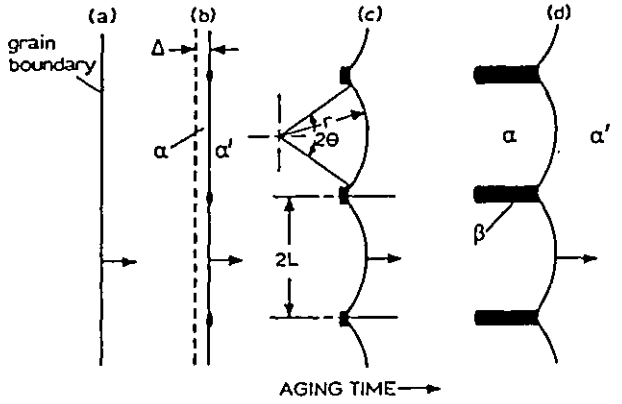

Fig.1.5 Schematic diagram showing essential steps in nucleation of reaction on a migrating boundary; after Fournelle and Clark[31]

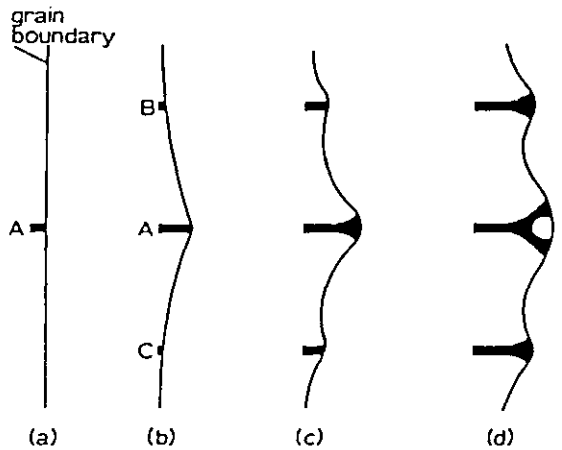

Fig.1.6 Schematic diagram showing nucleation mechanism proposed by Nes and Billdal[34] for Al—Zr alloys

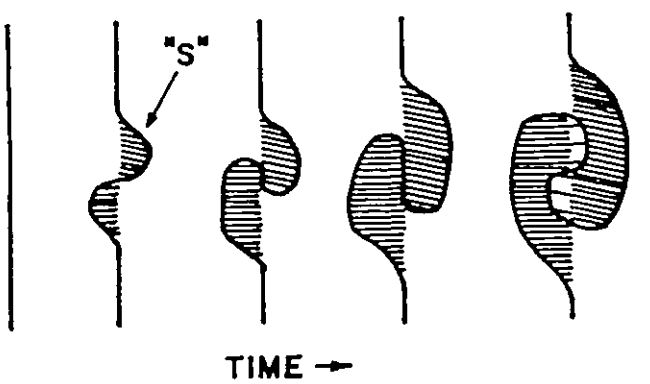

Fig. 1.7 mechanism for the formation of second cells at prior austenite grain boundaries.[64]

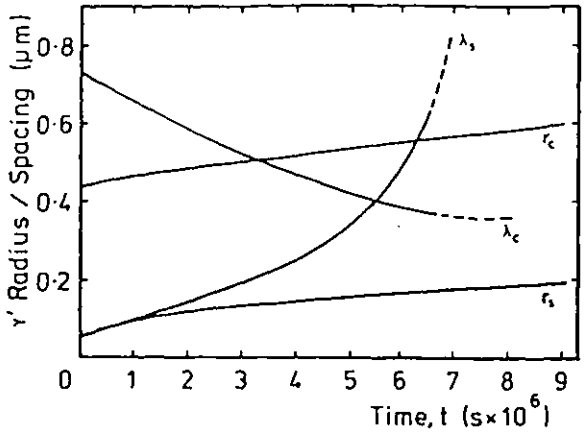

Fig. 1.8 Variation with time of mean γ' spheroid radius $\bar{r}_s$, mean γ' cuboid radius $\bar{r}_c$ and the respective mean precipitate spacings λ_s and λ_c within a dislocation slip plane during isothermal aging (1123 K) of IN-738.[83]

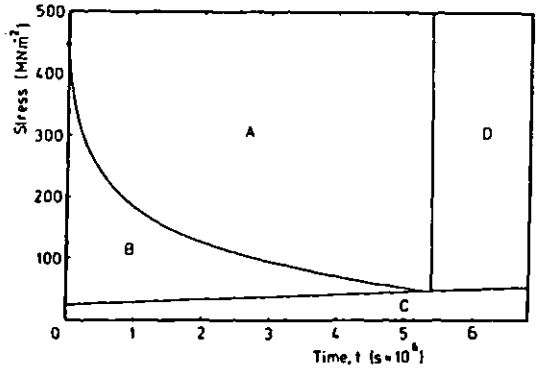

Fig. 1.9. Modes of dislocation movement during creep of IN-738 at 1123 K: A, bowing between spheroids and cuboids, $\lambda_s < \lambda_c$; B, climb over spheroids, bowing between cuboids; C, climb over both spheroids and cuboids; D, bowing between spheroids and cuboids, $\lambda_s > \lambda_c$.[83]

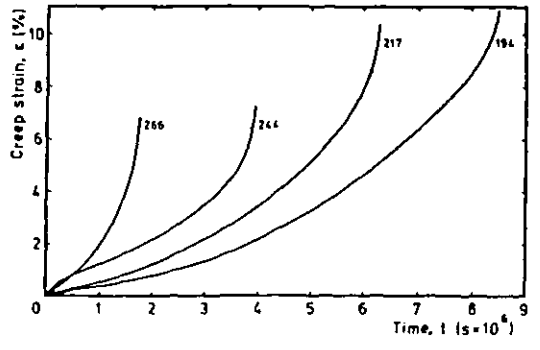

Fig. 1.10 Constant load creep rupture curves for IN-738 at 1123 K, with initial stresses (in MN m^{-2}) as marked.[83]

Table 1.1 Equations describing growth kinetics of discontinuous precipitation; after Gust[46]

Equation	Ref.
$V = \frac{C_0 - C_E}{C_0} \cdot \frac{2D_V}{\lambda}$	37
$V = \frac{C_0 - C_E}{C_0} \cdot \frac{D_B\delta}{\lambda^2}$	38
$V = 4\frac{C_\beta - C_E}{C_\beta - C_0} \cdot \frac{D_B\delta}{\lambda^2}$	40
$V = \frac{A}{K_C} \cdot \frac{D_B\delta}{\lambda^2}$	39
$V = 4AK_S D_B\delta \cos\theta$	137
$V = 48\frac{V_M\sigma_{\alpha\beta}(K_K - 1)}{q(\frac{1}{2} - a)^2} \cdot \frac{D_B\delta}{\lambda^3}$	138
$V = -8\frac{\Delta G}{RT} \cdot \frac{D_B\delta}{\lambda^2}$	33

Symbols

a = thermodynamic parameter used by Shapiro and Kirkaldy[138]
A = dimensionless-parameter introduced by Cahn [39]
C_E = composition of α in equilibrium with β lamellae
C_0 = bulk-alloy composition
C_β = equilibrium concentration of β lamellae
D_B = grain-boundary diffusion coefficient of solute atoms in α
D_V = volume-diffusion coefficient of solute atoms in α
ΔG = driving force for reaction
K_C = proportionality constant introduced by Cahn [39]
K_K = constant used by Shapiro and Kirkaldy
K_S = proportionality constant introduced by Sundquist[137]
q = thermodynamic parameter used by Shapiro and Kirkaldy[138]
R = gas constant
λ = interlamellar spacing
T = absolute temperature
V = growth rate of reaction
V_M = molar volume of discontinuous precipitates
δ = grain-boundary thickness
$\sigma_{\alpha\beta}$ = α/β interfacial energy
θ = angle between growth direction and normal to advancing interface

TABLE 1.2

Equations describing the dendrite spacing as a function of R and G*

	Reference
$\lambda_p = A\, R^{-0.25}\, G^{-0.5}$	113
$\lambda_p = A\, R^{-0.24}$	76
$\lambda_p = A\, R^{-0.27}$	111
$\lambda_p = A\,(GR)^{-0.3}$ $\lambda_s = A\,(GR)^{-0.4}$	96

* R - solidification rate
G - temperature gradient

TABLE 1.3

IN 738 Creep rupture tests[83]
(Conventionally cast material)

Temperature (K)	Initial Stress (MN m^{-2})	Rupture Life (s x 10^6)	Extension (%)
1123	266	1.74	6.8
1123	244	2.77 3.96	7.9 7.2
1123	217	6.27	10.3
1123	194	8.45	10.9
1023	457	5.54	4.4
1023	429	7.83	3.1

CHAPTER 2

EXPERIMENTAL METHODS

2.1 Alloy Preparation

Cast ingots of IN 738 with low carbon content and directionally solidified were supplied by the National Physical Laboratory in the shape of bars of 250 mm length and 12.5 mm diameter. The nominal composition was :

	C	Cr	Co	Ti	Al	Mo	Nb	W
wt%	0.12	15.8	8.3	3.44	3.46	1.72	0.83	2.58

Ta	Zr	Ni
1.77	0.055	bal.

The material originally supplied by Wiggin Alloys Ltd in 50 mm diameter bars was remelted at about 1470°C (Vacuum of ∿ 0.01 Pa) as a pre-stage for the directional solidification (DS), in order to obtain an ingot of adequate dimensions (12.5 mm) for the DS furnace. A layout of this furnace is drawn in Fig.2.1; it consists of a modified Bridgman crystal growing unit where temperature gradients of $13^{\circ}C\ mm^{-1}$ can be achieved, instead of the usual $5^{\circ}C\ mm^{-1}$ obtained by the usual industrial method. The ingots were contained in recrystallized alumina crucibles and the melting zone was determined by a 30 mm high carbon susceptor heated by induction. The ingot was then withdrawn at a controlled rate into a low melting point (60°C) alloy - Cerrolow 136 - which

helped in establishing the temperature gradient along the ingot; an argon atmosphere was kept throughout the solidification. When steeper temperature gradients ($20^{o}C\ mm^{-1}$) were needed, they could be achieved by agitation of the coolant alloy.

For these particular furnace set-ups, the ingot withdrawal rate was equivalent to the solidification rate.

The main solidification conditions investigated in the present work were based on variations of the solidification rate (the temperature gradient was $13^{o}C\ mm^{-1}$ for most conditions). Most of the research was carried out for the rates 60, 300, and 600 mm hr^{-1}, while other conditions have also been examined (Table 3.1). Of particular importance was the use of the 'interrupted-solidification' technique, which consisted in 'freezing' the high temperature solidification structure by quickly dropping the ingot into the metal cooling bath, thus interrupting the solidification process. Due to the existence of an approximately steady temperature gradient along the ingot (variations in the gradient may however occur close to the cooling bath), the resulting 'frozen structure' is expected to reveal the phase transformations according to the order that they occur at high temperature, and possibly to identify the temperatures for the reaction occurrence. The ingot prepared by this process was 'solidified' at 120 mm hr^{-1} (R) and $13^{o}C\ mm^{-1}$ (G).

2.2 Heat Treatments

Heat treatments have been carried out in vertical furnaces under air atmosphere, which allowed for quick quenching when necessary; in the isothermal treatments, the temperature control was within a $\pm\ 3^{o}C$ range. Some of the treatments required a controlled cooling rate from the solution temperature, and a programmable unit 'Eurotherm

211' has been used in connection with the vertical furnaces; again the temperature control was kept within ± 3°C.

The series of heat-treatments (Table 3.13) has been selected to investigate mechanisms related to the formation and growth of the phases present (mostly the γ' dispersions) and to characterize the structure resulting from the 'fully heat-treated' condition.

2.3 Optical Microscopy

Specimens for optical microscopy were cut from transverse and longitudinal sections of the ingot and ground on silicon carbide paper down to 600 grade. Polishing was carried out with diamond paste of grades 7 μm, 1 μm and 0.25 μm.

For microstructural examination, the main etch used throughout the work was $HCl:HNO_3$:glycerol in 3:1:1 parts, the time varying from 10 to 30 seconds; this reagent has the effect of etching out the γ' (Ni_3Al) phase. The other etch used was 1% citric acid-1% ammonium sulphate-distilled water, applied at 3 volts, 5-10 seconds which etches away the γ matrix and results in a better contrast for some of the sample conditions examined. For the primary carbide particles examination no etch was required, but simply a final polishing on alumina 0.1 μm grade, which polishes at different rates the matrix and carbides, thus delineating the carbides.

2.4 Electron Microscopy

The use of both scanning (SEM) and transmission (TEM) microscopy was required. The work was carried out in the TEM with the use of negative and extraction replicas; negative replicas were prepared by first etching the sample with a reagent that dissolved the γ' particles (3 HCl:1 HNO_3:1 glycerol), and then applying an acetate sheet softened in acetone over the metal surface. After drying, the

sheet was then removed and a carbon film of approximately 200 Å deposited over it. Small squares of the acetate/carbon film were cut off from the sheet and held by 200 mesh copper grids, where the carbon film has finally rested after the acetate was removed with the use of an acetone-ethanol solution.

For the preparation of extraction replicas, several methods were tried; the most successful one consisted of the following steps :

a) Etching the sample with the 3 HCl:1 HNO_3:1 glycerol reagent for removing the first layer of particles, in order to allow the extraction to start with a fresh layer.

b) Etching in a 1% citric acid-1% ammonium sulphate solution, 3 volts, with the time varying accordingly to the size of the particles to be extracted. For the very small γ' particles (∿ 0.01 μm), 10 seconds was appropriate while for the larger cuboidal particles (0.2 - 0.3 μm) or eutectic rods, the time required was 20 seconds.

c) Carbon coating (approximately 200 Å layer) and cutting small squares across the carbon film using a sharp blade.

d) By electroetching the sample again in the same solution (150 mV, ∿ 4 V) the carbon film containing the γ' particles becomes detached from the metal surface.

e) Complete separation could however only be achieved by placing the sample into a dish of distilled water, at a certain angle in order that the surface tension would completely release the small squares of the carbon film, which were then collected on copper grids for the TEM examination.

Under light etching conditions, it was possible to extract very small particles (approximately 0.01 μm in diameter), like the γ' spheroids resulting from the commercial heat treatment in such a way that agglomeration of particles was avoided, while the bigger particles (γ' cubes and carbides) were not extracted, but their shape was left visible on the carbon film. By using stronger etching conditions, the larger particles have been extracted, but multiple layers of the very small particles were extracted thus causing excessive agglomeration.

The use of extraction replicas improved the resolution as compared to the negative replicas, and allowed the size of the small spheroidal particles (0.01 μm) to be measured; compositional analyses were later carried out using these replicas.

The non-homogeneity of the distribution of γ' particles and the small volume fraction of some of the constituents, viz. γ-γ' eutectic and discontinuous phase, required that very extensive areas had to be examined, which could not be properly carried out by the replica techniques.

The use of scanning microscopy overcame this difficulty but only after a method for obtaining high resolution was developed; the use of the HCl-HNO_3-glycerol solution proved to be unsuitable for SEM examination as the γ' particles were etched away, thus not allowing direct particle examination. The citric acid-ammonium sulphate solution acted in the opposite way, i.e., etching away the matrix and preserving the particles. Nevertheless as the result of the strong etch conditions (5 volts) required for adequate examination of eutectic and discontinuous regions, the smaller particles agglomerated and remained firmly stuck to the surface of the sample; this difficulty was finally overcome by carrying out the electroetching simultaneously

with ultrasonic cleaning. Due to the great improvement brought about by this technique for the resolution of the continuous γ' particles and as it was the most suitable for all kinds of phases present (viz. γ' particles bigger than 0.1 μm), discontinuous γ', γ-γ' eutectic and carbides, SEM examination was carried out for most of the structural studies; the sample preparation technique described above also proved to be suitable for optical microscopy.

2.5 X-ray and Compositional Analysis

In order to identify the phases present and their composition a series of methods has been used; quantitative EDX analysis of carbide particles and regions from the matrix/γ' structure has been made using a Jeol 35 CF scanning microscopy attached to a microprobe analyser and Link microcomputing system, which provided results of good accuracy (maximum error 2%) and a resolution of approximately 1 μm. For the analysis of γ' particle composition, extraction replicas have been used in the TEMSCAN (transmission scanning) JEM 100 CX microscope. This method requires a very precise assessment of the particle thickness, which should not exceed 200 nm, due to the corrective programme for quantitative analysis being applicable only to thin areas; the resolution allowed particles of 0.01 μm to be analysed.

Also for identifying phases and for lattice parameter measurements, samples were examined by X-ray diffractometry; the samples used were either in the bulk condition or as particle residues obtained after electrolytical dissolution of one or more phases. The extraction was carried out using the alloy as anode, and a solution which would preferentially (according to the electrolyte used) dissolve the γ matrix or both the matrix and the γ' precipitates was used. The sample (anode) weighed approximately 3 grams and a small hole was made through using a spark machine; a platinum wire was used for sustaining the sample

and connecting it to the anode. The cathode consisted of a tantalum plate, with an area of $\sim$ 20 cm^2 inside the solution. The other conditions used were :

a) For extraction of carbides

electrolyte : 10% HCl-methanol (plus 1% tartaric acid)

voltage - 13 V

current - 1 A

time - 3 hours

The addition of tartaric acid is recommended for alloys containing tungsten, tantalum or niobium in order to prevent oxide formation.

Following the extraction, the residues were allowed to settle, and most of the solution removed; the residues were then washed several times in methanol and finally dried under an infra-red lamp. No particles remained adhering to the sample after it was cleaned in ultrasonic conditions. Thus by collecting the extracted residues with minimum losses and comparing with the loss in weight of the bulk sample, a reasonable evaluation of the amount of carbides present in the alloy should be made possible.

b) For the extraction of γ' phase plus carbides

electrolyte : 2% citric acid-2% ammonium sulphate-distilled water

voltage - 12 volts

current - 0.5 A

time - 3 hours

For these experiments the sample was introduced into a dialysis tube which retained all the residues, thus simplifying enormously the task of removing the electrolyte and washing the residues, as other separation methods were found to be unsatisfactory in dealing with

γ' particles as small as 0.01 μm. By comparing the amount of γ' plus carbide obtained by using this electrolyte, with results previously obtained for the carbide fraction, it was possible to obtain values for the total amount of γ' phase (continuous γ' plus discontinuous and eutectic) present in the alloy. These experiments were carried out on samples solidified at R = 600 mm hr^{-1}.

2.6 Classification and Distribution of Particle Sizes

For the study of the γ' particle sizes and distribution, both SEM and TEM micrographs have been used. There was no need of shape corrective factors, since for the spherical particles the use of the extraction replica technique (with the removal of the first layer of sectioned particles) revealed the true dimension of the particles.

For the particles examined by the SEM no corrective factor was also needed for measuring particle sizes, as the previously applied deep etch and ultrasonic cleaning removed the first layer of sectioned particles and revealed the whole dimension of the particles.

The examination of the micrographs was carried out using a 'Video plan' apparatus, which consists basically of a magnetic table attached to a microprocessing unit; a special pen connected to the system was used to draw around the particles. This method, although consuming more time, has been preferred compared to direct video analysis, which was found to be unsatisfactory in resolving the interfaces of nearby particles; this is of particular importance in alloys with a high density of γ' particles ($\sim$ 50 volume % in IN 738).

In analysing the cuboidal particles, the micrographs used had magnifications of approximately 20.000 x, while for the smaller spheroidal particles magnifications of up to 100.000 x were needed; in general more than 200 particles were measured for every condition

analysed. Samples for all the main solidification rates (60, 300, 600 mm hr^{-1}) were examined in the fully heat-treated condition (1120°C - 2 hr - AC + 845°C - 16 hr - AC) and coarsening studies have been carried out with samples solidified at 300 mm hr^{-1}. The temperatures considered were 850°C, 950°C, 1000°C and 1050°C, with all the coarsening treatments being preceded by a partial homogenization at 1120°C.

For the samples cast at 300 mm hr^{-1}, the solution treatment at 1120°C had the effect of putting all γ' from the 'core' regions into solution and reprecipitating fine ($\sim$ 0.01 μm) spheroidal particles during the air cooling, while in the interdendritic regions only partial solution of the γ' precipitates occurred, thus resulting in a bimodal structure consisting of cuboidal particles ($\sim$ 0.3 μm) and small spheroidal particles ($\sim$ 0.07 μm); comparison was made of the growth kinetics of the larger particles and of both systems of round particles (core and interdendritic regions). Also comparison was made of distribution of particles sizes with theoretical models predicted by Lifshitz[9] and Wagner[10].

2.7 Mechanical Properties

Microhardness tests were carried out on the Reichert microscope using a Vickers diamond pyramid indentation and a load of 100 gr.

Variations in hardness along the dendrite arms in the as-cast condition and after the full heat treatment were compared; the hardness of the discontinuous phase was also measured.

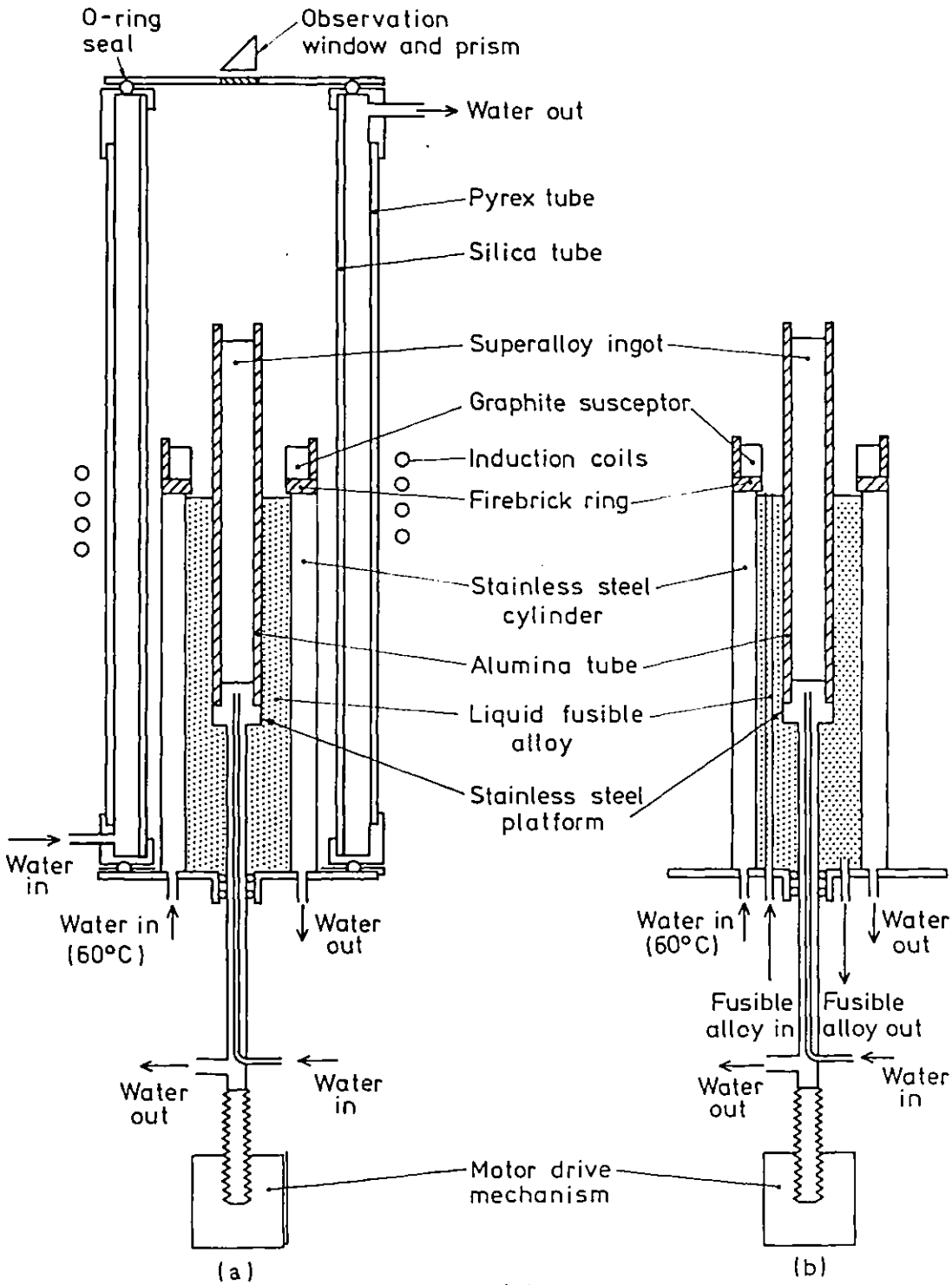

FIG. 2.1

a- Furnace lay out for a temperature gradiente of $13°Cmm^{-1}$
b- Furnace lay out for a temperature gradiente of $20°Cmm^{-1}$

CHAPTER 3

RESULTS

3.1 Introduction

The aims of the present investigation were to study the effect of different directional solidification conditions, viz. the solidification rate and the temperature gradient at the solid-liquid interface on the structure of the nickel based alloy IN 738 (low carbon type). It has been previously reported[96,98] that under certain solidification conditions, discontinuous γ' was found in the alloy; the effect of discontinuous phase on the mechanical properties of most alloys where it occurs is considered to be detrimental (section 1.2.3). In this respect, the study of the discontinuous phase formation in IN 738 constitutes an important part of the present work.

The alloy is mainly hardened by a dispersion of continuously precipitated γ' particles which according to their distribution in the dendritic structure, vary in size and morphology; this is also affected by the different solidification conditions and is reflected in the commercial heat treated structure and creep properties. The effect of the creep stress on γ' morphology has also been examined.

A comprehensive description of the distribution of γ' particles, their morphology and growth kinetics during ageing is attempted.

3.2 Morphology and Compositional Analysis

3.2.1 The as-solidified structures

The casting conditions studied as listed in Table 3.1 have included variations in the solidifcation rate from 9.6 to 1200 mm hr^{-1}; the temperature gradient at the solid-liquid (S-L) interface was 13°C mm^{-1} for most conditions, except for the highest solidification rate (1200 mm hr^{-1}) which required a modification of the cooling system of the furnace in order to avoid an excessive rise in the metal bath temperature, a gradient of 20°C mm^{-1} resulting in the modified apparatus; this gradient has also been used in conjunction with a low solidification rate (9.6 mm hr^{-1}) in order to obtain a plane front solidification. The research was carried out intially for the rates 60, 300 and 600 mm hr^{-1}, and was extended to other casting conditions when necessary.

The metallographic examination included optical and electron (scanning and transmission) microscopy, and the analytical work has used X-ray diffractometry and energy dispersive X-ray analysis (EDAX) with the electron microprobe, SEM and STEM.

In all the conditions examined the as-solidified structure (columnar grains and the dendritic or cellular structure) was well aligned for most of the ingot. The grains varied considerably in cross section reaching up to several millimetres (Fig.3.1), but no clear relation between the grain sizes and the solidification rates was observed.

The structure within the grains varied from an almost plane-front (R = 9.6 mm hr^{-1}, G = 20°C mm^{-1}) to a very fine dendritic (R = 1200 mm hr^{-1}, G = 20°C mm^{-1}), passing through cellular-dendritic and a range of different interdendritic spacings (Table 3.1).

MC carbide particles were present in all of the conditions

examined and varied in shape and size according to the solidification rate, tending to appear in a more angular and coarser morphology at the slower rates; long needle-like M_2CS particles were present in small volume fraction, although they were not revealed by X-ray diffraction.

The austenitic matrix presented a fine dispersion of γ' particles formed by continuous precipitation, which could not be properly resolved by optical microscopy; the use of electron microscopy (scanning and transmission) revealed that these particles were not uniform in size and morphology, regardless of the solidification rate considered.

The γ' phase was also present as discrete grain boundary particles, usually coarser than the matrix precipitates, and as part of γ-γ' eutectic colonies. Concerning the latter, it has been observed that they usually occurred in a 'fan' like morphology, their size decreasing as the solidification rate increased. The eutectic consisted of a fine dispersion of γ' rods separated by γ matrix, but for some colonies the front region presented a much coarser 'finger' morphology and occasional formation of massive particles ahead of the 'fingers'; the relative amount of the fine and the 'finger' type structures was found to vary according to the solidification rate, the amount of the fine rod structure increasing with slow solidification conditions.

Finally, for some of the conditions examined, large cells of rod-like γ' phase were observed to have been formed in grain boundary regions as a result of a discontinuous-type reaction; in some cases these cells transformed extensive regions of the matrix and covered a considerable area of the grain boundary. The existence of discontinuous γ' in directionally solidified IN 738 has been previously reported[96,98] but little information concerning its formation and characteristics was available.

The structuresof the different as-solidified and heat treated conditions examined are described next.

a) $\underline{R = 60 \text{ mm hr}^{-1},\ G = 13^{o}C \text{ mm}^{-1}}$

The solidification structure was cellular-dendritic (Fig.3.2) whereby the secondary arms are not fully developed; the primary arm spacing was approximately 190 μm, this value being obtained through the equation $\lambda = (\rho)^{-1/2}$ where ρ represents the number of primary arms per unit area (the examined area was large enough to allow for at least 200 counts).

The MC or M(C,N) carbide particles presented 'angular' morphology (Fig.3.3) and were situated in between the primary arms; the particle composition (average of three measurements) obtained from X-ray analysis in the SEM was :

	Ni	Al	Ti	Cr	Co	Nb	Mo	Ta
wt%	2.15	0.15	23.2	0.75	0.25	15.6	2.75	37.0

W	Zr	C+N
9.45	0.35	8.35

The MC carbides account for approximately 1.0 - 1.5 wt% of the alloy as revealed by phase extraction methods; although the above figure was originally obtained for experiments carried out for a higher solidification rate (600 mm hr^{-1}), it is believed to apply reasonably to a certain range of R values (60 to 600 mm hr^{-1}), as suggested by optical microscopical examination. Based on these figures, nearly 20 - 30 wt% of the total amount of Ta present in the alloy, 20 - 30 wt% of the Nb and most of the C content are deployed in the formation of primary carbides. A very reduced amount (< 0.1 wt%) of needle-like particles of Zr_2CS was also present usually in association with the γ-γ'

eutectic.

The electron microscopy studies of the γ' dispersions were first carried out with negative and extraction replicas using the TEM, and later by SEM examination of bulk samples prepared by a 'deep etch' technique. The continuously precipitated γ' particles situated in the 'core' regions presented a 'rounded cubic' morphology with average particle size (side length) ∿ 0.21 μm (Fig.3.4).

In the interdendritic regions particles showed irregular cubic morphology (side size ∿ 0.35 μm) or formed an 'ogdoadically diced' cube structure (Fig.3.5); Westbrook[19] used this term for a structure consisting of clusters of eight cubic particles (seen as four in a (001) plane section). In the present case, however, these particles have not often shown a perfect cubic morphology due to preferential growth at the corners.

In measuring the particle size, it was decided that a cluster of eight particles should count as a single one, as in many cases there was evidence of a common nucleus at the cluster centre, and some degree of 'coalescence' between the individual particles; the average cluster size was ∿ 0.45 μm while individual particles measured ∿ 0.22 μm (Table 3.2).

Values for γ' and MC lattice parameters have been calculated for the solidification rate 600 mm hr^{-1} (section 3.2.1c).

Microprobe analysis across the cellular-dendritic arms revealed that the interdendritic regions were richer in Ti, Nb, Ta and poorer in Cr, W, Co as compared to the 'core'; the composition determined for the main segregating elements is included in Table 3.3, together with data from other solidification conditions.

The γ' particle composition as obtained from the analysis of extraction replicas using the STEM gave the following average result

(full results in Table 3.4) :

	Ni	Al	Ti	Cr	Co	Nb	Mo	Ta	W
wt%	71.1	9.0	6.5	2.5	4.45	1.5	1.7	1.7	1.5

The accuracy of these values depends on the correct assessment of the examined particle thickness, as such information is required as a correction factor for absorption; it has been found that the aluminium composition is the most likely to be affected if the particle thickness is wrongly assessed, as can be seen from Table 3.5, where for the same γ' particle different thickness values have been introduced as correction factors, and the effect on γ' composition compared.

For many of the analyses carried out the level of Al in γ' was near 9.1 wt%; however it is believed that this value is significantly above the correct one and resulted from the wrong evaluation of the particle thickness, as explained above.

For an Al content as high as 9.1 wt%, the maximum possible amount of γ' in the alloy (assuming that there is a negligible amount of Al in solid solution in γ) would be 38 wt%, compared with reported[83,87] values of 45 and 50 wt(vol)%.

Thus a more correct evaluation of γ' composition is

	Ni	Al	Ti	Cr	Co	Nb	Mo	Ta	W
wt%	73.1	7.0	6.5	2.5	4.45	1.5	1.7	1.7	1.5

In the present work, the value found for the γ' weight fraction by the phase extraction method was 52.5% (the experiments were carried out for the solidification rate 600 mm/hr). This result is however higher than expected, also based on considerations of Al and Ti content

in γ', and could be due to small portions of the matrix not being completely dissolved during the extraction process and adding to the γ' residues; the most likely amount of γ' present in the alloy is 47 - 49 wt%.

The general matrix composition, after excluding the elements in solution in the carbides and γ' (Table 3.6) is :

	Ni	Al	Ti	Cr	Co	Nb	Mo	Ta	W
wt%	53.1	0.3	0.2	28.2	12.0	0	1.8	1.0	3.4

These figures may be compared with direct matrix analysis in the TEMSCAN (Table 3.6).

The γ' solvus temperature for the 'core' region was found to be not much above the temperature used for the first stage of the commercial heat-treatment, viz. 1120°C - 2 hrs (Fig.3.6) probably at 1130°C. It has been observed that the solvus varied slightly for the different solidification conditions; for the solidification rate R = 300 mm hr^{-1}, all the γ' particles in the core region were put into solution after 2 hrs exposure at 1120°C, but this did not happen for the 60 mm hr^{-1} and 600 mm hr^{-1} rates (refer to section 3.2.3). In the interdendritic regions, only eutectic γ' remained after 2 hours solution treatment at 1180°C or 1 hour at 1190°C; after 1 hour at 1180°C some γ' (continuous) was still left in those regions (Fig.3.7).

The γ-γ' eutectic structure, as already mentioned consisted either of an exclusively fine rod dispersion (Figs.3.12-3.15), or showed a broadening of the rods into a much coarser 'finger' morphology (Figs.3.8-3.11); the coarser morphology however, could be only partially resolved by optical microscopy (Fig.3.8), with its finer component requiring electron microscope techniques (Figs.3.9-3.10). For the solidification rate presently considered both morphologies seem to occur in approximately similar amounts. The size of the eutectic

regions was around (2-5).10^2 μm^2; the γ' rods had variable length (5-10 μm) and 0.15 - 0.25 μm thickness presenting a series of 'branches' as can be observed using the SEM after deep etching (Figs. 3.13-3.15). The surface of the rods could be either flat or serrated as revealed by TEM examination of extraction replicas (Fig.3.11).

The volume fraction of the eutectic phase, based on area fraction measurements, was found to be approximately 1.5%; in nickel based alloys the values for the γ' volume fraction are a good approximation for the γ' weight fraction.

The chemical composition of the γ' eutectic rods was similar to that obtained for the continuous γ' particles, also taking into account possible errors in Al composition

	Ni	Al	Ti	Cr	Co	Nb	Mo	Ta	W
wt%	73.5	6.55	6.15	3.3	4.15	1.15	1.0	1.7	2.55

The rod structure coarsened quickly after heat-treatments above 1100°C and some degree of spheroidization had occurred; after 2 hours at 1180°C the rod structure had completely broken up into coarse particles. After 1 hour at 1190°C only large 'pools' of eutectic γ' were left.

At the grain boundaries, γ' was present as coarse discrete particles (Figs.3.16-3.17). In some regions of the grain boundary rod-like γ' cells of discontinuous precipitation have formed (Figs.3.18-3.23); these cells were larger in size when compared to the eutectic colonies (average cell size = (4-8).10^2 μm^2) and also presented larger rod thickness (0.3-1 μm), rod length (15-40 μm) and inter-rod spacing (0.7-1.5 μm).

The morphology of the cells was broadly a fan-type similar to

the eutectic colonies; however the discontinuous rods tentatively approached parallel alignment after some growth has occurred.

The amount of discontinuously transformed areas was small (probably near to 1% volume fraction of the alloy) but a more precise assessment was made difficult due to the irregularity of the cell distribution along the grain boundaries and to the large size of the grains. This amount could however be more conveniently expressed by the number of discontinuous cells per unit length of grain boundary, the counts being taken in a longitudinal section. For this solidification condition ($R = 60$ mm hr^{-1}) the figure was near 50 cells per 10 mm of boundary length; comparative results with other solidification conditions are shown in Table 3.7.

There was no observed preference for the discontinuous reaction occurring at a particular side of the grain boundary.

The occasional occurrence of discontinuous phase at both sides of the same segment of grain boundary (Fig.3.19) could be the result of lateral growth of the moving front, in a similar way to that described by Fournelle[64] (Fig.1.7).

The use of the 'deep etch' method allowed the γ' constituent morphology to be properly identified as rods or laths (Fig.3.25) rather than lamellae, which are more usual for discontinuous-type reactions; rod branching has often occurred, probably in order to maintain the inter-rod spacing, during the diverging growth of the rods. Nucleation of new rods as a means of controlling the inter-rod spacing could not be clearly identified but it is possible that it occurred.

As growth proceeded, the moving boundary aligned itself with preferential crystallographic planes; these changes in the growth direction caused the formation of steep curvatures in the rod morphology (Fig.3.20) and brought about a higher degree of parallelism between

the rods and growth perpendicular to the moving boundary.

An attempt has been made to identify the crystallographic orientation adopted by the migrating grain boundaries using as references the <001> directions as indicated by the γ-γ' interfaces and by the alloy's solidification direction, which is perpendicular to the plane of the micrograph. In several cases the line representing the grain boundary interception with the (001) plane, lay parallel to a <001> direction, sometimes in relation to the opposite grain and others, to the same grain from which the growth originated; also a 45° orientation was preferred, which could result either from {111} or {110} planes. However, in some cases the angle relationships suggested higher index planes such as {210}, {310} and {320}.

The interfaces of the discontinuous γ' rods have commonly developed 'dendritic' type instabilities (Figs.3.24-3.26); the formation of such a 'dendritic' morphology in solid state formed γ' is very rare and not previously reported to occur in discontinuous phase. Some possible reasons for this occurrence are discussed in Chapter 4.

Chemical analysis of the discontinuous γ' rods using the STEM gave values close to those obtained for the continuous and eutectic constituents (Table 3.9); the analysis has been carried out both for the centre of the rods and the dendritic instabilities and average results are presented below, already with corrected values for the Al composition.

	Ni	Al	Ti	Cr	Co	Nb	Mo	Ta	W
rod centre	72.2	7.0	7.6	3.0	4.7	2.0	1.3	1.9	0.3
dendritic perturbation	69.3	7.0	8.0	3.0	4.4	2.4	0.8	3.7	1.4

The results have shown a possible trend for a low content of W in the discontinuous rods.

The discontinuously formed γ' cells often appeared adjoining γ-γ' eutectic regions (Fig.3.21) which initially suggested that the eutectic colonies which usually form first, may have interfered with the nucleation or growth of the discontinuous phase. In order to investigate the earlier stages of the discontinuous reaction and to attempt to increase the volume fraction of the discontinuously transformed regions, a series of heat treatments has been carried out (Section 3.2.3). However, none of the attempted experiments has resulted in forming new cells of discontinuous phase, or in visibly increasing the size of the existing ones. In attempting to investigate the earlier stages of discontinuous cell formation, an alternative method has been used consisting in the examination of an 'interrupted solidification' sample; the process has already been described under 'Experimental Methods' (Chapter 2) and the results obtained are to be considered later (Section 3.2.2).

From the series of applied heat treatments the solvus temperature for the discontinuous phase was identified as 1170°C, although breaking up of the rods into aligned particles was observed at lower temperatures; while this occurred after only a few hours at 1160°C, it required 96 hours at 1050°C. A more detailed description of the effect of the heat treatments on the alloy's microstructure is reported in Section 3.2.3.

b) $R = 300$ mm hr^{-1}, $G = 13^{\circ}C$ mm^{-1}

The overall structure was finer as compared to the previous slower solidification rate (60 mm hr^{-1}), viz. the dendritic arm spacing, the particle size of carbides and γ', and the size of the γ-γ' eutectic

regions.

The solidification structure was fully dendritic, with the development of secondary and tertiary arms (Fig.3.27); the average primary arm spacing was $\sim$ 120 μm and the secondary arm spacing $\sim$ 42 μm. The composition in the core and interdendritic regions, and the segregation ratio are included in Table 3.3.

The distribution of the γ' particles was similar to that described for the solidification rate R = 60 mm hr^{-1} i.e. smaller particles in the core region and larger ones in the interdendritic region (Figs.3.29, 3.30); however, the 'ogdoadically diced' cube structure was in this case present in only very reduced amount, although particles in the interdendritic region usually presented some instability formation at the cube corners. Particles in the core region were more rounded when compared to the 60 mm hr^{-1} solidification rate. The average particle sizes for the interdendritic and core region were respectively 0.19 μm (side length) and 0.1 μm (diameter).

The volume fraction of the γ-γ' eutectic was measured using the Videoplan as $\sim$ 1.5%, which is near to the figure for R = 60 mm hr^{-1}. Concerning the relative amounts of the two different γ-γ' eutectic morphologies (Figs.3.31,3.32), there was a relative increase in the amount of the 'finger-type' morphology. The average size of the eutectic colonies was 30-70 μm^2. Only a few regions of small discontinuous γ' cells were present.

c) R = 600 mm hr^{-1}, G = 13°C mm^{-1}

A further refining at the structure resulted from this fast solidification condition (Fig.3.33). Values for the primary and secondary arm spacings were respectively 105 μm and 35 μm; the segregation ratios are included in Table 3.3.

The MC carbide particles presented a 'Chinese script' morphology as shown in Fig.3.34; extracted carbide particles can be seen in Fig.3.35. The extraction of the carbide particles by electrolytical dissolution of the matrix has allowed the determination of its percentual fraction (1-1.5 wt%) and its lattice parameter (4.365 Å) from X-ray analysis.

The γ' particle morphology was more regular than that observed for the slower solidification conditions; the particles in the 'core' region (Fig.3.36a) presented either a rounded cubic or a near spherical shape, while those in the interdendritic regions (Fig.3.36b) were rounded cubic. The diffraction pattern(Fig.3.37) corresponds to a (001) orientation and refers to Fig.3.36; average particle sizes were respectively 0.075 μm (diameter) and 0.13 μm (side length).

The total amount of the γ' phase present has been determined by the phase extraction method as 52.5 wt%, but its real figure is expected to be (47-49 wt%) due to a probable contamination with undissolved matrix. The γ' lattice parameter calculated from X-ray examination of the extracted residues is 3.59 .

Videoplan measurements indicated the eutectic area (or volume) fraction as 2%; the γ-γ' eutectic was present in groups of small sized colonies (∿ 10-20 μm^2) which presented a 'coarse' γ' rod structure (Fig.3.38). Comparative results on the eutectic size and volume fraction are in Table 3.8.

Although no discontinuous γ' phase could be found by optical microscopy, detailed SEM examination of the grain boundaries revealed the existence of small discontinuous cells (γ' rods : 3-5 μm long, 0.2-0.25 μm thick), presenting similar morphological features to those previously observed for largely developed cells, viz. a general 'fan' shape and dendritic formation at the rod surfaces (Fig.3.39).

d) Other solidification conditions

The research has been extended to include other solidification rates and temperature gradients in order to obtain additional information on the effect they have, either through the cooling rate GR or the ratio G/R, on the solidification structure, dendritic or cellular arm spacing and γ' phase formation. A high G/R ratio was expected to approach a plane front solidification structure according to a constitutional supercooling analysis[110] and probably suppress the γ-γ' eutectic formation; the cooling rate was expected to influence particle sizes and discontinuous formation (refer to Table 3.1 for all the solidification structures).

$R = 9.6$ mm hr^{-1}, $G = 20^{\circ}C$ mm^{-1}

The solidification structure was virtually plane-front (Fig.3.44), although some grains presented slight cellular solidification. No γ-γ' eutectic or discontinuous formation was observed.

$R = 9.6$ mm hr^{-1}, $G = 13^{\circ}C$ mm^{-1}

The smaller temperature gradient, although with the same solidification rate as compared with the previous casting condition, resulted in a more cellular solidification structure and a few eutectic colonies and discontinuous cells being formed.

$R = 12$ mm hr^{-1}, $G = 13^{\circ}C$ mm^{-1}

This casting condition resulted in some degree of cellular texture (Fig.3.40), and the intercellular spacing was ∿ 160 μm.

SEM examination of the γ' distribution, revealed the existence of a ring of coarser particles (∿ 1 μm) around the centre of the cell where particles measured ∿ 0.5 μm (Fig.3.41) . Particles in both regions

consisted of 'ogdoadically diced' cubes (Fig.3.42) and in many cases a more complex structure, consisting of clusters with more than eight particles has been formed (Fig.3.43).

The γ-γ' eutectic was present in a very reduced amount and the colonies consisted of fine rods with apparently no rod broadening ('finger-type') as observed in other solidification conditions. Discontinuous phase was present as large cells but also in reduced amount ($\sim$ 10 cells per 10 mm of grain boundary).

$R = 30$ mm hr^{-1}, $G = 13^{o}C$ mm^{-1}

The solidification structure was cellular-dendritic (Fig.3.45) presenting primary arm spacing $\sim$ 245 μm.

There was a major increase in the amount of discontinuous γ' precipitation ($\sim$ 100 cells per 10 mm of grain boundary length) as compared to all other conditions examined (Fig.3.46); the size of the cells was also very large, thus affecting large sectorsof the grain boundaries. The rod morphology was the same as observed previously (Figs.3.47-3.49).

$R = 120$ mm hr^{-1}, $G = 13^{o}C$ mm^{-1}

The solidification structure was cellular-dendritic , however the primary arm spacing could not be well defined due to an irregular solidification pattern. The fraction of discontinuous phase was 50 cells per 10 mm of grain boundary.

$R = 1200$ mm hr^{-1}, $G = 20^{o}C$ mm^{-1}

This solidification condition resulted in a very fine dendritic structure, with primary arm spacing $\sim$ 90 μm and secondary arm spacing $\sim$ 27 μm. The γ-γ' eutectic colonies size was very small, and no

discontinuous phase could be observed by optical microscopy; however no further investigation was carried out.

Structure of the 'pre-cast' material

The material supplied by the manufacturers (Wiggin Alloys Ltd) was originally 'conventionally' cast into rods of 70 mm diameter. The central region (half the radial distance) presented an equiaxed grain structure and was very rich in eutectic colonies of very coarse structure, and no discontinuous γ' phase was present; the outer region presented a columnar grain structure aligned with the radial direction and both discontinuous γ' phase and γ-γ' eutectic have been formed in amounts comparable to those observed in some of the directionally solidified conditions, viz. R = 60 to 120 mm hr^{-1}, G = 13°C mm^{-1};

3.2.2 Interrupted solidification - R = 120 mm hr^{-1}, G = 13°C mm^{-1}

In order to retain the high temperature solidification structure, a method has been applied consisting of interrupting the solidification process by dropping the ingot quickly into the metal bath (Cerrollow 136) as already described in Chapter 2; this method has been previously used for microsegregation studies[77] and for investigating phase formation[82] (carbides, γ-γ' eutectic and continuous γ'). The aims of the present experiment were to investigate the early stages of the precipitation and growth of the phases present, mostly in respect to the identification of the initiation mechanism for the discontinuous reaction.

Fig.3.50 refers to the start of the solidification process, and the first phase transformations to occur are indicated, viz. :

- solid-liquid interface ('liquidus')
- appearance of faceted MC carbides

- development of surface instabilities (arms) in the MC carbides
- entrapment of liquid with eutectic composition.

Figure 3.51 is a transverse section and refers to the formation of the MC carbides (section as indicated in the longitudinal micrograph), which nucleate initially from the liquid; a fine distribution of Chinese script carbides is also visible, but they form during the fast cooling and thus are not part of the high temperature structure. Fig.3.52 shows regions of the remaining liquid with eutectic composition, which can be seen with higher magnification in Fig.3.53. At this stage the solidification of the γ-γ' eutectic has not yet started although otherwise suggested by the micrograph where regions of γ' particles are visible, but they in fact form during cooling.

The whole sequence of phase formation, from the start of solidification to the solid state precipitation of γ' is included in Fig.3.54 :

- solid-liquid interface ('liquidus')
- MC carbide formation
- entrapment of liquid with eutectic composition
- start of γ-γ' eutectic solidification
- start of continuous γ' precipitation (interdendritic region)
- start of discontinuous γ' reaction
- end of the γ-γ' eutectic solidification ('solidus')
- continuous γ' precipitation in the core region.

It can be seen (Fig.3.55) that the eutectic solidification occurs at a 'long' distance (4 mm) from the apparent end of the freezing range; before the eutectic solidification was completed, both continuous

(Fig.3.56) and discontinuous γ' have nucleated.

The continuous γ' particles in the interdendritic regions have soon developed into an 'ogdoadically diced' cube structure (Fig.3.57), while particles in the core were presenting a least developed 'ogdoadically diced' cube structure (Fig.3.59).

The continuous precipitation had the effect of competing with the discontinuous reaction by halting the grain boundary migration; as precipitation occurred last in the core regions, the discontinuous reaction could still grow into those regions (Fig.3.58).

An attempt has been made to deduce temperatures for the occurrence of the main reactions, assuming that the temperature gradient at the solid-liquid interface ($13^{o}C\ mm^{-1}$) has remained steady along most of the ingot; the 'liquidus' temperature was considered as $1315^{o}C$[74]. According to these assumptions, the respective temperatures were :

'liquidus' (solid-liquid interface)	$1315^{o}C$
carbide nucleation	$1310^{o}C$
development of carbide arms	$1295^{o}C$
start of γ-γ' eutectic solidification	$1227^{o}C$
start of continuous γ' precipitation (interdendritic region)	$1218^{o}C$
discontinuous γ' reaction	$1218^{o}C$
start of continuous γ' precipitation (core region)	$1185^{o}C$

The temperature assessments for the solid state precipitation of γ' appears to be considerably higher than expected, as for the core region, the γ' 'solvus' found by heat treatments is around $1120^{o}C$ -

1130°C; this indicates that the assumption for a constant temperature gradient is a gross approximation, and the gradient must be higher closer to the metal bath (lower part of the ingot).

EDX analysis carried out at the SEM indicated the composition of the 'liquid' regions before eutectic solidification occurred (average of three measurements, Table 3.10) as

	Ni	Al	Ti	Cr	Co	Nb	Mo	Ta	W	Zr
wt%	56.5	2.4	5.6	14.5	7.8	2.8	2.7	1.3	1.8	4.6

There is an observed high concentration of Ti and Nb (γ' forming elements) and an excessively high concentration of Zr, which is nominally present in the alloy as only 0.05 wt%; needles of Zr_2CS often occur associated with the γ-γ' eutectic[86,96] (Fig.3.63).

The analysis carried out in regions where the continuous γ' was first to precipitate has shown (average of three measurements, Table 3.11)

	Ni	Al	Ti	Cr	Co	Nb	Mo	Ta	W
wt%	64.2	3.5	4.5	14.5	7.8	1.1	1.6	1.0	1.8

In the core region, where γ' precipitated last, the composition was (average of three measurements, Table 3.11)

	Ni	Al	Ti	Cr	Co	Nb	Mo	Ta	W
wt%	64.1	3.0	2.4	16.2	8.8	0.5	1.2	0.7	2.9

It is immediately observed that the main compositional differences between the core and interdendritic regions are in relation to the levels

of Ti, Cr, Nb, W and possibly Co. Some of these elements have a strong influence on the earlier precipitation in the interdendritic region during cooling, and thus on the final coarser particle size that results (to be further discussed in Chapter 4).

Figs.3.60-3.62 refer to the eutectic solidification; in Fig.3.60 a broadening of the γ' rods is observed ('fingers') and a region of 'liquid'. The solidification may also proceed without broadening of the rods, as can be seen in Figs.3.61,3.62, which will give origin to a structure consisting only of fine γ' rods.

The earlier stages of grain boundary migration and discontinuous reaction are shown in Figs.3.63-3.68 which refer to the same transverse section, before the γ-γ' eutectic solidification was completed.

In Figs.3.63-3.65 the discontinuous phase can be observed to be in close association with colonies of γ-γ' eutectic; in fact, the first two of these micrographs where the grain boundary is at a very early migration stage suggest that the γ' eutectic rods are intrinsically related to the initiation mechanism of the discontinuous reaction. This is to be discussed further in Chapter 4, together with a model proposing the several steps leading to the development of the discontinuous reaction. No significant compositional differences were found between matrix regions on both sides of a grain boundary near to the discontinuous cells in the earlier formation stages, as indicated by the results in Table 3.12.

The development of the dendritic instabilities on the surface of the discontinuous rods had already initiated at earlier stages of the reaction (Fig.3.66), and grew during the cooling. The spread of the continuous γ' precipitation had the effect of halting the discontinuous reaction, as revealed by Figs.3.67, 3.68. In Fig.3.67 one of the discontinuous cells is still growing into a γ' free region,

while the other cell has its growth stopped by γ' continuous precipitation. Some more examples that support the proposed idea of the effect of the γ' eutectic rods in originating the discontinuous reaction are included in Figs.3.69-3.77; they refer to the solidification rate R = 60 mm/hr (fully solidified) and are the result of an extensive examination by scanning electron microscopy. An approximate position for the original grain boundary is indicated on the micrographs, separating the 'eutectic' and the 'discontinuous' region formed after boundary migration.

One of the 'eutectic-discontinuous' structures has been re-examined after several microns have been removed by polishing (Figs. 3.73,3.74); it confirmed the initial observations.

In Figs.3.75-3.77 it can be observed that the γ' 'finger' type eutectic has not resulted in any boundary migration and discontinuous phase formation; it is believed that only when fine eutectic rods solidify close to the grain boundary, a discontinuous reaction may result.

3.2.3 The heat-treated structures

A series of heat-treatments has been carried out (Table 3.13) with the following aims :

a) Commercial or full heat treatment in order to compare the structure of the three main solidification conditions (60, 300, 600 mm hr^{-1}) with respect to the effect on the γ' morphology and distribution, and on the other phases present.

b) Treatments to form or increase the size of the discontinuous cells - this was attempted by isothermal

exposures and by solution treatments followed by slow continuous cooling.

c) γ' coarsening treatments - both the effect on γ' morphology and the coarsening kinetics are considered, the latter as part of Section 3.3.

a) The commercial or full heat treatment (FHT)

This was the same treatment usually applied to the conventionally cast material, viz. 1120°C-2 hr-AC plus 845°C-16 hr-AC (for γ' particle sizes refer to table 3.14). The first stage had the effect of taking most of the γ' particles into solution from the 'core' regions and re-precipitating very small spheroidal particles during the air cooling; this has happened to a greater extent for the alloy solidified at R = 300 mm hr^{-1}, where all the original γ' from the 'core' was removed and a ring of very coarse particles formed around it (Figs. 3.78a,3.79a,3.80a).

In the interdendritic regions, only limited γ' solution resulted, and a regular cubic morphology (Figs.3.78b,3.79b,3.80b) has substituted for the previous 'ogdoadically diced' cube structure (R = 60 mm hr^{-1}) and irregular shaped particles (R = 300 mm hr^{-1}, 600 mm hr^{-1}). As the particle sizes of the regular cubes are close to the values observed for the clusters of 'ogdoadically diced' cubes (as-cast structure, R = 60 mm hr^{-1}), this indicates that the individual particles forming the clusters have coalesced with the heat-treatment, giving origin to a larger single particle, which finally acquired a regular cubic shape.

The second part of the heat-treatment has the effect of bringing the γ' volume fraction to its 'full' amount and slightly increasing the size of both cubic and spheroidal particles; some

coalescence of the spheroidal particles occurs at the second stage mainly in the core region (Figs.3.81-3.83).

Area fraction measurements carried out using the 'Videoplan' revealed that the amount (area or volume fraction) of the cubic shape particles in regions with the highest particle density in the interdendritic region was ∿ 50%, while in the core it was very small or even none (for R = 300 mm/hr). The distribution of cubic particles in the interdendritic region was, however, heterogeneous, varying considerably in volume fraction and size, which has limited the assessment of the total amount of the γ' cubes in the alloy by the use of visual counting techniques; a reasonable figure is believed to be around 25%, considering a distribution of 35 vol% in the interdendritic region and 10 vol% in the core region. The total amount of the spheroidal particles would then account for ∿ 22 vol%. For the rate R = 300 mm hr^{-1}, the fraction of cubic particles is slightly smaller, as they do not form in the core region.

The total amount of the γ' phase present in the fully heat treated condition was calculated by phase extraction techniques similar to the experiments carried out with the as-cast material, but no separation of the respective fractions of small (spheroids) and large (cuboids) particles was attempted. The experimentally obtained fraction for the fully heat treated condition was nearly the same as that for the as-cast structure (∿ 52 wt% including the γ' eutectic phase), but the results for both conditions are probably higher than the real values as previously mentioned, possibly due to some γ matrix adding to the extracted γ'; the real figure for the full heat treated condition is probably slightly over the amount existing in the as-cast state (47-49 wt%).

The first stage of the commercial heat treatment (1120°C-2 hr-AC) had the effect on the eutectic phase of partially breaking up the

fine rods (Fig.3.87) and coarsening the structure. On the discontinuous phase, serrations were formed at the γ' rod interface (Fig.3.84) while the dendritic instabilities were mostly removed; at the opposite side to the discontinuous front, a coarser γ' rod has developed suggesting a coarsening discontinuous reaction (Figs.3.85,3.86).

The effect of the first stage treatment on the grain boundaries was to coarsen the γ' cubic particles (Figs.3.89-3.91). After the second stage (845°C-16 hr-AC), a continuous layer of $M_{23}C_6$ has formed along the grain boundaries (Figs.3.88-3.89,3.92-3.93); $M_{23}C_6$ has also formed around the MC particles (Fig.3.94). The elements in the $M_{23}C_6$ carbide phase were found to be Cr, Mo, Ti, W, Nb and Ta.

b) i - The effect of isothermal treatments on the discontinuous phase

After 24 hours exposure at temperatures ranging from 600°C to 1160°C no increase in the size, or in the number, of the discontinuously transformed areas was noticeable; some degree of rod coarsening has occurred for the higher temperatures.

At 1000°C the rod interfaces have considerably flattened (Fig.3.95) and incipient breaking up of the rods was observed (Figs.3.96-3.98), while at the grain boundaries a layer, possible of γ', has formed (Fig.3.98). Exposures above 1100°C have considerably shortened the time for breaking up the rod structure; the effect of 2 hours at 1160°C is shown in Fig.3.99.

After the 1050°C treatment (24 hours), the structure was similar to that from the first stage of the commercial heat-treatment (1120°C-2 hr-AC) in respect to the formation of large discrete γ' particles at the grain boundaries (Fig.3.103), serrations on the discontinuous rods and the coarsening discontinuous reaction (Fig.3.100).

Longer exposures (48 hours) at this temperature (Fig.3.101) revealed an increase in the size of the regions transformed by the discontinuous coarsening reaction to the detriment of the initial finer rod cell size, thus suggesting a grain boundary receding mechanism. After 96 hours at 1050°C the rods have completely broken up into coarse particles (Fig.3.102).

ii - The continuous cooling heat-treatments

These treatments aimed at simulating the cooling conditions under which discontinuous phase has previously formed during the casting process. An initial γ' solution treatment was applied at 1180°C for a short period (0.5 hr), in order to avoid extensive homogenization; furnace cooling has followed, down to a set of different temperatures (ranging from 1160 to 600°C), at a controlled cooling rate (13°C min^{-1}), and holding at these temperature for 24 hours. The applied cooling rate is equivalent to the original solidification conditions (R = 60 mm hr^{-1}, G = 13°C mm^{-1}) which previously resulted in discontinuous γ' formation. Nevertheless only continuous γ' precipitation formed for all the treatments carried out (Fig.3.104).

c) Coarsening of the continuous γ'

A study has been made of the effect of isothermal treatments (ranging from 850°C to 1100°C) on the morphology of the γ' continuously precipitated; the coarsening kinetics are to be considered in Section 3.3 . The investigation was carried out using the specimens solidified at R = 300 mm hr^{-1}.

A first stage treatment consisting of 1120°C-2 hrs-AC was applied in order to replace the initial particle distribution by regular shaped cubic particles, and also to form a fine distribution of spheroidal particles; the latter resulted from the partial γ' solution

occurring at 1120°C.

The effect of the long term ageing treatments apart from the expected particle coarsening (refer to Table 3.15) for particle sizes), was to increase particle coalescence, this occurring at shorter times for the higher temperatures;the effect on the cubic particles is shown in Figs.3.106-3.110. It can also be observed that the particles become more rounded.

In the core region the initial distribution of spherical particles, gradually changed into a cubic morphology as coarsening proceeded; while this was true after ∿ 170 hours at 950°C (Fig.3.111) no morphological changes in this direction happened after ∿ 2,000 hours at 850°C (Fig.3.107b) even with particle sizes larger than those at 950°C where the shape change had occurred.

3.2.4 The Effect of creep stress on γ' morphology

Mechanical tests have been carried out by the National Physical Laboratory for the samples solidified at 300 mm/hr, both for the as-cast and for the full heat treated material, under the following conditions : 1 - stress- 250 N/mm^2, temperature 850°C. Rupture occurred after 1988 hours at 29% elongation for the fully heat treated sample and after 995 hours at 18% elongation for the as-cast material.

The combined effect of stress and temperature on the γ' structure can be compared with the single effect of temperature, as Fig.3.107 refers to the part of the test piece not submitted to any stresses. The applied stress (parallel to the <001> solidification direction) has resulted in the coalescence of the γ' particles in a direction perpendicular to the stress axis (Figs.3.113-3.115); of interest, however, is the formation of faceted interfaces orientated at 45° to the stress axis.

For the as-cast test-piece as the test was performed for shorter time and deformation levels, the degree of γ' particle coalescence (Fig.3.116) was smaller than that for the fully heat treated test piece.

3.2.5 Microhardness measurements

These tests have been carried out with a Vickers indentation and a 100 g load; the results presented in Table 3.17 are an average of 10 measurements. For the as-cast structures (60, 300, 600 mm hr^{-1}), hardness in the interdendritic region was higher than the values observed for the core, mainly for the solidification rates 300 mm hr^{-1} and 600 mm hr^{-1}; after the full heat treatment, the hardness for the interdendritic region for these two conditions remained nearly the same, while the measured values for the core increased. For the rate 60 mm hr^{-1}, which presented low hardness in the interdendritic region in the as-cast condition, after the full heat treatment the level was comparable to the other rates.

The hardness of the discontinuous phase regions was similar to that found at other regions (interdendritic and core), both before and after the full heat treatment.

3.3 Coarsening Kinetics of the Continuously Precipitated γ'

The increase in particle sizes as a function of time during isothermal treatments has been investigated for the solidification rate R = 300 mm hr^{-1} both for cubic shaped and spherical γ' particles. The initial structure was obtained by exposure at 1120°C for 2 hours which resulted in a bimodal distribution of cubic and smaller spherical particles in the interdendritic regions, and only spherical particles in the dendrite cores (Figs.3.79, 3.81, 3.83). The size of the γ'

cubes was found to vary considerably in different areas of the interdendritic region; in attempting to obtain consistent results for the various samples examined, measurements in the interdendritic regions were carried out in areas where the volume fraction and the particle sizes were apparently the highest.

The coarsening kinetics of the spherical γ' were investigated for particles both in the dendrite cores (no cubic particles present) and in the interdendritic region (bimodal distribution), where the presence of the cubic particles could have possibly interfered with their coarsening; this examination was carried out only for temperatures below 950°C, since for higher temperatures the bimodal distribution was replaced by a single distribution of cuboids after short time exposure. All particle sizes are listed in Table 3.15.

For all the temperatures examined the cube power of the average particle size (radius for the spheroids and half the side length for the cubic particles), was plotted as a function of the aging time in Fig.3.117 and Fig.3.118; straight lines were fitted to the experimental data using a least squares method, the slope representing the coarsening rate constant K^3 according to the Lifshitz-Wagner theory (section 1.2a)

$$r^3 - r_o^3 = \frac{8 \gamma D C_e V_m^2 t}{9RT}$$

where $$K^3 = \frac{8 \gamma D C_e V_m^2}{9RT}$$

The intercept with the y axis is in the present case meaningless, as values for the initial particle size when the coarsening mechanism becomes operative are not known; the coarsening rates are shown in Table 3.16. Further analysis of the coarsening data is included in Chapter 4.

3.4 Growth Kinetics of the Discontinuously Precipitated γ'

Attempts have been made to measure the growth rate of the discontinuous phase boundary and possibly to associate it with a current theory on discontinuous growth kinetics. It has been observed in the 'interrupted solidification' specimen, that most of the final discontinuous cell size is achieved shortly after the initial growth stages before the continuous precipitation becomes the main transformation mechanism; it is possible to estimate that the discontinuous mode occurs mainly in the temperature range $\sim 1185^{o}$ - $1160^{o}C$, corresponding to a reaction time of $\sim$ 30 seconds. This is based on a cooling rate condition of $40^{o}C\ min^{-1}$. This proposed higher value for the cooling rate (although the casting conditions were GR = $26^{o}C\ min^{-1}$) takes into account that a higher temperature gradient possibly $20^{o}C\ mm^{-1}$ should exist closer to the 'cooler' side of the ingot (section 3.2.2). An average distance of 20 μm is estimated to have been swept by the moving boundary in 30 seconds; thus the velocity of the boundary is estimated at approximately $v \simeq 0.6\ 10^{-4}$ cm sec^{-1}.

Other characteristics of the discontinuous cells in this growth stage included a rod thickness, $\ell \simeq 0.25$ μm and an inter-rod spacing, $\lambda \simeq 0.7 - 1$ μm (the rod thickness increases during the continuous cooling).

The effect of the continuous γ' precipitation in slowing down the boundary velocity is difficult to quantify; however it has been verified that nucleation of continuous particles ahead of the grain boundary drastically reduces and soon halts the migration (Figs.3.58, 3.67-68).

3.5 The Discontinuous γ' Coarsening (Secondary) Reaction Kinetics

The coarser rod structure observed after isothermal heat-

treatments (Figs.3.86, 3.100-101) was found to originate from a grain boundary receding mechanism and partial replacement of the initial rod dispersion. The growth rate in this case was much slower compared to the original discontinuous formation; at 1050°C the experimentally observed value was $v = 1.4\ 10^{-8}$ cm sec^{-1}.

Concerning the cell characteristics, the inter-rod spacing was found to decrease as the boundary receded (Fig.3.86), thus not allowing its precise measurement. The observed values for the inter-rod spacing λ and rod thickness ℓ were :

	ℓ (μm)	λ (μm)
original cell	0.35	0.7
coarsened cell (24 hrs at 1050°C)	1.3	2.0-4.0

The values above are not the average from several cells, but refer to a single cell as according to Gust's[46] proposition, the investigation of discontinuous phase growth kinetics should refer to individual cell characteristics and not to average values.

As-solidified structure

Fig.3.1 R = 60 mm hr^{-1} : grain structure. Optical micrograph. Transverse section.

Fig.3.2 R = 60 mm hr^{-1} : cellular-dendritic solidification structure. Optical micrograph.
a. Transverse section : interdendritic carbides
b. Longitudinal section : no secondary arm development

Fig.3.3 R = 60 mm hr^{-1} : carbide particles. Optical micrograph.
a. Transverse section
b. Longitudinal section

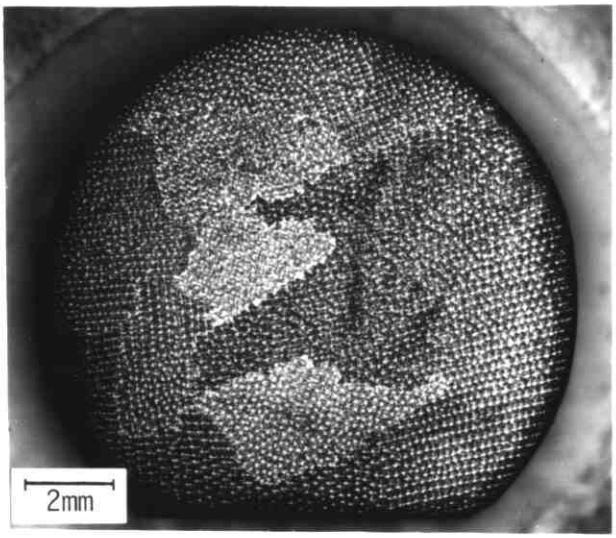

Fig. 3.1

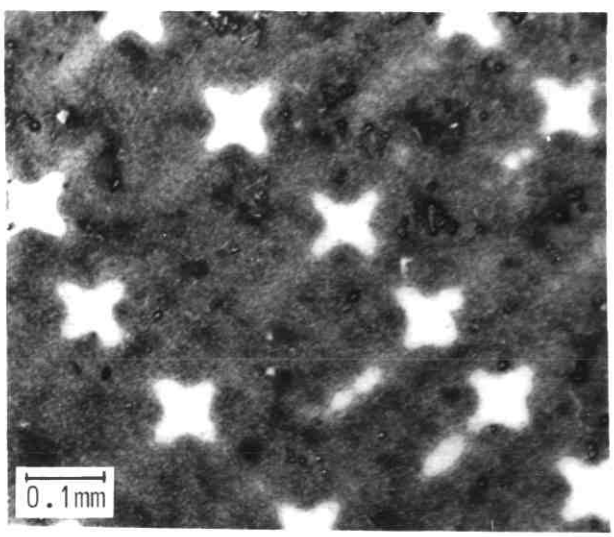

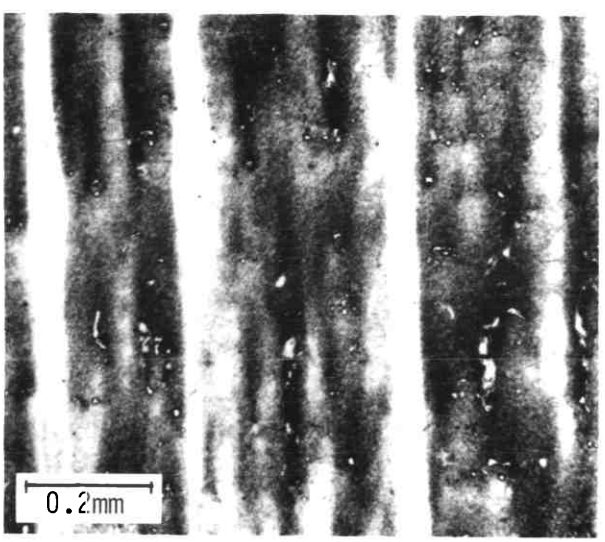

Fig. 3.2 a b

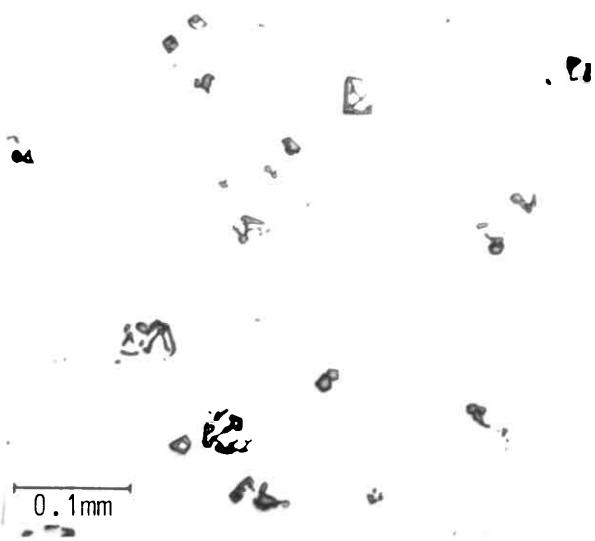

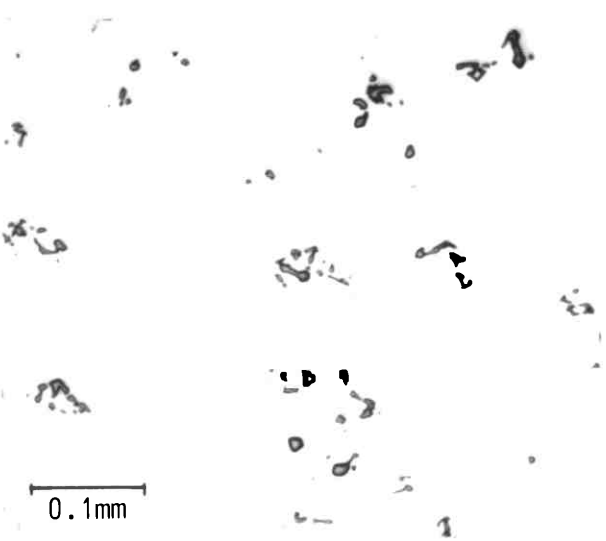

Fig. 3.3 a b

As-solidified structure

Fig.3.4 R = 60 mm hr^{-1} : γ' particles in the core region; observe shape perturbations.
a. Scanning electron micrograph
b. Extraction replica

Fig.3.5 R = 60 mm hr^{-1} : γ' particles in the interdendritic region : ogdoad clusters.
a. Scanning electron micrograph
b. Extraction replica : showing different degrees of cluster development

Fig.3.6 R = 60 mm hr^{-1} : partial γ' solution in the core region after 1120°C - 2 hrs. Scanning electron micrograph.

Fig.3.7 R = 60 mm hr^{-1} : γ' particles in the interdendritic region after 1180°C - 1 hr - WQ. Optical micrograph.

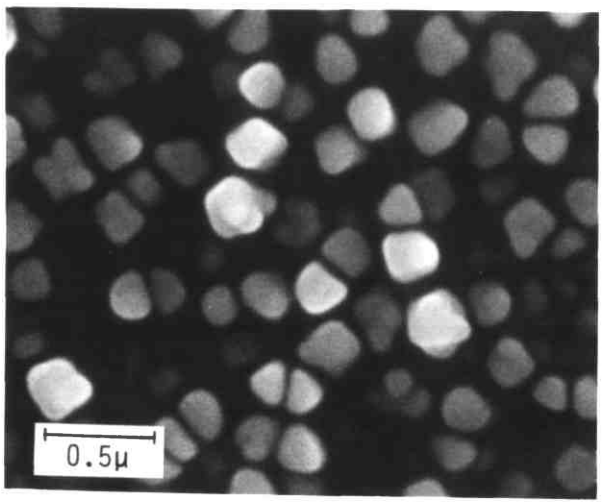

Fig. 3.4 a

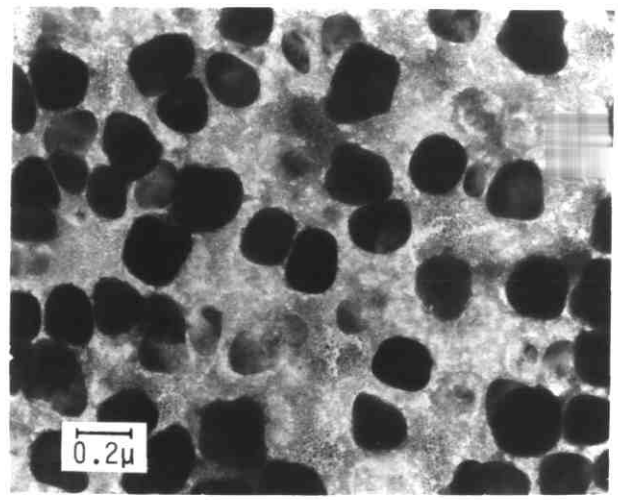

b

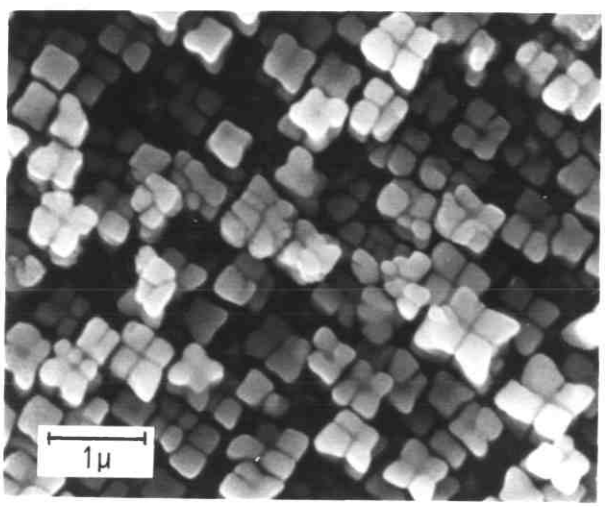

Fig. 3.5 a

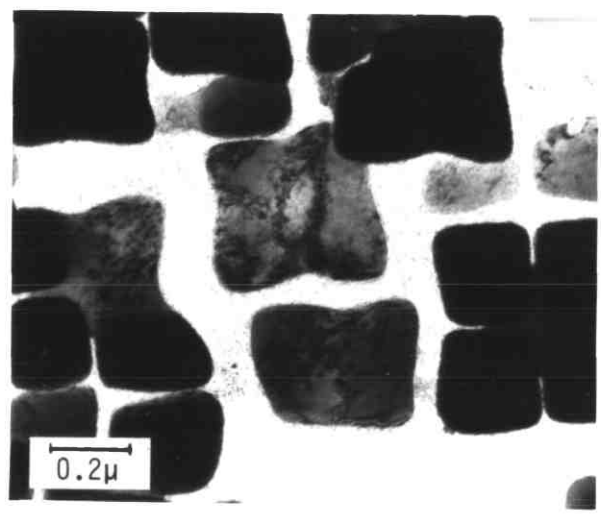

b

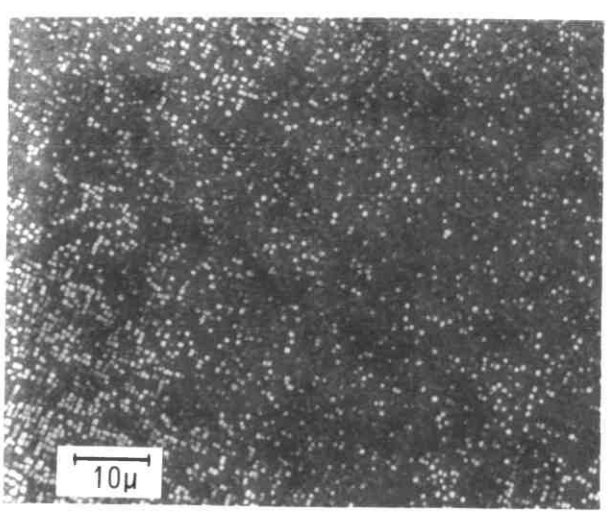

Fig. 3.6

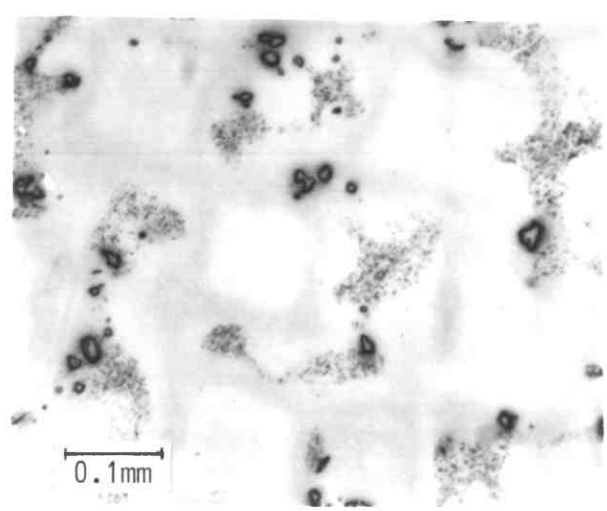

Fig. 3.7

As-solidified structure

Fig.3.8 R = 60 mm hr^{-1} : γ-γ' eutectic colonies. Optical micrograph.

Fig.3.9 R = 60 mm hr^{-1} : γ-γ' eutectic colony : 'finger type' morphology.
Scanning electron micrograph.

Fig.3.10 R = 60 mm hr^{-1} : γ-γ' eutectic colony revealed by deep etch technique : 'finger type' morphology.

Fig.3.11 R = 60 mm hr^{-1} : γ-γ' eutectic colony : detail of the rod morphology (smooth and serrated rods).

Extraction replicas.

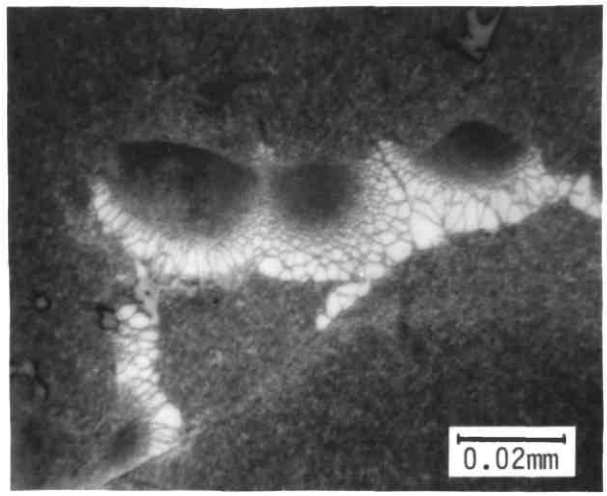

Fig. 3.8

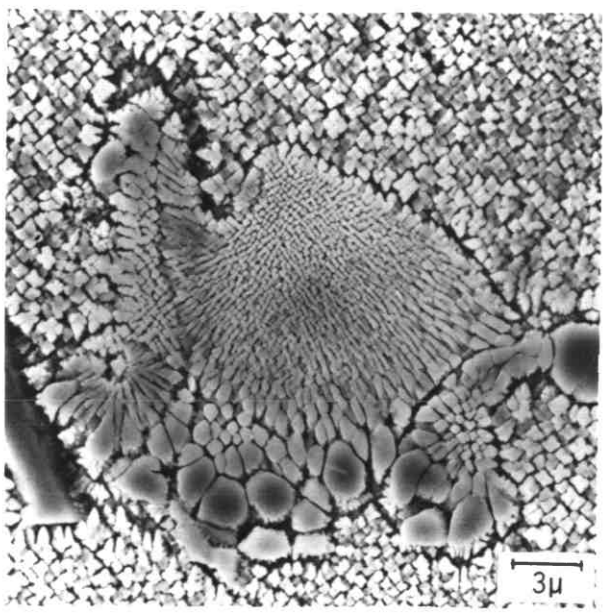

Fig. 3.9

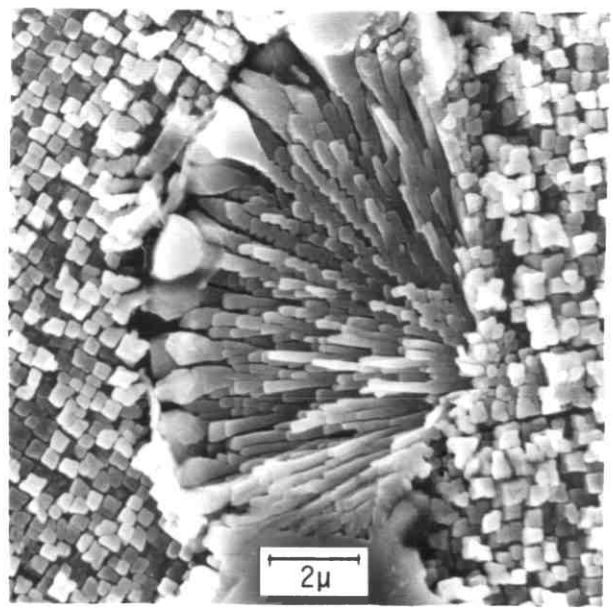

Fig. 3.10

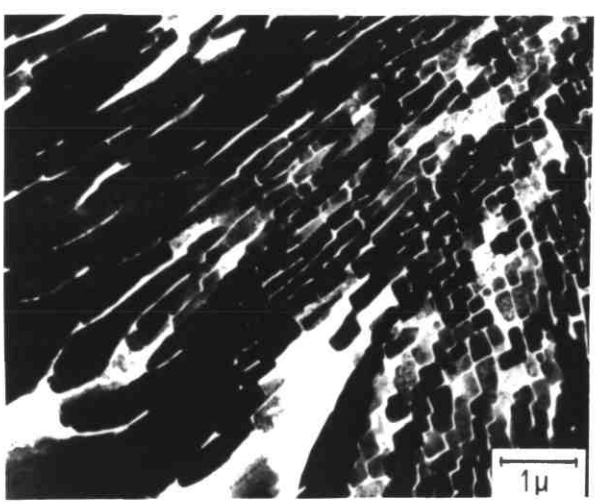

Fig. 3.11 a

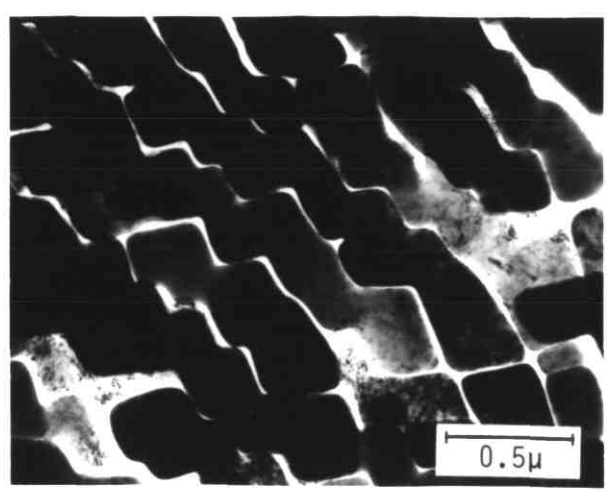

b

As-solidified structure

Fig.3.12 R = 60 mm hr^{-1} : γ-γ' eutectic.
Optical micrograph.

Figs.3.13 - 3.15 R = 60 mm hr^{-1} : γ-γ' eutectic : fine rod morphology.
Scanning electron micrographs.

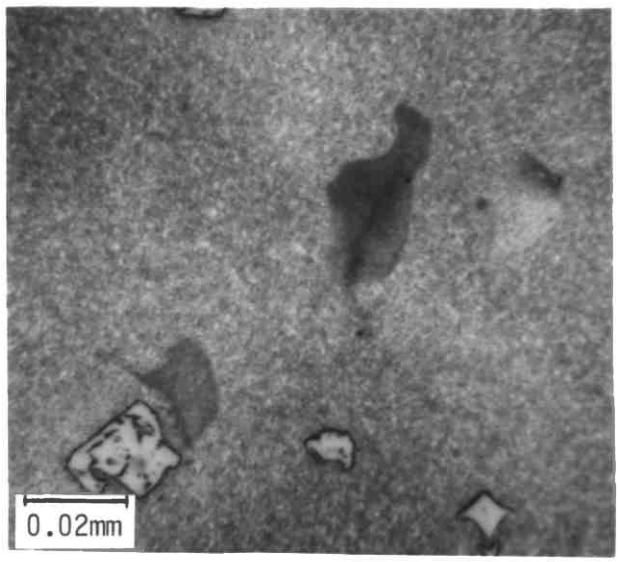

Fig. 3.12

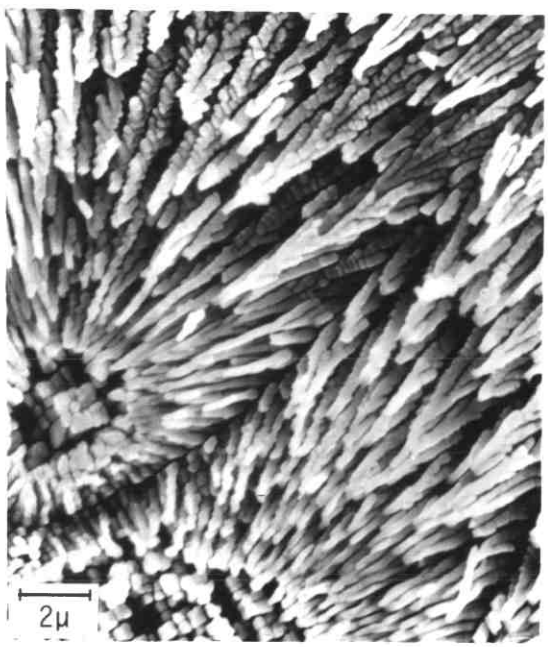

Fig. 3.13

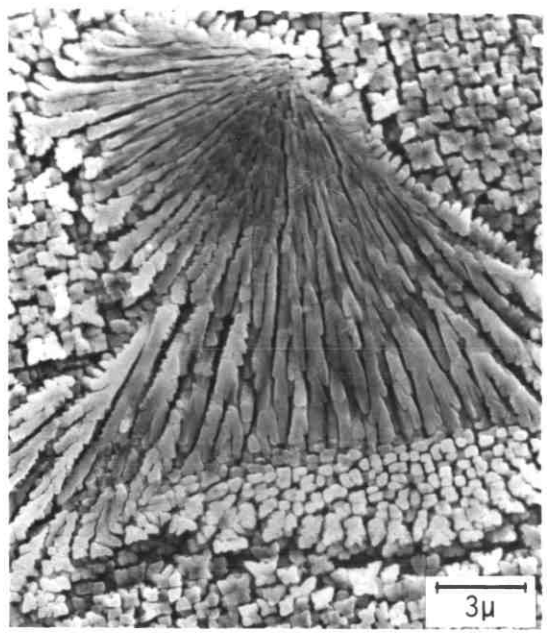

Fig. 3.14

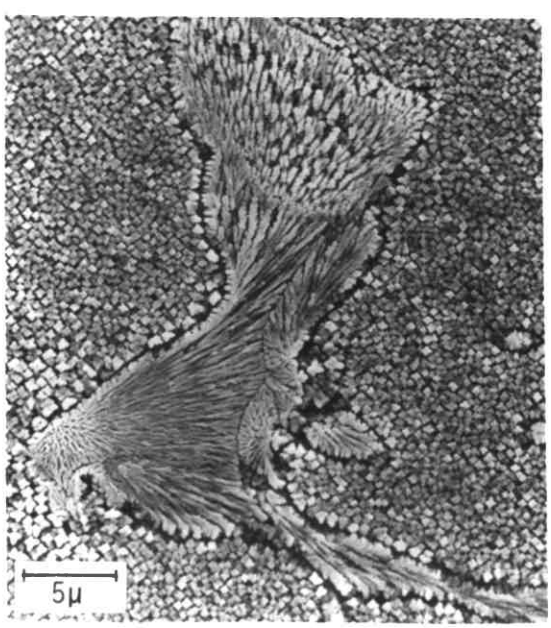

Fig. 3.15 a

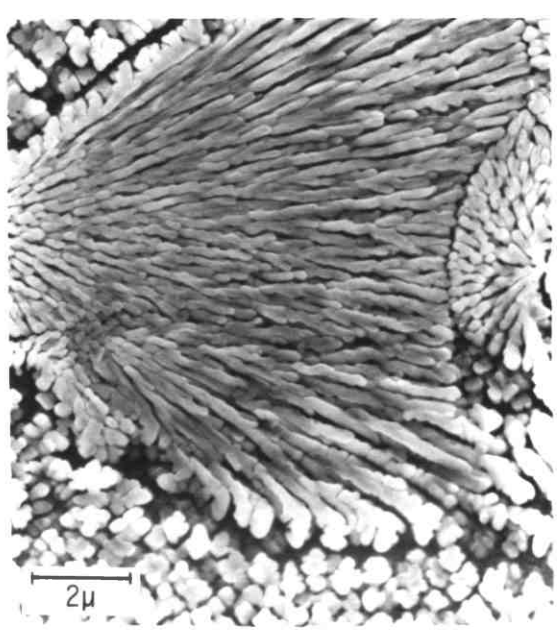

b

As-solidified structure

Figs.3.16-3.17 R = 60 mm hr^{-1} : γ' Particles formed at the grain boundary : effect of different etch solutions.

Fig.3.16 Matrix etched away. Scanning electron micrograph.

Fig.3.17 γ' particles etched away. Scanning electron micrograph.

Figs.3.18-3.19 R = 60 mm hr^{-1} : Discontinuous γ' cells formed at the grain boundary.

Fig.3.18 Optical micrograph.

Fig.3.19 'Double' cell morphology (see Fournelle mechanism in Figure 1.7). Optical micrograph.

Figs.3.20-3.22 R = 60 mm hr^{-1} : Discontinuous γ' cells.

Fig.3.20 Steep curvatures in rod morphology. Scanning electron micrograph.

Fig.3.21 Cell adjacent to γ-γ' eutectic (top left). Scanning electron micrograph.

Fig.3.22 Scanning electron micrograph.

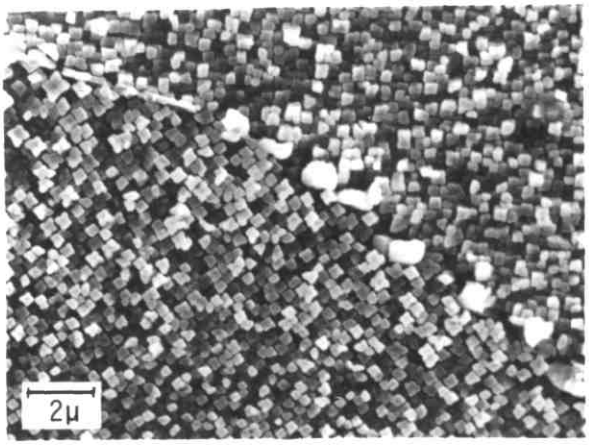

Fig. 3.16

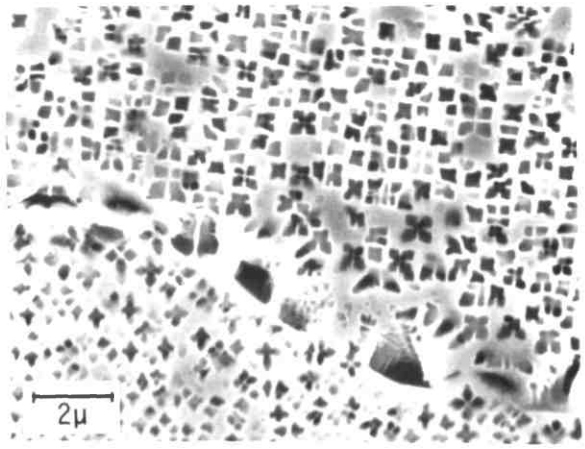

Fig. 3.17

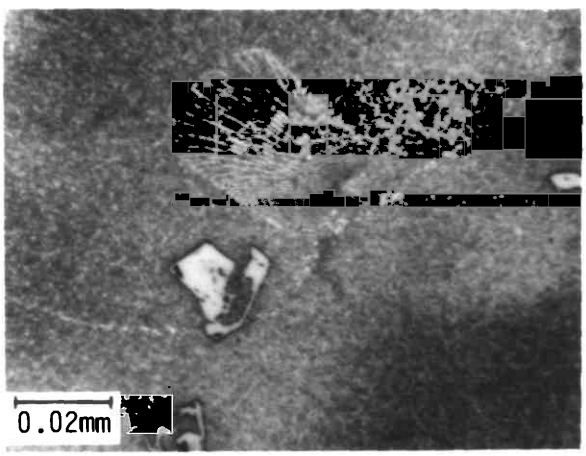

Fig. 3.18

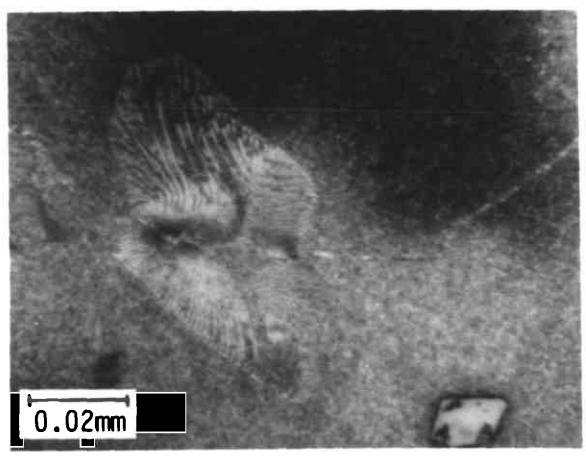

Fig. 3.19

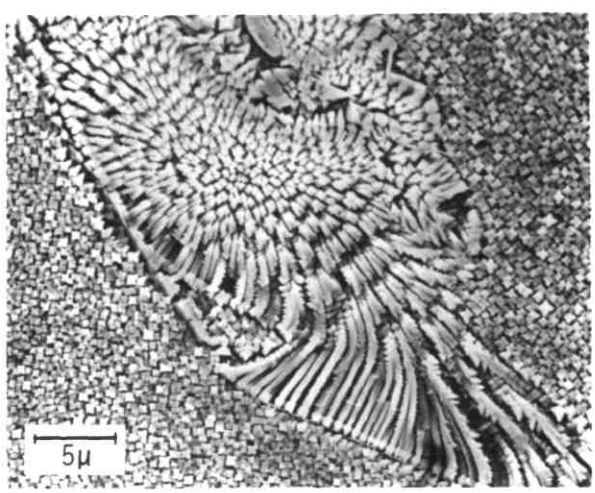

Fig. 3.20

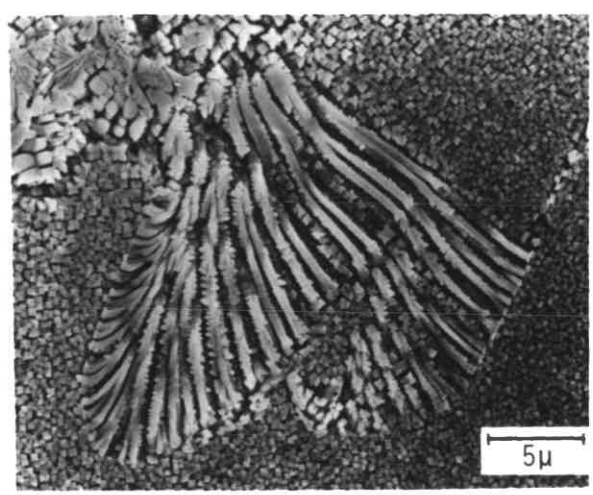

Fig. 3.21

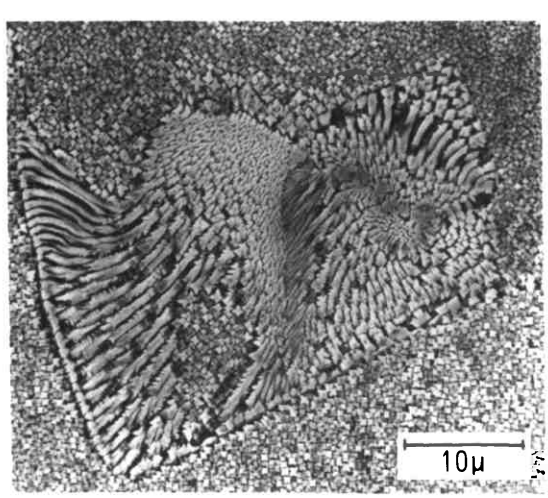

Fig. 3.22

As-solidified structure

Fig.3.23 R = 60 mm hr^{-1} : Discontinuous γ' cells : rod morphology.
a. Curved rods. Scanning electron micrograph.
b. Detailed examination : smooth rod surface with small dendritic formation in the final growth stage. Scanning electron micrograph.

Figs.3.24-3.26 R = 60 mm hr^{-1} : Discontinuous γ' cells : well developed dendritic instabilities (deep etch technique). Scanning electron micrographs.

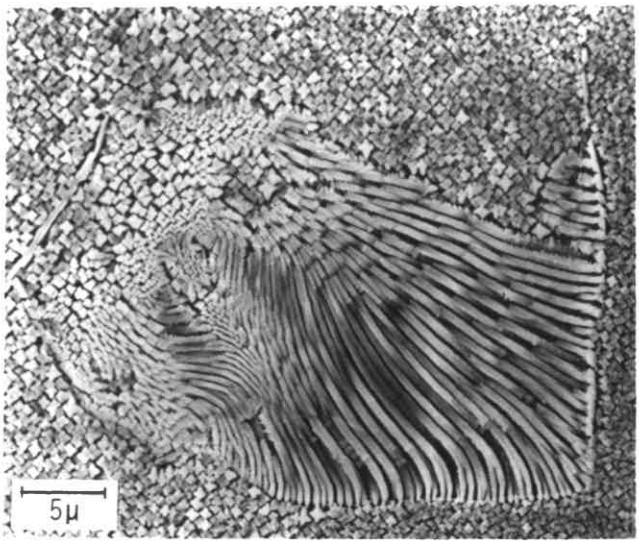

Fig. 3.23 a

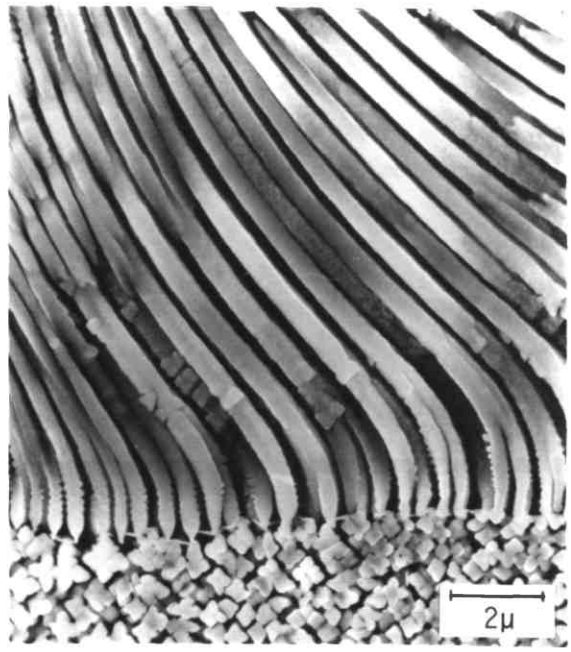

b

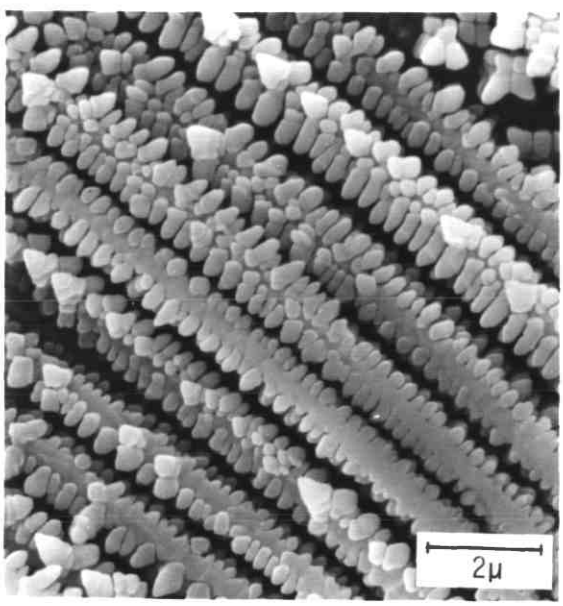

Fig. 3.24

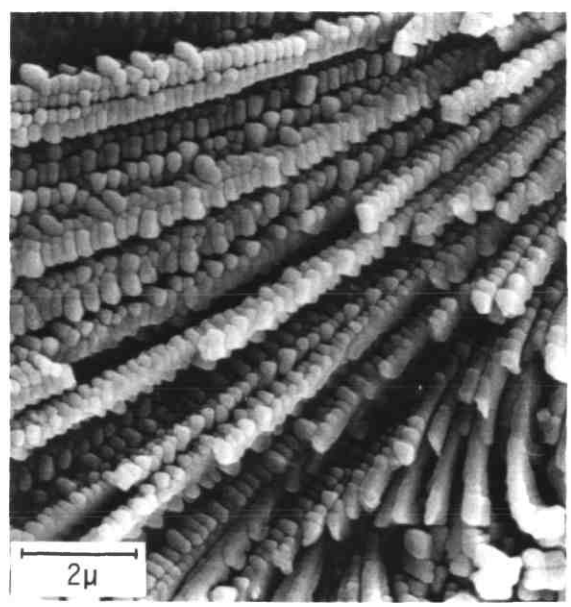

Fig. 3.25

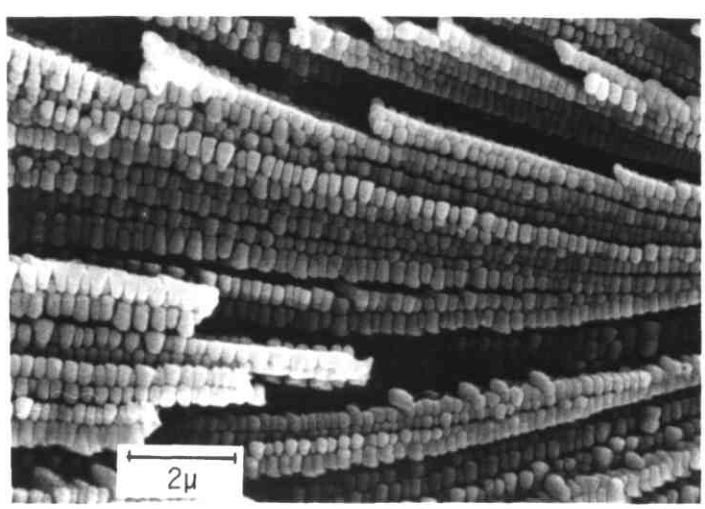

Fig. 3.26

As-solidified structure

Fig.3.27 R = 300 mm hr^{-1} : dendritic solidification. Optical micrograph.
a. Transverse section
b. Longitudinal section in secondary and tertiary arm development.

Fig.3.28 R = 300 mm hr^{-1} : carbide particles. Optical micrograph.
a. Transverse section
b. Longitudinal section

Fig.3.29 R = 300 mm hr^{-1} : γ' particles in the core region : rounded morphology. Extraction replicas.

Fig.3.30 R = 300 mm hr^{-1} : γ' particles in the interdendritic region : cubic shape showing preferential growth at the corners. Extraction replicas.

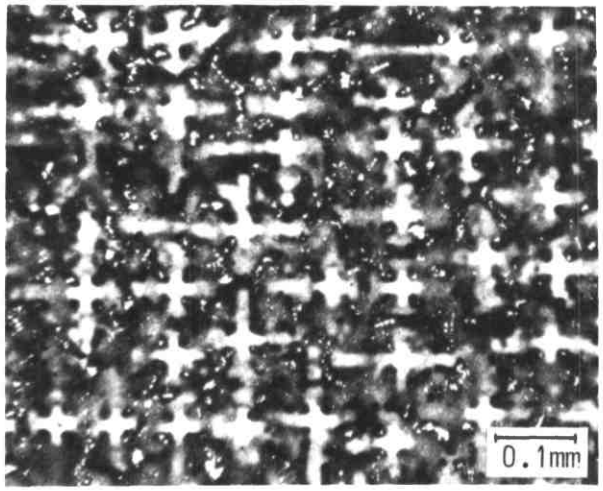

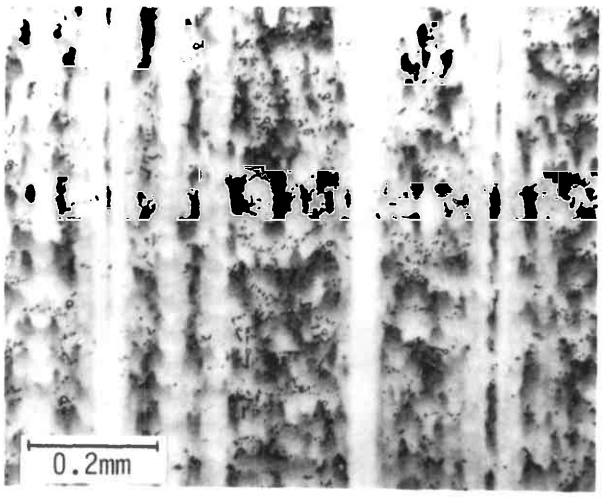

Fig. 3.27 a b

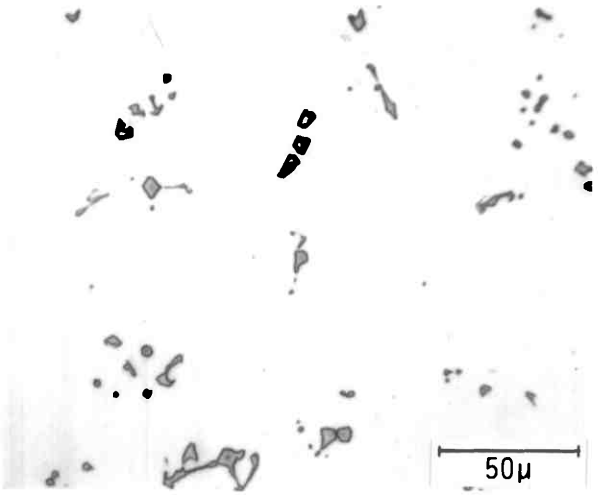

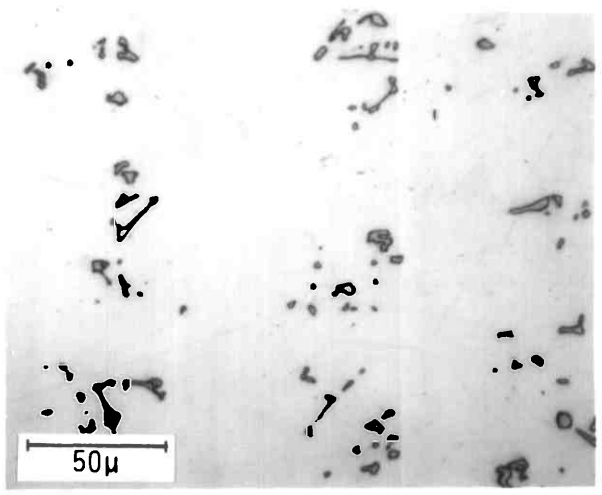

Fig. 3.28 a b

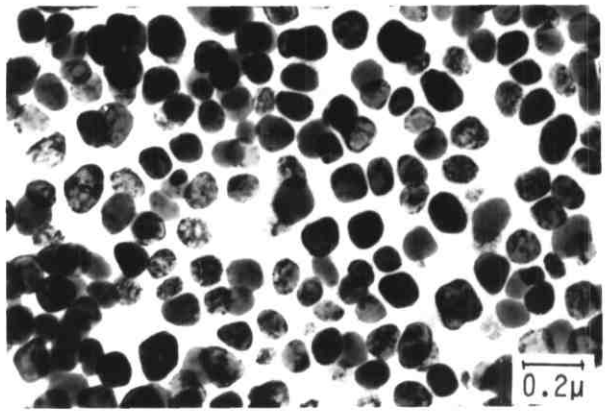

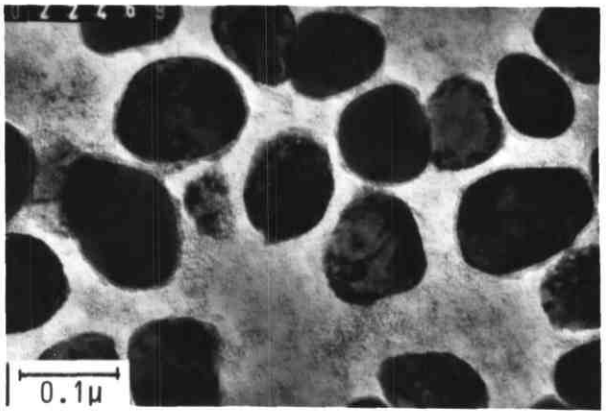

Fig. 3.29 a b

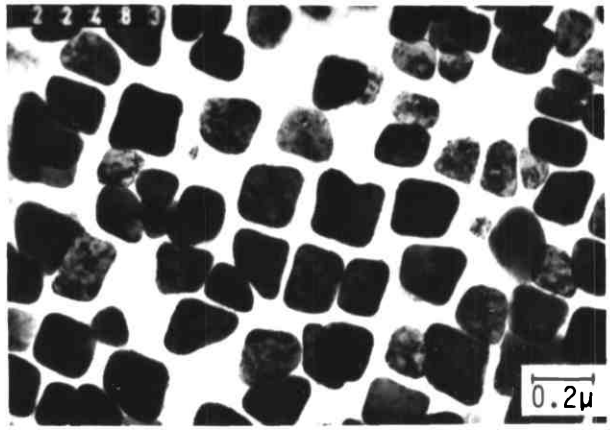

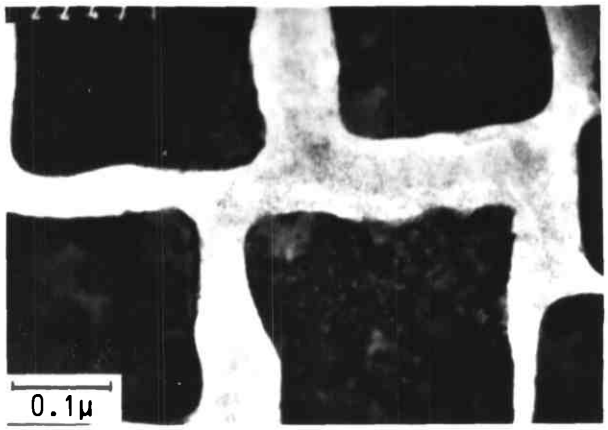

Fig. 3.30 a b

As-solidified structure

Fig.3.31 R = 300 mm hr^{-1} : γ-γ' eutectic : 'finger type' morphology. Scanning electron micrograph.

Fig.3.32 R = 300 mm hr^{-1} : γ-γ' eutectic : detail of rod morphology.

a. Extraction replica
b. Extraction replica : smooth rod surface and rod branching
c. Extraction replica : serrated rod surface.

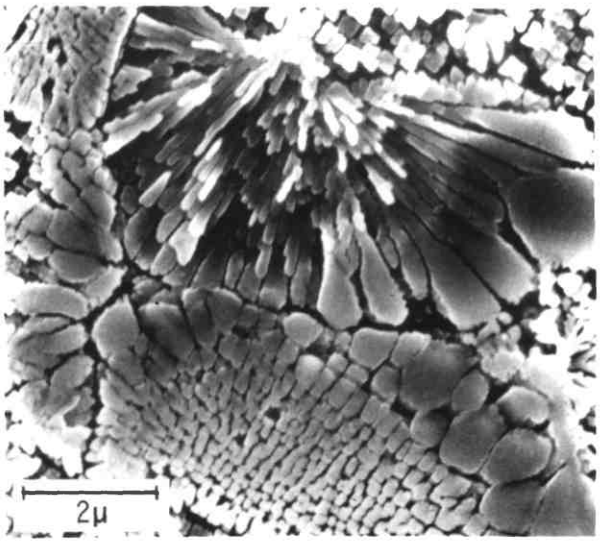

Fig. 3.31

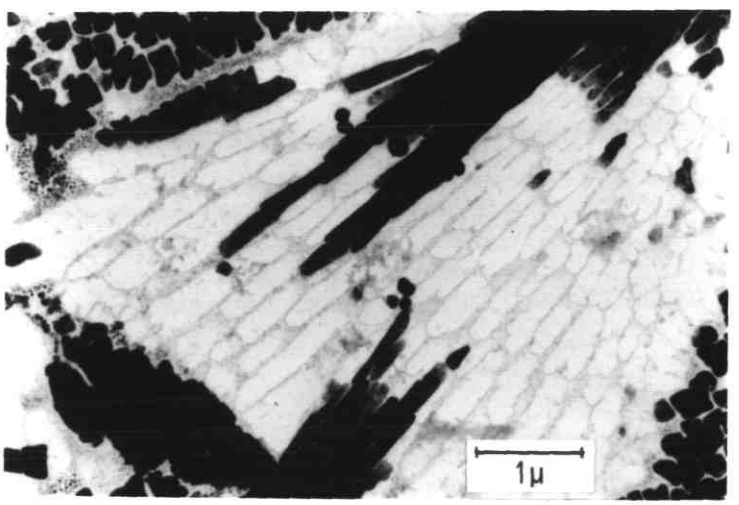

Fig. 3.32

a

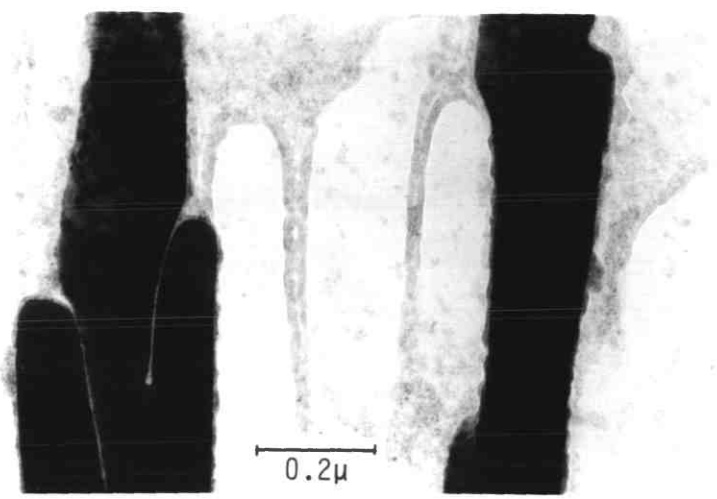

b

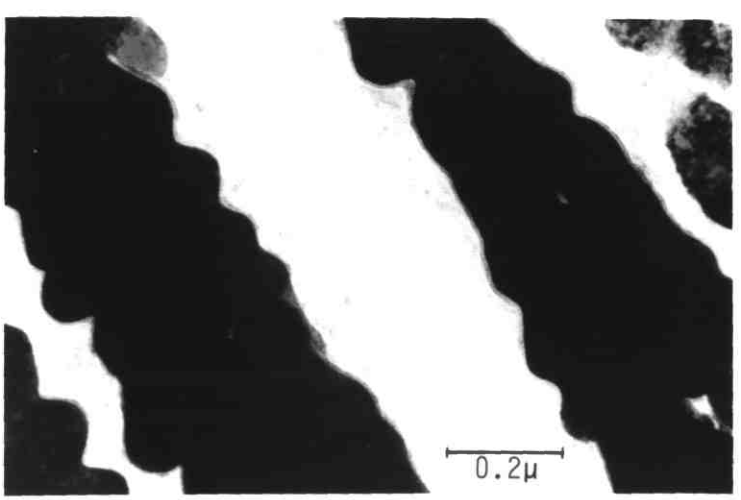

c

As-solidified structure

Fig.3.33 R = 600 mm hr^{-1} : dendritic solidification. Optical micrograph (reverse etching conditions).
a. Transverse section : carbides formed in inter-dendritic regions
b. Longitudinal section : formation of secondary and tertiary arms.

Fig.3.34 R = 600 mm hr^{-1} : carbide particles. Chinese-script morphology. Optical micrograph.
a. Transverse section
b. Longitudinal section.

Fig.3.35 R = 600 mm hr^{-1} : extracted carbide particles : shape instabilities. Scanning electron micrographs.

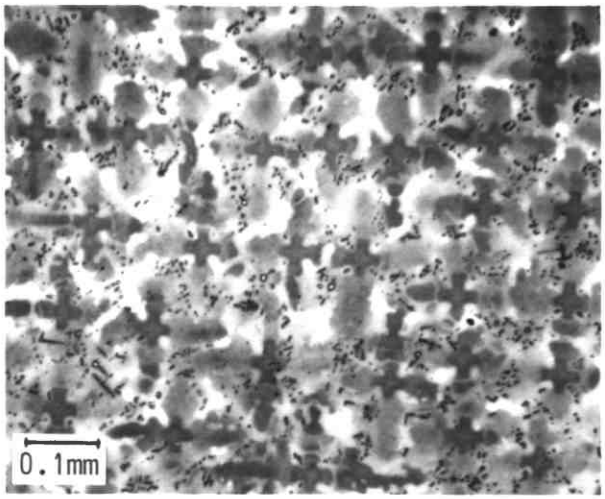

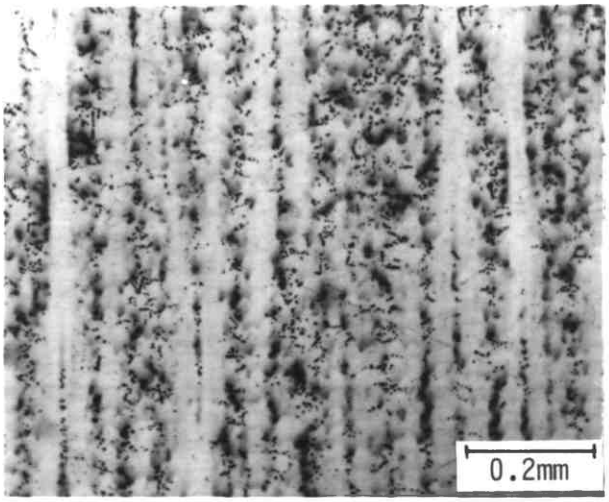

Fig. 3.33 a b

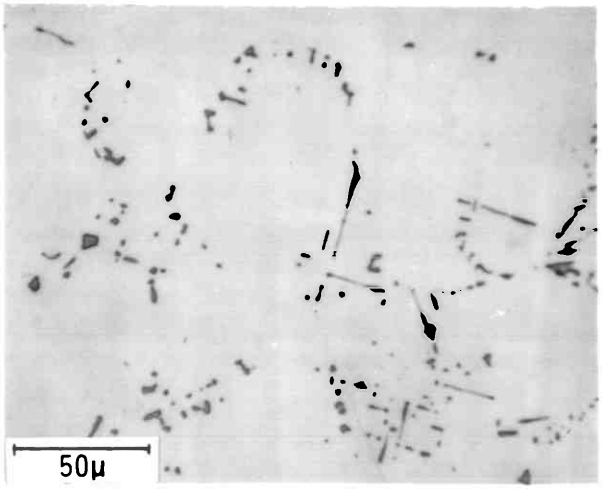

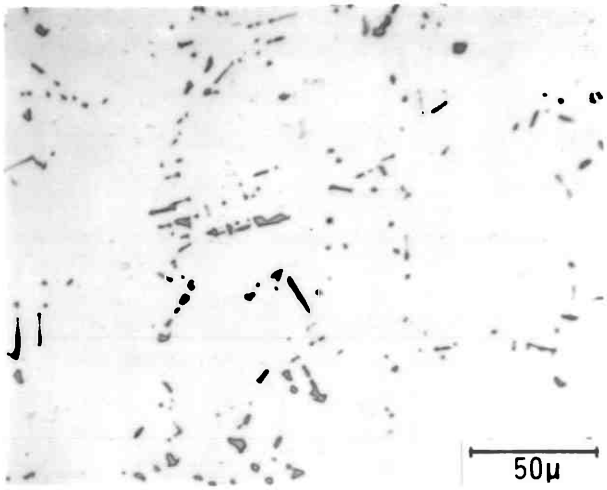

Fig. 3.34 a b

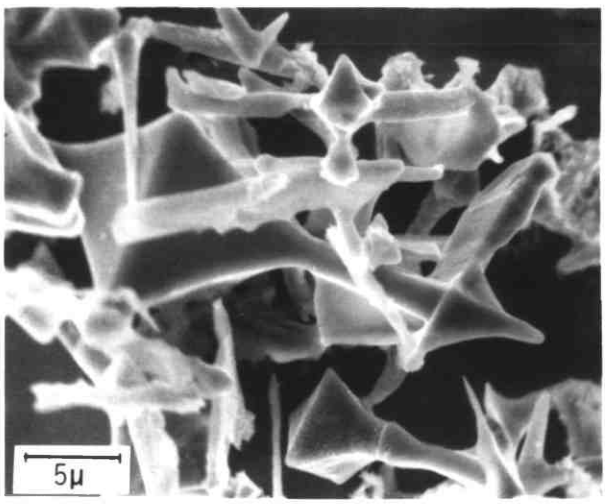

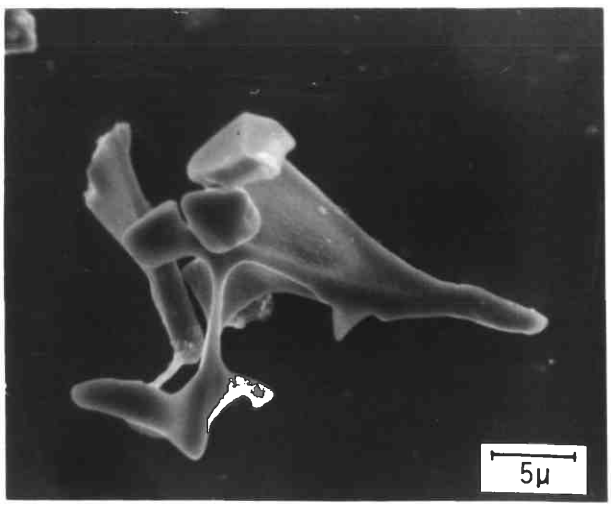

Fig. 3.35 a b

As-solidified structure

Fig.3.36 R = 600 mm hr^{-1} : γ' particles. Extraction replicas.
a. Core region : near-spherical morphology
b. Interdendritic region : rounded-cubic morphology.

Fig.3.37 Diffraction pattern relative to Fig.3.36b : (001) orientation.

Fig.3.38 R = 600 mm hr^{-1} : small γ-γ' eutectic colony of the 'finger type' morphology. Scanning electron micrograph.

Fig.3.39a R = 600 mm hr^{-1} : γ-γ' eutectic (E) and discontinuous cell (D). Scanning electron micrograph .

b. Detail of the discontinuous cell : dendritic perturbations can be observed.

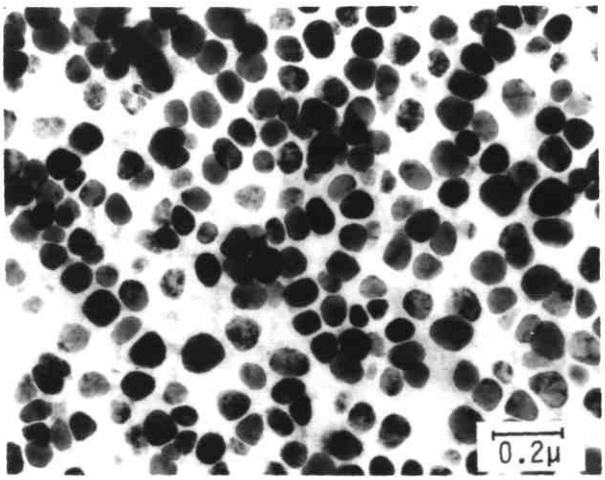

Fig. 3.36 a

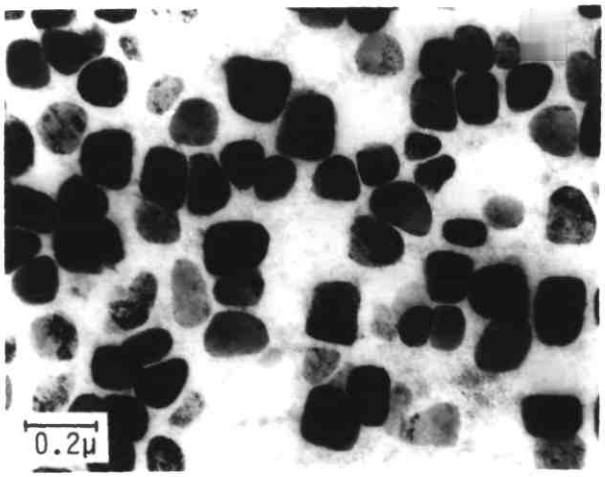

b

Fig. 3.37

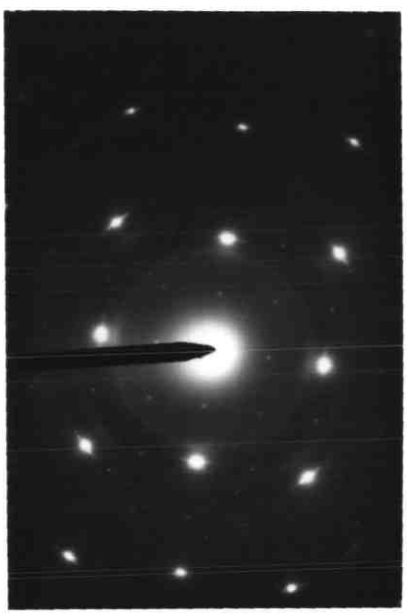

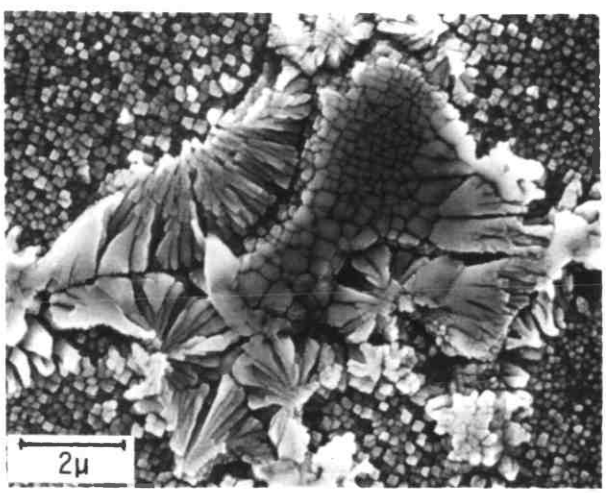

Fig. 3.38

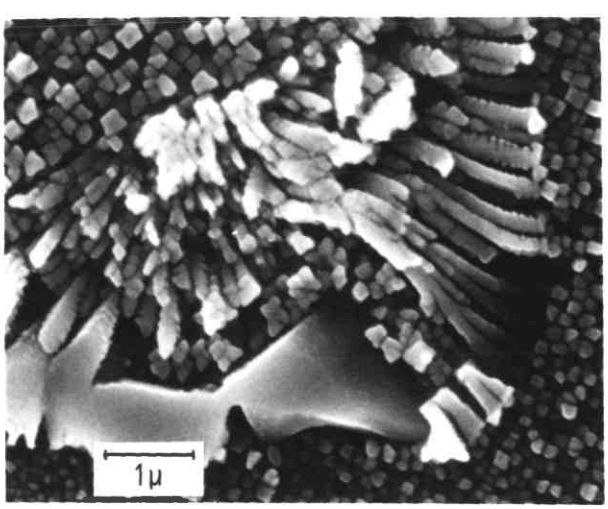

Fig. 3.39 a b

As-solidified structure

Fig.3.40 R = 12 mm hr^{-1} (G = 13°C mm^{-1}) : cellular solidification structure. Scanning electron micrograph.
a. General structure.
b. Coarser γ' particles in the cellular ring.

Fig.3.41 R = 12 mm hr^{-1} (G = 13°C mm^{-1}) : detail of the coarser γ' particles (central band from top left to bottom right). Scanning electron micrograph.

Fig.3.42 R = 12 mm hr^{-1} (G = 13°C mm^{-1}) : γ' particles forming ogdoad clusters : particles joined by common nucleus (deep etch technique). Scanning electron micrograph.

Fig.3.43 R = 12 mm hr^{-1} (G = 13°C mm^{-1}) : γ' particles forming clusters with more than eight particles; plate-shaped particles have also developed (see possible plate configurations in Fig.4.4). Scanning electron micrograph.

Fig.3.44 R = 9.6 mm hr^{-1} (G = 20°C mm^{-1}) : near plane-front solidification structure. Optical micrograph.

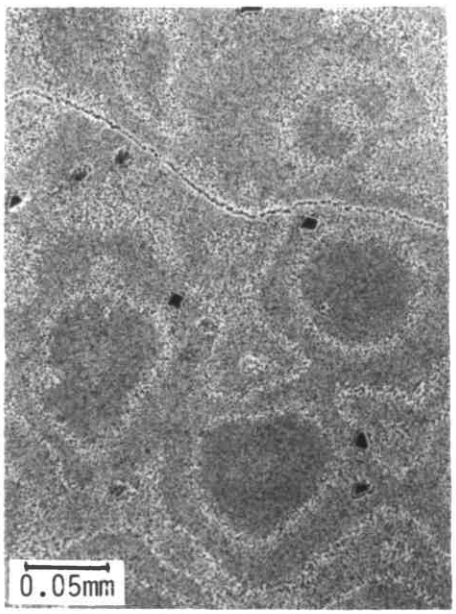

Fig. 3.40 a

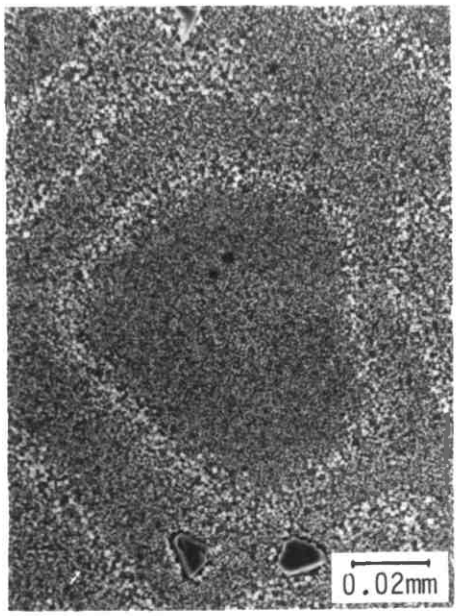

b

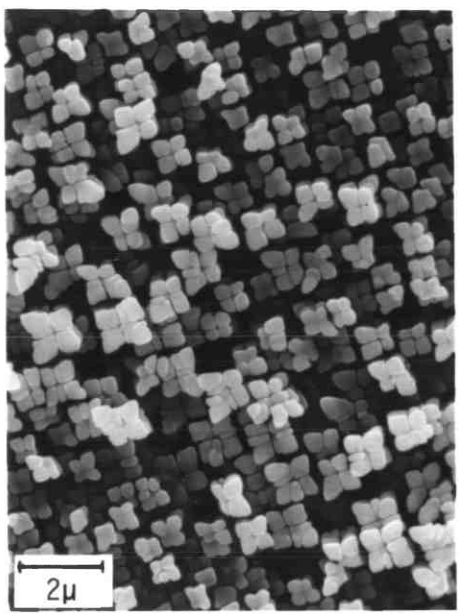

Fig. 3.41

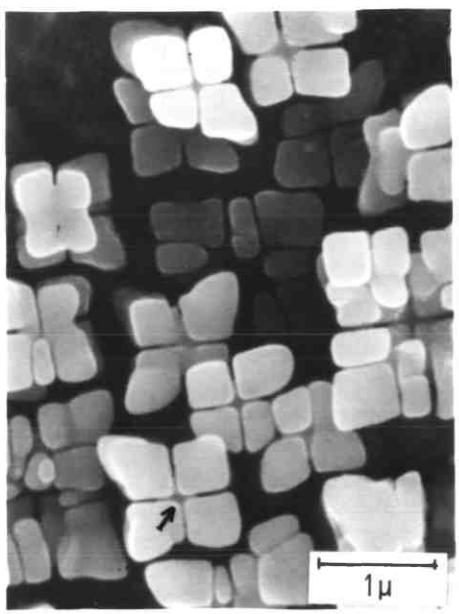

Fig. 3.42

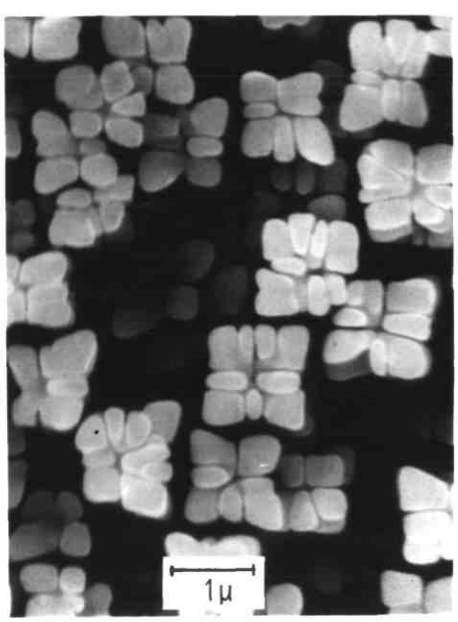

Fig. 3.43

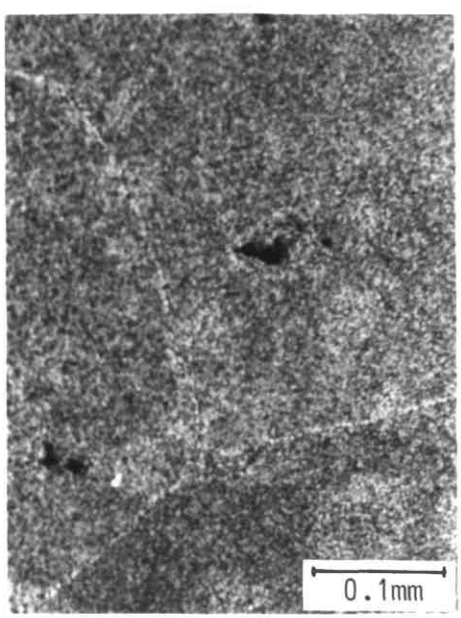

Fig. 3.44

As-solidified structure

Fig.3.45 R = 30 mm hr^{-1} : cellular-dendritic solidification structure. Optical micrograph.

Fig.3.46 R = 30 mm hr^{-1} : large volume fraction of discontinuous γ' cells. Optical micrograph.

Fig.3.47 R = 30 mm hr^{-1} : discontinuous cell showing the same morphological features as observed for other cooling rates. Scanning electron micrographs.

Fig.3.48 R = 30 mm hr^{-1} : discontinuous γ' rods : smooth rod surface and some small dendritic instabilities. Scanning electron micrograph.

Fig.3.49 R = 30 mm hr^{-1} : discontinuous cells : large γ' particles grown in the inter-rod spacing; also fine γ' particles. Scanning electron micrograph.

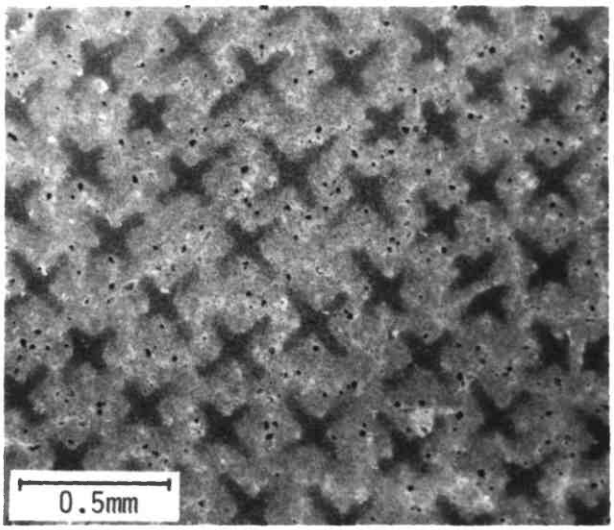

Fig. 3.45

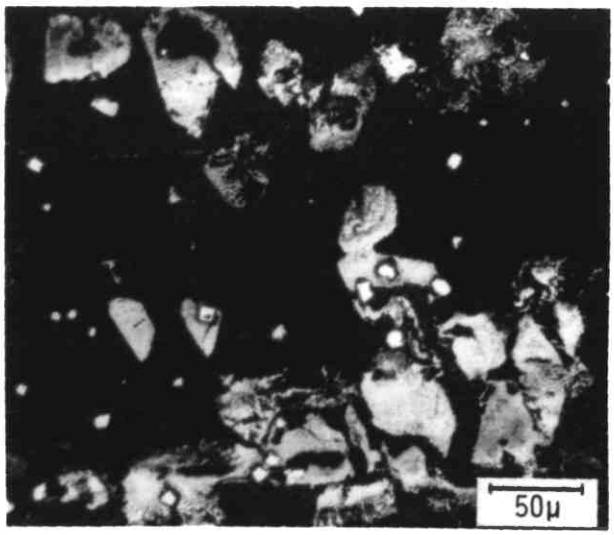

Fig. 3.46

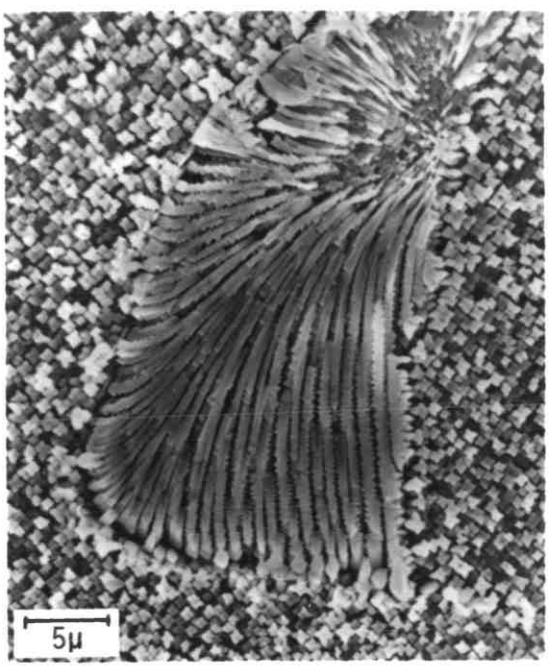

Fig. 3.47 a

b

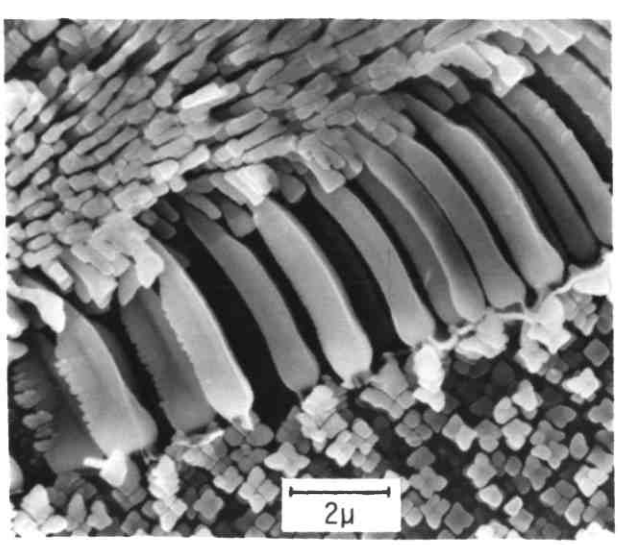

Fig. 3.48

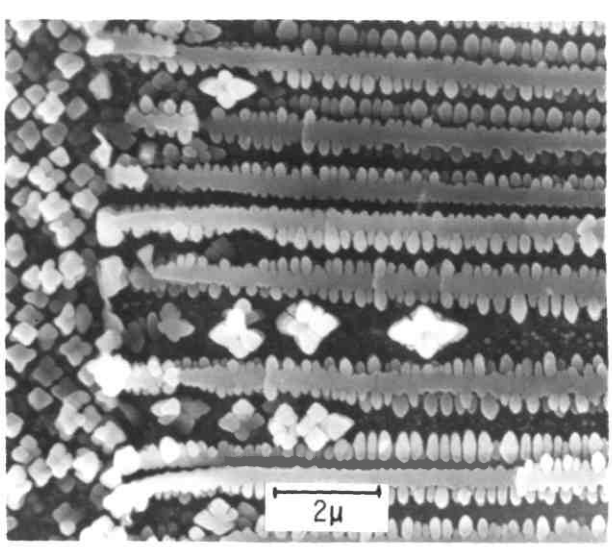

Fig. 3.49

Interrupted solidification

$R = 120$ mm hr^{-1}, $G = 13^{o}C$ mm^{-1}

Fig.3.50 Longitudinal section (solid-state γ' precipitation not included). Optical micrograph. The phase reactions are as indicated :
1. Solid-liquid interface.
2. Formation of faceted MC carbides.
3. Development of surface instabilities in the MC carbides.
4. Entrapment of liquid with eutectic composition.

Fig.3.51 Transverse section corresponding to section 2 : MC carbide formation from the melt (the Chinese-script morphology formed during the quenching). Optical micrograph.

Fig.3.52 Transverse section 4 : regions of eutectic liquid (A) in the interdendritic region. Optical micrograph.

Fig.3.53 Transverse section 4 : detail of the eutectic 'liquid' (A); the γ' particles visible in the micrograph result from a cooling effect and are not part of the high temperature structure. Scanning electron micrograph.

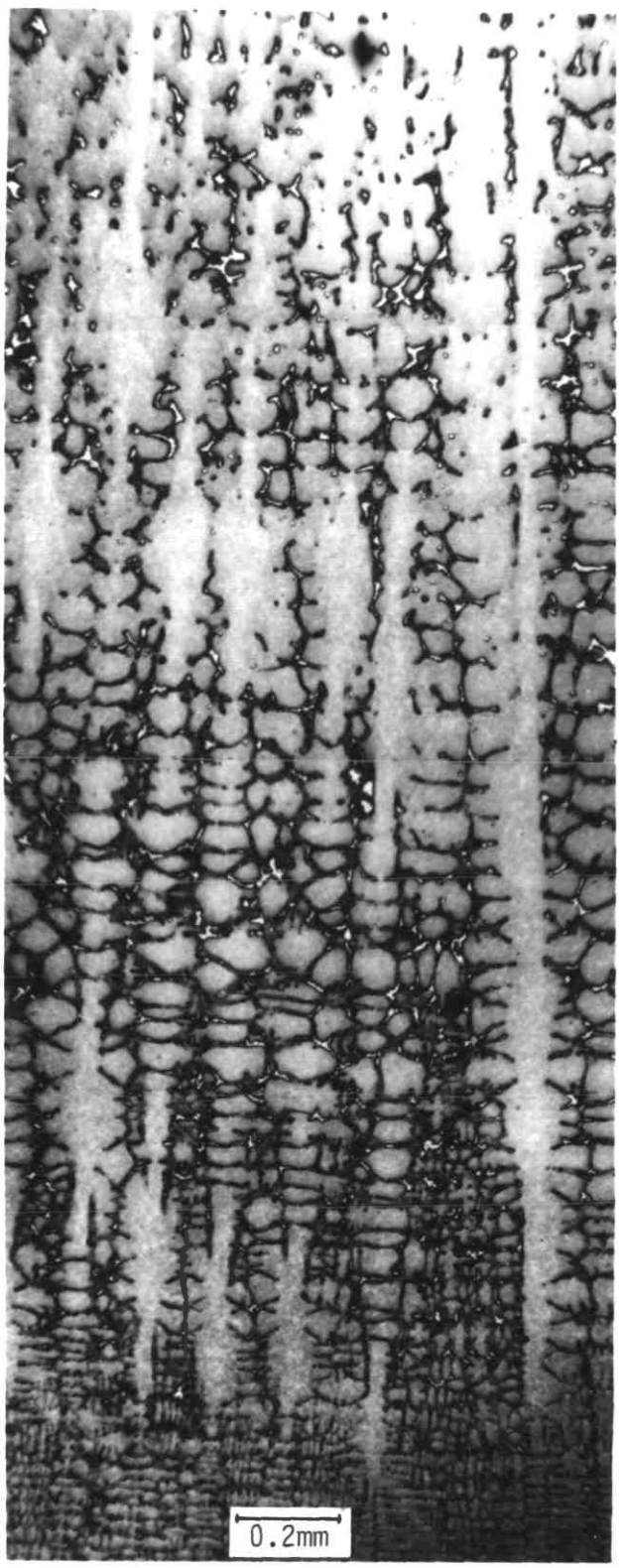

Fig. 3.50

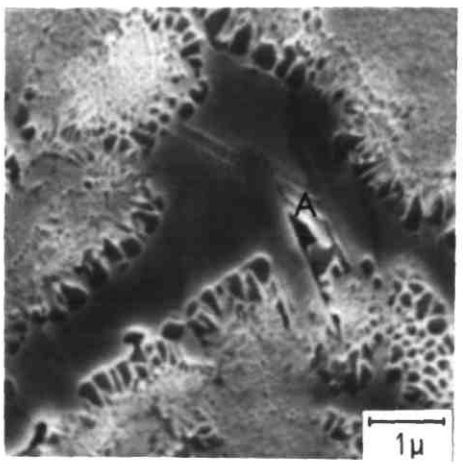

Fig. 3.53

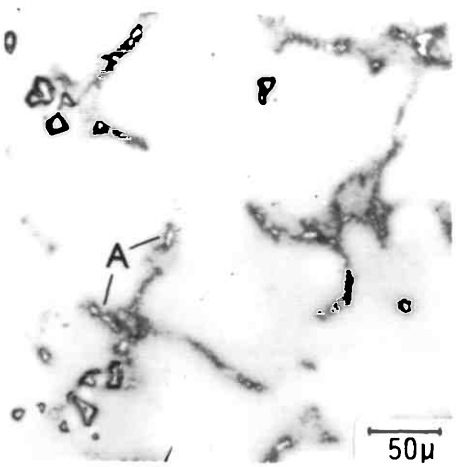

Fig. 3.52

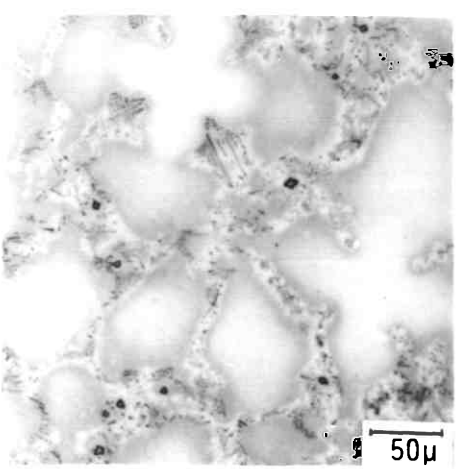

Fig. 3.51

— 4

— 3

— 2

— 1

Interrupted Solidification

$R = 120$ mm hr^{-1}, $G = 13^{o}C$ mm^{-1}

Fig.3.54 Longitudinal section (all transformations included). Optical micrograph. The phase transformations are as indicated :
1. Solid-liquid interface.
2. MC carbide formation
3. Entrapment of liquid with eutectic composition.
4. Start of γ-γ' eutectic solidification.
5. Start of continuous γ' precipitation (interdendritic region).
6. Start of the discontinuous γ' reaction.
7. End of the γ-γ' eutectic solidification.
8. Start of continuous γ' precipitation in the core region.

Fig.3.55 Transverse section 5-7 : γ-γ' eutectic solidification; observe remaining 'liquid' and continuous γ' particles. Scanning electron micrograph.

Fig.3.56 Transverse section 5-7 : continuous γ' precipitation in interdendritic regions. Optical micrograph.

Fig.3.57 Transverse section 5-7 : γ' particles growing into the ogdoad morphology in the interdendritic region. Scanning electron micrograph.

Fig.3.58 Transverse section 6-7 : discontinuous phase growth halted by continuous precipitation; in the core region (bottom of the micrograph) no continuous precipitation has yet occurred and one segment of the grain boundary may still migrate. Scanning electron micrograph.

Fig.3.59 Transverse section 8 : continuous γ' precipitation in the core region; particles formed some least developed ogdoad clusters. Scanning electron micrograph.

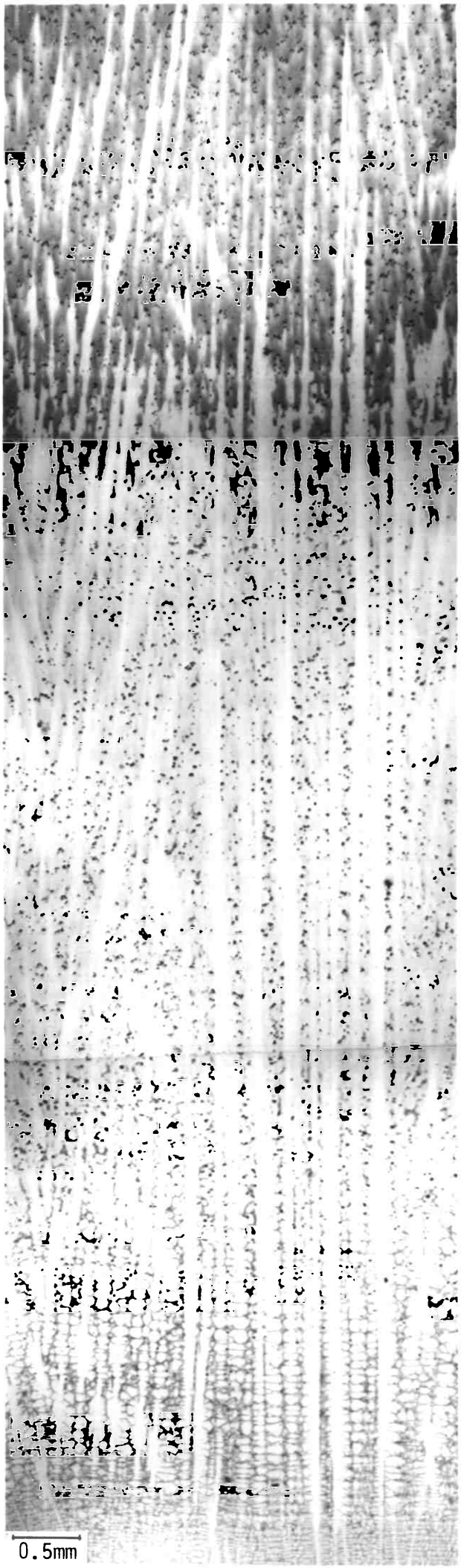

Fig. 3.54

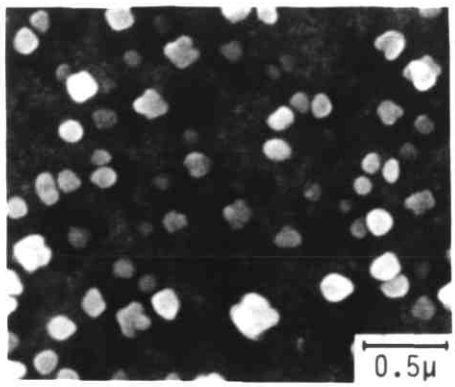

Fig. 3.59

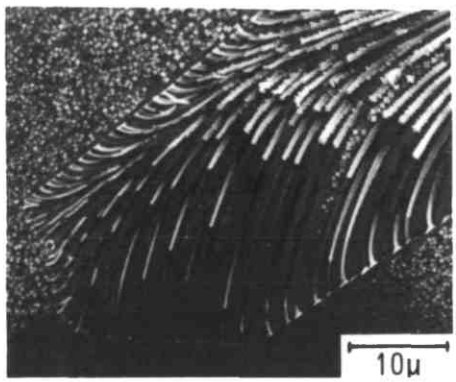

Fig. 3.58

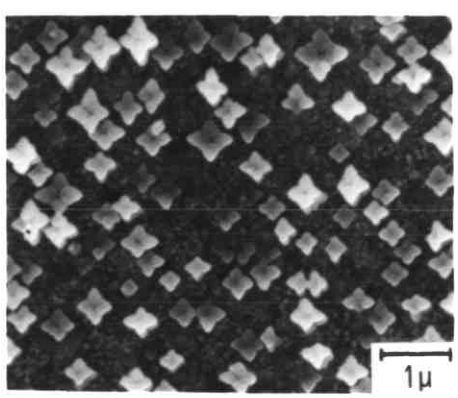

Fig. 3.57

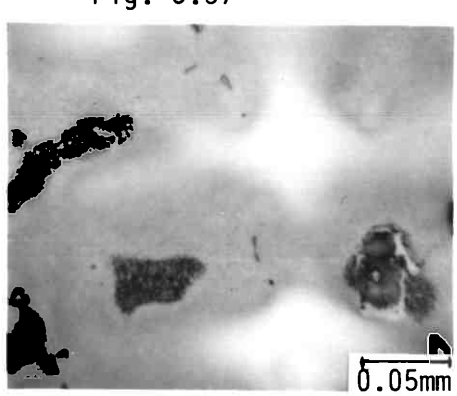

Fig. 3.56

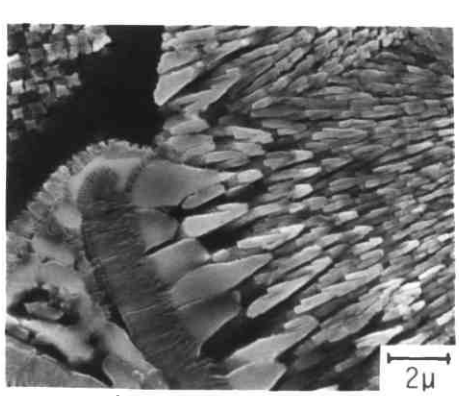

Fig. 3.55

Interrupted Solidification

$R = 120$ mm hr^{-1}, $G = 13^{o}C$ mm^{-1}

Fig.3.60 γ-γ' eutectic solidification : finger-type structure. Region of liquid (L) is indicated. Scanning electron micrographs.

Fig.3.61 γ-γ' eutectic solidification : fine rod morphology. The micrograph suggests the existence of a solidification front. Scanning electron micrographs.

Fig.3.62 γ-γ' eutectic solidification : fine rod morphology. Scanning electron micrograph.

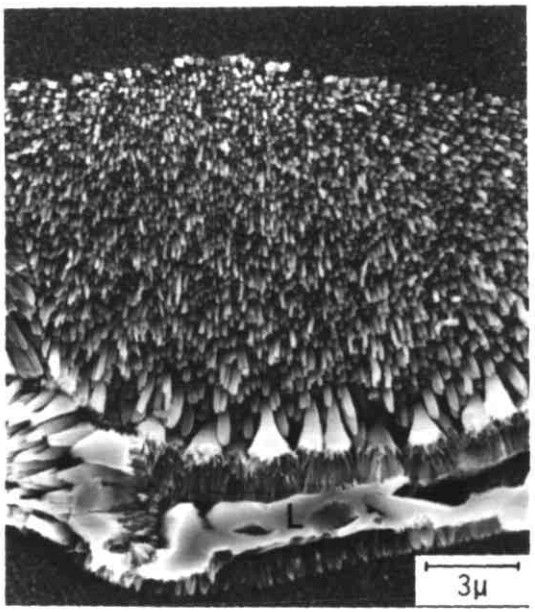

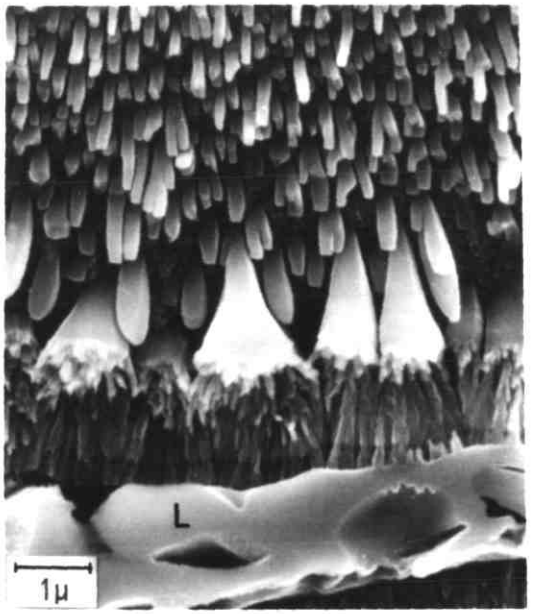

Fig. 3.60 a b

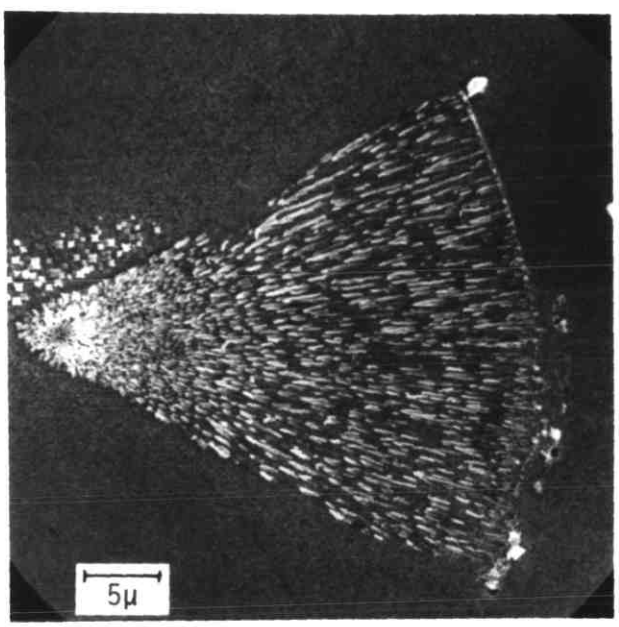

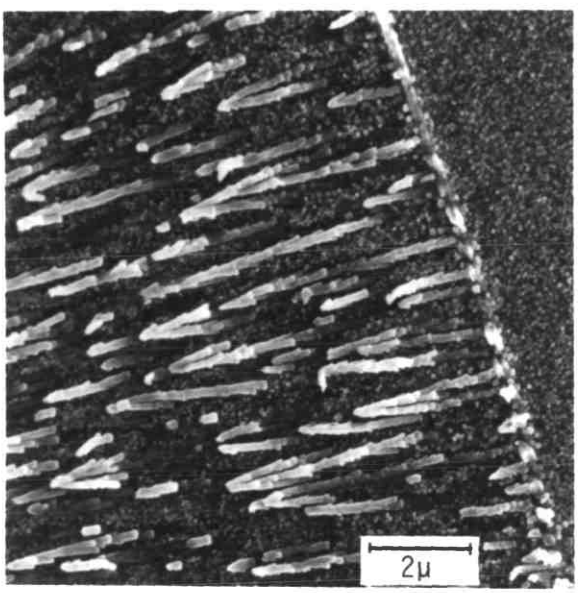

Fig. 3.61 a b

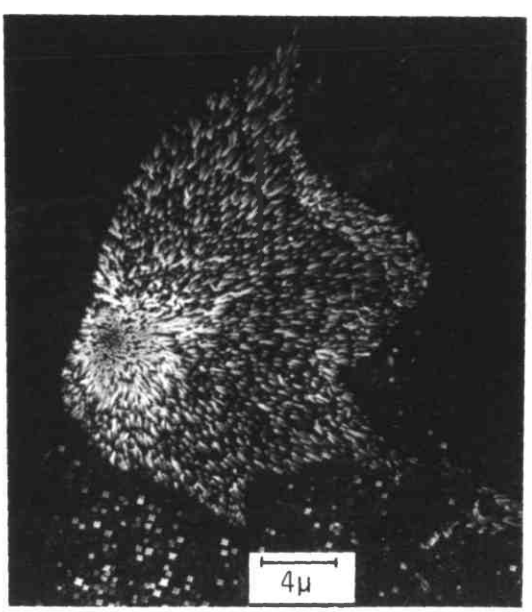

Fig. 3.62

Interrupted Solidification

$R = 120$ mm hr^{-1}, $G = 13^{o}C$ mm^{-1}

Approximate temperature : $1150^{o}C$

Fig.3.63 Initiation of the grain boundary migration and discontinuous reaction : γ-γ' eutectic rods activate the boundary movement; a needle of Zr_2CS is also seen (right side). Scanning electron micrograph.

Fig.3.64 More advanced stage of the discontinuous reaction; the γ-γ' eutectic rods are perpendicular to the micrograph. Scanning electron micrograph.

Fig.3.65 Discontinuous cell growth adjacent to a region of γ-γ' eutectic (top). The discontinuous growth front has not achieved yet a crystallographic orientation. Scanning electron micrograph.

Fig.3.66 Discontinuous cell growth halted by continuous precipitation, as indicated by the rod broadening near to the grain boundary; development of dendritic instabilities at the rod surface, which will tend to grow during the cooling. Scanning electron micrograph.

Fig.3.67 Discontinuous cell growth into a region where continuous γ' has not yet precipitated (top) while the other cell (bottom) had its growth halted by an earlier continuous γ' precipitation. Scanning electron micrograph.

Fig.3.68 This micrograph refers to Fig.3.58, also showing the effect of the continuous precipitation in interrupting the movement of a crystallographically orientated grain boundary. Scanning electron micrograph.

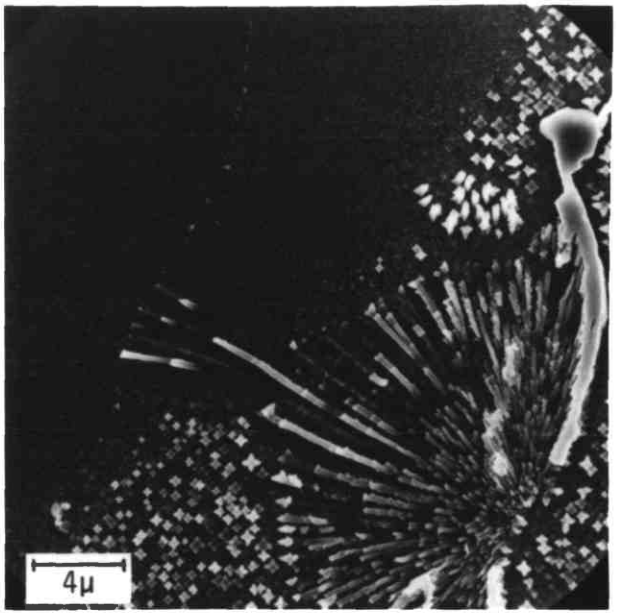

Fig. 3.63

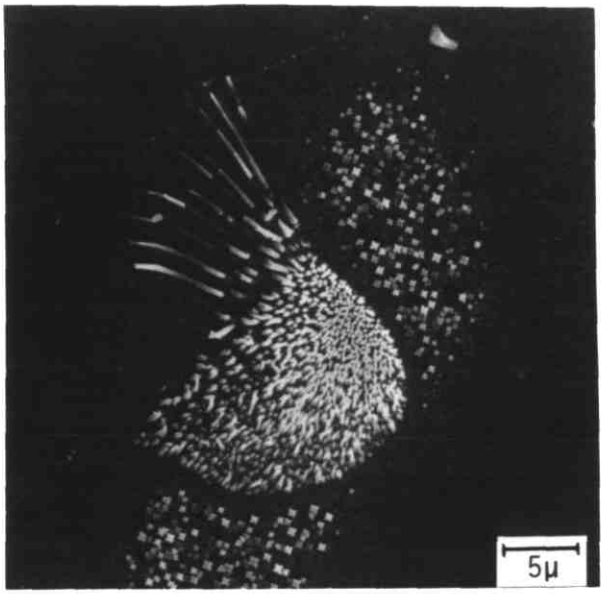

Fig. 3.64

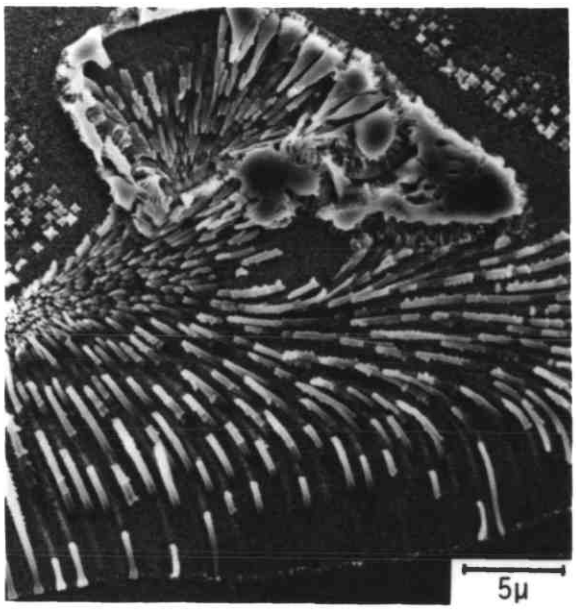

Fig. 3.65

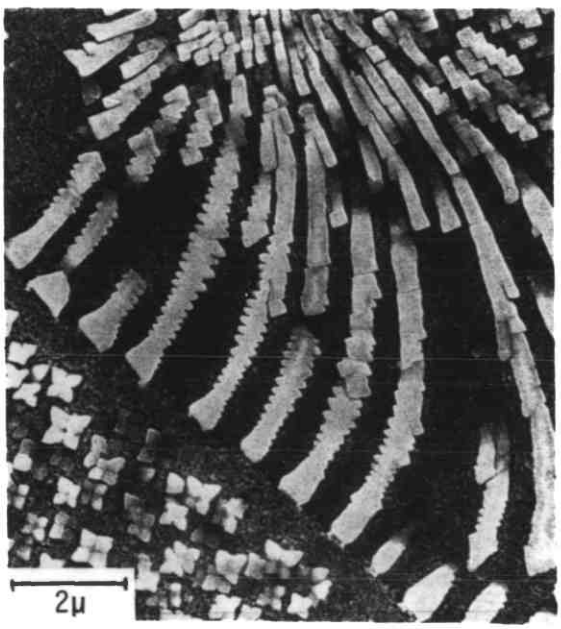

Fig. 3.66

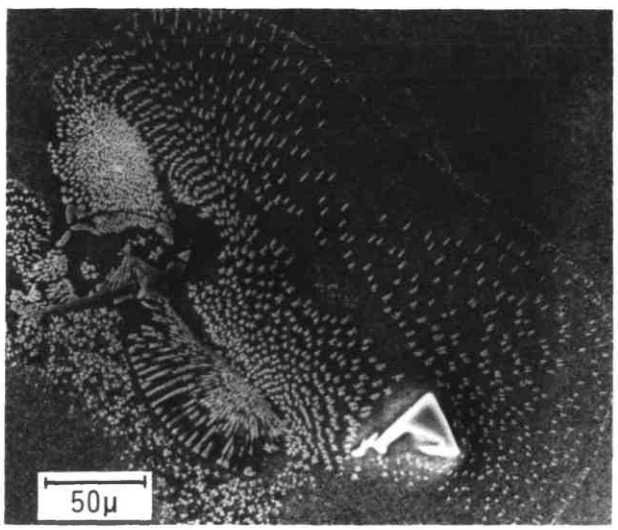

Fig. 3.67

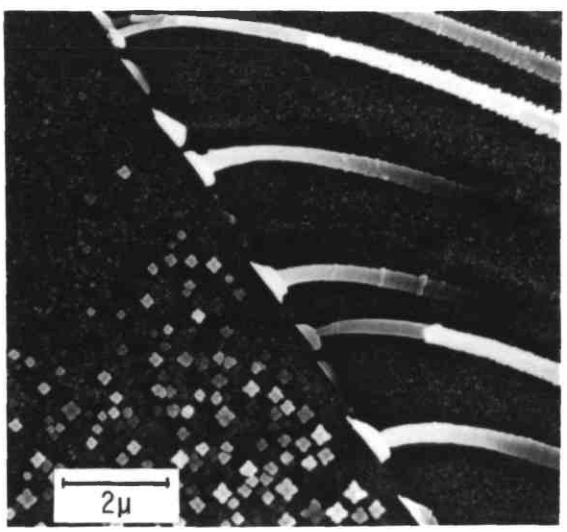

Fig. 3.68

As-solidified structure

$R = 60$ mm hr^{-1}

Figs.3.69-3.70 The micrographs reveal fully developed discontinuous cells originating from the γ-γ' eutectic (see micrographs 3.63-3.65). The regions of eutectic (E) and discontinuous (D) are indicated, as well as the approximate position for the grain boundary before the reaction started. Scanning electron micrographs.

Fig.3.69a Eutectic-discontinuous.
Fig.3.69b Eutectic.
Fig.3.69c Intermediate region separating the eutectic and discontinuous.

Fig.3.70a Eutectic-discontinuous.
Fig.3.70b Eutectic.
Fig.3.70c Eutectic-discontinuous detail.

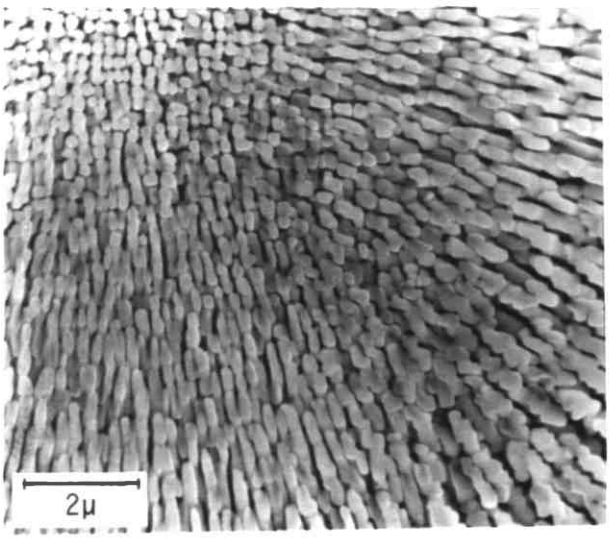

b

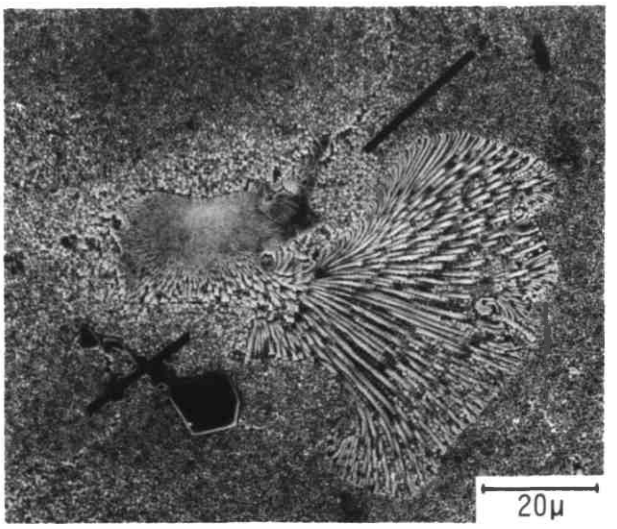

a

Fig. 3.69

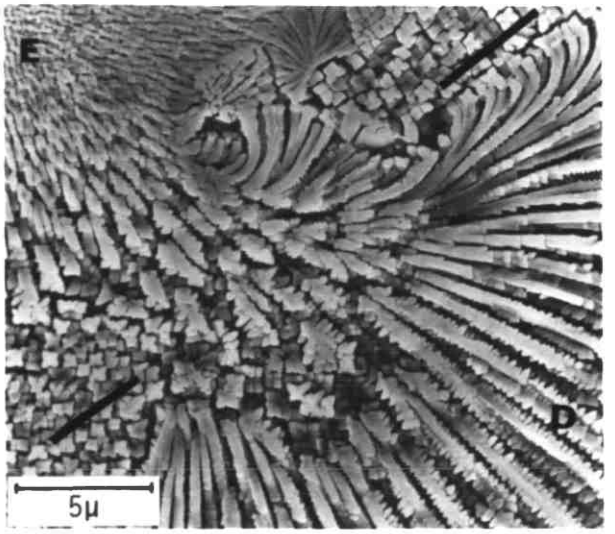

c

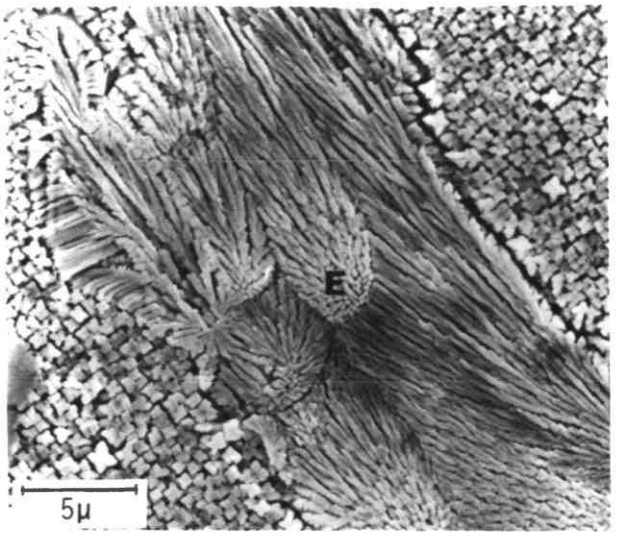

b

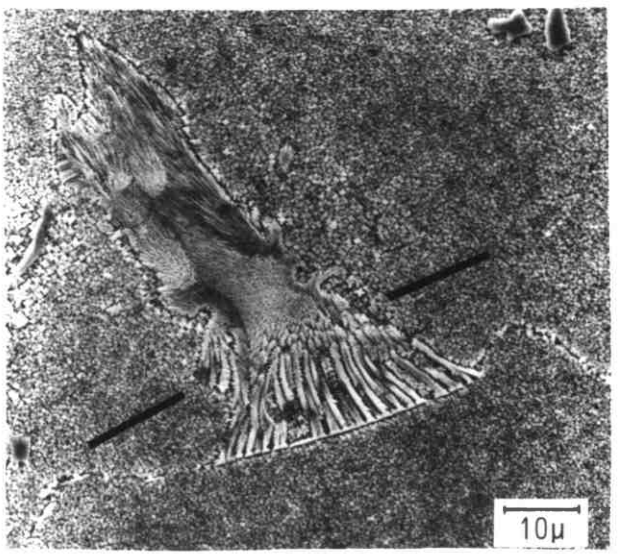

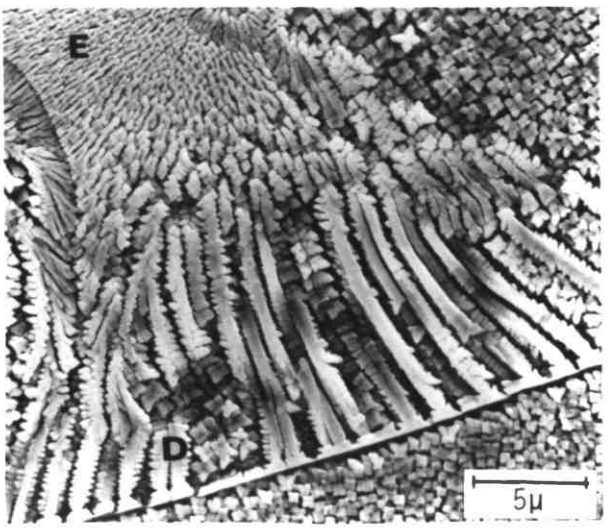

Fig. 3.70 a c

As-solidified structure

$R = 60 \text{ mm hr}^{-1}$

Figs.3.71-3.72 The micrographs show the eutectic-discontinuous feature (refer to Figs.3.69-3.70). The regions of eutectic (E), discontinuous (D) and the separation between them are indicated. Scanning electron micrographs.

Fig.3.71a Eutectic-discontinuous.
Fig.3.71b Eutectic.
Fig.3.71c Discontinuous.

Fig.3.72a Eutectic-discontinuous.
Fig.3.72b Eutectic-discontinuous.

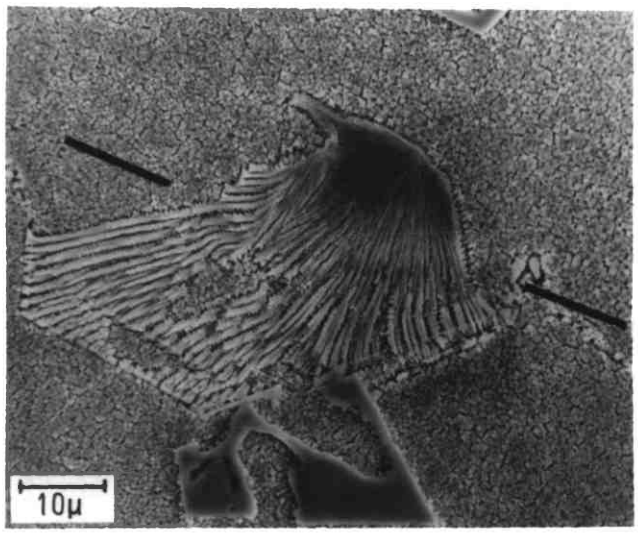

a

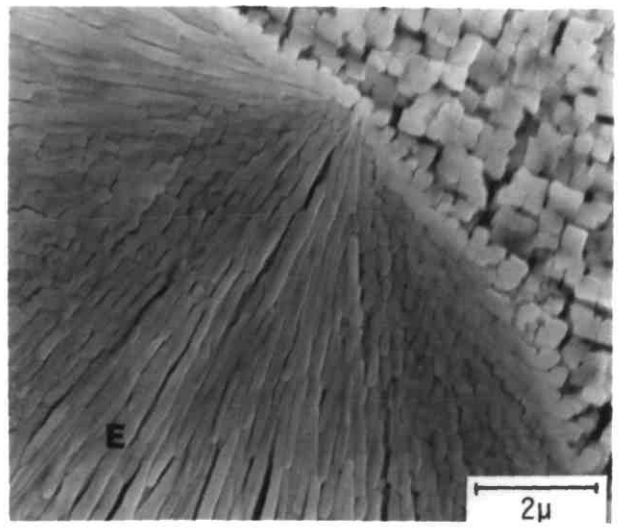

b

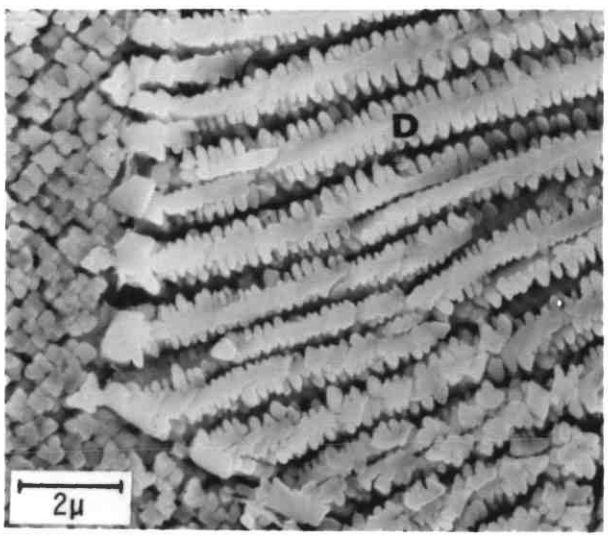

c

Fig. 3.71

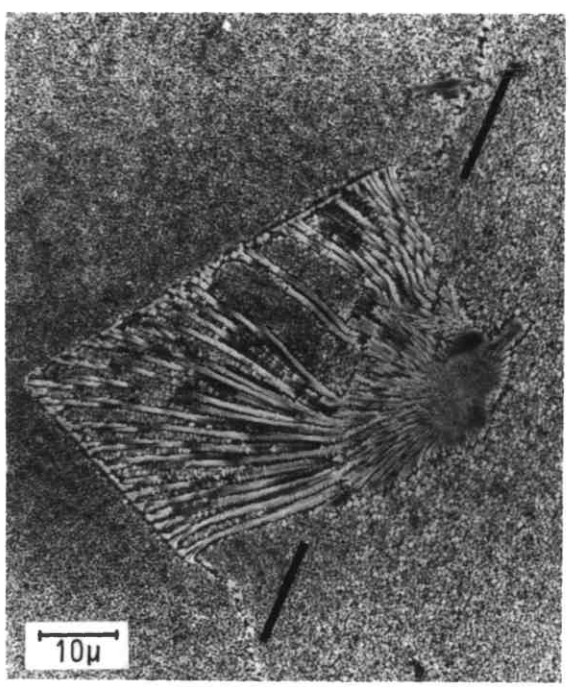

a

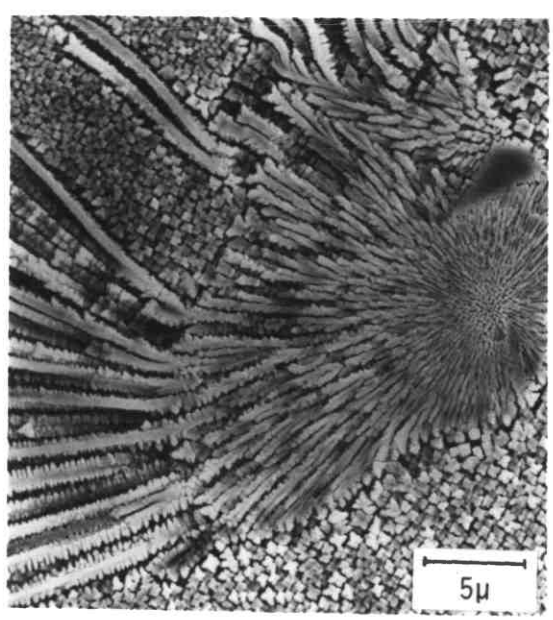

b

Fig. 3.72

As-solidified structure

$R = 60$ mm hr^{-1}

Figs.3.73-3.74 Both micrographs refer to the same eutectic (E) - discontinuous (D) feature, but to different sectioning, as several microns were removed by polishing. It shows a good example of the origin of the discontinuous cell according to the observations of Figs.3.63-3.65 and 3.69-3.72. (The layer observed at the grain boundary resulted from exposure at 950°C.)

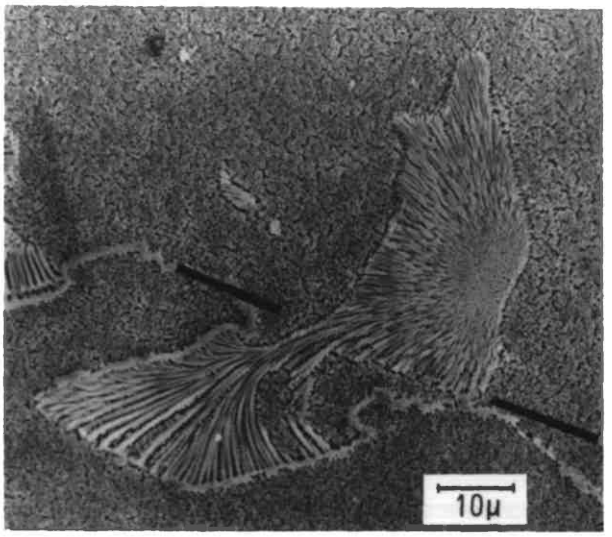

a

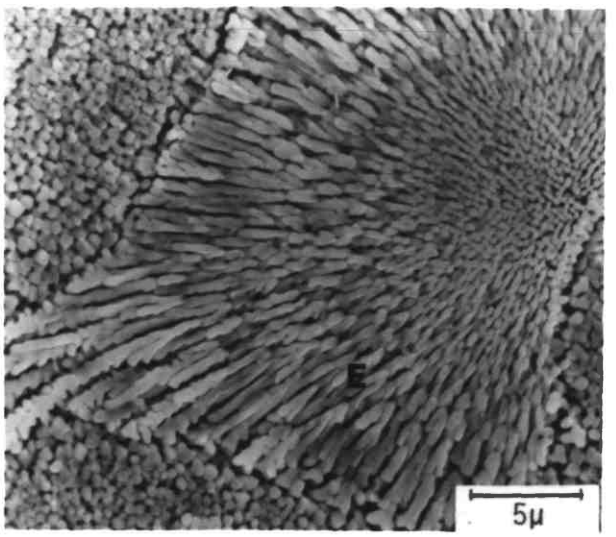

b

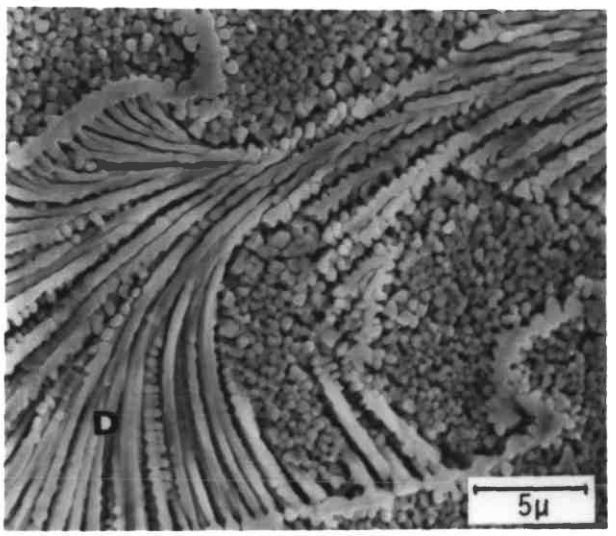

c

Fig. 3.73

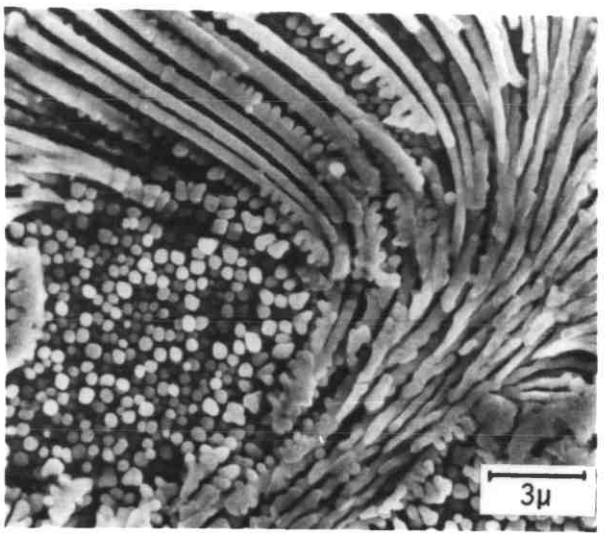

c

Fig. 3.74

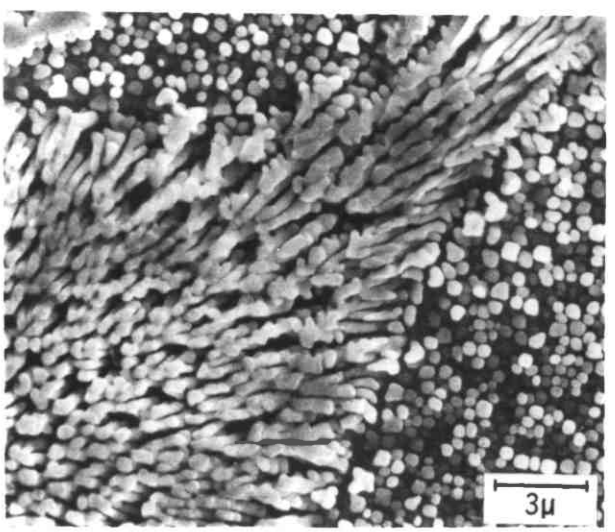

b

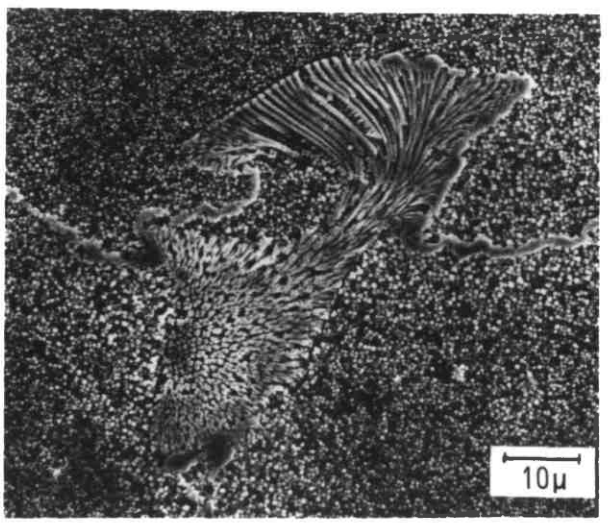

a

As-solidified structure

$R = 60$ mm hr^{-1}

Fig.3.75 The micrograph reveals a eutectic (E) - discontinuous (D) feature; the eutectic shows some rod broadening ('fingers'), but where the discontinuous reaction has developed the eutectic has probably consisted of fine γ' rods. Scanning electron micrograph.

Figs.3.76-3.77 The γ-γ' eutectic solidified in a finger-type morphology has not given origin to a discontinuous reaction at the grain boundary, as seen previously for Figs.3.63-3.65 and 3.69-3.75. Scanning electron micrographs.

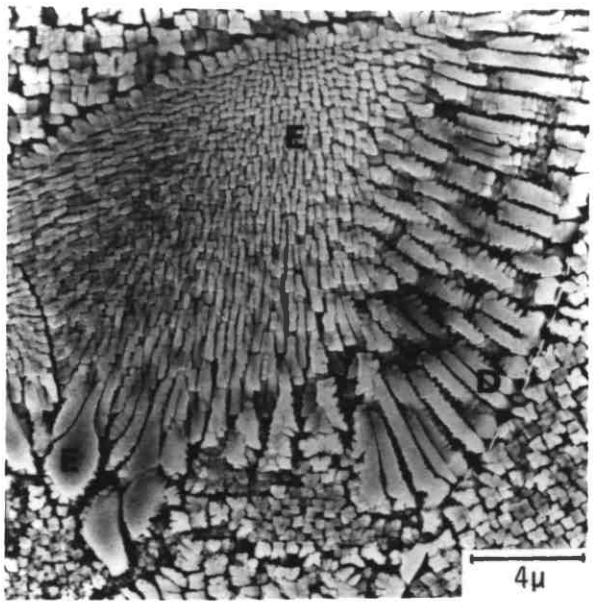

Fig. 3.75

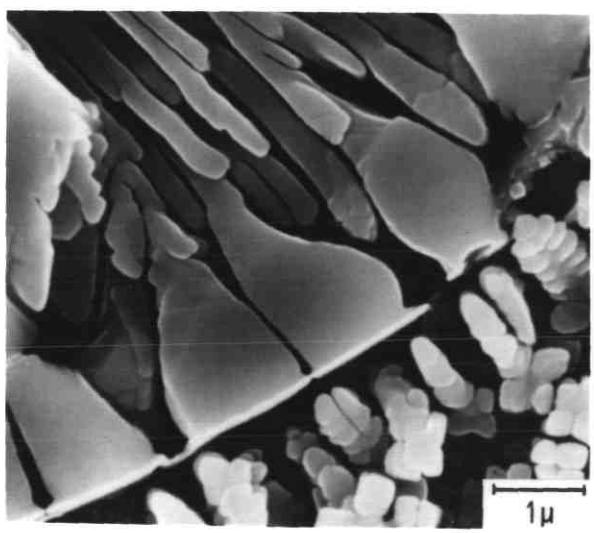

Fig. 3.76

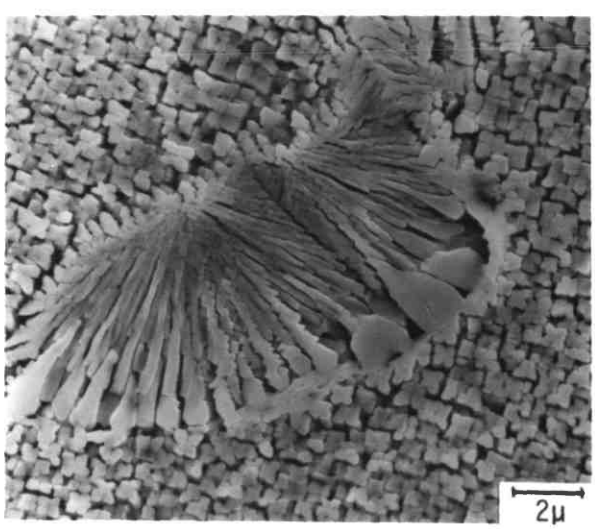

Fig. 3.77

Full heat treatment

$1120^{\circ}C$-2 hrs-AC + $845^{\circ}C$-16 hrs-AC

γ' particle distribution. Scanning electron micrograph

Fig.3.78 R = 60 mm hr^{-1}

a. Core region : low volume fraction of cubic particles and large amount of small spheroidal particles.
b. Interdendritic region : bimodal distribution presenting high volume fraction of cubic particles.

Fig.3.79 R = 300 mm hr^{-1}

a. Core region : no cubic particles present, thus indicating full solubility of the original particle distribution; a ring of coarse particles delineates the core region.
b. Interdendritic region : distribution similar to Fig.3.78b, but with smaller cubic particle sizes.

Fig.3.80 R = 600 mm hr^{-1}

a. Core region : increase in the amount of the 'near cubic' shaped particle as compared to the rates 60 mm hr^{-1} and 300 mm hr^{-1}.
b. Interdendritic region : distribution similar to the rate 300 mm hr^{-1} (Fig.3.79b).

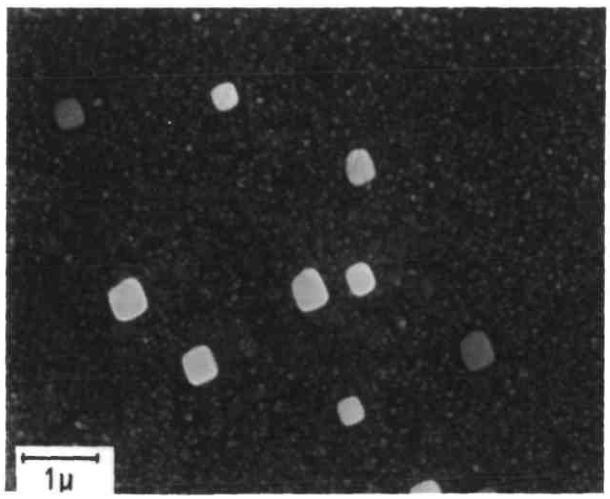

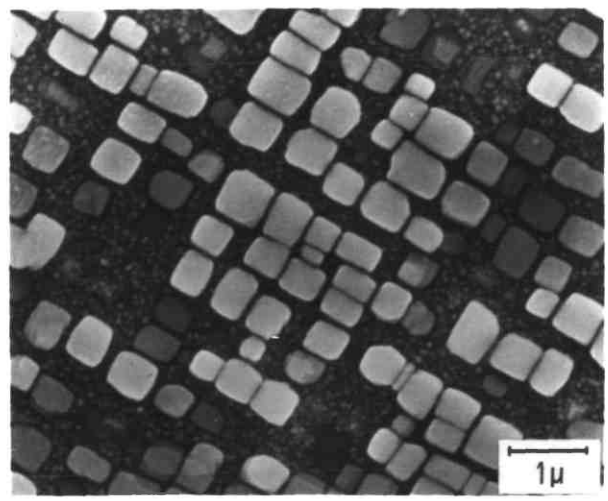

Fig. 3.78 a b

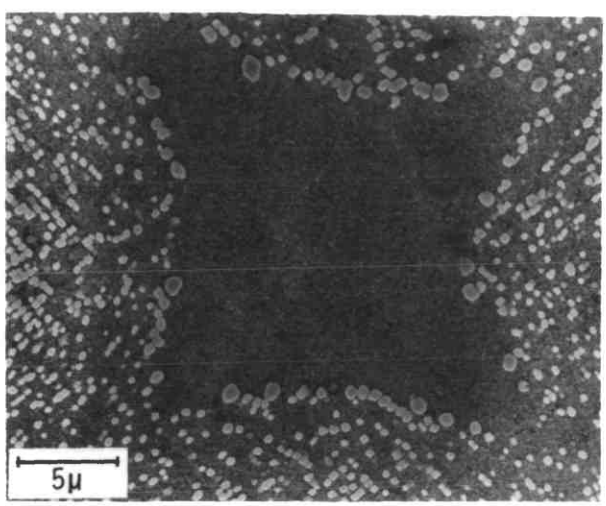

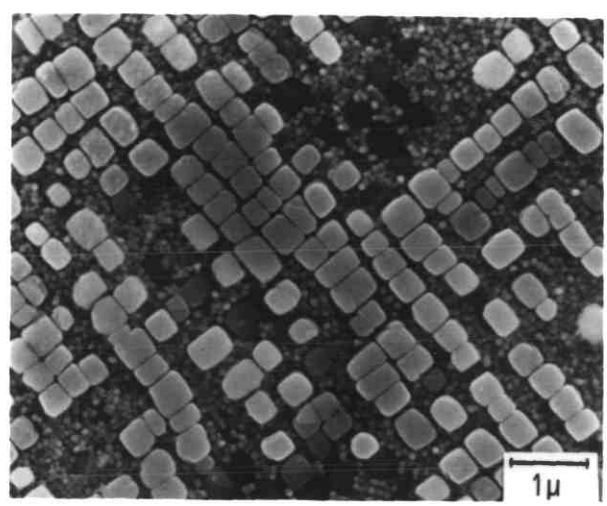

Fig. 3.79 a b

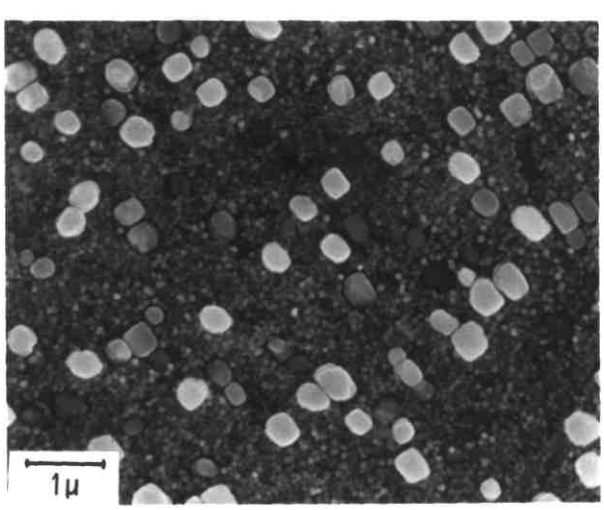

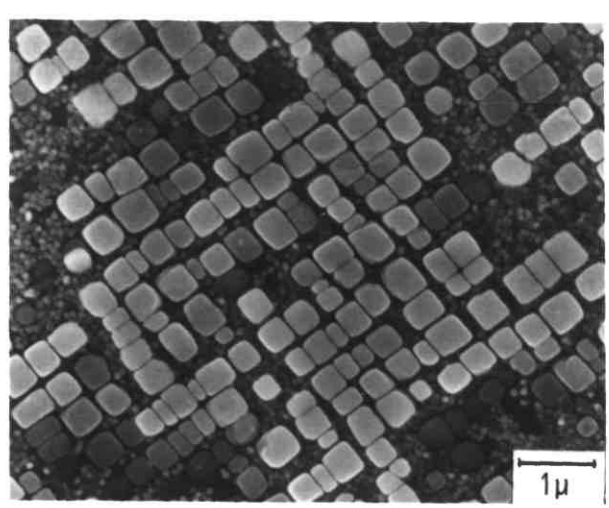

Fig. 3.80 a b

Heat treatments

Fig.3.81 R = 300 mm hr^{-1} : heat treatment - 1120°C-2 hr-AC. It shows the resulting γ' spherical particle distribution in the core region. Extraction replica.

Fig.3.82 R = 600 mm hr^{-1} : heat treatment - 1120°C-2 hr-AC. γ' spheroidal particles in the core region. Extraction replica.

Fig.3.83 R = 300 mm hr^{-1} : full heat treatment (1120°C-2 hrs-AC + 845°C-16 hrs-AC). Extraction replicas.

a. Spherical particles in the core region; some of the particles have coalesced during the treatment.
b. Bimodal distribution in the interdendritic region; the larger cubic particles were not extracted.

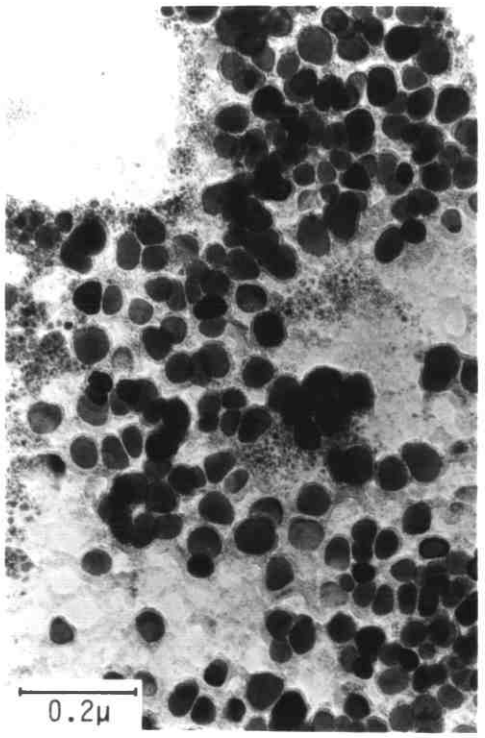

Fig. 3.81

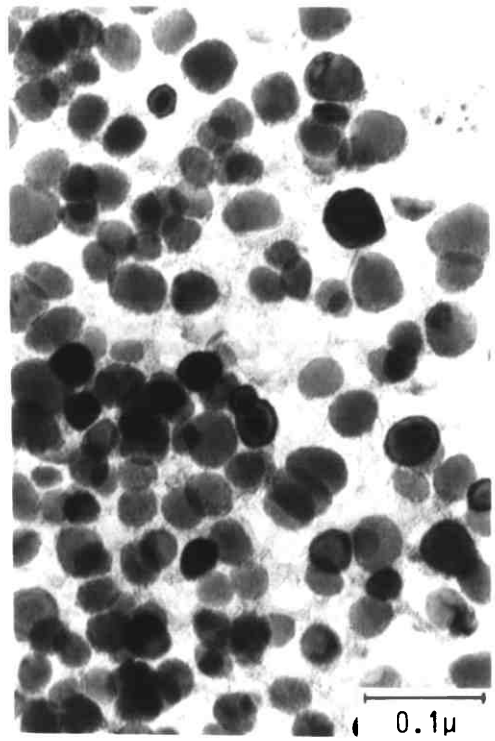

Fig. 3.82

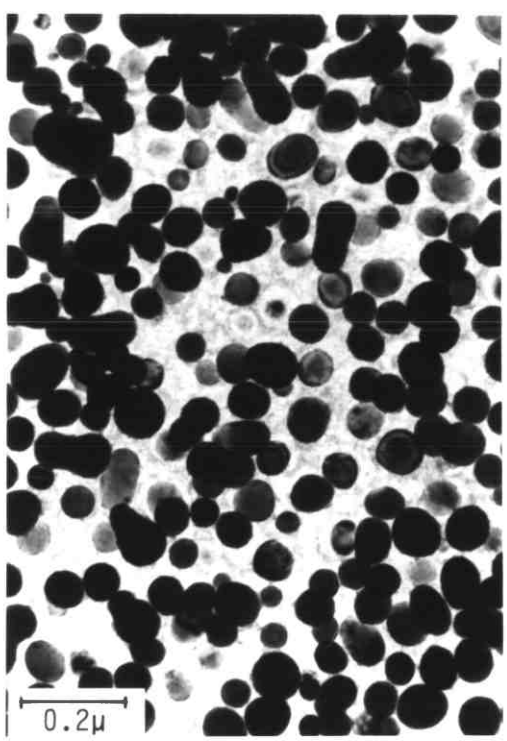

Fig. 3.83 a

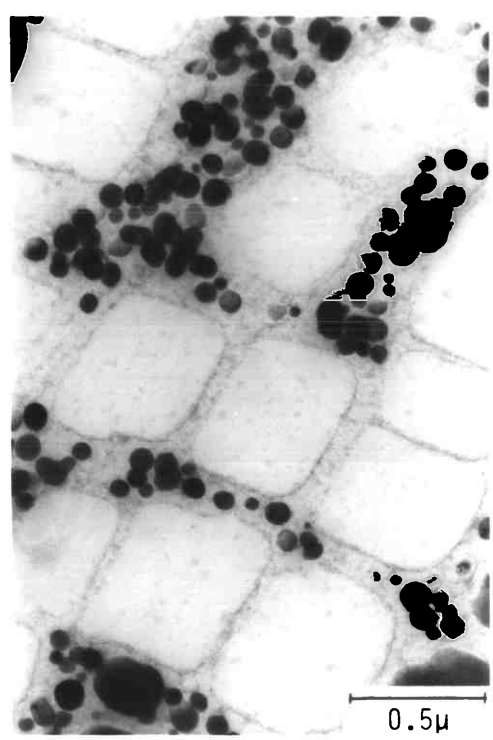

b

Full heat treatment

1120°C-2 hrs-AC + 845°C-16 hrs-AC

Fig.3.84 R = 60 mm hr^{-1} : effect on the discontinuous phase : formation of serrations in replacement of the dendritic perturbations. Scanning electron micrographs.

Fig.3.85 R = 60 mm hr^{-1} : Effect on the discontinuous phase : occurrence of a discontinuous coarsening reaction during the first stage of the heat treatment; a layer of $M_{23}C_6$ has formed during the second stage. Scanning electron micrographs.

Fig.3.86 R = 60 mm hr^{-1} : well developed discontinuous coarsening reaction; observe the variation in the inter-rod spacing as the reaction proceeds. Scanning electron micrograph.

Fig.3.87 R = 60 mm hr^{-1} : effect on the γ-γ' eutectic : partial breaking up of the original rod structure, coarsening and faceting (compare with Fig.3.9). Scanning electron micrograph.

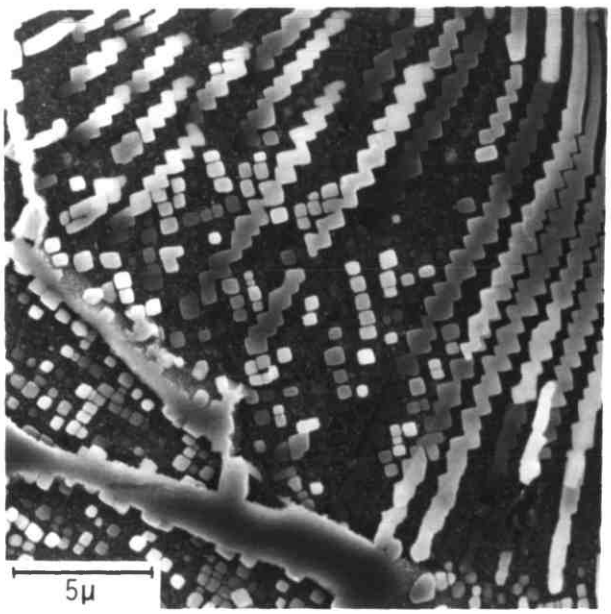

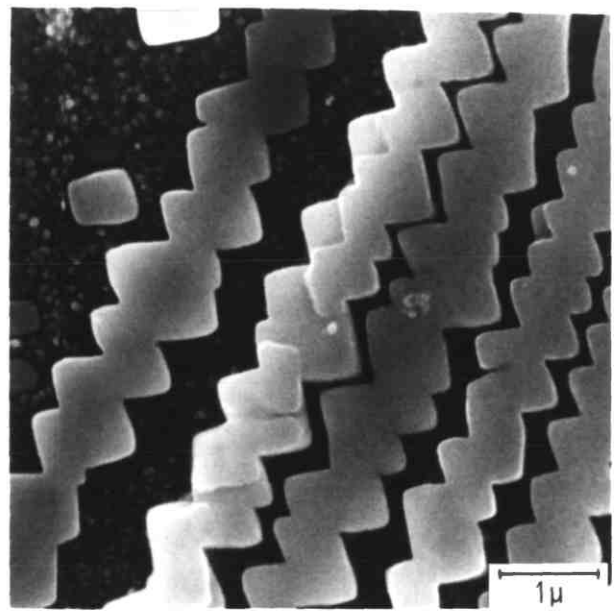

Fig. 3.84 a b

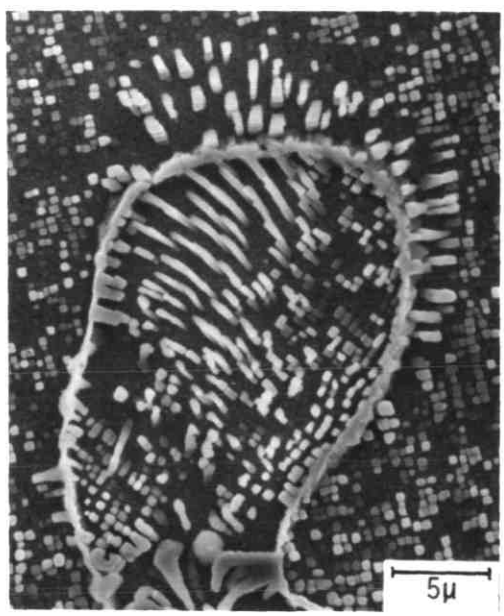

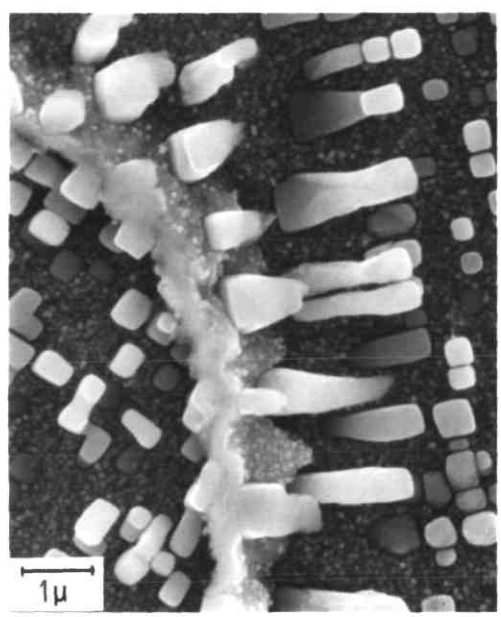

Fig. 3.85 a b

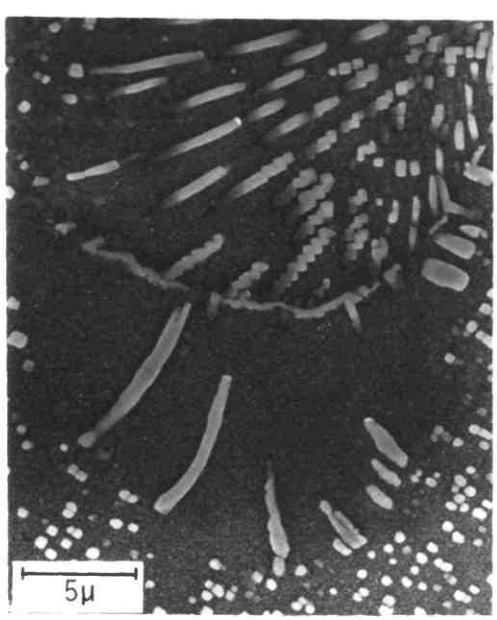

Fig. 3.86

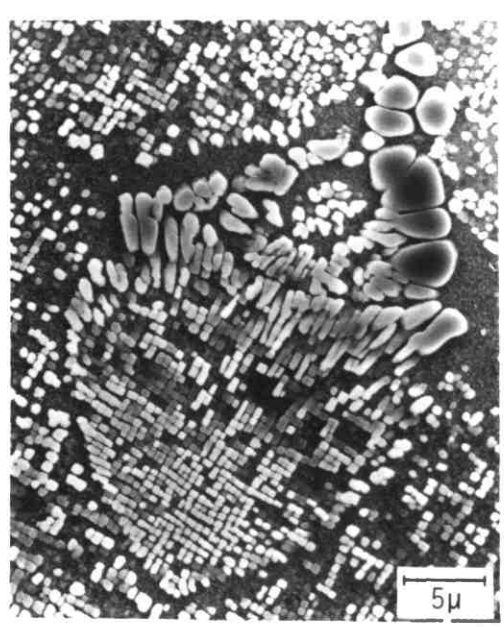

Fig. 3.87

Heat treatments

Figs.3.88-3.89 Full heat treatment

1120°C-2 hrs-AC + 845°C-16 hrs-AC

Fig.3.88 R = 60 mm hr^{-1} : $M_{23}C_6$ layer formed after the second part of the treatment (845°C-16 hrs). Scanning electron micrograph.

Fig.3.89 R = 60 mm hr^{-1} : coarsening of the γ' particles resulting from the first stage (1120°C-2 hrs-AC) treatment; $M_{23}C_6$ grain boundary layer. Scanning electron micrograph.

Figs.3.90-3.91 R = 300 mm hr^{-1}, heat treatment : 1120°C-2 hrs-AC : coarsening of the grain boundary γ' precipitates resulting both from particle coalescence and grain boundary solute diffusion.

Fig.3.90 Scanning electron micrograph.

Fig.3.91 Extraction replica

Fig.3.92 R = 60 mm hr^{-1} : full heat treatment. Etched with gliceregia in order to dissolve γ' particles and reveal the $M_{23}C_6$ grain boundary layer. Scanning electron micrograph.

Fig.3.93 R = 600 mm hr^{-1} : full heat treatment. Extracted residue from the $M_{23}C_6$ grain boundary layer. Scanning electron micrograph.

Fig.3.94 R = 600 mm hr^{-1} : full heat treatment. Extracted MC carbides with a seam of $M_{23}C_6$. Scanning electron micrograph.

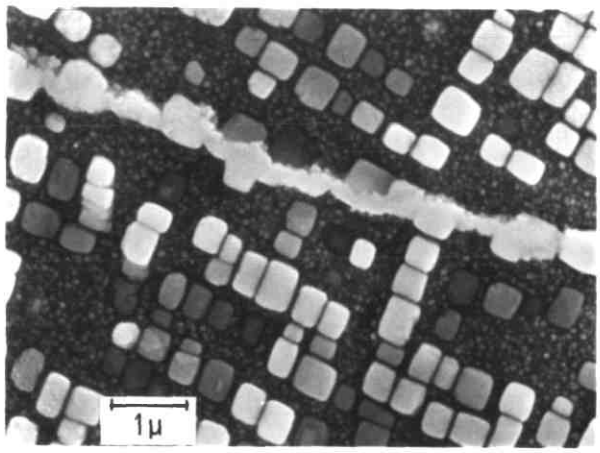

Fig. 3.88

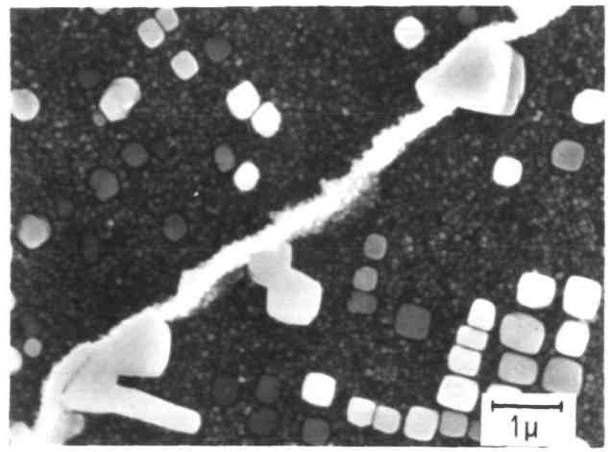

Fig. 3.89

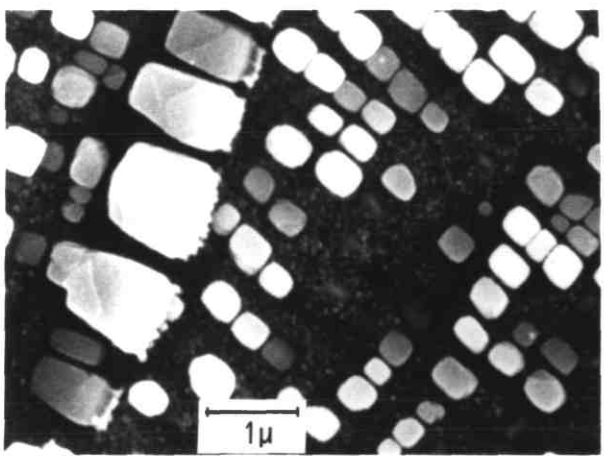

Fig. 3.90

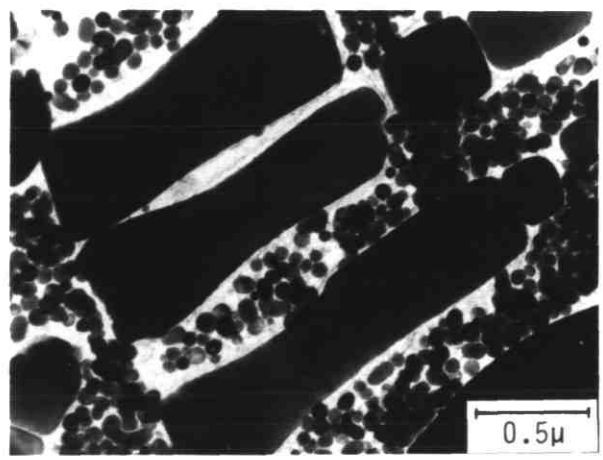

Fig. 3.91

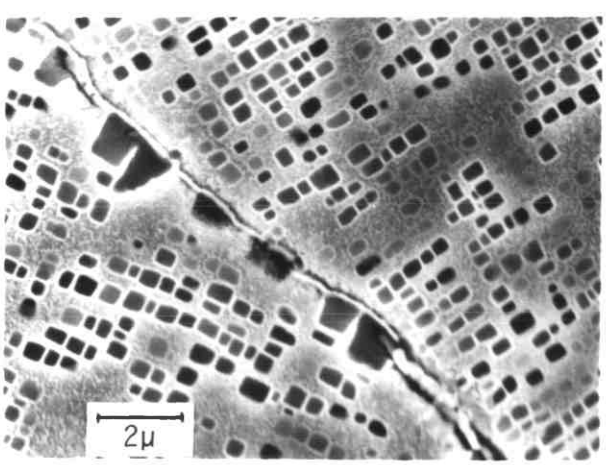

Fig. 3.92

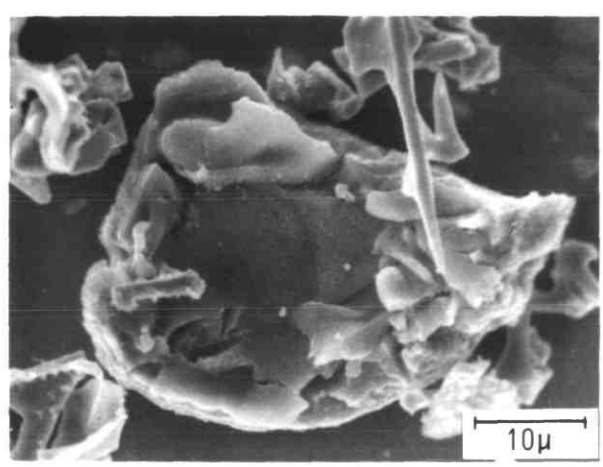

Fig. 3.93

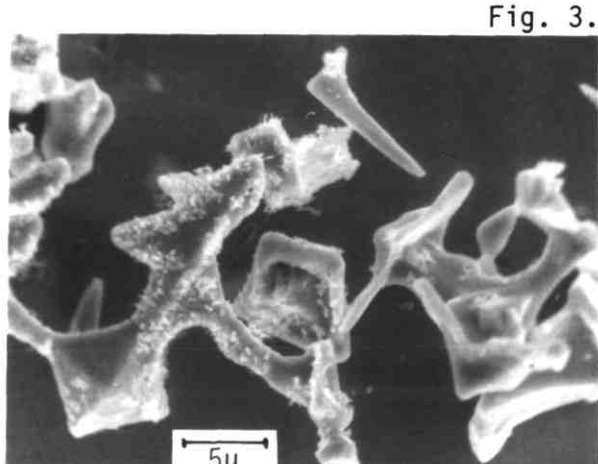

Fig. 3.94

Heat treatments

Figs.3.95-3.98 R = 60 mm hr^{-1} Heat treatment

$1000^{o}C$-24 hrs-AC

Fig.3.95 Smoothening of the dendritic discontinuous rods. Scanning electron micrograph.

Fig.3.96 Partial breaking up of the discontinuous rods by spheroidization. Scanning electron micrograph.

Fig.3.97 Smoothening of the discontinuous rods as the dendritic perturbations are detached by spheroidization. Scanning electron micrograph.

Fig.3.98 Formation of a grain boundary layer possibly of γ'. Scanning electron micrograph.

Fig.3.99 R = 60 mm hr^{-1}, heat treatment : $1160^{o}C$-2 hrs-WQ : Fast spheroidization of the discontinuous γ' rods.

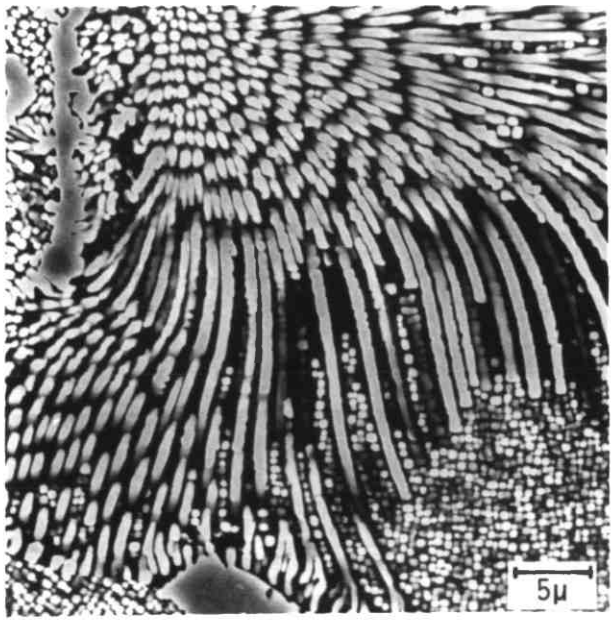

Fig. 3.95

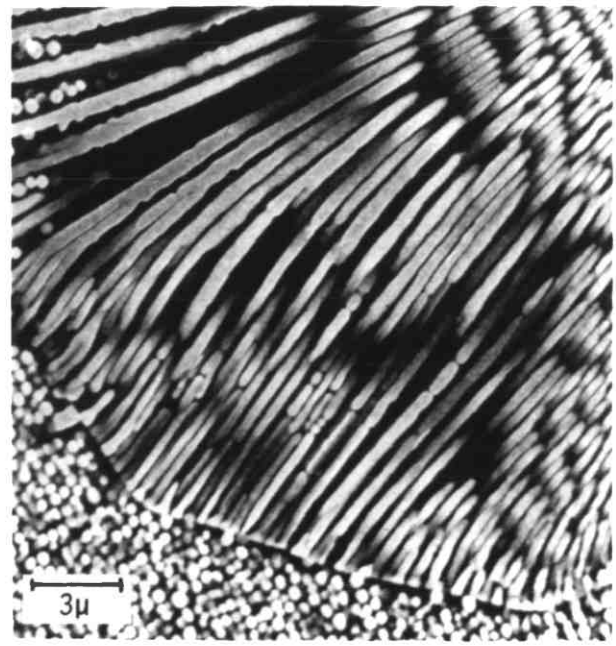

Fig. 3.96

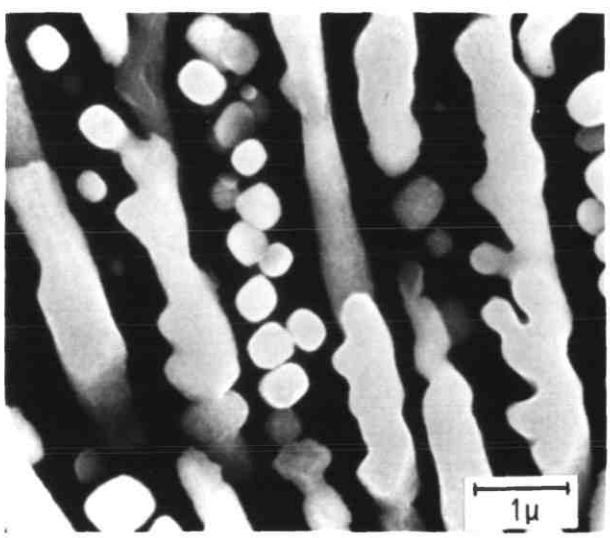

Fig. 3.97

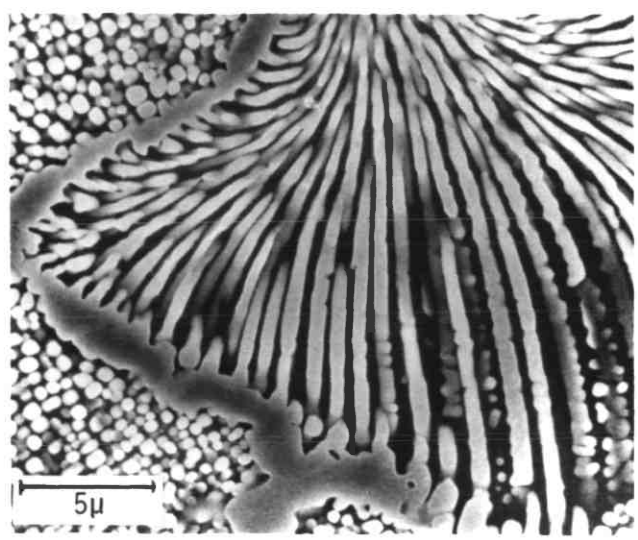

Fig. 3.98

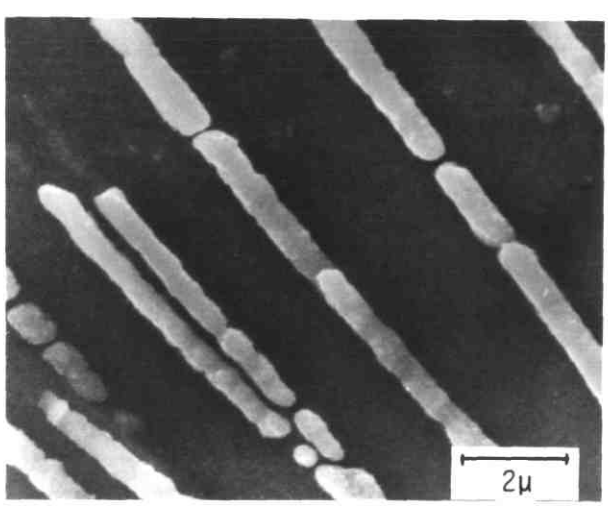

Fig. 3.99

Heat treatments

Fig.3.100 R = 60 mm hr^{-1}, heat treatment : 1050°C-24 hrs-WQ. Discontinuous coarsening reaction; the secondary rods are coarser and the inter-rod spacing is variable. Scanning electron micrograph.

Fig.3.101 R = 60 mm hr^{-1}, heat treatment : 1050°C-48 hrs-WQ. It shows an increase in the area occupied by the coarsening reaction. Scanning electron micrographs.

Fig.3.102 R = 60 mm hr^{-1}, heat treatment : 1050°C-100 hrs-WQ. The coarsening reaction substitutes for most of the original discontinuous cells, with occurrence also of rod spheroidization. Scanning electron micrograph.

Fig.3.103 R = 60 mm hr^{-1}, heat treatment : 1050°C-24 hrs-WQ. Coarsening of the grain boundary γ' precipitates. Scanning electron micrograph.

Fig.3.104 R = 60 mm hr^{-1}, heat treatment : 1180°C-0.5 hr-furnace cooled at 13°C min^{-1} down to 1140°C-1 hr-WQ. The heat treatment attempted unsuccessfully to originate discontinuous cells; the grain boundary only showed a chain of γ' particles. Optical micrograph.

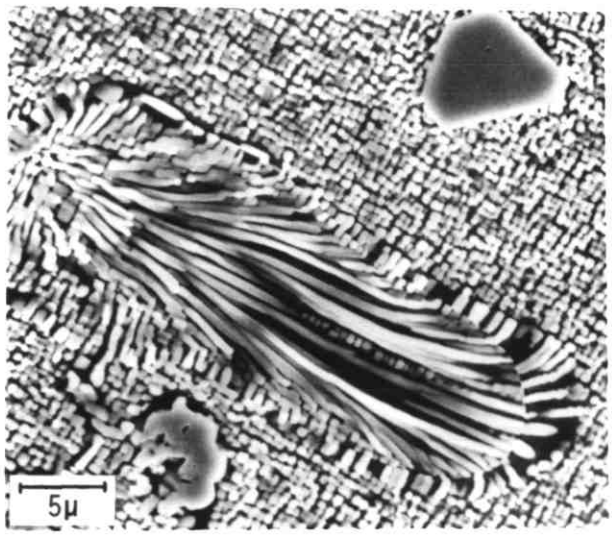

Fig. 3.100 a

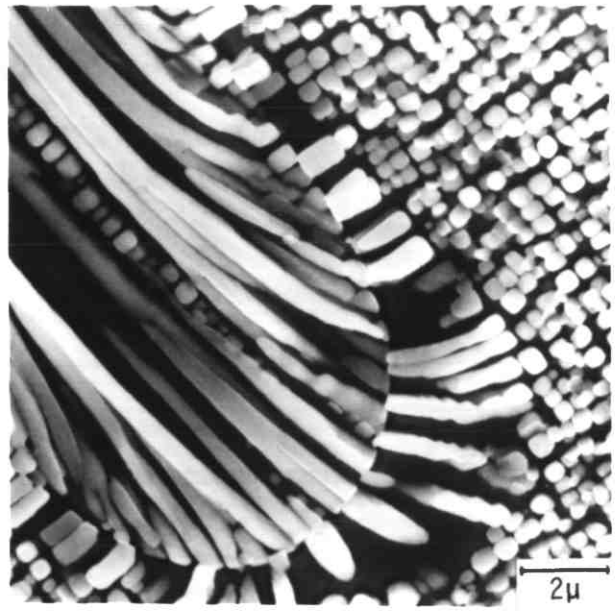

b

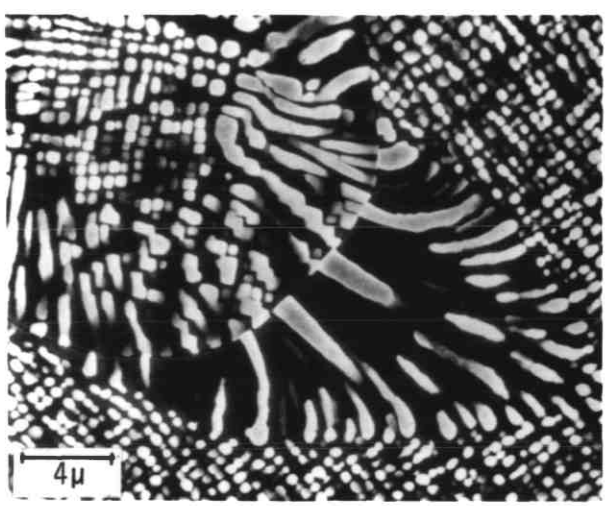

Fig. 3.101

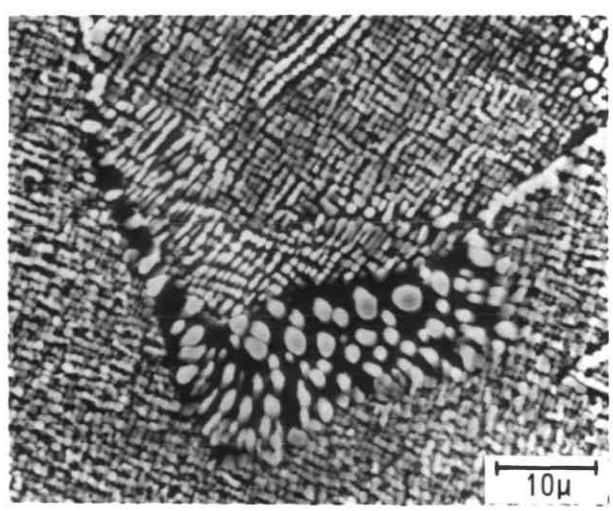

Fig. 3.102

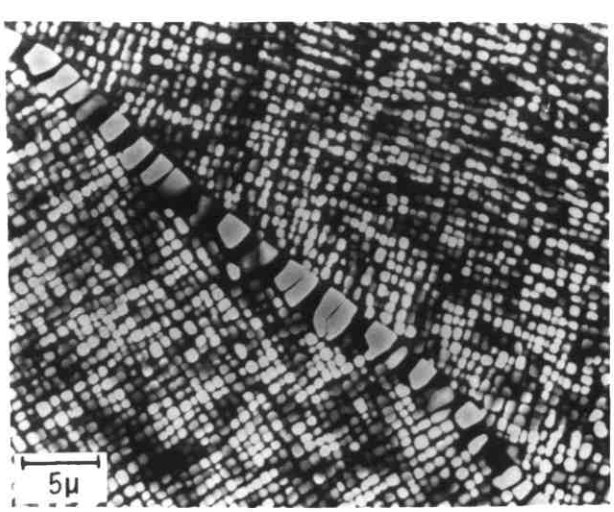

Fig. 3.103

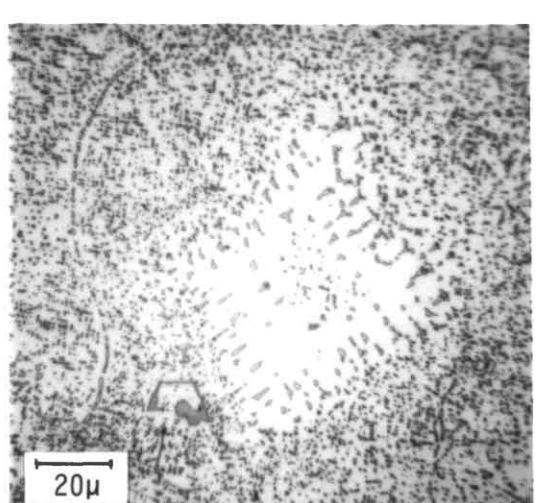

Fig. 3.104

Heat treatments

Fig.3.105 R = 300 mm hr^{-1}, full heat treatment : 1120°C-2 hrs-AC + 845°C-16 hrs-AC : bimodal γ' distribution. Negative replica.

Fig.3.106 R = 300 mm hr^{-1}, heat treatment : 850°C-550 hrs. Decrease in the volume fraction of the spheroidal particles. Extraction replica.

Fig.3.107 R = 300 mm hr^{-1}, heat treatment : 850°C-2000 hrs.

a. Interdendritic region : coalescence of the cuboidal particles, which became partially rounded. Scanning electron micrograph.
b. Core region : spherical γ' particles. Scanning electron micrograph.

Fig.3.108 R = 300 mm hr^{-1}, heat treatment : 1050°C-360 hrs. Slight changes in the cubic particles morphology. Scanning electron micrograph.

Fig.3.109 R = 300 mm hr^{-1}, heat treatment : 1100°C-360 hrs. Occurrence of particle coalescence and changes into more rounded shape (original cubic morphology). Scanning electron micrograph.

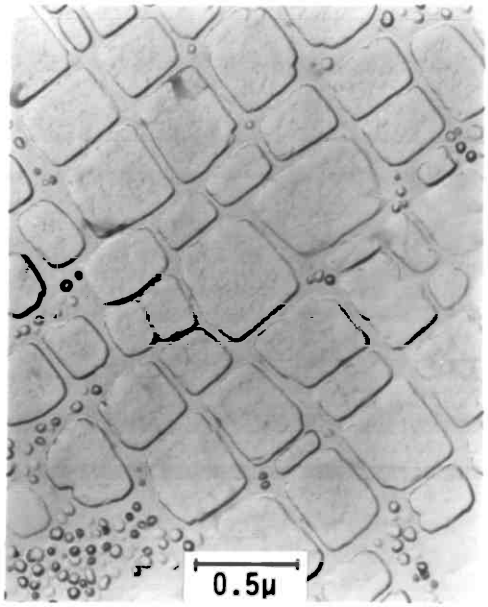

Fig. 3.105

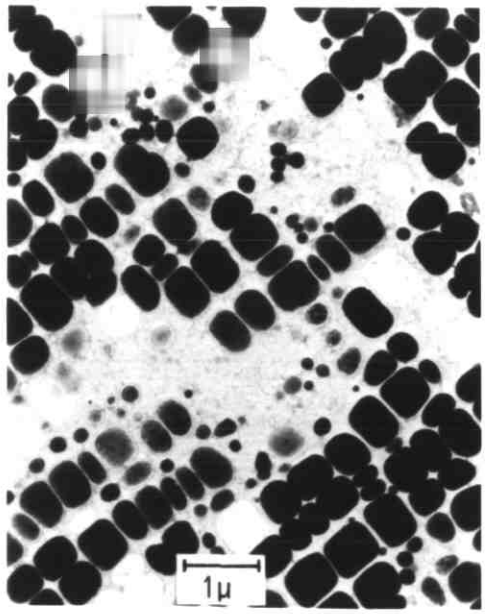

Fig. 3.106

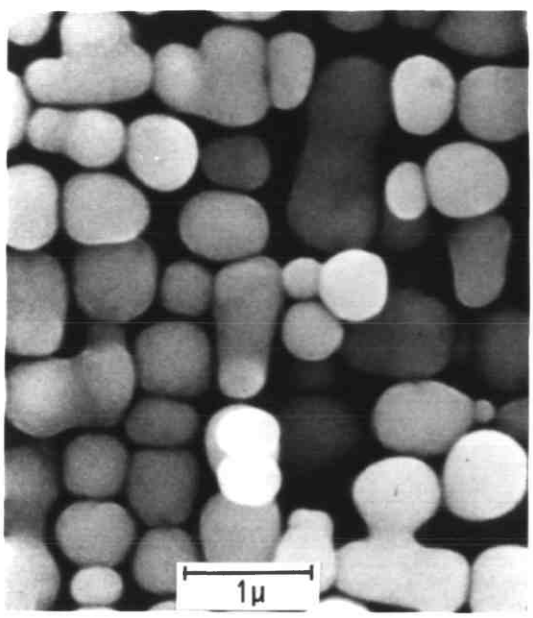

Fig. 3.107 a

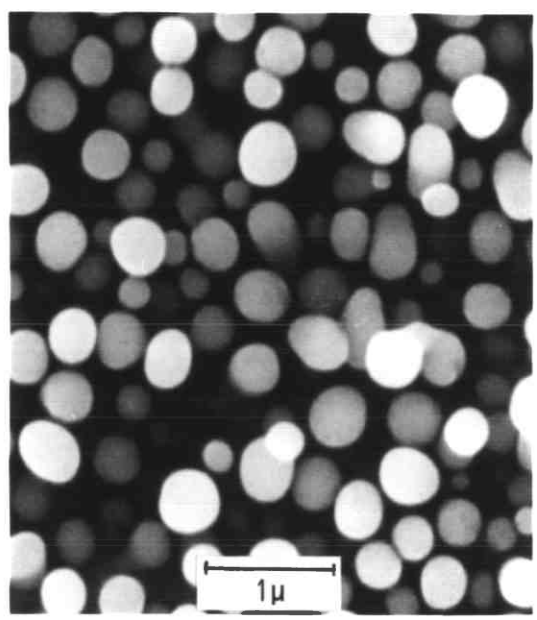

b

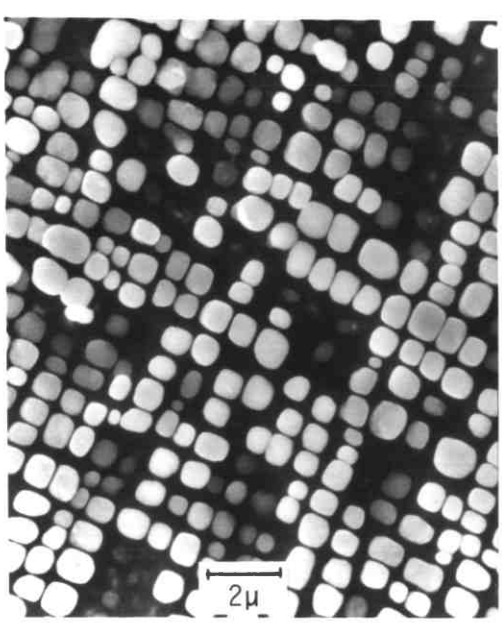

Fig. 3.108

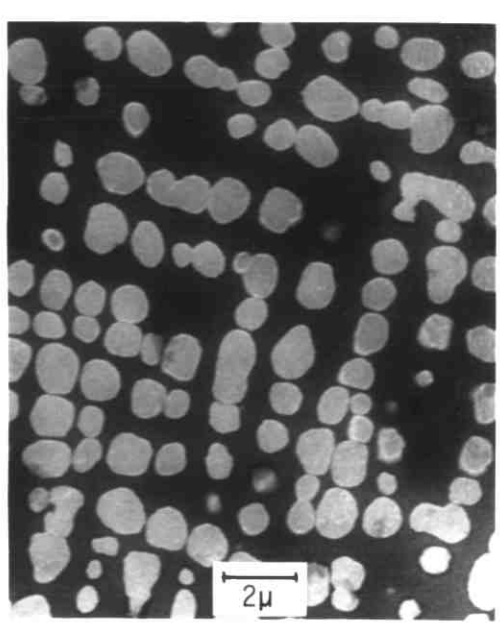

Fig. 3.109

Heat treatments

Fig.3.110 R = 300 mm hr^{-1}. Effect of temperature exposure at 950°C on γ' morphology in the inter-dendritic region. Scanning electron micrographs.
a. 51 hrs : particle dispersion comprising cubic particles with no spherical particles left.
b. 360 hrs : development of coalesced particles.

Fig.3.111 R = 300 mm hr^{-1}. Effect of different exposures at 950°C on the γ' particles situated in the core region. Scanning electron micrographs.
a. 51 hrs : γ' particles showing a near-spherical morphology.
b. 169 hrs : γ' particle morphology changing into cubic.
c. 360 hrs : development of an aligned structure.
d. 600 hrs : further coarsening.

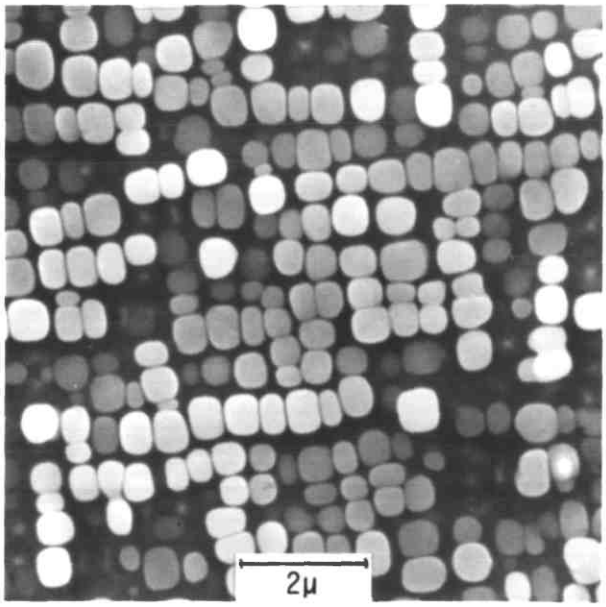

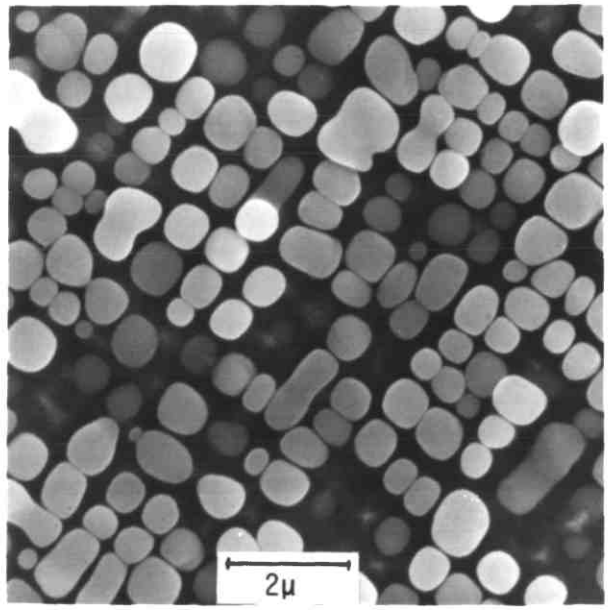

Fig. 3.110 a b

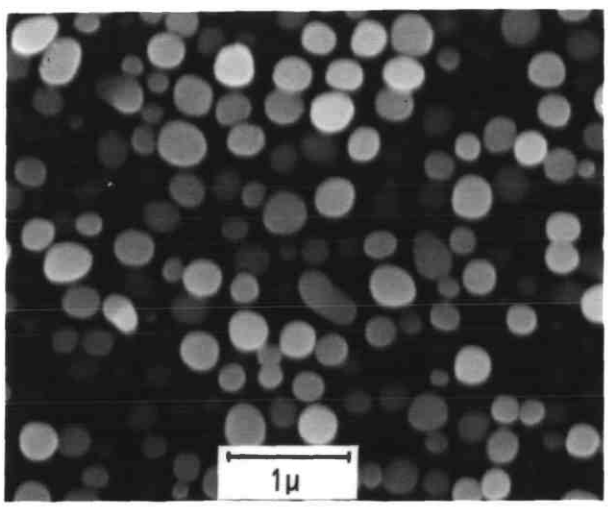

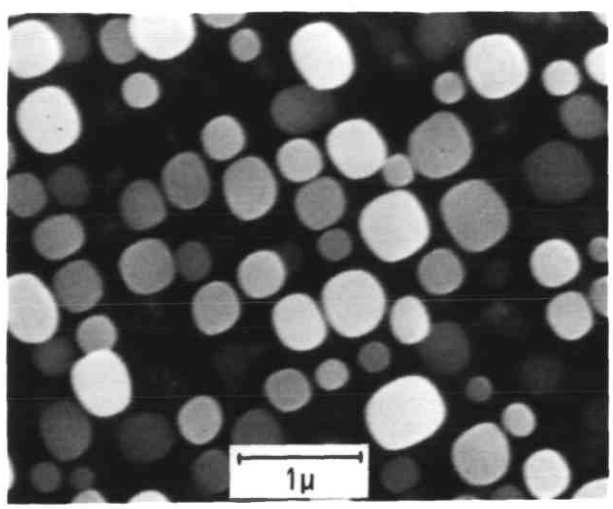

Fig. 3.111 a b

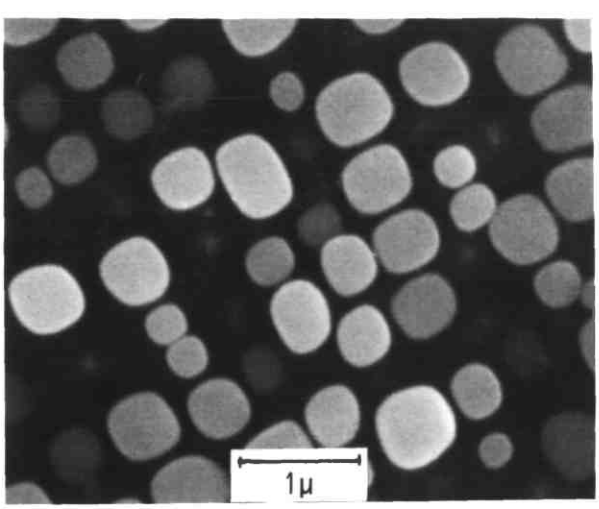

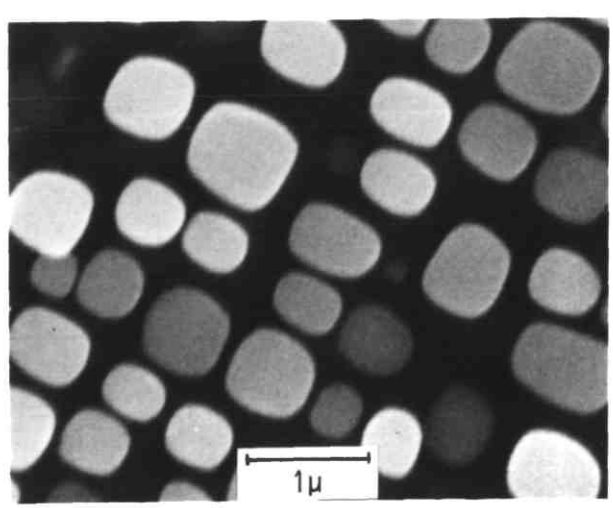

c d

Creep structure

Fig.3.112 R = 300 mm hr^{-1}, full heat treatment, longitudinal section. Scanning electron micrograph.

Figs.3.113-3.114 R = 300 mm hr^{-1}, full heat treatment plus creep test : 250 N mm^{-2} at 850°C (2000 hrs up to rupture), 29% elongation. Scanning electron micrographs.

Fig.3.113 It shows the alignment of the smaller particles from the core region perpendicular to the stress axis.

Fig.3.114 The γ' particles from the interdendritic region became strongly aligned perpendicularly to the stress axis; facets are present on the particle surface thus suggesting a shearing mechanism.

Fig.3.115 Similar to Fig.3.114. Negative replica.

Fig.3.116 R = 300 mm hr^{-1}, as-solidified plus creep test : 250 N mm^{-2} at 850°C (1000°C up to rupture), 18% elongation. The γ' particles showed a smaller degree of coalescence as compared with the previous micrographs. Interdendritic region. Negative replica.

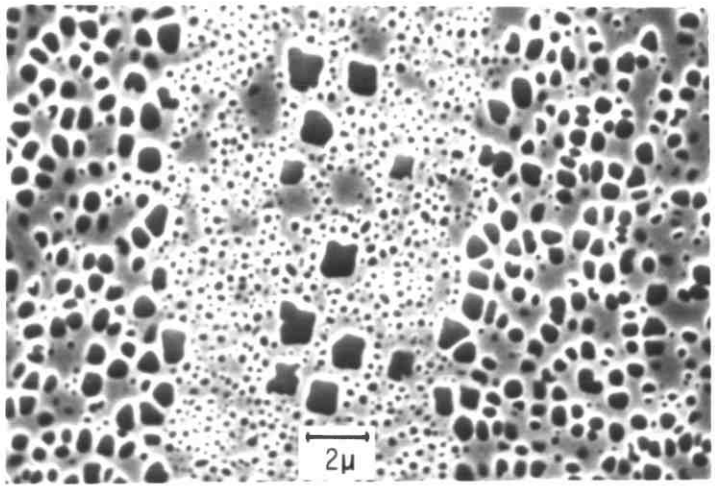

Fig. 3.112

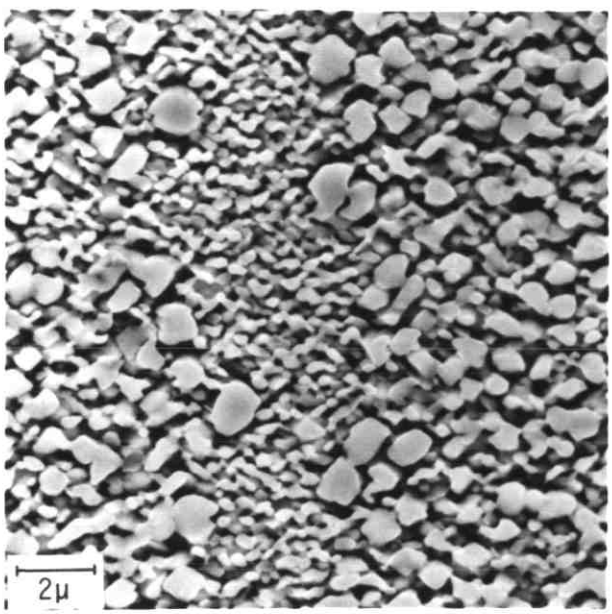

Fig. 3.113

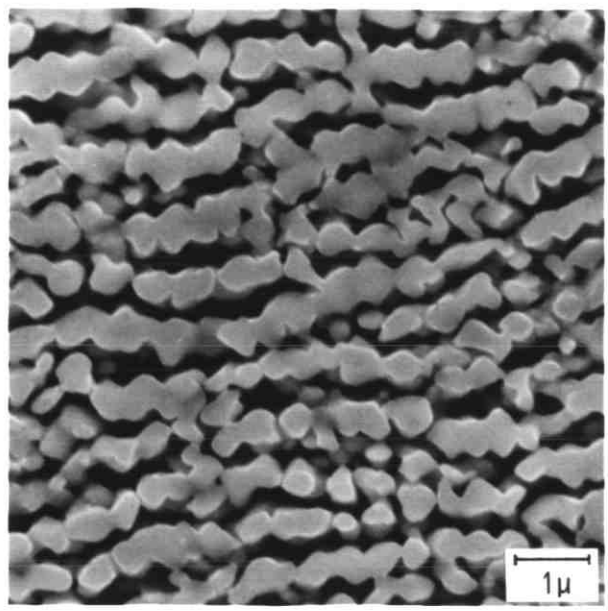

Fig. 3.114

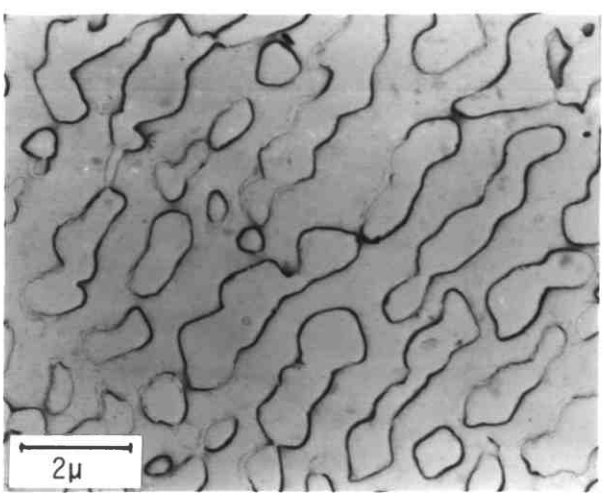

Fig. 3.115

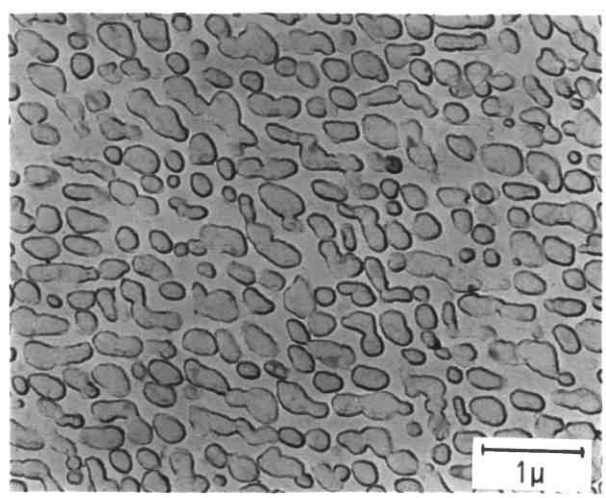

Fig. 3.116

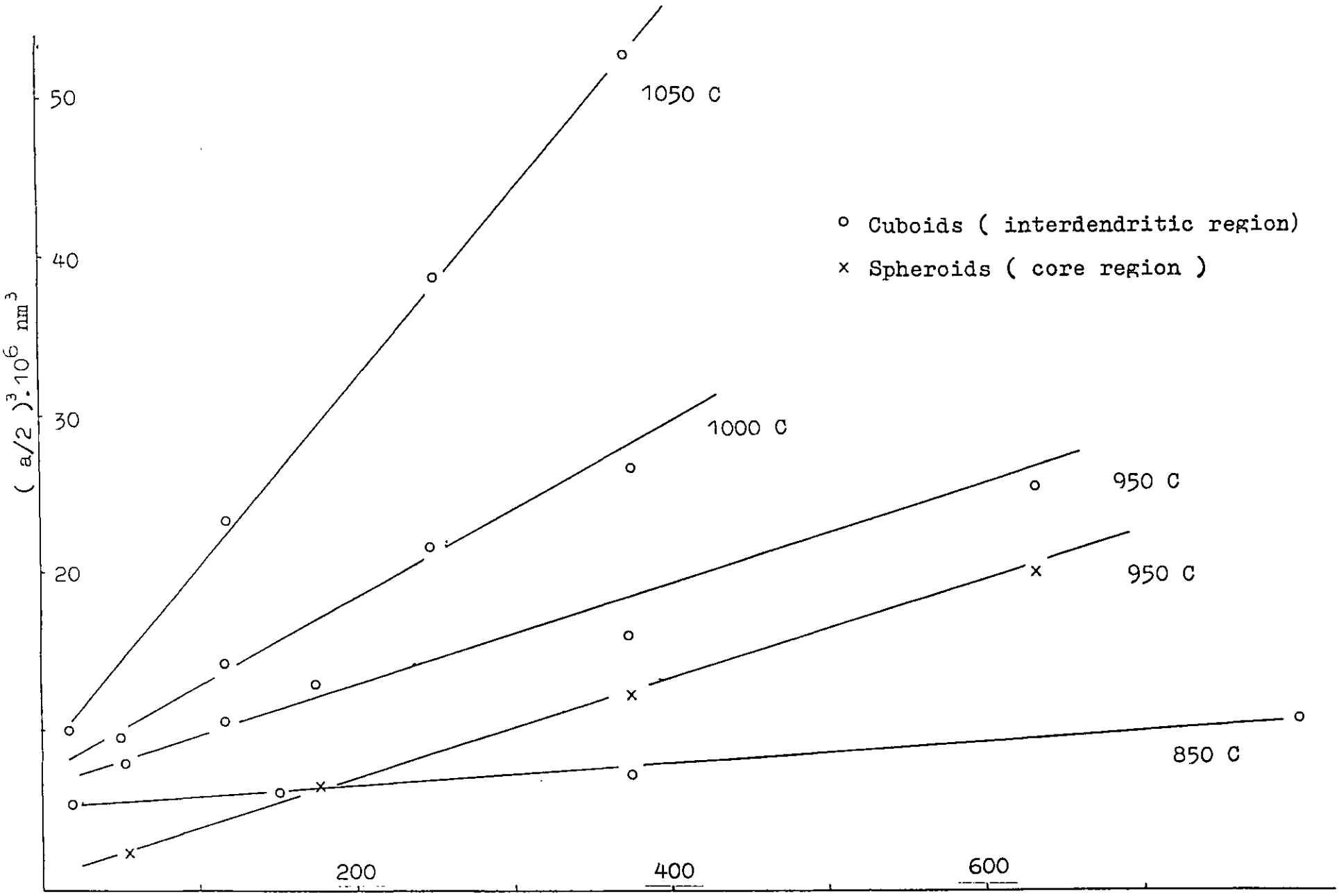

Fig 3.117 - γ' Coarsening

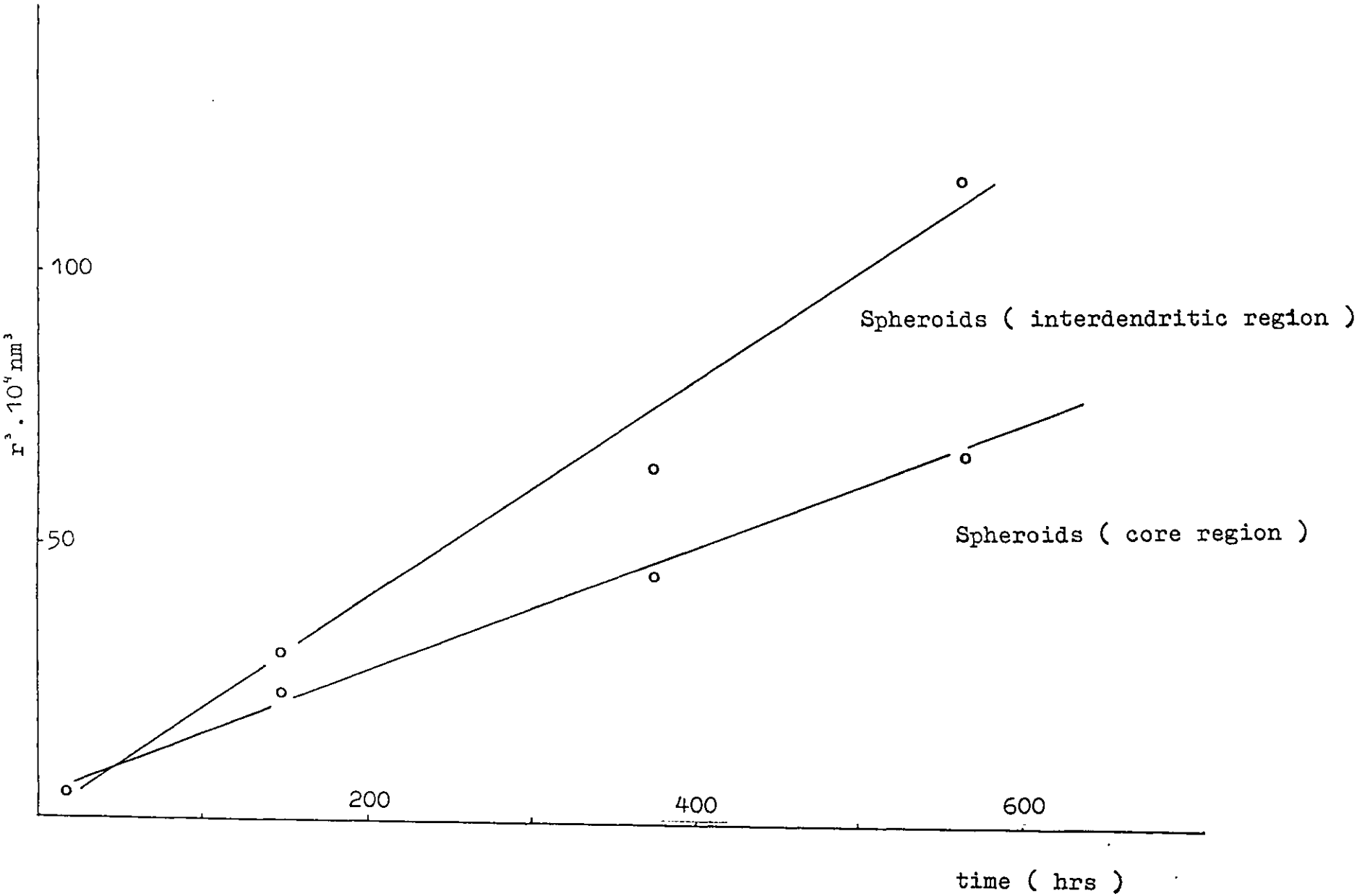

Fig.3.118-γ' Coarsening

TABLE 3.1

Solidification structure and arm spacing

R solidification rate ($mm\ hr^{-1}$)	G temperature gradient ($^{o}C\ mm^{-1}$)	structure	GR cooling rate ($^{o}C\ hr^{-1}$)	G/R ($^{o}C\ hr\ mm^{-2}$)	primary spacing (mm)	secondary spacing (mm)
9.6	20	near plane front	192	2.1		
9.6	13	plane front/cellular	125	1.3		
12	13	cellular	156	1.08	0.160	
30	13	cellular-dendritic	390	0.43	0.245	
60	13	cellular-dendritic	780	0.21	0.190	
120	13	cellular-dendritic	-	-	-	
300	13	dendritic	3900	0.04	0.120	0.042
600	13	dendritic	7800	0.021	0.105	0.035
1200	20	dendritic	24000	0.016	0.09	0.027

TABLE 3.2

γ' particle sizes* - as-solidifed conditions

G = 13°C mm^{-1}	Core region (μm)	†Interdendritic region (μm)
R = 60 mm hr^{-1}	L = 0.21	L_1 - 0.32
		L_2 - 0.45
		L_3 - 0.22
R = 300 mm hr^{-1}	D = 0.11	L = 0, 23
R = 600 mm hr^{-1}	D = 0.075	L = 0, 13

* cubic particle sizes are expressed by the cube side and near-spherical particles by the particle diameter

† L_2 - ogdoadically diced cube
L_3 - individual particles in the ogdoads
L_1 - irregular shaped cuboids (less developed ogdoads)

Compositions in Tables 3.3-3.6 and 3.9-3.12 have been rounded to the first decimal, thus the total sum may not be exactly 100%.

TABLE 3.3

Microsegregation analysis*

R		60 mm hr^{-1}	120 mm hr^{-1}	300 mm hr^{-1}	600 mm hr^{-1}
Element					
Nb	CM	1.3	1.1	2.6	1.0
	Cm	0.5	0.5	0.4	0.5
Ti	CM	4.4	4.5	3.5	5.2
	Cm	2.4	2.5	1.9	2.3
Mo	CM	2.1	1.6	-	2.4
	Cm	1.4	1.4	-	1.4
W	CM	3.2	1.8	3.1	3.0
	Cm	1.8	2.9	1.4	1.3

CM - maximum concentration
Cm - minimum concentration

* The compositionsfor the rates 60, 300 and 600 mm hr^{-1} were obtained from line analysis, and that for R = 120 mm hr^{-1} was obtained from point analysis (refer to Table 3.11 for the complete analysis).

TABLE 3.4

γ' composition (particles continuously precipitated)

	Estimated particle thickness (nm)	Ni (wt%)	Al	Ti	Cr	Co	Nb	Mo	Ta	W
A	150	74.2	7.9	6.8	3.2	4.5	1.1*	1.0*	0*	1.3*
	200	69.0	9.1	5.7	2.1	3.9	1.2*	1.5*	4.8	2.6*
	200	70.7	9.1	6.7	2.4	4.2	1.4*	2.2*	1.5*	1.7*
	200	71.8	9.0	6.0	3.0	4.2	1.1*	1.5*	2.1*	1.2*
B	400	66.5	6.4	6.6	6.9	3.2	2.3	0.9*	4.2	2.9
	400	68.4	8.7	6.3	5.9	3.2	2.0	2.1	1.6*	1.8*
	400	63.8	12.4	6.5	5.6	3.2	1.9	1.8	2.4	2.3
	400	72.6	7.5	7.1	3.7	3.6	1.1	0.7*	2.9	0.9*
	250	68.9	7.6	7.1	4.7	3.5	1.3	1.4	3.7	1.9*
	400	66.5	10.0	7.0	4.6	3.4	1.5	1.6	3.5	1.9*
	400	70.8	8.2	6.9	4.3	3.5	1.6	1.7	1.9*	1.1*
C	100	63.9	6.4	6.3	8.7	3.3	2.8	3.9	1.7*	2.9*
	100	68.6	7.3	5.8	5.2	3.2	1.3*	2.2	1.4*	4.9

* Peak area < 2 sigma (standard deviation of the background)
A - R = 60 mm hr^{-1}, as-solidified structure
B - R = 300 mm hr^{-1}, heat treatment : 1120°C-2 hrs-AC + 845°C-360 hrs-AC; cubic particles analysed
C - same condition as B; spherical particles analysed

TABLE 3.5

Effect of the estimated γ' particle thickness on the compositional analysis

Estimated particle thickness (nm)	Ni	Al	Ti	Cr	Co	Nb	Mo	Ta	W
300	67.5	11.0	6.4	2.5	4.2	1.3*	2.1*	0*	4.9*
200	69.5	9.0	6.45	2.55	4.3	1.2*	2.0*	0*	5.0*
100	71.5	7.0	6.5	2.6	4.4	1.1*	1.8*	0*	5.0*

* Peak area < 2 sigma (standard deviation of the background)

TABLE 3.6

Compositional Analysis

	Ni	C	Al	Ti	Cr	Co	Nb	Mo	Ta	W	Zr
alloy composition	61.9	0.12	3.46	3.44	15.8	8.3	0.83	1.72	1.77	2.58	0.055
MC carbide	2.15	8.35*	0.15	23.2	0.8	0.25	15.6	2.7	37.0	9.45	0.4
γ' (TEMSCAN)	73.1	-	7.0	6.5	2.5	4.4	1.5	1.7	1.7	1.5	-
matrix (difference : alloy-(γ' + carbide))	53.1	0.04	0.31	0.2	28.2	12.0	0	1.8	1.0	3.4	-
matrix** (TEMSCAN analysis)	57.1		1.9	1.3	21.0	14.5	1.6	2.0	0.5	4.1	-
interdendritic region ($\gamma+\gamma'$)	64.2		3.5	4.5	14.5	7.8	1.1	1.6	1.0	1.8	-
core region ($\gamma+\gamma'$)	64.1		3.0	2.4	16.2	8.8	0.5	1.4	0.7	2.9	-
eutectic liquid	56.5		2.4	5.6	14.5	7.8	2.8	2.7	1.3	1.8	4.6
discontinuous γ' (rod centre)	72.3		6.8	7.6	3.0	4.7	2.8	1.2	2.0	0.3	-
eutectic γ'	72.6		7.0	6.0	3.5	4.6	1.2	1.0	1.4	2.7	-
$M_{23}C_6$ carbide				x	x		x	x	x	x	-

* The figure for the C content also includes N.

**The matrix composition was obtained from direct TEMSCAN analysis of a residue extracted in the replica technique for the γ' particles; the fit index for the X-rays peaks was however high (4.6) and could have introduced small errors in the measurement.

TABLE 3.7

Discontinuous phase formation as a function of the casting conditions

Solidification rate (mm hr^{-1})	Temperature gradient (^{o}C mm^{-1})	Number of discontinuous cells per 10 mm of grain boundary
9.6	20	0
12	13	10
30	13	100
60	13	50
120	13	50
300	13	$\sim$ 0*
600	13	$\sim$ 0*

* Discontinuous cells of very small sizes

TABLE 3.8

γ-γ' eutectic formation as a function of the casting parameters

Solidification rate (mm hr^{-1})	Temperature gradient (^{o}C mm^{-1})	Volume %	Size of the eutectic colonies (μm^2)
9.6	20	eutectic free	
12	13	$\sim$ 0	
30	13	-	
60	13	1.5	200-500
120	13	-	-
300	13	1.5	30-70
600	13	2	10-20

TABLE 3.9

Composition of the γ' constituent in the discontinuous phase

Estimated rod thickness (nm)	Ni	Al	Ti	Cr	Co	Nb	Mo	Ta	W
				Rod centre					
200	71.7	7.6	7.3	2.9	5.1	3.0	0.8*	2.3*	0*
200	71.1	8.4	8.0	2.1	4.5	2.9	1.0*	0.9*	1.0*
150	74.3	4.4	7.6	4.0	4.6	0.6*	1.9*	2.7*	0*
				Dendritic perturbation					
200	67.4	6.4	8.4	2.7	4.4	1.8*	0.5*	4.6*	3.9*
200	71.6	7.2	7.9	2.4	4.6	1.6*	1.5*	1.4*	1.9*
150	71.9	6.2	8.0	2.2	4.7	1.8*	1.2*	4.1*	0*
150	66.4	8.1	7.7	4.8	4.0	4.4*	0*	4.6*	0*

* Peak area < 2 sigma (standard deviation of the background)

TABLE 3.10

Composition of the eutectic liquid (wt%)
(R = 120 mm hr^{-1}, interrupted solidification)

Ni	Al	Ti	Cr	Co	Nb	Mo	Ta	W	Zr
50.7	1.7	3.8	16.9	8.3	3.8	2.9	1.3	1.6	8.9
55.9	2.4	5.6	15.7	7.6	2.4	3.2	1.5	2.4	3.4
61.6	3.0	7.3	11.3	8.4	2.8	1.5	1.2	1.2	1.7

TABLE 3.11

Composition of the core and interdendritic regions (wt%)
(R = 120 mm hr^{-1}, interrupted solidification)

Ni	Al	Ti	Cr	Co	Nb	Mo	Ta	W
Core region								
63.1	3.3	2.2	16.2	8.9	0.6	1.8	0.7*	3.0
64.2	2.8	2.3	16.3	8.8	0.5	1.1	0.8*	3.2
63.9	3.1	2.8	16.3	8.9	0.6	1.4	0.5*	2.6
Interdendritic region†								
63.8	3.6	4.5	14.4	7.7	1.0	1.7	1.2	2.0
63.6	3.5	4.5	14.5	8.0	1.2	1.6	1.4	1.7
63.9	3.3	4.7	14.5	8.1	1.2	1.7	0.6*	1.8

* Peak area < 2 sigma (standard deviation of the background)
† The values for the interdendritic region express the highest segregation point, as indicated by earlier γ' precipitation in the 'interrupted solidification' specimen.

TABLE 3.12

Compositional analysis near migrating grain boundaries (wt%)
(R = 120 mm hr^{-1}, interrupted solidification)

The regions analysed are those indicated in the diagram.

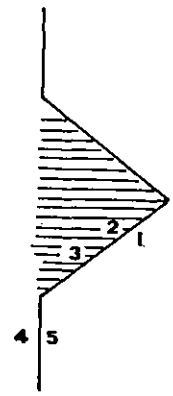

	Ni	Al	Ti	Cr	Co	Nb	Mo	Ta	W
1	63.3	3.2	3.6	15.7	8.4	0.9	1.6	1.2	2.1
2	62.8	3.4	4.0	15.5	8.2	0.9	1.8	1.0	2.0
3	63.8	3.1	3.8	15.3	8.0	0.9	1.6	1.2	2.2
4	63.2	3.2	3.8	15.9	8.3	1.0	1.4	0.9	2.2
5	62.9	3.3	3.7	15.9	8.4	1.0	1.6	0.8*	2.3

* Peak area < 2 sigma (standard deviation of the background)

TABLE 3.13

Main heat treatments

1. Commercial or full heat treatment (FHT) :

   1120°C - 2 hr - AC + 845°C - 16 hr - AC

   Samples : 60, 300, 600 mm hr^{-1}

2. γ' solution treatments

   Temperatures : 1170°C, 1180°C, 1190°C

   Times : 1 hr, 2 hrs

   Samples : 60, 600 mm hr^{-1}

3. γ' coarsening treatments

   Pre-treatment : 1120°C - 2 hr - AC

   Coarsening temperatures : 850°C, 950°C, 100°C, 1050°C

   Times : 16 hrs to 600 hrs

   Sample : 300 mm hr^{-1}

4. Continuous cooling plus aging

   Solution treatment : 1180°C - 0.5 hr - controlled furnace cooling

   Cooling rate : 13°C min^{-1} (R = 60 mm hr^{-1}, G = 13°C mm)

   Aging temperatures : 1140°C, 1120°C, 1100°C, 1050°C, 1000°C, 950°C, 850°C, 600°C

   Aging time : 24 hours

   Sample : R = 60 mm hr^{-1}

TABLE 3.14

γ' Particle sizes* - as-solidified and fully heat-treated conditions

Solidification rate R (mm hr^{-1})		as-solidified (μm)	1120°C-2 hrs-AC spheroids (μm)	FHT (μm) spheroids size	spheroids volume %	cuboids size	cuboids volume %
60	core	0.21	-	-	-	0.34	∿ 8
	interdendritic	1 0.45 2 0.22 3 0.32	-	0.062	∿ 10	0.38	∿ 47
300	core	0.11	0.044	0.070	∿ 30	-	0
	interdendritic	0.23		0.072	∿ 10	0.34	∿ 47
600	core	0.075		-	-	0.31	∿ 16
	interdendritic	0.13	0.036	0.056	∿ 10	0.33	∿ 47

* Spheroids - particle diameter
Cuboids - side length

1 - ogdoadically diced cubes
2 - individual particles in the ogdoads
3 - irregular shaped particles (less developed ogdoads)

The volume fraction of the cuboidal particles in the interdendritic region (∿ 47%) refer to the areas presenting the highest particle density at that region.

TABLE 3.15

γ' Particle Sizes* - Coarsening Treatments
(R = 300 mm hr^{-1})

Temperature	Time (hrs)	Cubic Particles Interdendritic region (μm)	Spheroidal Particles Core Region	Spheroidal Particles Interdendritic Region (μm)
850°C	16	0.35	0.07	0.07
	144	0.36	0.13	0.12
	360	0.38	0.17	0.15
	550	-	0.21	0.18
950°C	51	0.39	0.26	-
	112	0.44	-	-
	169	0.47	0.38	-
	360	0.50	0.46	-
	609	0.59	0.54	-
1000°C	51	0.43		
	112	0.84		
	240	0.56		
	360	0.60		
1050°C	16	0.43		
	112	0.57		
	240	0.68		
	360	0.75		

* Cuboids - side length
Spheroids - particle diameter

TABLE 3.16

γ' Coarsening rates (nm^3 sec^{-1})

Temperature	Cubic particles	Spherical particles Core region	Spherical particles Interdendritic region
850°C	1.5	0.7	0.3
950°C	8.3	8.7	-
1000°C	15.2	-	-
1050°C	34.5	-	-

TABLE 3.17

Microhardness test results

Load 100 gr
Vickers indent

Solidification rate R ($mm\ hr^{-1}$)	Core region		Interdendritic region	
	as-cast	FHT	as-cast	FHT
60	459	514	473	538
300	469	514	530	522
600	493	530	563	553

discontinuous phase (H_v = 464 (as-cast sample), H_v = 525 (FHT sample))

FHT - full heat treatment : 1120°C - 2 hrs - AC + 845°C - 16 hrs - AC

CHAPTER 4

DISCUSSION

4.1 Introduction

The investigation of the effect of variations in the casting parameters R, the solidification rate and G, the temperature gradient at the solid-liquid interface, on the structure of nickel based alloy IN 738 low carbon, has been described in the previous chapter. It has been revealed that a general refinement of the structure, viz the dendritic or cellular-dendritic arm spacing, the size of the γ-γ' eutectic colonies and that of γ' and carbide particles occurred with increased cooling rates (GR); quantitative data has been presented. Discontinuous γ' phase was found to be present for slow cooling rates, and an initiation mechanism for the reaction appeared to be related to the existence close to the grain boundary of dispersions of fine γ-γ' eutectic colonies; the γ' rods resulting from the discontinuous reaction usually presented dendritic perturbations at the surface.

The γ-γ' eutectic colonies consisted either of a dispersion of fine γ' rods, or presented a finger-type morphology, where the rods progressively broaden at the eutectic front.

All these morphological characteristics are to be discussed, together with the kinetics for continuous γ' coarsening and discontinuous growth following grain boundary migration.

4.2 Morphology

4.2.1 General solidification structure

The effect of G and R on the solidification structures, viz. dendritic, cellular-dendritic, cellular and near plane front is shown in Table 3.1, together with values for the primary and secondary arm spacing. In accordance with Tiller and Rutter's supercooling proposition[110], the transition from a cellular into a plane front condition occurs when $\frac{G}{R} \geq \frac{\Delta T}{D}$, where D, the effective diffusion coefficient of atoms in the liquid, is 5.10^{-5} cm^2 sec^{-1}; the melting range in IN 738 has been previously established as 85°C (1315 - 1230°C), thus by this approach $\frac{G}{R} \geq 4.7$ °C hr mm^{-2} should be needed. From the experimental conditions, this transition was found to be just above 2.1 °C hr mm^{-2}; this coincides with the value found by McLean and Schubert[74] (2.3 °C hr mm^{-2}) for IN 738.

The transition from cellular into a cellular-dendritic structure was found to occur for 12 mm hr^{-1} < R < 30 mm hr^{-1} (G = 13°C mm^{-1}), and that from cellular-dendritic into dendritic for 120 ≲ R ≲ 300 mm hr^{-1} (G = 13°C mm^{-1}).

The cooling rate GR is often related to the dendritic and cellular-dendritic arm spacing. In Fig.4.1 a log-log plot has been made of the variation of primary arm spacing with cooling rate; for the primary arms a straight line was found to fit well except for the value corresponding to the inter-cellular spacing, which presented a large deviation. The line slope obtained by a least square method (after excluding the cellular condition) indicated the relationship $\lambda_p \propto (GR)^{-0.247}$; considering only the effect of the solidification rate (thus, including only the rates where the gradient is constant) the result was $\lambda_p \propto (R)^{-0.283}$. For the secondary arm spacing also plotted in Fig.4.1 the relation was $\lambda_s \propto (GR)^{-0.243}$, thus indicating

that λ_p and λ_s vary equally with the cooling rate.

Quested et al[96], also investigating the effect of the cooling rate on λ_p and λ_s found different relations over a similar range of GR values for IN 738 alloy :

$$\lambda_p \propto (GR)^{-0.3}$$

$$\lambda_s \propto (GR)^{-0.4}$$

thus suggesting that the secondary arm spacing decreases faster than the primary for increased GR; a similar trend was found by Kotler[75] (for Pb-Sn alloys). Tewari[76] found the relation $\lambda_p \propto R^{-0.24}$ for IN 100 while Lasak[111] found $\lambda_p \propto R^{-0.27}$ for IN 792.

It has been recently suggested[112] that the cellular dendritic spacing exhibits the same dependence on GR as the secondary dendrite arm spacing; results for the cellular dendritic spacing in a Ni-Al-Cr alloy were in fact fitting very well on the straight line (log-log plot) for the secondary arm spacing. Similar results were found when plotting the data against the solidification rate R. In the case of IN 738, the cellular dendritic spacing was found to fit perfectly with the primary dendrite spacing; instead, the cellular spacing could present a better fitting with the secondary arm spacing, the GR dependence being adjusted to $(GR)^{-0.35}$, which agrees closer with the result from Quested et al[96]. Plotting λ_s as a function of R, the dependence was $R^{-0.38}$. It is important to observe that in the present work the designation 'cellular dendritic' is used in relation to a solidification structure exhibiting in the transverse section the shape of 'Maltese crosses', while the work by Montoya-Cruz et al seems to use this term for a cellular structure.

Hunt[113] proposed that the λ_p dependence on G and R is in accordance with the relation

$$\lambda_p = A\, R^{-0.25}\, G^{-0.5}$$

When G is constant, the equation is reduced to $\lambda_p \propto R^{-0.25}$, which agrees with most experimental results (λ_p vs R). However when considering both the effect of G and R, the data for IN 738 does not fit so well (Fig.4.2) as with the $(RG)^a$ relation.

4.2.2 Microsegregation

Compositional analysis has been carried out for the cellular-dendritic and dendritic structures in order to investigate micro-segregation (Table 3.3). It was found that the interdendritic region was richer in Nb, Ti, Mo while the core region contained higher amounts of W, Cr, Co. Piearcey[69] et al verified that Cr segregated to the interdendritic region in Mar M200; in fact Cr is usually reported[1] to follow the same segregation pattern as Ti and Al, thus presenting a reverse pattern in IN 738.

Not a very clear trend was established for the effect of the solidification rate and temperature gradient on the microsegregation. The method used for obtaining the values, viz. microprobe analysis along a trace line, may present some limitations, and full maps of the regions are recommended so as to avoid interference by the presence of carbides or γ-γ' eutectic. In this respect, Quested et al[96], carried out microprobe work on IN 738 mapping large areas; the results coincided in some cases with the present work, but a variation trend with changes in R and G could not be identified either.

4.2.3 Carbides

The results obtained included values for weight fraction, morphology, composition and lattice parameter of the MC carbides;

qualitative analysis of the $M_{23}C_6$ carbides has also been carried out. It was verified that for smaller values of the solidification rate R, the MC particles were coarser and presented a regular angular shape, while as the solidification or cooling rate increased arm instabilities were formed, and for some conditions a Chinese-script morphology developed. The examination of the 'interrupted solidification' ingot, revealed that a fine Chinese-script carbide structure was present in the earlier solidification stages (Fig.3.51) and at the 'liquid' side of the solid-liquid interface; this suggests that the MC carbides resulted directly from the liquid, and growth in the liquid is likely to control the final carbide size. Fernandez et al[82] used the 'interrupted solidification' technique for investigating MC carbide formation in IN 100; they found that the carbide arm instabilities grow in <111> directions, and resulted from the local gradient and growth rate and not from a compositional effect; it was suggested that a decrease in G/R ratio favours this morphology, thus not relating it to the cooling rate. They carried out some solidification experiments to prove that the carbides formed in the liquid, and only a limited amount of coarsening would occur from solid state diffusion.

4.2.4 Continuous precipitation of γ'

For all the solidification conditions examined, variations in particle size (Table 3.2) and morphology have occurred in different regions of the matrix. This was found to occur to a lesser extent with the near-plane front solidification condition. For the columnar dendritic solidification ($R \geq 300$ mm hr^{-1}, $G = 13^{o}C$ mm^{-1}), particles in the core region were smaller and rounded cubic or near spherical, while those in the inter-dendritic region were closer to a cubic shape, but also presenting rounded corners. For the cellular-dendritic

solidification (R = 30-120 mm hr^{-1}, G = 13°C mm^{-1}), γ' particles in the inter-dendritic region presented an 'ogdoadically diced' cube structure, while particles in the core region presented either an irregular cubic morphology or small clusters of not fully developed ogdoads. Finally, for the cellular or near-plane front condition (R = 9.6-12 mm hr^{-1}, G = 13 or 20°C mm^{-1}) all particles were in the form of clusters, with eight (ogdoads) or more particles.

The cooling rate GR had a marked influence on the particle sizes in both core and inter-dendritic regions, the sizes decreasing with increased cooling rates.

The differences in particle sizes (and morphology) in different regions across the solidification pattern, results from preferential solute segregation for one or the other region. Compositional analysis for the dendritic and cellular-dendritic structures revealed (Table 3.3) that the core region was richer in Cr, Co, W, while Ti and Nb segregated into the interdendritic region. All these elements are considered[2] to bring earlier precipitation of γ' to different extents : Ti, Nb, Cr strongly increase γ' formation, while the effect of Co and W is less.

The results obtained for γ' composition (Table 3.4) indicated that all the main elements present in the alloy were found to be part of the γ' composition, mostly Ni, Al, Ti and Co. According to Bieber and Mihalisin[85], in IN 738 8 at % of Ni in γ' is substituted by other elements (Co, Cr, Mo, W) mainly by Co, while Ti, Ta, Nb, W, Cr (mainly Ti) substitute for nearly 50% of the Al content in relation to stoichiometric Ni_3Al.

It is expected that an earlier precipitation during cooling (from the liquid) in the inter(cellular)dendritic region due to decrease in γ' solubility, will result in a final larger particle

size, as the growth kinetics are faster at higher temperature levels ($\sim$ 1180°C); in the core regions precipitation started only at temperature levels of $\sim$ 1120°C, thus resulting in a smaller particle size. As particle morphology may vary with size and local concentration gradient, this would account for the verified changes from near-spherical into near-cubic particles as the particle size increased. γ' particles usually nucleate as coherent spheres and gradually change with growth into cubes in order to reduce the strain energy; the surface energy S associated with the {001} planes is also low although S/vol. increases. For the conditions resulting from the directional solidification (continuous cooling) a transition from spherical into a near-cubic shape occurred at approximately 0.13 μm (for both R = 300 and 600 mm hr^{-1}).

The decrease in particle sizes with increased cooling rate probably results from a higher under-cooling, thus retarding the precipitation and decreasing the growth kinetics.

The 'ogdoadically diced' cubes

Concerning the formation of the γ' cluster structure two main theories have been proposed. The original one by Westbrook[19] suggested that the eight cubes that form the cluster originate from a single nucleus, while it has been later proposed by Ardell and Nicholson[14] that elastic interactions between individual particles would be the cause of such alignment.

The present work clearly indicates a mechanism similar to that proposed by Westbrook, which can be seen in Figure 4.3 : preferential growth at the particle corners occurred due to local concentration gradients, but as these perturbations were comprised of high index faces, a lowering of the interfacial energy would be

favoured by the development of (001) γ-γ' interfaces.

For IN 738 directionally solidified at R = 300 mm hr^{-1}, particles in the inter-dendritic regions developed preferential growth at the corners in the <111> directions, similar to the particles observed in the core region for R = 60 mm hr^{-1}; this is considered to be the first stage for the cluster development. In Fig.3.5b (R = 60 mm hr^{-1}, inter-dendritic region), different stages of cluster development can be compared, viz. dendritic instabilities formation at the particle corners, a cluster partially developed, and a fully developed cluster; Fig.3.57, from the 'interrupted solidification' sample, reveals that the ogdoadically diced cube structure becomes well developed at high temperatures, occurring in the earlier stages of continuous γ' precipitation, and enhanced by slow cooling conditions.

The alloy systems investigated by Westbrook[19], viz. Ni - 7.5 at % Ti - 5 at % Al and Ni-W-Al were however cooled under fast conditions; Singhal and Martin[114] observed the formation of dendritic instabilities in Ni_3Ti particles precipitated in stainless steel during isothermal treatment and identified the growth direction as <112>. Seregin[115] has investigated the formation of ogdoads and star-like γ' precipitates in several nickel-based alloys aged at high temperature following slow cooling.

Ricks et al[116] in a recent paper have examined the ogdoadically diced cubes and classical γ' dendritic formation in several Nimonic type alloys; particles changed from spherical into cubes and finally dendritic, with preferential growth occurring in <111> directions which are minimum compression directions. They proposed that the elastic anisotropy of the system favoured the development of {001} planar facets of the ogdoads.

The existence of a supersaturated matrix appears to be essential

for the development of surface instabilities, according to Mullins and Sekerka[117]. They studied the stability of a spherical particle growing by diffusion in low supersaturation conditions and isotropic interfacial free energy; two opposing factors were considered, viz. a solute gradient effect favouring the growth of the perturbation and an interfacial energy effect opposing it. Their analysis indicated that the sphere growing under these conditions is unstable above a certain critical radius R_c, which is seven times the critical radius r_c of the nucleation theory; a later analysis[118] found that the important point was not the start of the perturbation but whether it grows faster than the sphere, and established $R_c > 21\ r_c$.

It has been often observed that the cubes comprising the cluster grew to produce a small interparticle distance between them, with the very rare occurrence of coalescence. Westbrook[19] suggests that this results from difficulty for diffusion between the cubes, and from the possibility of neighbouring cubes possessing a small disregistry (as γ' is an ordered structure). This is a view also expressed by Nash[20] in considering the barriers to particle coalescence; according to his analysis, an energy barrier equivalent to the antiphase boundary has to be overcome, and this could occur when particles become incoherent (after growth) as a reduction in the surface energy could be equivalent to the antiphase boundary energy. In the present case, for many of the clusters examined, the individual particles have not presented a perfect cube morphology but an irregular shape with excessive growth at the free corners, as the concentration gradient effect predominates over the surface energy; it is believed that such growth has not necessarily resulted in incoherency as coalescence has not occurred, similarly to observations[116] in some Nimonic alloys. After isothermal heat-treatments, such as the first stage of the full

heat-treatment (1120°C - 2 hrs), full coalescence of the particles comprising the clusters has occurred and a very regular cube shape has formed; with the isothermal treatment it was possible to overcome the energetic barrier for coalescence and regular (001) γ-γ' interfaces were formed, possibly favoured by the high lattice strain.

For the very slow cooling rates (cellular structure) the γ' clusters consisted of arrangements of cubes and plate shaped particles in numbers superior to eight particles (Fig.3.43). If for the ogdoad formation, growth along <111> directions is favoured, at this slower cooling rate, growth is also facilitated in <001> directions (less compression); the nature of the diffusion field is certainly more complex. Several arrangements of cubes and plates seem to be possible; in this respect, the work by Miyazaki et al[119], on favoured γ' plate arrangements in a Ni-Al system seems to be useful. They proposed that four types of arrangements along the orthogonal <100> directions are favoured (Fig.4.4).

a. two plates with parallel faces;
b. two perpendicular plates with edge-edge configuration;
c. two perpendicular plates with face-edge configuration;
d. two plates with their broadest face in the same plane.

In Fig.3.43, some exaples of cases a. and c. can be observed, and the occurrence of the other arrangements may also have occurred, but it is not always possible to distinguish a broad plate face from a cubic particle in such complex clusters.

The effect of heat treatments on the continuous γ'

The effect of the full heat treatment (1120°C - 2 hr - AC + 845°C - 16 hr - AC) in the interdendritic regions was to produce a bimodal distribution of regular shaped cuboidal particles and a fine distribution of spheroidal particles, while in the core region almost only the spheroidal particles have resulted. This cuboidal denuded zone at the core arises from the first stage of the heat treatment as the temperature is above the local γ' solvus, reduced by the lower Ti concentration. It is interesting to note that only for R = 300 mm hr^{-1} full γ' solution at the core was achieved, as a result of even further reduction in local Ti concentration as compared to the other rates (Table 3.3) and a ring of very coarse γ' particle formed around the core. McColvin[87] reported a similar occurrence with conventionally cast Nimocast alloy 738 attributing the γ' ring formation to the high Ti segregation in that region.

The effect of long term aging on the cuboidal distribution was to produce particle coalescence, giving origin to plate and L-shaped particles, and to change gradually the particle morphology into a more spherical one due to coherency loss. For the spheroidal distribution, aging at 950°C changed the shape into cuboids after ∿ 170 hrs, the transition particle size being around 0.33-0.37 μm, while a fully aligned distribution of cubic particles was only achieved at greater particle sizes (Fig.3.111c).

At 850°C however, after 2000 hrs particles measuring 0.40 μm were still spherical (Fig.3.107b). It is possible that at higher temperatures as the amount of atoms in solid solution increases, so does the γ-γ' mis-match and the strain energy, thus resulting in an earlier change into a cubic shape to reduce the strain energy. The modulated structure arises from elastic interactions as proposed by

Ardell, Nicholson and Eshelby[14].

4.2.5 γ-γ' eutectic

The size of the eutectic colonies decreased with increasing cooling rate, while the volume fraction possibly showed a slight increase; as a plane front condition was nearly achieved, the eutectic has been completely suppressed due to changes in the segregation pattern.

Of interest was the existence of two distinct eutectic colony morphologies : one consisting only of fine γ' rods (Fig.3.12-3.15) and the other where the γ' rods gradually broadened into a 'finger-type' shape (Figs.3.8-3.11). Although both morphologies co-existed for many of the solidification conditions (R = 30-300 mm hr^{-1}), there was a trend for a higher proportion of the 'finger' morphology at the higher solidification rates; for R = 600 mm hr^{-1} almost all the eutectic presented the 'finger' type morphology, while for R = 12 mm hr^{-1}, only the fine rod structure was present. In most nickel based alloys only the 'finger' type morphology has been reported. The importance in discussing this difference lies in the fact that the fine eutectic rods were found to be responsible for the formation of discontinuous phase in IN 738, according to a mechanism to be later proposed in section 4.2.6.

The formation of both kinds of eutectic colonies occurs by coupled growth of γ' and matrix γ by the movement of a solid-liquid interface, as suggested by Fig.3.61; the difference between them is supposed to arise from the level of solute build-up. From the compositional analysis of the eutectic 'liquid' (Table 3.10) there is an observed high level of γ' forming elements Ti and Nb, even higher than the amount found in the interdendritic regions where the continuous

γ' first precipitated; Mo is present also with a high content, but according to Decker[2] it does not exert influence on γ' solubility. Noticeable is the exceptionally high concentration of Zr ($\sim$ 4.5 wt %), which is present in the alloy as only 0.05 wt %; the high level of Zr, usually associated with the γ-γ' eutectic regions, generally led to the formation of Zr_2CS needle-like particles (Fig.3.63) as previously reported[96].

The composition of the fine γ' rods was found to be similar to that of the cube particles but no analysis of the coarser fingers has been carried out. The Zr content of the γ' rods has not been measured, but it has been reported[120] that the solid solubility limit for Zr in Ni_3Al is 2 at % Zr (0.9 wt %); Zr is considered to lower the melting point[120] similarly to the effect of Hf in Mar M 200 which lowers the melting point to 1205°C. Hf has a much higher solubility in γ' than Zr (7 at %, 8 wt %) and a low solubility in the matrix ($\sim$ 1 at %)[121,122]; thus as Zr solubility in Ni is small (and also in γ') it should segregate strongly to the eutectic front and locally decrease the solidification temperature. This could account for the fact that when the fine rod eutectic solidification was completed (Fig.3.61-3.62), regions of liquid were still remaining ahead of the broad 'fingers' (Fig.3.60); both micrographs refer to the same transverse section along the 'interrupted solidification' sample. The formation of the Zr_2CS needles would naturally depend on the local carbon level , which is known to be reduced as most carbon is forming MC carbides or is segregated at the grain boundaries. If the Zr_2CS needles form at the beginning of the eutectic solidification as in Fig.3.61, this could possibly decrease the segregation levels at the solidification front. The Zr_2CS phase has also been observed in association with the coarser γ-γ' eutectic morphology.

The fact that slower cooling rates appear to favour the fine eutectic rods, while the faster rates would act in the opposite way could be a result of the segregation patterns associated with the different solidification parameters. Also a fast cooling rate may force a faster movement of the eutectic solid-liquid interface, further reducing the solubility of Zr (or other segregating elements) in γ or γ' and increasing the solute build-up.

4.2.6 Discontinuous precipitation of γ'

The formation of discontinuous cells with some of the cooling rate conditions was such that it occurred mostly for the cellular-dendritic solidification (R = 30-120 mm hr^{-1}); few large nuclei were observed for the cellular solidification R = 12 mm hr^{-1} and for the dendritic solidification (R = 300-600 mm hr^{-1}) although the nuclei sizes were very small for these latter conditions. The relation between the size of the cells and the cooling rate GR was clear, sizes increasing with GR decreasing; the reasons for this are discussed later in this section.

a) Initiation mechanism

The earlier stages of the discontinuous γ' reaction have been investigated, mainly by the use of the 'interrupted solidification' technique. The examination of Figs.3.63-3.65 has shown that the initial migration of the grain boundary was caused by an interaction with γ' eutectic rods; this was further supported by Figs.3.69-3.74, where the discontinuous and eutectic constituents can be clearly identified.

This interaction could occur by a similar mechanism to that proposed by Nes and Billdal[34] for discontinuous formation in an Al -

0.8 wt % Zr alloy (Fig.1.6); they suggested that semi-coherent Al_3Zr precipitated perpendicularly to the grain boundaries during heat-treatment in order to minimize its high energy contact surface (high angle) with the boundary. As a result of fast grain boundary solute diffusion, increase in the precipitate-boundary contact surface was to occur. However, in order to maintain its low energy requirements (minimize the precipitate-grain boundary contact surface) the precipitate exerts a force and pulls out locally the grain boundary also causing a catalytic effect in the neighbouring precipitates, and finally activating boundary migration and discontinuous reaction. The grain boundary diffusion would eventually force changes in the precipitate morphology also not compatible with the low energy of the particle-matrix semicoherent interface, and as a result branching occurs, thus maintaining the low energy configuration and resulting in fan-shape cells; a straight reaction front was finally achieved and the reaction proceeded helped by the supersaturation ahead of the boundary.

The discontinuous γ' formation in IN 738 is believed to have occurred as the fine γ' eutectic rods (0.2 μm thickness) completed solidification and reached the grain boundary (Fig.4.5) . As the contact surfaces between the γ' rods and the grain boundary are probably high angle (high energy) and the γ'-matrix interface is coherent (low energy), a very similar mechanism to that proposed by Nes and Billdal may occur, also resulting in fan-shape cells. The difference however is that the proposed mechanism for discontinuous formation in IN 738 does not require any previous grain boundary precipitation, in which it also differs from the mechanisms proposed by Tu and Turnbull[30], and Fournelle and Clark[31]. All the known mechanisms for precipitate-induced grain boundary migration require

however, an induced 'force' upon the grain boundary in order to activate the migration, and this arises from the interfacial energy balance at the precipitate-boundary interface.

It has been observed that the finger-type eutectic morphology has not resulted in discontinuous reaction (Figs.3.75-3.77). This probably results from the fact that the 'fingers' have a larger contact surface with the grain boundary; thus solute atoms diffusing from the grain boundary would not substantially affect this surface and consequently the energy level will not change substantially. As the fingers are probably incoherent, they would not have a low energy shape to preserve, which in the case of the fine coherent rods could also exert a force on the grain boundary.

b) Growth

The main driving forces usually operating during discontinuous phase growth are[123] :

$$\Delta E_T = \Delta E^C + \Delta E^S + \Delta E^\gamma + \Delta E^D$$

where ΔE^C is the reduction in chemical potential

ΔE^S is the change in coherency strain energy

ΔE^γ is the change in γ-γ' interfacial energy

ΔE^D is the internal energy due to plastic deformation.

ΔE^D is very small in the present case as no external deformation has been applied; ΔE^S is also small, as no changes in γ' coherency are likely to have occurred, and ΔE^γ is usually low in nickel based alloys. Thus the main driving force ΔE^C results from the reduction in the supersaturation level (chemical potential) of the matrix.

In the case of isothermal discontinuous coarsening, characterised

by coarser γ' rods replacing the initial distribution (Figs.3.85, 3.86, 3.100, 3.101), the surface energy ΔE^{γ} must play an important role but the growth kinetics were found to be too slow compared with the previous mechanism (section 4.5 - 4.6).

The verified differences in the discontinuous cell size with cooling rate arises mainly from two facts :

- the growth kinetics are faster at higher temperatures and will be favoured by low cooling rates
- low cooling rates will also retard the precipitation of continuous γ' which was found to halt the grain boundary migration

(Figs.3.58, 3.67).

Although the continuous γ' precipitation starts at the same temperature levels as the discontinuous phase, it occurs initially at only very limited size regions (e.g. Fig.3.56) and will not spread rapidly to other regions for slow cooling rates thus favouring the discontinuous transformation.

The decrease in the number of discontinuous cells with increased cooling rate could result from the reduced amount of fine-rod γ-γ' eutectic colonies as opposed to the increased number of the finger-type morphology; as seen under 'initiation mechanisms' only the fine γ' rods resulted in discontinuous formation. As for the cellular solidification (R = 12 mm hr^{-1}) although only fine γ-γ' eutectic colonies were present, their volume fraction was small thus also reducing the number of discontinuous cells.

The migrating boundary usually lay in preferential crystallographic orientation planes; both low index planes, viz. {001}, {110}, {111} and higher index {210}, {310}, {320} were possibly identified; Scarlin[98]

had previously suggested that this orientation in IN 738 was along {111} planes. In the present work although it was sometimes found that a low index orientation was in relation to the grain from which discontinuous phase grows, it is believed that the opposite grain should control the migration, and that the lowest index orientation, viz. {001} is gradually pursued as indicated by the γ' rod curvatures; however the boundary movement may cease as a result of the start of continuous γ' precipitation before that orientation is achieved.

In some cases the identification was straightforward with less than 1^{o} deviation from the expected angle relationships, while sometimes a 7^{o} deviation was apparent. The success of the crystallographic orientation identification using scanning electron micrographs (method described in section 3.2.1a) clearly depends on the correct sectioning of the ingot perpendicularly to the <001> solidification direction and on the good alignment of the columnar grains with the solidification direction; failure in complying with one of these two conditions led to some of the erratic results. Although more examination using the scanning microscope or the use of transmission electron microscopy techniques should be favoured, there was enough evidence to substantiate the proposed orientation relationships; if examination at the transmission microscope is to be followed, it should be carried out with specimens solidified at R = 30 mm hr^{-1} (G = $13^{o}C$ mm^{-1}), which gave the highest amount of discontinuously transformed material.

c) Rod morphology

The discontinuous γ' rods usually presented steep curvatures probably due to changes in growth direction as the grain boundary tentatively approached a plane front aligned to a crystallographic

plane and further into a {001} orientation; the curvatures were not necessarily an indication of incoherency, as the existence of dendritic instabilities on the rod surface suggests reduced interfacial diffusion due to a small γ-γ' mismatch.

Some of the rod surfaces were smooth; however, dendritic instabilities (wavelength 0.15 - 0.25 μm) were observed to occur very regularly at all solidification conditions where discontinuous phase has formed; Scarlin[98] in examining discontinuous phase in IN 738 LC solidifed at R = 150 mm hr^{-1} has not reported the dendritic morphology occurrence, probably due to the etching conditions used for scanning microscopy which preferentially removed the γ' constituent and did not allow suitable examination. The γ' constituent appeared many times as short rods or rows of particles, but these apparent morphologies are often the result of sectioning through the γ' rods, as revealed by deep etching.

The occurrence of dendritic growth of γ' or even in other solid state reactions has been rarely reported; surface perturbations could not be seen in discontinuous γ' formed by recrystallization[124] of IN 738. Additions of Hf to Alloy 713-C were supposed to originate the dendritic growth observed on some of the platelets of the γ-γ' eutectic[125] (it has been shown[120] that Hf usually segregates to the γ'). Thin castings of IN 100 have reportedly[126] presented dendritic shaped $Ni_3(Al,Ti)$ particles as a result of the excess in γ' forming elements and the long time at the γ' forming region. The other reported cases refer to the formation of 'ogdoadically diced' cubes as discussed in section 4.2.4, although Ricks et al[116] have reported a classical dendritic γ' shape formation for Nimonic type alloys. The classical cases usually refer to γ-phase dendritic formation in Cu-Zn β brass or related alloys[127], for instance γ precipitation in β Cu Zn Sn, which

are to be further discussed in this section.

The formation of shape instabilities leading to dendritic-like precipitates or interfaces is a usual occurrence in solid-liquid systems as a result of constitutional supercooling (Fig.4.5); a solute build-up close to the solid-liquid interface lowers the solidification temperature thus supercooling a region of the liquid. Any bump formed at the interface will grow and possibly accelerate due to increased supersaturation.

The occurrence of shape perturbations in the solid state has been considered by Mullins and Sekerka[117], Shewmon[128] and recently reviewed by Doherty[129]. Mullins and Sekerka have analysed the problem of the stability of a spherical particle growing by diffusion in low supersaturation conditions, as previously mentioned in section 4.2.4 in relation to the formation of the ogdoads. From their analysis it was possible to calculate the expression for the smallest stable wavelength :

$$\lambda_o = 2\pi \left(\frac{C_o \Gamma}{G}\right)^{1/2}$$

where $\Gamma = \frac{\sigma\Omega}{RT}$ is the capillarity constant

σ is the interfacial free energy per unit area

Ω is the precipitate volume per mole of its principal constituent

G is the gradient in the matrix at the interface.

The equation expresses that the interfacial energy and the concentration gradient at the interface are opposing terms in the development of surface perturbations. The wavelength corresponding to a maximum growth rate was

$$\lambda_m = \sqrt{3}\,\lambda_o$$

Shewmon[128] made quantifications about the conditions that contribute to stabilisation of the interface, viz. :

- anisotropic interfacial energy
- partial or total interface diffusion control (reduces the concentration gradient at the interface)
- diffusion within the precipitate or along the interface (it smooths the perturbation reducing the surface area)[130].

Vogel[131] pointed out that the proximity of precipitates also acts as a stabilising factor by inducing 'soft' impingement of the diffusion fields, thus reducing the solute gradient.

Malcom and Purdy's results for brass[127] reinforced the role of the interfacial free energy (low in the brass sytem e.g. 50 ergs/cm^2), and of the anisotropy of the interfacial free energy; they suggested the existence in the earlier stages of γ' precipitation in β-brass of a correlation between perturbation wavelength and precipitate thickness.

The importance of the interface mobility in developing shape perturbations is stressed by the absence of dendritic instabilities in Widmanstatten α plates precipitated in β-Cu Zn, where the strong crystallographic constraint will in the case of low interface mobility, restrict the surface perturbations[127] (stepped boundaries were formed); the interfacial reaction without the need of ledges may occur if a high local thermodynamic driving force exists[132].

In the case of nickel based alloys, several conditions favour dendritic perturbations[129] :

- the cube-cube orientation between phases of the same structure (γ' and the austenitic γ matrix) fulfils requirements of the 'isotropic' interfacial energy
- low diffusivity within γ' (ordered structure)
- low lattice mismatch between γ' and γ reducing the interfacial diffusivity.

However, Vogel's condition of widely spaced precipitates increasing the gradient at the interface as a result of 'soft impingement' appears to be critical, as it is usually not fulfilled for γ' precipitation in nickel based alloys. Shape instabilities on the discontinuous γ' rods of IN 738 started to form in the earlier stages of the discontinuous growth (Figs.3.63-3.68) and grew during the cooling; the decrease in temperature is matched by a reduction in the solubility of γ'-forming elements in the initially solute depleted austenitic matrix constitutent of the discontinuously transformed region. A strong concentration gradient at the rod surface, aided by the reduced interfacial diffusivity (the γ' rod surface is probably semi-coherent), and mostly by the wide inter-rod spacing ($\sim$ 0.7-1.5 μm) resulted in dendritic formation; a comparison with rod dimensions and inter-rod spacing in other nickel based alloys where discontinuous phase has formed, is presented in Table 4.1. The effect of the inter-rod spacing in suppressing or easing shape perturbations is further stressed in Figs.3.23, 3.48 where smooth interfaces resulted from closely arranged rods, and small instabilities developed as this space increased; also a relation between dendritic shape perturbations and rod thickness may exist, as suggested by Malcom and Purdy[127].

Both the dendritic instabilities at the rod interfaces and the

'ogdoadically diced' cubes originate probably from similar mechanisms; however, the dendritic instabilities at the rod surfaces have not developed (unlike the ogdoads) faceted interfaces during the continuous cooling. It is possible that for the ogdoads a higher solute concentration strained the matrix favouring {001} interfaces. Ricks et al[116] observed that the development of a non-faceted dendritic morphology could occur at either partially coherent interfaces (alloys with negative misfit, viz. the lattice parameter of the matrix is greater than that of γ') or at interfaces without full coherency loss (positive misfit); the elastic anisotropy of the system would control the faceting for the coherent surfaces.

The effect of isothermal heat treatment (1050°C - 1120°C) in replacing the rod dendritic instabilities by a serrated surface (Fig.3.84) is also possibly due to the increase in the strain energy by increasing the solute concentration at higher temperature levels; this concentration is enhanced by the dispersion of finely precipitated γ' particles usually present in the inter-rod spacing of the as-cast structure (Fig.3.49).

d) The effect of heat treatments on the discontinuous phase

Temperature exposures above 1000°C (for 2 hrs) had the effect of partially breaking up the rods by a spheroidizing mechanism (Figs.3.96, 3.99); at 1000°C the dendritic instabilities became detached from the rods by a similar mechanism (Fig.3.97) leaving a smooth rod interface, while at 1050°C or above serration development at the rod surfaces was preferred. The smoothing of the dendritic surface by spheroidization requires smaller diffusion distances as compared with the faceting mechanism, thus being favoured at lower temperatures. It has also been observed that the discontinuous

coarsening occurred by a grain boundary receding mechanism for temperatures above 1050°C, while at 1000°C a grain boundary layer (probably of γ') developed instead. For the coarsening reaction the driving force is the reduction in surface energy of the discontinuous region as a thicker rod structure partially replaced the initial rod distribution (Fig.3.100-102); the reason for this not occurring at 1000°C is either the reduction in grain boundary diffusivity (by a factor of 5 to 10 approximately) or pinning of grain boundaries by the precipitated layer. For temperatures above 1000°C discrete γ' particles were present at grain boundaries (Figs. 3.90-91, 100-103) and it is possible that these particles helped to initiate the discontinuous coarsening reaction similarly to the Nes and Billdal mechanism previously discussed.

4.3 The Effect of the Structure on the Mechanical Properties

Creep tests on directionally solidified IN 738 (as-solidified and fully heat treated) have been carried out by the National Physical Laboratory[96], including solidification rates varying from 60 to 1200 mm hr^{-1} (Table 4.2). In the as-solidified condition rupture life was found to be higher and minimum creep rate smaller for R = 600 and 1200 mm hr^{-1}; for R = 60 mm hr^{-1} the result was poorer compared to the conventionally cast material. After the full heat treatment (FHT) the results for R = 60 mm hr^{-1} improved considerably, showing properties close to R = 300 mm hr^{-1} FHT which presented only a small improvement in relation to the as-cast condition. For the faster rates the improvements with FHT turned out to be insignificant.

From the observed structure it is possible to suggest that the main reason for the poor performance of the specimen solidifed at R = 60 mm hr^{-1} (as-cast) was due to the distribution of 'ogdoadically diced'

cube γ' particles; for the other rates the γ' particles presented more regular shape and sizes. There is no evidence to confirm a detrimental effect by the discontinuous cells at that rate (60 mm hr^{-1}) as the hardness values found for the discontinuous regions were comparable to those for the interdendritic region (Table 3.17), thus not causing a softening of the grain boundary region and premature failure. Scarlin however, found lower hardness (-25%) for the discontinuous regions. It is possible that the volume fraction of the discontinuous phase (< 1%) was too small compared with the total γ' (∿ 45%) to cause significant harm to the properties.

Concerning the behaviour of the γ' particles after FHT, a study on the interaction of a bimodal distribution of γ' particles (IN 738 conventionally cast) with dislocations has been carried out by Stevens and Flewitt[88] (Fig.1.9). The spheroids control the deformation initially; however, as the spacing between the cuboids decreases with aging and that of the spheroids increases, the cuboids eventually become the main barrier to dislocation movement.

For the core region (for all DS conditions) the spheroids control the deformation at all stages, as there were only a few cuboids. The great improvement after FHT shown by the test pieces solidified at R = 60 mm hr^{-1} is probably due to the replacement by the heat treatment of the initial distribution of 'ogdoadically diced' cubes.

No comparison between the creep tested structures of the different solidification conditions was attempted. The only rate examined, R = 300 mm hr^{-1} presented an alignment of the γ' particles perpendicularly to the stress axis (Figs.3.113-116), probably due to elastic interaction between particles and in order to decrease the interfacial energy. It has been reported[133] that tensile stresses can cause γ' alignment perpendicular to the stress axis while

compressive stresses cause alignment parallel to the axis. Faceted γ' interfaces were however observed, possibly at {111} planes as a result of particle shearing, as other dislocation interaction mechanisms such as 'looping' may be inhibited by the large size of the aligned particles. This has not been however a main area of concern in the present work.

4.4 Coarsening Kinetics of the Continuously Precipitated γ'

The coarsening rates of the cubic and spheroidal particles have been measured for temperatures varying from 850°C to 1050°C; the results are summarized in Table 3.16. It can be observed that when comparing the coarsening of the spheroidal particles as part of the bimodal distribution or as a single distribution (core region) the latter resulted in faster growth kinetics; particle coalescence was also observed to occur more extensively in the core region. This increase in particle sizes probably results from an increased value for Ce, the solute equilibrium concentration in the matrix.

It is interesting to observe that while at 850°C the coarsening rate of the cuboidal particles was greater than that from the spheroids (core region), at 950°C both coarsening rates presented very similar values.

From the equation representing the coarsening rate $r^3 - r_o^3 = K^3 t$, where

$$K^3 = \frac{8 \gamma D C_e V_m^2}{9RT}$$

the diffusion coefficient D may be considered the only term to vary significantly with temperature (assuming that C_e is approximately constant) and is given by an Arrhenius type equation $D = D_o e^{-Q/RT}$, where D_o is the frequency factor and Q the activation energy for

diffusion. Then the following relation results :

$$\ell n\ (K^3T) = \text{constant} - \frac{Q}{RT}$$

The activation energy can be obtained by plotting $\ell n\ (K^3T)$ versus $\frac{1}{T}$ (Fig.4.6). For the cubic particles (four temperature points), the activation energy was found to be 48.0 K cal mole^{-1} (2.0×10^2 KJ mole^{-1}), while for the spheroids (two temperature points) a higher value was found Q = 72.0 K cal mole^{-1} (3.0×10^2 KJ mole^{-1}); these results, mainly that for the cubic particles, differ from reported[14,83] values for γ' containing alloys which are usually close to the activation energy for Al (2.7×10^2 KJ mole^{-1}) or Ti (2.57×10^2 KJ mole^{-1}) diffusion in the γ matrix. By assuming C_e, the equilibrium concentration of γ' forming elements in the matrix to be independent of temperature, a miscalculation may have been introduced into the calculation of the activation energy value; while for the temperature range 750°C - 850°C, like the conditions used in Stevens and Flewitt[83] work, Ce is probably relatively constant, it is however likely to increase considerably for the higher temperatures of the range studied in the present work (850°C - 1050°C). This should decrease the K^3T/C_e term for higher temperatures thus possibly explaining the slightly higher activation energy found for the spheroidal particles, but it could not account for the low value found for the cubic particles. In relation to the accuracy of the particle size measurements, it should be noted that for some of the conditions examined (mostly for the 850°C coarsening studies) there was a calibration problem in the examination of extraction replicas in the transmission electron microscope, which could have introduced a maximum error of ± 5% ; the other measurements were carried out in the scanning electron microscope.

However, the fact that for the lower temperatures a bimodal particle distribution (spheroids and cuboids) was present for most of the coarsening times, while for the higher temperatures a single cubic shape distribution was soon achieved, may have an effect on the respective coarsening rates and explain the unexpected low value for the activation energy.

Stevens and Flewitt's work[83] has investigated the coarsening kinetics of the γ' spheroids as part of the bimodal distribution and found the activation energy $Q = 2.69 \times 10^2$ KJ mole^{-1}; the values they found are included in Figure 4.7 . Their data at 850°C is not in full agreement with the present work, with their value for the coarsening rate K^3 (~ 7.5 nm^3/sec) being twice that obtained in this present work (3.2 nm^3/sec).

The γ'-matrix interfacial energy can be estimated from the coarsening rate equation. V_m, the molar volume of γ', is given by $N_o\ d^3$, where N_o is Avogadro's number and d^3 the volume of the unit cell where $d = 3.59$ Å has been measured from the X-ray experiments (V_m = 27.85 cm^3 mole^{-1}) . Values for C_e, the equilibrium concentration of γ' forming elements in the matrix and the volume diffusion coefficient can only be estimated from the limited reported data ($C_e = 1.44 \times 10^{-2}$ mol cm^{-3} at 1000°C for ~~A~~UDIMET alloy ; $D = 1.2 \times 10^{-10}$ cm^2 s^{-1} for Al diffusion in Ni-Cr at 1000°C). The result obtained for the interfacial energy using these approximations is 8 mJ m^{-2}, which compares well with results obtained by Ardell (14 mJ m^{-2}) and Nash (8.9 mJ m^{-2}).

4.5 Discontinuous γ' Growth Kinetics

Most of the theories that predict the growth rate for the discontinuous phase are based on Turnbull's model[38]

$$v = \frac{C_o - C_E}{C_o} \cdot \frac{D_B \delta}{\bar{\lambda}^2}$$

where C_o is the supersaturated matrix composition

C_E is the composition in the discontinuous matrix in equilibrium with the γ' rods

D_B is the grain boundary diffusion coefficient

δ is the grain boundary thickness

$\bar{\lambda}$ is the mean inter-rod spacing

The concentration term of the equation concerns the driving force behind the boundary migration, while the second part of the equation refers to the boundary mobility.

Aaronson and Liu's[40] modified equation has taken into account the effect of curved lamellae tips :

$$v = \frac{4\ C_B - C_E}{C_B - C_o} \cdot \frac{D_B \delta}{\bar{\lambda}^2}$$

where C_B is the composition of the discontinuous rods (γ' phase). Or in an approximated version

$$v = \frac{4\ D_B \delta}{\bar{\lambda}^2}$$

The value of δ, the grain boundary thickness, is usually estimated[29] as 5 nm, while the interlamellar spacing was experimentally measured as $\sim$ 1.0 μm; the growth rate of the migrating boundary was calculated from the experimental data as 0.6×10^{-4} cm sec^{-1}. The value for the diffusion coefficient at the grain boundary D_B has to be approximated from the data available, mostly on binary or ternary Ni alloys. During the coarsening of continuously precipitated γ', Al and Ti lattice

diffusion is usually considered to control the mechanism; however, in relation to grain boundary diffusion, the effect of a wide range of different solute atoms on the diffusion coefficient is unknown. In an incoherent grain boundary space limitations are probably not so critical as in the lattice; thus the atomic sizes of the diffusing atoms are not likely to be a determining factor.

According to Smidoda et al[134], D_B at 900°C in a Ni-Cr-Al alloy is 4.95×10^{-4} cm^2 sec^{-1} for a migrating boundary and 1.1×10^{-7} cm^2 sec^{-1} for a static boundary; for temperatures around 1150°C, their values should be increased by a factor of 10^2 approximately. Nevertheless, Mittemeijer and Beers[55] and Grovenor[56] found similar values for D_B at migrating and stationary boundaries.

Some experiments on the effect of the crystallographic orientation on the surface diffusion of Ni in Ni-single crystals[135], compared the diffusion coefficients for the orientations (100), (110), (111). For temperatures around 1120°C - 1170°C the coefficients were of the order of 10^{-5} cm^2 sec^{-1}, but no clear trend as to which orientation resulted in the highest coefficient was apparent. Grain boundary diffusion coefficients of Cr in Inconel 600 at temperatures from 400°C to 800°C were obtained[136] using the equation $D_B = 0.86 \times 10^{-1}$ $\exp(-Q/RT)$ cm^2 sec^{-1}, $Q = 179.5$ KJ mol^{-1}. Extrapolating the equation to the temperature of 1150°C the diffusion coefficient was found to be 2.3×10^{-8} cm^2 sec^{-1}, but extrapolation over a large temperature range should be considered cautiously.

As it can be seen, the data on the grain boundary diffusion coefficient as a function of temperature for different alloys is limited and sometimes contradictory. It is however believed that $D_B = 10^{-5}$ cm^2 sec^{-1} is a reasonably approximation[134,135] for diffusion at $\sim$ 1150°C and finally, $\delta D_B/\bar{\lambda}^2 = 5 \times 10^{-4}$ cm sec^{-1}.

The concentration term of the growth rate equation according to Turnbull's[38] equation, viz. $C_o - C_E/C_o$, is probably near 1, as the concentration of Al and Ti in the matrix after γ' precipitation is much reduced (see Table 3.6); then the equation result is a good approximation with the experimentally found values for the growth rate (0.6×10^{-4} cm sec^{-1}).

Aaronson and Liu's[40] simplified equation, viz. $v = 4\ D_B\ \delta/\bar{\lambda}^2$ would give results nearly five times larger than those obtained using Turnbull's equation; the assessment of D_B is however not accurate enough to allow the identification of the best fit for the experimental data.

4.6 Discontinuous Coarsening Reaction Kinetics

For the isothermal discontinuous coarsening reaction, it has been found that the growth rate of the migrating boundary is reduced by a factor of $10^3 - 10^4$ as compared with the discontinuous reaction occurring during continuous cooling. This partially arises from the decrease in grain boundary mobility at lower temperatures, but mostly by the significant decrease in the driving force. As previously discussed (section 4.2.6), the main driving force for the reaction during continuous cooling arises from the supersaturation of the matrix, a condition which is greatly reduced after the continuous (and discontinuous) precipitations.

The discontinuous phase is, however, in metastable equilibrium and its replacement by a coarsened structure results from a reduction in the interfacial free energy; the initial mechanism for this reaction appears to originate from grain boundary γ' precipitates growing perpendicularly to the boundary, similar to a mechanism proposed by Nes and Billdal[34], which also caused the formation of the original

discontinuous cells (section 4.2.6).

Livingston and Cahn[65] proposed that for a coarsening reaction reduction in free energy is given by

$$-\Delta F = 2\gamma\upsilon\left(\frac{1}{\lambda_1} - \frac{1}{\lambda_2}\right)$$

where γ is the surface energy

υ is the molar volume

λ_1, λ_2 are the inter-rod spacings

The equation was originally proposed to apply to discontinuous coarsening of aligned eutectoids and represents an upper limit to the driving forces available to the process.

In the present case, the surface energy was found to be ~ 8 mJ m^{-2} and the molar volume 27.8 cm^3 mol^{-1}; $\lambda_1 = 0.7$ μm, $\lambda_2 = 3$ μm (at 1050°C). Then $\Delta F = -487$ mJ mol^{-1} (0.116 cal mol^{-1}). A simple approximation for the growth rate may be calculated from the Hornbogen and Pettermann[33] equation for discontinuous growth

$$v = -8\frac{\Delta F}{RT}\frac{D_B\,\delta}{\lambda^2}$$

where ΔF in the original equation relates to concentration differences in ideal solutions. If ΔF is considered to result only from the interfacial free energy, the growth rate for the discontinuous coarsening reaction can be obtained (the term λ^2 is then substituted by λ_2^2, where λ_2 is the inter-rod spacing after coarsening).

At 1050°C the grain boundary diffusion coefficient D_B is considered to be $\sim 10^{-6}$ cm^2 sec^{-1} and the experimental values for the inter-rod spacings would refer to a growth rate $G = 1.7 \times 10^{-8}$ cm sec^{-1} which compares well with the experimental measured value of

1.4×10^{-8} cm sec^{-1}. The reduction in the interfacial energy should not however be the only driving force for the coarsening reaction, and some minor chemical effect is likely to have a role.

Livingston and Cahn pointed out in their analysis of discontinuous coarsening of aligned eutectoids, that the free-energy ΔF available for the reaction can be dissipated also by processes other than the boundary migration; for instance the existence of oblique lamellae (rods) retards the movement of the migrating boundary thus consuming an extra portion of the available driving force. If θ is the angle between the lamellae and the boundary, the total force exerted on the grain boundary is $2\gamma \sin^2\theta/\lambda_1$ and the difference $2\gamma/\lambda_1$ in the total available driving force (which accounts for at least half of the total free-energy change) is dissipated by forces parallel to grain boundary.

Livingston and Cahn[65] deduced the following equation for the growth rate :

$$V = \frac{C_b^e}{(C_\beta - C_\alpha) f_\alpha^2 f_\beta^2} \cdot 8 \frac{D_B \delta}{\lambda_2^2} \frac{\gamma \upsilon}{RT} \left(\frac{1}{\lambda_1} - \frac{1}{\lambda_2}\right)$$

where C_b^e is the equilibrium boundary concentration

C_β is the concentration of the β lamellae

C_α is the concentration of the α lamellae

f_α and f_β are the volume fractions of the α and β phases

The second part of the equation is equivalent to the Pettermann and Hornbogen equation accounting for a driving force equivalent to the total reduction in free energy ΔF.

The data on the concentration values are not available in the

present case, to enable comparison to be made with the theoretical approach proposed by Livingston and Cahn.

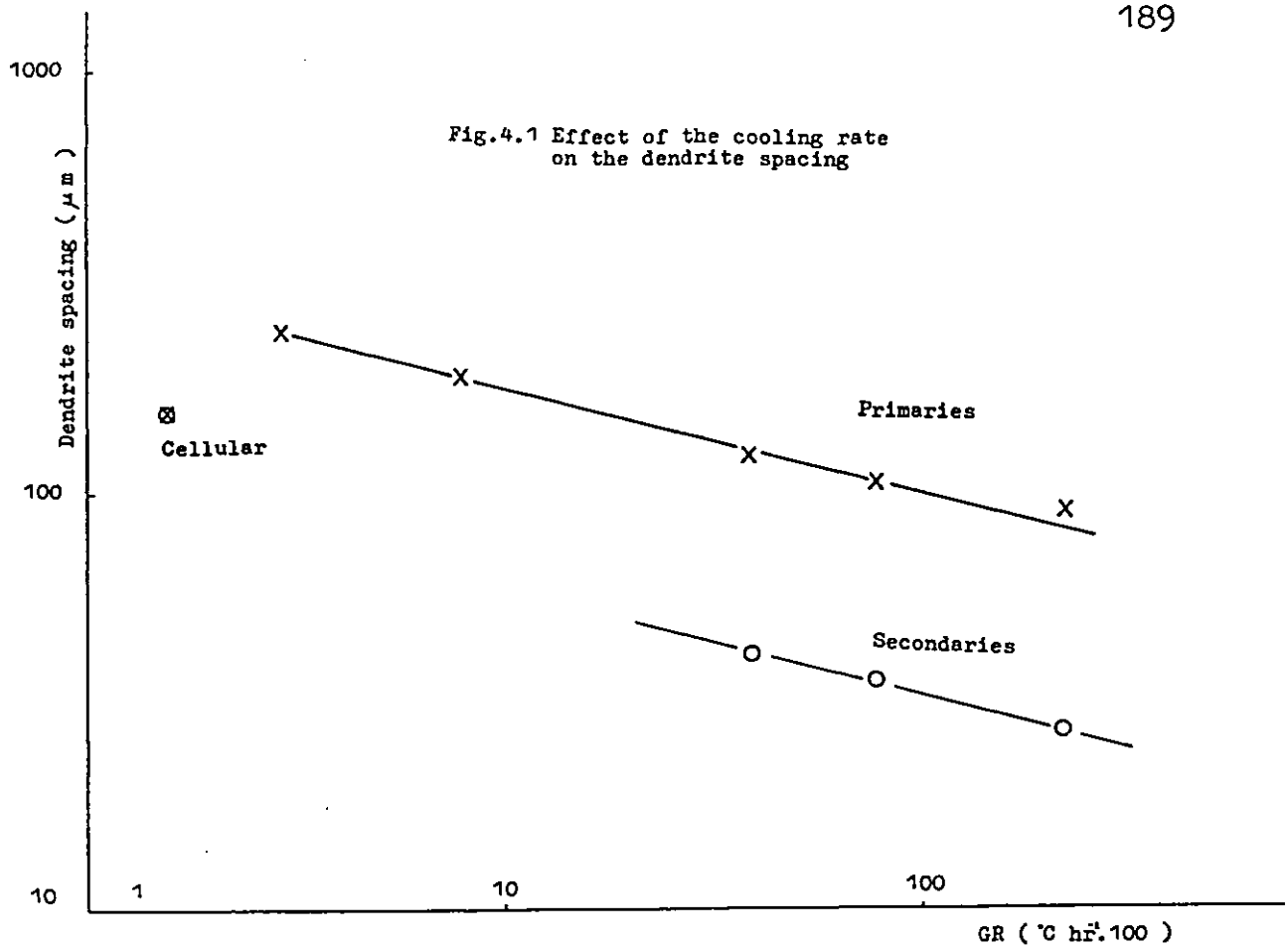

Fig.4.1 Effect of the cooling rate on the dendrite spacing

Fig.4.2 Dendrite spacing:Hunt's equation

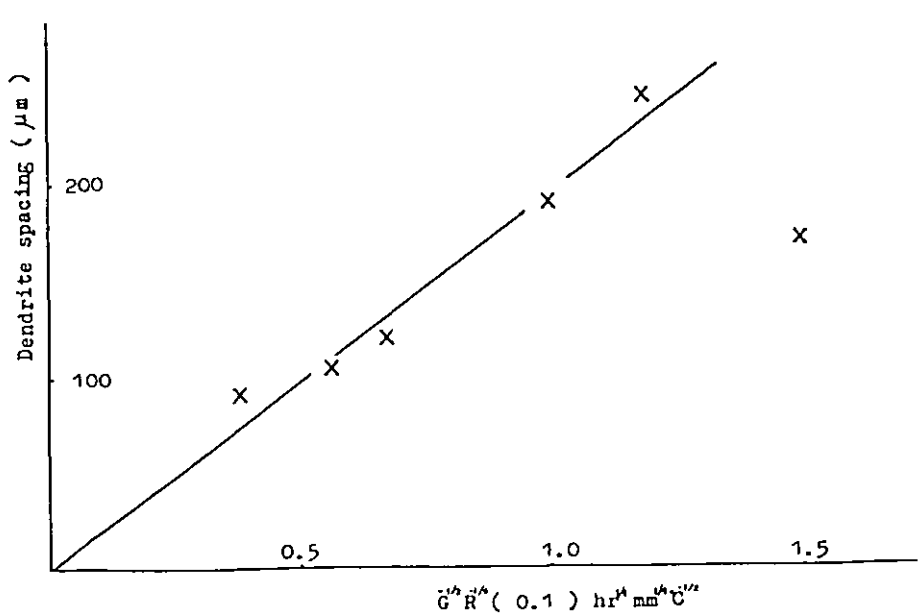

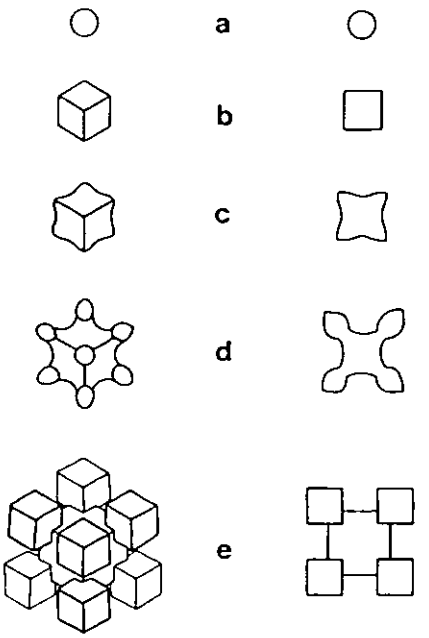

Fig.4.3 Ogdoadically diced cube formation

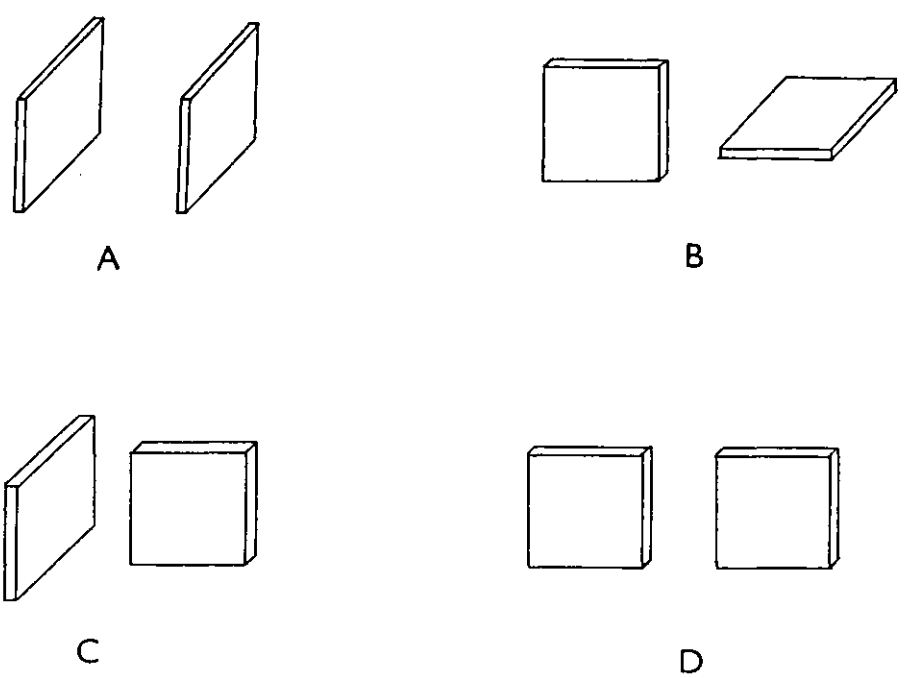

Fig.4.4 Equilibrium plate configurations

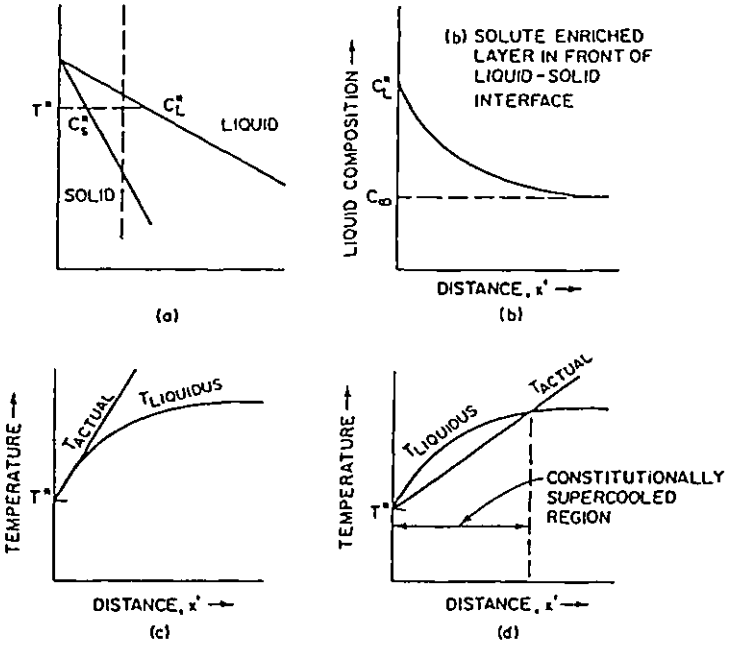

FIGURE 4.5
Constitutional supercooling in alloy solidification. (*a*) Phase diagram; (*b*) solute-enriched layer in front of liquid-solid interface; (*c*) stable interface; (*d*) unstable interface.

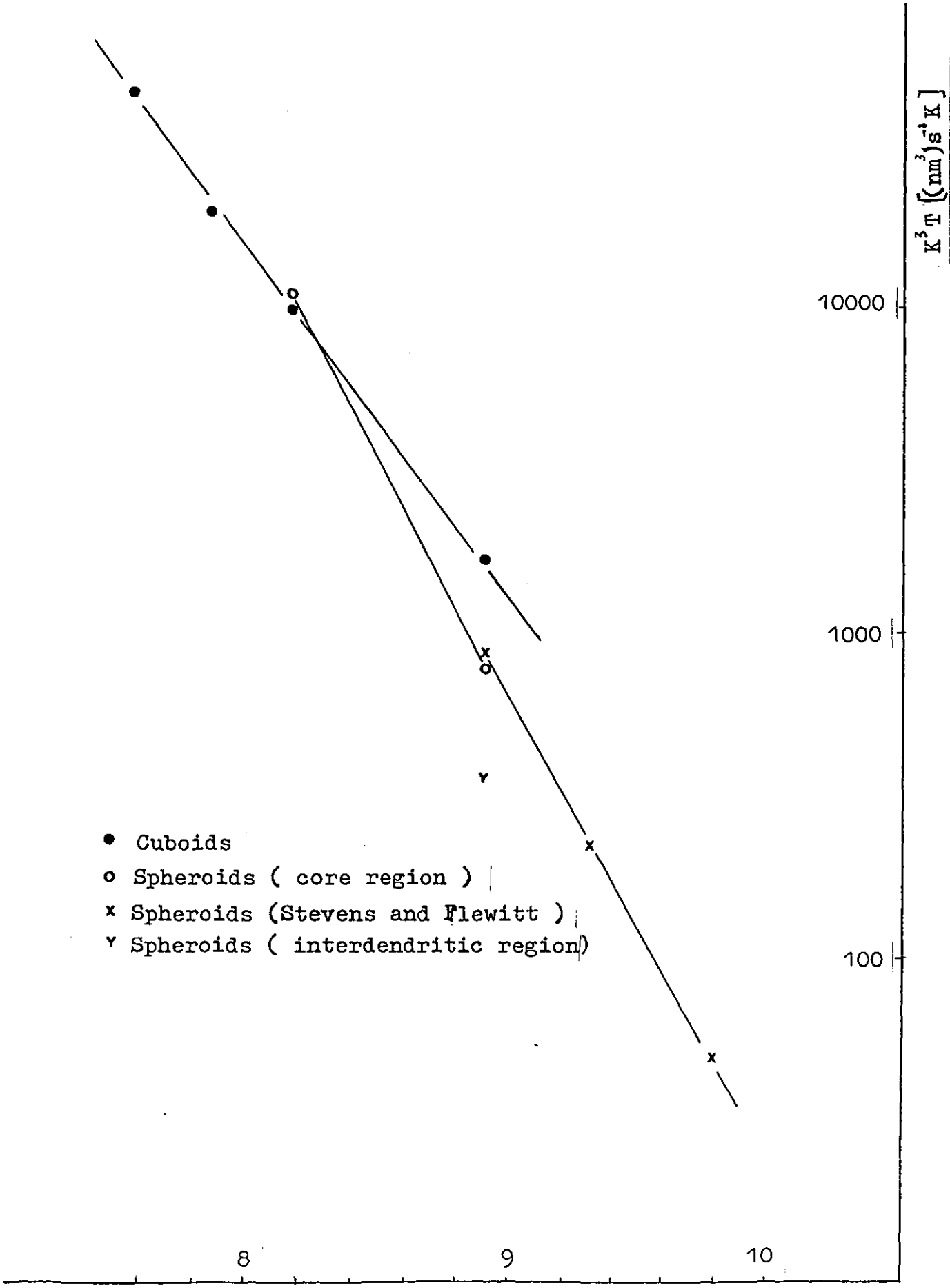

Fig.4.6 _ Activation energy

Table 4.1

Discontinuous γ' lamellae dimensions for several alloys

System	Lamellae Thickness (μm)	Interlamellar spacing (μm)
Ni-Al[142]	0.025-0.075	0.05
Ni-Co-Al[143]	0.03	0.10
Co-Ni-Ti [59]	0.05	0.11
Co-Ni-Ti-Al[144]	0.015	0.03

Table 4.2- Creep Results[96]

IN738LC processed in various ways and tested with a stress of 250 MPa at 850°C

Preparation	Heat treatment	Minimum creep rate h^{-1}	Time to 1% extension h	Rupture life h	Creep elongation %	Reduction in area %
60 mm h^{-1}, LMC	✓	1.67×10^{-5}	324	2088	23	48
60 mm h^{-1}, LMC	-	6.4×10^{-5}	146	797	24	34
60 mm h^{-1}, LMC	-	3.0×10^{-5}	299	1168	18	20
300 mm h^{-1}, LMC	-	3.9×10^{-5}	176	1708	29	49
300 mm h^{-1}, LMC	✓	2.3×10^{-5}	320	1988	29	46
300 mm h^{-1}, LMC	✓	1.9×10^{-5}	334	2145	21	48
300 mm h^{-1}, LMC	-	6.7×10^{-5}	106	995	18	28
600 mm h^{-1}, LMC	-	4.8×10^{-5}	174	1438	25	45
600 mm h^{-1}, LMC	-	4.1×10^{-5}	108	1791	25	43
600 mmhh^{-1}, LMC	✓	2.10×10^{-5}	306	1775	28	52
600 mm h^{-1}, LMC	✓	2.05×10^{-5}	254	1504	23	46
200 mm h^{-1}, ex CRM	✓	3.6×10^{-5}	188	1293	30	42
200 mm h^{-1}, ex CRM	✓	1.5×10^{-5}	315	1651	24	39
1200 mm h^{-1}, PLMC	✓	3.2×10^{-5}	224	1671	25	58
1200 mm h^{-1}, PLMC	-	4.0×10^{-5}	266	1781	22	46
conventionally cast ex H. Tipler[139]	✓	2.69×10^{-5} 2.57×10^{-5}	? ?	1038 1138	5.8 5.6	6.5 7.0

CHAPTER 5

CONCLUSIONS AND SUGGESTIONS FOR FUTURE WORK

5.1 Conclusions

The present work has investigated the structure of the nickel based alloy IN 738, low carbon, directionally solidified with several conditions of solidification rate (R) and temperature gradient at the solid-liquid interface (G); the effect of post-solidification heat treatments has also been examined. The numerical data are compiled in Tables included in Chapters 3 and 4, and a summary of the main observations and conclusions follows below.

1. The solidification structure varied according to the casting parameters, including a near plane-front condition ($\frac{G}{R} \geq 2.1\ ^{o}C\ hr\ mm^{-2}$), cellular solidification, cellular-dendritic, and several degrees of refinement for the dendritic solidification. The primary arm spacing was found to be proportional to $(GR)^{-0.247}$, the cellular-dendritic arm spacing data fitting well with the dendritic arm spacing; the inter-cellular spacing was found to fit better with the secondary arms (dendritic solidification) supplying a dependence proportional to $(GR)^{-0.35}$.

2. Microprobe investigation indicated preferential segregation of niobium, titanium, and molybdenum into the interdendritic regions, while tungsten, chromium and cobalt segregated to the core region;

no clear trend for the variations with G and R was observed. Compositions for the γ' and MC carbide phases have been determined.

The microsegregation, mostly that of Ti and Nb, raised the γ' solvus and had the effect of causing an earlier precipitation of γ' particles in the interdendritic regions during the cooling, thus resulting in larger particle sizes and a particle morphology closer to cubic shape; particles in the core region were more spherical.

3. A general refinement of the phases present, viz. MC carbides, continuous precipitated γ', γ-γ' eutectic colonies, and discontinuous γ' cells has been observed at higher cooling rates. The MC carbide particle sizes appear to be controlled by growth in the liquid, and the morphology changes from angular into Chinese-script for increased cooling rates. The effect on the γ' particle sizes arises from possible changes in the precipitation temperature due to increased undercooling for the faster cooling rates, and from the reduced time exposure at high temperatures, thus reducing solute diffusion and particle growth. The discontinuous reaction is also time dependent as it is controlled by grain boundary diffusion. Thus faster cooling rates decreased the size of the discontinuous cells and hence their volume fraction. However, also for low cooling rates approaching a cellular solidification structure, the volume fraction of the discontinuous was reduced (together with that of the γ-γ' eutectic), but this related to the initiation mechanism for the reaction rather than the growth kinetics.

4. The method termed 'interrupted solidification' allowed the investigation of the earlier stages of phase formation, and in particular the identification of the initiation mechanism for the γ'

discontinuous reaction. It has been found that fine γ' eutectic rods solidifying into the grain boundary have the effect of causing a local boundary migration and the discontinuous reaction, the driving force for further growth being supplied by the matrix supersaturation.

The way the γ' eutectic rods interact with the boundary is probably similar to a mechanism proposed by Nes and Bildall[34] for an Al-Zr alloy, which depended on the precipitation of Al_3Zr perpendicular to the grain boundary. The precipitate or, as in the present case, the γ' eutectic rod would present a high energy contact surface with the grain boundary; any morphological changes brought about by grain boundary diffusion which tended to increase this surface, would be opposed by a local force on the boundary thus initiating a local boundary migration. Matrix supersaturation supplied the driving force for the mechanism to continue.

The γ'-matrix interface being low energy would also not favour morphological changes, but the high flow of solute atoms into the rods forces lower energy branching configurations and a final fan-shape cell results.

5. The migrating boundary was usually observed to lie in preferential crystallographic plane orientations and several possible orientations were identified; however, it is believed that a (001) orientation in relation to the opposite grain is favoured and should be gradually attained, thus explaining the usual curved rod morphology.

6. The discontinuous rods presented the development of dendritic instabilities for all cooling rate conditions where the discontinuous reaction has taken place, although smooth rod surfaces have also been observed; the theoretical concepts on the development of surface

perturbations by Mullins and Sekerka[117], and by Shewmon[128] have been reviewed and applied to the present case. The large inter-rod spacing, associated with high solute concentration in the adjacent matrix resulting from the continuous cooling, favoured the mechanism; the other conditions are usually fulfilled in nickel based alloys viz. a cube-cube orientation between γ' and the matrix, low diffusivity within γ' (ordered structure) and low interfacial diffusivity (low lattice mismatch between γ' and the matrix).

7. A discontinuous coarsening (secondary) reaction characterised by a grain boundary receding mechanism was found to occur during isothermal treatment at temperatures in the range 1050°C - 1120°C, and the initiation mechanism is considered to result from grain boundary γ' precipitates exerting a local force upon the boundary in order to attain a low energy configuration (classical Nes and Billdal[34] mechanism).

8. The γ-γ' eutectic constituent was found to occur in two distinct morphologies, one consisting only of fine γ' rods and the other where the rods presented a gradual broadening (finger-type) towards the eutectic front. The coarser morphology probably arises from an increased segregation build up of γ'-forming elements at the eutectic front; a possible decrease in the local melting point occurs due to the presence of excessive amounts of zirconium ($\sim$ 4.5 wt %). Both morphologies exist for most of the cooling rates examined, but the finger-type appears to be favoured by fast rates where the solute build up is higher. The fine eutectic rod structure was found to be related to the initiation mechanism for the discontinuous reaction as opposed to the finger-type structure.

9. At lower cooling rates ($2.1 \leq GR \leq 26^{o}C\ min^{-1}$) the continuously precipitated γ' particles developed surface instabilities which resulted in the formation of 'ogdoadically diced' cube clusters. While for the rates in the top of the above range, the clusters were situated mainly in the interdendritic regions, for those rates at the bottom range the whole γ' particle distribution consisted of clusters, in some cases comprising more than eight cubic particles, or even plate-shaped particles.

The development of the cluster structure has been discussed with a similar approach to that given for the dendritic instabilities formed on the discontinuous γ' rods.

10. The effect of the commercial heat treatment ($1120^{o}C$-2 hr-AC + $845^{o}C$-16 hr-AC) on the γ' particle dispersion, was to originate a bimodal distribution of large regular cubic particles and smaller spheroidal particles in the interdendritic regions due to partial solution of the original γ' distribution during the first stage of the heat treatment. In the core region the γ' solution was more extensive, and for one solidification rate condition (300 mm hr^{-1}) all γ' particles were put into solution and a fine distribution of spheroidal particles resulted from cooling.

11. The commercial heat treatment had also the effect (first stage) of removing the dendritic instabilities from the discontinuous γ' rods and developing a serrated rod surface. After the second stage ($845^{o}C$-16 hrs-AC) a continuous layer of $M_{23}C_6$ (M = Cr,Mo,Ti,W,Nb,Ta) developed along the grain boundaries.

12. Concerning the results obtained by the National Physical

Laboratory for creep rate and rupture life (specimens solidified at R = 60, 300 and 600 mm hr^{-1}), there is no clear evidence to suggest that the discontinuous cells formed at 60 mm hr^{-1} were responsible for the poorer performance of the as-cast material. The hardness of the discontinuous cell regions was found to have similar levels to those from the matrix. It is more likely that the continuous γ' structure, consisting of ogdoad clusters, had a detrimental effect on the mechanical properties far greater than that caused by a small volume fraction of discontinuous cells.

13. The coarsening kinetics of the continuously precipitated γ' particles have been studied for temperatures ranging from 850°C to 1050°C; values for the coarsening rates have been obtained and are given in Table 3.17. The activation energies found for the diffusion mechanism during coarsening of the cuboidal and spherical particles were 2.0×10^2 KJ $mole^{-1}$ and 3.0×10^2 KJ $mole^{-1}$ respectively; the high value for the spherical particles as compared with previously found values for Al or Ti diffusion in Ni based alloys (2.7×10^2 KJ $mole^{-1}$ and 2.57×10^2 KJ $mole^{-1}$ respectively) could be explained by the assumption of a temperature independent C_e factor. However, the low activation energy obtained for the cuboidal particles would require a more complex explanation, if it is assumed that the particle sizes and coarsening rates have been correctly assessed; this may arise from the fact that a bimodal distribution of γ' particles (spheres and cuboids) were present for most of the coarsening times studied at low temperatures, while at temperatures above 950°C, the distribution consisted only of cubic particles after short time coarsening.

The γ-γ' surface energy was estimated at 8 mJ m^{-2}.

14. The growth rate of the migrating boundary during discontinuous γ' formation has been experimentally calculated at $\sim 0.6\ 10^{-4}$ cm sec^{-1}. Although approximate results could be found applying Aaronson and Liu's or Turnbull's theoretical approach, these depended on the assessment of the grain boundary diffusion coefficient, and any extrapolation for complex alloys should be treated cautiously.

15. The growth rate for the coarsening discontinuous (secondary) reaction was found to be much slower $v = 1.4\ 10^{-8}$ cm sec^{-1}, which closely agreed with the Petterman and Hornbogen equation, assuming the decrease in free energy for the coarser rod structure to drive the boundary migration and without energy dissipation. Caution should also be considered for the applied grain boundary diffusion coefficient value.

5.2 Suggestions for Further Work

For future work it is considered to be important to cover some areas not fully investigated presently, in relation to the discontinuous phase formation. Thin foil studies would be necessary in order to identify more properly the preferential crystallographic orientation for the migrating boundary, as well as studies of the γ-γ' interface; determination of the transformed matrix composition is important for the growth kinetics. These studies should be perferably carried out with specimens solidified at R = 30 mm hr^{-1} and G = 13°C mm^{-1} which resulted in the highest volume fraction of discontinuous cells for the conditions examined.

Further examinations of 'interrupted solidification' specimens are also needed in relation to the initiation mechanism for the discontinuous reaction. In the literature mention has often been made of the expected advantages in terms of mechanical properties of controlling the discontinuous phase growth in order to produce a fully aligned rod or lamellar structure more refined than that usually obtained at eutectic composites. It is possible that the mechanisms for discontinuous formation and growth presented in this thesis have a contribution to make in this direction, thus justifying further research.

It is also suggested that further investigation of the solute segregation during eutectic solidification should be carried out; in this respect the work is recommended to include binary Ni-Al alloys, with additions of other elements such as Zr.

REFERENCES

1. C.T. Sims and W.C. Hagel, The Superalloys, John Willey and Sons, New York, 1972.

2. R.F. Decker, Strengthening Mechanisms in Nickel-base Superalloys, International Nickel Company, New York, 1969.

3. G.P. Sabol, R. Stickler, Phys.Stat.Sol., vol.35, p.11, 1969.

4. L.M. Brown, R.K. Ham, Strengthening Methods in Crystals, Elsevier, Amsterdam, 1971, pp.9-135.

5. V. Gerold, H. Haberkorn, Phys.Stat.Sol., vol.16, p.675, 1966.

6. P. Beardmore, R.G. Davies, T.L. Johnston, Trans-AIME, vol.245, p.1537, 1969.

7. J.J. Jackson, M.J. Donachie, R.J. Henricks, M. Gell, Met. Trans., vol.8A, p.1615, 1977.

8. G.W. Greenwood, Acta.Met., vol.4, p.243, 1956.

9. I.M. Lifshitz, V.V. Slyozov, J.Phys.Chem.Solids, vol.19, 1961.

10. C. Wagner, Z. Electrochem., vol.65, p.581, 1961.

11. A.J. Ardell, Acta Met., vol.20, p.61, 1972.

12. J.D. Livingstone, Trans-AIME, vol.215, p.566, 1959.

13. D.H. Ben Israel, M.E. Fine, Acta Met., vol.11, p.1051, 1965.

14. A.J. Ardell, R.B. Nicholson, J.D. Eshelby, Acta Met., vol.14, p.1295, 1966.

15. W.O. Gentry, M.E. Fine, Acta Met., vol.20, p.181, 1972.

16. A.J. Ardell, R.B. Nicholson, J.Phys.Chem.Solids, vol.27, p.1793, 1966.

17. A.J. Ardell, Acta Met., vol.16, p.511, 1968.

18. W.H. Hagel, H.J. Beattie, Trans-AIME, vol.215, p.967, 1959.

19. J.H. Westbrook, Z. Kristallogr., vol.110, p.21, 1958.

20. P. Nash, PhD Thesis, University of London, 1978.

21. J.K. Tien, S.M. Copley, Met.Trans., vol.2, p.215, 1971.

22. E.H. van der Molen, J.M. Oblak, O.H. Kriege, Met.Trans., vol.2, p.1627, 1971.

23. D.J. Chellman, A.J. Ardell, Acta Met., vol.22, p.577, 1974.

24. P.K. Rastogi, A.J. Ardell, Acta Met., vol.29, p.321 , 1971.

25. V. Biss, D.L. Sponseller, Met.Trans., vol.4, p.1953. 1973.

26. H.O. Kirchner, Met.Trans., vol.2, p.2861, 1971.

27. A.J. Ardell, Acta Met., vol.20, p.601, 1972.

28. M. Hillert, Met.Trans., vol.3, p.2729, 1972.

29. D.B. Williams, E.P. Butler, International Metals Review, no.3, p.153, 1981.

30. K.N. Tu, D. Turnbull, Acta Met., vol.15, p.1317, 1967.

31. R.A. Fournelle, J.B. Clark, Met.Trans., vol.3, p.2757, 1972.

32. B. Predel, W. Gust, Met.Trans., vol.3, p.1237, 1975.

33. J. Petterman, E. Hornbogen, Z. Metall., vol.59, p.814, 1968.

34. E. Nes, H. Billdal, Acta Met., vol.25, p.1039, 1977.

35. C.S. Smith, ASM Trans.Quart., vol.45, p.533, 1953.

36. K.N. Tu, Met.Trans., vol.3, p.2769, 1972.

37. C. Zener, Trans-AIME, vol.167, p.550, 1946.

38. D. Turnbull, Acta Met., vol.3, p.55, 1955.

39. J.W. Cahn, Acta Met., vol.7, p.18, 1959.

40. H.I. Aaronson, Y.C. Liu, Scripta Met., vol.2, p.1, 1968.

41. M.S. Sulonen, Acta Met., vol.12, p.749, 1964.

42. H. Bohm, Z.Metall., vol.52, p.518, 1961.

43. H.I. Aaronson, J.B. Clark, Acta Met., vol.16, p.845, 1968.

44. E. Hornbogen, Met.Trans., vol.3, p.2717, 1972.

45. G. Meyrick, Scripta Met., vol.10, p.649, 1976.

46. W. Gust, Phase Transformations, vol.1, II.27, Inst. of Metallurgists, London, 1979.

47. H. Gleiter, Phys.Stat.Sol., vol.45, p.9, 1971(b).

48. W.W. Mullins, Acta Met., vol.4, p.421, 1956.

49. R. Wirth, H. Gleiter, Acta Met., vol.29, p.1825, 1981.

50. H. Westgren, N. Ryen, Mat.Sci.Eng., vol.34, p.227, 1978.

51. P.H. Pumphrey, H. Gleiter, Phil.Mag., vol.32, p.881, 1975.

52. W. Hawn, H. Gleiter, Acta Met., vol.29, p.601, 1981.

53. K. Lücke, G. Gottstein, Acta Met., vol.29, p.779, 1981.

54. R.W. Balluffi, J.W. Cahn, Acta Met., vol.29, p.493, 1981.

55. E.J. Mittemeijer, A.M. Beers, Thin Solid Films, vol.74, p.257, 1980.

56. C.R.M. Grovenor, Scripta Met., vol.16, p.317, 1982.

57. E. Hornbogen, M. Roth, Z.Metall., vol.58, p.842, 1967.

58. C. Frantz, M. Gantais, Proc. 3rd Int. Conf. on Strength of Metals and Alloys, Cambridge, vol.1, p.331, 1973.

59. O.V. Tsinenko, L.S. Pshenina, Y.K. Nazarov, A.D. Korotayev, Fiz.Met.Metall., vol.32, p.58, 1971.

60. K. Detert, H. Pohl, Z.Metall., vol.55, p.36, 1964.

61. J.M. Oblak, W.A. Owzarski, Trans-AIME, vol.242, p.1563, 1968.

62. R.O. Williams, Trans-AIME, vol.215, p.1026, 1959.

63. K. Smidoda, C. Gottschalk, H. Gleiter, Metal Science, vol.13, p.146, 1979.

64. R.A. Fournelle, Acta Met., vol.27, p.1135, 1979.

65. J.D. Livingston, J.W. Cahn, Acta Met., vol.22, p.495, 1974.

66. J. Petterman, E. Hornbogen, Z.Metall., vol.59, p.814, 1968.

67. C.Y. Barlow, B. Ralph, J.Mat.Sci., vol.14, p.2500, 1979.

68. F.L. Versnyder, R.W. Guard, Trans.ASM, vol.52, p.485, 1960.

69. B.J. Piearcey, B.H. Kear, R.W. Smashey, Trans.ASM, vol.60, p.634, 1967.

70. B.J. Piearcey, B.E. Terkelson, Trans-AIME, vol.239, p.1143, 1967.

71. W.A. Tiller, J.W. Rutter, K.A. Johnson, B. Chalmers, Acta Met., vol.1, p.428, 1953.

72. J.K. Tien, R.P. Gamble, Mat.Sci.Eng., vol.8, p.152, 1971.

73. J.K. Tien, R.P. Gamble, 2nd Int. Conf. Strength Met. Alloys, ASM, vol.3, p.1037, 1970.

74. M. McLean, F. Schubert, High Temp. Alloys for Gas Turbines, Applied Sci.Pub.Ltd., London, p.423, 1978.

75. G.R. Kotler, K.W. Carey, G.S. Cole, Met.Trans., vol.3, p.723, 1972.

76. S.N. Tewari, A.M. Sriramamurthy, Met. Trans., vol.12A, p.137, 1981.

77. G.D. Merz, T.Z. Kattamis, Met.Trans., vol.8A, p.295, 1977.

78. A.K. Bhambri, T.Z. Kattamis, J.E. Morral, Met.Trans., vol.6B, p.523, 1975.

79. E.P. Whelan, J.Inst.Metals, vol.100, p.333, 1972.

80. P. Viatour, D. Coutsouradis, L. Habraken, J.M. Drapier, High Temp. Alloys for Gas Turbines, Applied Sci.Pub.Ltd., London, vol.3, p.875, 1978.

81. S.C. Fegan, T.Z. Kattamis, J.E. Morral, A.K. Bhambri, J.Mat. Sci., vol.10, p.1266, 1975.

82. R. Fernandez, J.C. Lecomte, T.Z. Katamis, Met.Trans., vol.9A, p.1381, 1978.

83. R.A. Stevens, P.E.J. Flewitt, Mat.Sci.Eng., vol.37, p.237, 1979.

84. M.C. Bacon, R.F. Smart, Metalurgia, vol.45, p.68, 1978.

85. C.G. Bieber, J.R. Mihalisin, 2nd Conf. Strength Met. Alloys, ASM, vol.3, p.1031, 1970.

86. W. Hoffelner, E. Kny, R. Stickler, W.J. McCall, Report 76 - UW - COST B6, Vienna.

87. G.M. McColvin, Metal Science, vol.10, p.447, 1977.

88. R.A. Stevens, P.E.J. Flewitt, J.Mat.Sci., vol.13, p.367, 1978.

89. G.S. Ansell, J. Weertman, Trans-AIME, vol.215, p.841, 1959.

90. Y. Lindblom, High Temp. Alloys for Gas Turbines, Applied Sci. Pub.Ltd., London, p.285, 1978.

91. H. Gleiter, E. Hornbogen, Mat.Sci.Eng., vol.2, p.285, 1967/68.

92. V. Lupino, T.B. Gibbons, High Temp. Alloys for Gas Turbines, p.335, Applied Sci.Pub.Ltd., London, 1978.

93. G.M. McColvin, High Temp. Alloys for Gas Turbines, p.599, Applied Sci.Pub.Ltd., London, 1978.

94. M.C. Bacon, R.F. Smart, High Temp. Alloys for Gas Turbines, p.653, Applied. Sci. Pub. Ltd., London, 1978.

95. E. Bachelet, G. Lesoult, High Temp. Alloys for Gas Turbines, p.665, Applied Sci. Pub. Ltd., London, 1978.

96. P.N. Quested, M. McLean, K. Menzies, P. Henderson, Progress Report on Cost 50 Programme UK20, NPL, 1981.

97. R. Sallemark, Progress Report 2 Cost 50 Programme, Sweden, October 1975.

98. R.B. Scarlin, Scripta Met., vol.10, p.711, 1976.

99. M. Dahlen and L. Winberg, Acta Met., vol.28, p.41, 1980.

100. D.A. Woodford, J.J. Frawley, Met.Trans., vol.5, p.2005, 1974.

101. R.B. Scarlin, M.O. Speidel, Final Report on Cost 50 Programme, CH3/3, 1976.

102. G.W. Meetham, High Temp. Alloys for Gas Turbines, p.837, Applied Sci. Pub. Ltd., London, 1978.

103. T. Geiger, R. Stickler, G.H. White, High Temp. Alloys for Gas Turbines, p.317, Applied Sci. Pub. Ltd., London, 1978.

104. C.J. Burton, ed. by Superalloys, Metallurgy and Manufacture, Proc.3rd Int.Symp.High Temp.Alloys Committee AIME, Seven Springs, Pa New York, p.147, 1976.

105. P.J. Henderson, NPL Internal Report, 1981.

106. R.A. Stevens, P.E.J. Flewitt, Mat.Sci. and Eng., vol.50, p.271, 1981.

107. E. Orowan, Symposium on Internal Stresses in Metals, Institute of Metals, London, p.451, 1948.

108. M.O. Speidel, High Temperature Alloys for Gas Turbines, p.469, Applied Sci.Pub.Ltd., London 1978.

109. J.W. Cahn, J.D. Pan, R.W. Balluffi, Scripta Met., vol.13, p.503, 1979.

110. W.A. Tiller, J.W. Rutter, Can.J.Phys., vol.34, p.729, 1956.

111. L.S. Lasak, M.Sc Thesis, Rensselaer Polytechnic Institute, Troy, New York, 1976.

112. J.J. Montoya-Cruz, R. Kadalbal, T.Z. Kattamis, A.F. Giamei, Met.Trans., vol.13A, p.1153, 1982.

113. J.D. Hunt, Solidification and Casting of Metals, p.3., The Metals Society, London, 1979.

114. L.K. Singhal, J.W. Martin, Journal of the Iron and Steel Institute, September 1967, p.947.

115. G.V. Seregin, Fiz. Metall. Metalloved, vol.50, p.81, 1980.

116. R.A. Ricks, A.J. Porter, R.C. Ecob, Acta Met., vol.31, p.43, 1983.

117. W.W. Mullins, R.K. Sekerka, J.Appl.Phys., vol.34, p.323, 1963.

118. R.F. Sekerka, J. Cryst. Growth, vol.3, p.71, 1968.

119. T. Miyazaki, H. Imamura, H. Mori, T. Kozakai, J.Mat.Sci., vol.16, p.1197, 1981.

120. J.E. Doherty, B.H. Kear, A.F. Giamei, J.Metals, vol.23, p.59, November, 1971.

121. V.Y. Markiv, V.V. Burnashova, Izv. Aked. Nauk, USSR Metally, No.6, p.1356, 1969.

122. R.B. Elliot, Constitution of Binary Alloys, Supplement 1, McGraw Hill, 1965.

123. M. Oblak, W.A. Owczarski, Trans.AIME, Vol.242, p.1563, 1968.

124. M. Dahlen, L. Winberg, Acta Met., vol.28, p.41, 1980.

125. P.S. Kotval, J.D. Venables, R.W. Calder, Met.Trans., vol.3, p.453, 1972.

126. C.M. Potter, J.A. Spittle, Phase Transformations, Spring Conference, The Institution of Metallurgists, 1979.

127. J.A. Malcom, G.R. Purdy, Trans.Met.Soc.AIME, vol .239, p.1391, 1967.

128. P.G. Shewmon, Trans.Met.Soc.AIME, vol.233, p.736, 1965.

129. R.D. Doherty, Met.Sci., vol.16, p.1, 1982.

130. F.A. Nichols, W.W. Mullins, Trans.Met.Soc.AIME, vol.233, p.1840, 1965.

131. A. Vogel, DPhil thesis, 1977, University of Sussex.

132. J.W. Cahn, Acta Met., vol.8, p.556, 1960.

133. J.K. Tien, S.M. Copley, Met.Trans, vol.2, p.215, 1971.

134. K. Smidoda, W. Gottschalk, H. Gleiter, Acta Met., vol.26, p.1833, 1978.

135. N. Azerri, R.L. Colombo, Metallography, vol.9, p.233, 1976.

136. D.D. Pruthi, M.S. Anand, R.P. Agarwala, J.Nucl.Met., 64 (1/2), p.206, 1977.

137. B.E. Sundquist, Met.Trans., vol.4, p.1919, 1973.

138. J.M. Shapiro, J.S. Kirkaldi, Acta Met., vol.16, p.579, 1968.

139. H.R. Tipler, M.S. Peck, 2nd Progress Report on COST 50 Programme, UK-17, 1980.

140. J. Heslop, Cobalt, vol.24, 128, 1964.

141. W.I. Mitchell, Z. Metall,, vol.57, p.586, 1966.

142. E. Hornbogen, Z. Metall., vol.58, p.842, 1967.

143. C.K.L. Davies, P. Nash, R.N. Stevens, J.Mat.Sci., vol.15, p.1521, 1980.

144. O.V. Tsinenko, L.S. Pshenina, Yu,K. Nazarov, A.D. Korotayev, Fiz.Met.Metall., no.4, vol.31, p.84, 1971.

145. R.L. Fleischer, The Strengthening of Metals, Reinhold, New York, p.93, 1964.

146. M. Avrami, J.Chem.Phys., vol.7, p.1103, 1939.

147. B.E.P. Beeston, I.L. Dillamore, R.E. Smalman, Met.Sci.J., vol.2, p.12, 1968.

APPENDIX

Nickel Based Alloy Compositions

wt%	Ni	C	Cr	Co	Ti	Al	Mo	Nb	W	Ta	Zr	Hf	B
IN 738 LC	balance	0.12	15.8	8.3	3.44	3.46	1.72	0.83	2.58	1.77	0.055	-	-
IN 100	balance	0.15	10.0	15.0	4.7	5.5	3.0	-	-	-	0.05	-	0.015
Mar-M200	balance	0.13	9.0	10.0	2.0	5.0	-	1.0	12.0	-	0.05		0.015
Mar-M002	balance	0.15	9.0	10.0	1.5	5.5	-	-	10.0	2.5	-	1.5	-
IN 713 LC	balance	0.05	12.0	-	0.6	5.9	4.5	2.0	-	-	0.08	-	0.010
Mar-M246	balance	0.15	9.0	10.0	1.5	5.5	2.5	-	10.0	1.5	0.05	-	0.015